THE UNIVERSITY OF HULL

MODEL BASED METHODS FOR SENSOR FAULT-TOLERANT CONTROL OF RAIL VEHICLE TRACTION.

being a thesis submitted for the Degree of

PhD

in the University of Hull

by

STEPHEN BENNETT

M. Eng. Electronics Systems (York)

November 1998

Stephen Bennett.

Model Based Methods for Sensor Fault-Tolerant Control of Rail Vehicle Traction.

This thesis explores the application of modern fault-detection methods to electric rail traction drives. Such drives consist of three main components, induction motors, power inverters and the control system. The power electronics are relatively simple so the scope for fault-tolerance is limited, whilst fault-detection techniques for induction motors are already well developed. There is however scope for work on the instrumentation. The thesis concentrates on the use of model-based techniques to produce a torque and flux estimator for an induction motor which is tolerant to intermittent sensor disconnections.

The motors are controlled on torque and flux, these cannot be measured directly and are estimated from measurements of the applied voltages and the resulting currents. The existing estimator has poor steady-state performance at low speed and because of it's transient dynamics it is prone to sensor noise and disconnections.

Induction motors have speed-dependent dynamics and the resulting state-space model has terms which are multiplied by speed, this model is strongly bilinear. Speed-dependent feedback is needed to give desirable dynamics to the state estimates. Starting from a state-space model for the induction motor, a closed-loop observer can be designed to estimate the motor states. A range of feedback methods for the observer have been considered, from gain scheduling to sliding mode techniques. These are evaluated in simulation, using a simplified model of the traction system. The simulation neglects many second order effects which would affect the real application. Using data from an induction motor test-rig the observers are shown to be able to track the motor torque during a change in operating condition. Only a limited set of data is available. The influence of parameter mis-match, noise and speed sensor errors are considered by deriving frequency domain expressions for the estimation error in the presence of uncertainty or disturbances. The effect of the observer's gain on its sensitivity to these are considered under conditions which occur in the real application.

Using observer feedback to decouple sensors from the estimation a range of sensor fault-detection schemes are developed. In this way a bank of observers is designed which are independent of a different subset of sensors, this enables sensor faults to be isolated. These method are compared in simulation.

A motor, inverter and instrumentation are set up, with a DSP to run an observer based sensor fault-detection scheme in real-time. This enables implementation aspects to be explored, such as discretisation, model mis-match and motor loading. These affect the

detection by increasing fault-free residual or reducing the fault residual. For a each type of sensor the area of the motor operating range, where a fault is detectable is defined.

Abstract

This thesis explores the application of modern fault-detection methods to electric rail traction drives. Such drives consist of three main components, induction motors, power inverters and the control system. The power electronics are relatively simple so the scope for fault-tolerance is limited, whilst fault-detection techniques for induction motors are already well developed. There is however scope for work on the instrumentation. The thesis concentrates on the use of model-based techniques to produce a torque and flux estimator for an induction motor which is tolerant to intermittent sensor disconnections.

The motors are controlled on torque and flux, these cannot be measured directly and are estimated from measurements of the applied voltages and the resulting currents. The existing estimator has poor steady-state performance at low speed and because of it's transient dynamics it is prone to sensor noise and disconnections.

Induction motors have speed-dependent dynamics and the resulting state-space model has terms which are multiplied by speed, this model is strongly bilinear. Speed-dependent feedback is needed to give desirable dynamics to the state estimates. Starting from a state-space model for the induction motor, a closed-loop observer can be designed to estimate the motor states. A range of feedback methods for the observer have been considered, from gain scheduling to sliding mode techniques. These are evaluated in simulation, using a simplified model of the traction system. The simulation neglects many second order effects which would effect the real application. Using data from an induction motor test-rig the observers are shown to be able to track the motor torque during a change in operating condition. Only a limited set of data is available. The influence of parameter mis-match, noise and speed sensor errors are considered by deriving frequency domain expressions for the estimation error in the presence of uncertainty or disturbances. The effect of the observer's gain on its sensitivity to these are considered under conditions which occur in the real application.

Using observer feedback to decouple sensors from the estimation a range of sensor fault-detection schemes are developed. In this way a bank of observers is designed which are independent of a different subset of sensors, this enables sensor faults to be isolated. These method are compared in simulation.

A motor, inverter and instrumentation are set up, with a DSP to run an observer based sensor fault-detection scheme in real-time. This enables implementation aspects to be explored, such as discretisation, model mis-match and motor loading. These effect the detection by increasing fault-free residual or reducing the fault residual. For a each type of sensor the area of the motor operating range, where a fault is detectable is defined.

Acknowledgements.

The author would like to acknowledge the financial support of the ESPRC and the Mechanical Engineering Centre, part of GEC-Alsthom, in funding the ESPRC-CASE Award, also the additional support of the MEC in funding the building of the test-rig and loan of DSP equipment and the ESF COSY program for the exchange visits with Aalborg University in Denmark.

Thanks are due to all who helped, either directly or indirectly, with this thesis. The author wishes to thank the following people specifically:-

- *Peter Knight* has head of the control group at MEC and *Dominic Newton* as project manager of the Advanced Traction and Braking project for supporting the initial CASE award, making the facilities at MEC available and there continued support.

- *Mogens Blanke, Claus Tyubo, Per Bras* and *Henrik Rasmussen* at the Control Group of Aalborg University for practical help with designing the test-rig and access to data from the test-rig in Aalborg.

- *Derek Shields* at Coventry University for help and support with Bilinear Observers and Stability Theory.

- At MEC, *Bob Page* for help with the power electronics, *Mike Tometski* for locating components and *Pete Bates* for building the Hardware.

- *Robert Bennett, John Lewis* and *Barbara Smith* for proof-reading the various drafts of the thesis.

Special thanks are due to my two supervisors.

Ron Patton at Hull University for setting up the initial contact with GEC, enabling me to attend several major conferences which help establish the connections which proved to be invaluable and encouragement throughout.

Steve Daley, who far exceeded all that could be expected of an industrial supervisor, with regular supervision in the early days, encouragement to submit work to conferences, suggesting appropriate reading and later helping to find additional funding to build the test-rig.

This thesis is dedicated to the memory of *E.K.B.*

Declaration

This thesis describes the results of my own work. Any reference to the work of other researchers is clearly indicated in the text. Neither the whole nor any part of this work has already, or is currently being, submitted for any other degree or diploma to this or any other university or institute of learning.

The materials contained in the following papers previously published by the author have been incorporated in this thesis;

- 'Methods for fault diagnosis in railway vehicle traction and braking systems.' S. Daley, D.A. Newton, S.M.Bennett and R.J.Patton. IEE Colloquium Qualitative and Quantitative modelling methods for fault diagnosis. York 1995 Digest No. 1995/079

- 'Model based intermittent fault tolerance in an induction motor drive'. S.M.Bennett, R.J.Patton, S.Daley. Computer Engineering in systems applications conference, Lille France. July 1996.

- 'Torque and flux estimation for a rail traction system in the presence of intermittent sensor faults.' S.M.Bennett, R.J.Patton, S.Daley and D.A.Newton. Control 96, UK Exeter 1996. IEE Conf Pub 412.

- 'Rapid Proto-typing of a sensor fault tolerant traction control system.' IEE Colloquium Fault diagnosis in process systems. York Digest No. 1997/174

- 'Using a bilinear motor model for a sensor fault-tolerant rail drive.' S.M.Bennett, R.J.Patton and S.Daley. IFAC-Safeprocess Hull. 1997.

- 'Using a bilinear motor model for a sensor fault tolerant rail traction drive.' S.M.Bennett, R.J.Patton and S.Daley. Accepted for publication in Control Engineering Practise.

Acronyms and Abbreviations

The following commonly used acronyms are used throughout:

EMU	Electric Multiple Unit
PWM	Pulse Width Modulation
GTO	Gate Turn Off Thyristor
IGBT	Insulated Gate Bipolar Transistor
DOS	Dedicated Observer Scheme
GOS	Generalised Observer Scheme
FDI	Fault Detection and Isolation
DSP	Digital Signal Processor
DC	Direct Current
AC	Alternating Current
UIO	Unknown Input Observer
TDM	Time Division Multiplexing
IO	Input Output
EKF	Extended Kalman filter
DTI	Department of Trade and Industry
PI	Proportional Integral
ESF	European Science Foundation
BR	British Rail

Matlab, *Simulink* and *Real-Time workshop* are products of Mathworks Inc.

Cockpit and *Trace* are products of D-Space GmbH.

Table of contents

Chapter 1:

Introduction

1.1 The industrial support behind this project

During the uncertainty of the privatisation of British Rail the Department of Trade and Industry, DTI, funded a programme of large railway related projects under the 'Track Transport Initiative'. These were aimed at stimulating research and development of new technologies and techniques for the design and operation of electric multiple unit trains, EMUs. One such project was the 'Advanced Traction and Braking project' which was co-ordinated by the Mechanical Engineering Centre, MEC, a part of GEC-Alsthom. The aim of this project has been to improve the design of traction and braking control for electric rail vehicles using the current Networker class of train as a benchmark, Newton (1995).

1.2 The advanced traction and braking project

Rail transport offers two fundamental advantages over road haulage, guidance and low rolling resistance. Through the use of rails, heavy loads can be moved without the need for steering and once moving require less than a tenth of the force required by equivalent road vehicles to maintain a constant speed. The major disadvantage is the low adhesion available between metal wheels on metal rails. The co-efficient of friction is less than 28% and under poor conditions can become as low as 5%, thus limiting the acceleration and gradient that a train can climb. Problems of poor adhesion are made worse on electric trains by the control method and the brake design.

- Speed control is achieved using power-coast operation, this minimises operating inefficiencies but results in sudden torque changes on the axles.
- Modern trains use disc-brakes rather than pads braking onto the wheel rim. This reduces wear on wheels and is less susceptible to brake fade during prolonged application. However, one advantage of the old method was that the cast-iron brake pads which were used also cleaned and roughened the wheel rims which resulted in better adhesion under poor conditions.

To avoid unnecessary wheel slip / slide associated with poor adhesion, more precise control of power and braking is needed. To explore this problem the Advanced traction and braking project set out the following objectives:-

- To model a benchmark system.
- Consider improved controller designs.
- Consider better estimation of control variables.
- Investigate the application of fault-tolerance.

As part of the investigation into the last two points, MEC sponsored the work covered in this thesis.

1.3 Outline of thesis

Chapter 2 focuses on identifying the aims and objectives for this thesis. It begins by describing briefly the three major power systems in an EMU train; traction, braking and auxiliary power. The main body of the chapter considers the existing industry practice and recent academic theory on fault detection and fault tolerance as applicable to rail vehicles in general and the traction system in detail. The basic terms and methodologies for fault handling are defined.

The braking system is a safety critical system which already contains several forms of fault-tolerance. However, for the traction system fault handling techniques are not so well incorporated. The main groups of traction system faults are identified and classified into three types, mechanical, electrical and instrumentation. For each of these types of fault detection and possible applications of fault-tolerance are described.

For both electrical and mechanical faults it is shown that there is limited scope for further work. Either such work is not practical or has been developed and is awaiting implementation. This chapter argues that there is still scope for further work on the instrumentation side, with the aim of improving the quality of the estimation of control variables and making the estimates tolerant to sensor faults.

Chapter 3 outlines the development and validation of a model for the traction system which can be used as a basis for further work. Later this model is used to test new estimator designs and fault handling schemes in simulation under realistic motor operating conditions.

The basic principle of the traction system is simple. A DC supply is obtained from either a DC third rail or by rectification of an AC overhead line. Using an inverter the DC supply is chopped to produce pseudo 3 phase AC voltages to drive the induction motors. The motors are controlled by PI loops on torque and flux, which are estimated from other measurements.

In reality the traction system is complex and non-linear, because of the physics of the motors, the controller design and inverter operation. The model developed makes several assumptions and simplifications all of which are explained. The simplified model then consists of four sub-models; the motors which are modelled in a bilinear two axis state space form, the inverter as either ideal sinewave or pulse width modulated (PWM), the train dynamics which are represented by a large rotating inertia with losses and an open-loop controller. The model is validated against key operating features of the real train data supplied by GEC-Alsthom.

Chapter 4 considers the design of the estimator for torque and flux. The control variables, torque and flux, are not directly measured but are estimated from measurements of applied voltages and stator currents. The existing estimator is based on a well documented method using an open-loop model for the stator circuit. The practical implementation of this has undesirable low speed errors and transient dynamics. This chapter focuses on closed-loop observers which use error feedback to force a model to track the real plant to improve the quality of the estimates. For linear plants observer design is straightforward, however for the induction motor the dynamics are speed-dependent which complicates the design considerably. The speed-dependent dynamics create scope for a wide range of observer designs with different behaviour and characteristics. This chapter reviews the range of observer designs from the available literature and proposes several novel designs, the merits and limitations of which are compared.

The most promising designs are compared on real motor data supplied by Aalborg University. For state space observers the sensitivity of the design to noise, speed sensor errors and parameter changes can be evaluated by calculating the coupling between these effects and the observer's estimation error. With the use of frequency domain sensitivity analysis and the time domain simulations this chapter starts to outline a range of tools for the evaluation of observer-based fault detection and isolation (FDI) schemes for later use. The speed-dependency further complicates this by increasing the number of variables which must be considered.

Chapter 5 considers how the estimation of torque and flux can be made tolerant to sensor faults. This chapter initially describes the range of generic sensor fault types. This chapter focuses mainly on disconnections. These are relatively large faults and could be detected relatively easily by threshold methods. However, such faults may be intermittent and have a very brief duration. Such intermittent faults must not be capable of exciting transient dynamics in the estimator.

Since a model already exists, model-based methods for FDI are considered. From the available model-based techniques observer methods are best suited to sensor fault handling. Two techniques called the dedicated observer scheme, (DOS), and the generalised observer scheme, (GOS), are considered, these need to be extended to the bilinear motor model and to exploit the nature of three phase electrical systems. These basic observer techniques involve a bank of observers each using a different subset of the sensors. The sensitivity of these two schemes to faults is compared in the time domain. When combined with the sensitivity tools described in Chapter 4 a toolbox of methods becomes available to evaluate the observer FDI scheme under more realistic conditions. The chapter ends by considering the speed sensor which is a different type of sensor from the FDI point of view, with some unique fault modes.

It is hardly necessary to state that there are many differences between simulation and the real engineering world. Up to this point the work developed in this thesis has only been tested in simulation or through the use of sensitivity analysis. Rather than trying to develop the theory further to include some of the more recent ideas in FDI the next development was to implement the work from Chapters 4 and 5 on real hardware.

Chapter 6 describes the design of the hardware. For reasons of cost, safety and limited time it has not been possible to implement the scheme on hardware of a similar power to the real traction system, therefore a small scale test-rig was designed and built. To do this a D-Space DSP card and Matlab Real-Time Workshop was made available to run the FDI algorithm in real-time using measurements from an induction motor test-rig. This chapter details the construction of a hardware test-rig and describes the methods used to identify the parameters of the induction motor model. The DSP card offers very high floating point computing performance, onboard IO and auto-code generation from Simulink block diagrams, but it also has several limitations. The card has only four analogue input channels and the efficiency of the code produced is not necessarily very high. To overcome the limited inputs the sensors are time division multiplexed together in pairs. The main advantage of the DSP card is that it can generate the PWM switching signals onboard, which greatly simplifies the inverter hardware.

The second part of Chapter 6 focuses on identifying the model parameters for the induction motor. This involved exciting the motor dynamics to identify the unknown parameters in the model. Again there is a range of techniques available from which an appropriate method is selected. The chapter ends by validating the model and considering the load on the DSP as a consequence of running this model.

Chapter 7 considers the steps necessary to implement the generalised observer scheme method in real-time on the test-rig built in Chapter 6. For faster execution speed the algorithm has to be discretised, rather than using a numerical integration routine at each time step. This introduces two more variables into the problem; sampling rate and discretisation method, the choice of which influence the complexity and accuracy of the discrete system. A suitable choice of discretisation method and observer design is made and implemented in software for the DSP. The method is tested in real-time for a range of operating conditions. The results shown can only demonstrate that the fault handling methods can be made to work in this case and it cannot be assumed to be so for all applications. With this is mind it is not intended to try to give definitive results from the hardware. The factors which affect the detectability of sensor faults are identified. Using the analysis tools developed in Chapters 4 and 5 the methods to assess the suitability of the GOS method to the application are described.

The chapter ends by highlighting how the results of the comparisons in Chapter 5 between the sensitivities of the DOS and GOS methods predict the unsuitability of DOS methods for this application.

Chapter 8 considers the factors which influence the detectability of sensor faults which have not been analysed so far. These are model non-linearities comprising mainly saturation, more detailed consideration of the nature of noise in the system and the non-ideal behaviour of the inverter as loading increases.

Chapter 2:

Background.

This chapter explains the major systems in a modern EMU. The current industry practices and academic methods are reviewed. The application of fault tolerance as an extension to fault detection and isolation are considered using the braking system as an example. The three major fault types in the traction system are identified as; electrical, motor and instrumentation. The present work and scope for further work is considered for these systems, with a view to locating areas of possible work. The chapter ends by stressing the major factors which govern the post-privatised industry.

2.1 The Networker class of train

The Networker is a two or four carriage EMU train operated mainly on regional commuter services in the UK, Harrison & Dare (1995). The train consists of two powered carriages and up to two optional unpowered carriages, all carriages have a braking system. Typically the train carries 80 passengers per carriage at up to 90mph. The train is designed for almost continual use on stop-start urban commuter routes with minimal maintenance. The trains are designed with a capability of being coupled together automatically to form 8 or 12 unit trains. The train consists of three main systems; traction, braking and auxiliary systems mounted underneath the carriages, as shown in Fig. 2.1.

2.1.1 The traction system

The electrical power comes from either a 10KV AC overhead line or a 750V DC third rail. On the overhead system the AC is rectified to a nominal voltage of 750 DC, filtered with a large inductor to supply the inverters. The inverter 'chops' the DC supply into three phase AC to drive the traction motors. These motors are 3 phase induction motors which are spring mounted onto the bogie driving the axles through a fixed gear ratio.

2.1.2 The braking system

The train has two methods for braking, *dynamic braking* which uses the traction motors as generators to slow the train or *friction braking* which uses pneumatically operated disc brakes. The pneumatics are driven from electric compressors taking their power from the auxiliary electrical system. The braking system is a complex electro-pneumatic system, designed to be fault-tolerant and fail-safe as well as providing compensation for carriage loading and slide-prevention.

2.1.3 The auxiliary supply system

This provides electrical power for the braking system, the control equipment, the signalling systems as well as lighting, heating, air-conditioning and door operation. The supply voltage is reduced to a nominal voltage in the range 52-110V DC. This can then be converted to 50Hz AC for heating and air-conditioning or used directly e.g. for lighting. The auxiliary system also has a large lead-acid battery pack used to maintain safety-critical functions during supply interruptions and at start-up.

Pantograph
Supply filter
Drivers Cab
Powered carraige
Unpowered
Powered carraige
Train systems
Train systems
Controller
Inverter
Pnuematic System.
Air-Conditioning
Auxcillary
Power system
Disc Brakes
Motor
Coil spring
Suspension arm

2.2 Literature review of fault handling on railway systems

In general most of the fault handling presently used in the rail industry is simple condition monitoring. The older Diesel locomotives had many complex faults which could be diagnosed from the multitude of available measurements such as temperatures, oil pressures, fuel consumption and vibrations, Fry (1995). The basic electric traction equipment is acknowledged by the operators to have proved to be very reliable. Any remaining problems affecting reliability are associated with the support hardware, Mylroi (1995). Most traction system faults are with the electronics such as sensor faults or faults with the onboard computers.

It is also necessary to monitor many other systems such as the door mechanisms, heating and cooling systems, lighting, battery condition and toilet water tank levels. The development of condition monitoring for trains, in this country, has largely been done by BR Research, Preston (1995). The first system to be put into regular use was called DEMON (Diesel Engine MONitoring). Though initially only designed for diesel locomotives with their lower reliability, similar systems have been applied to electric trains and the same DEMON acronym used.

The system developed for the Networker class monitors the following information: passenger loading, door operation, brake performance, vehicle speed and acceleration, geographical position from a GPS receiver, traction system parameters, air compressor condition, battery condition and heating systems. This system is similar to many others, being developed around the world, see Roberts (1989) and Bruce & Hatton (1989). There are two distinct ways in which measured data is handled;

Logging. The unit simply stores measured data with minimal processing, it is then relayed by cellular radio at regular intervals or retrieved only when a fault occurs, Bruce *et al* (1989). The statistics gathered in this way can be used to build up a database of information for the design of maintenance schedules or new monitoring schemes.

Monitoring. The unit monitors incoming data and processes the information to make onboard decisions. When a fault is detected the unit will radio the base centre with a notification of the problem and a recommendation of the action to be taken, Fry (1995) and McDonald & Richards (1995).

With so many measurement types and the enormous volume of data available for monitoring systems a lot of work has focused on developing algorithms to handle this. These range from simple fault-tree analysis software, Rasphorst *et al* (1995), to self-learning neural network schemes, Morrelly (1995).

Brake pad wear is the limiting factor for the maintenance schedule of the Networker class of train, Preston (1995). For safety reasons the schedule is designed so that brake pads are only worn down to 50% before being replaced. Depending on the train's usage this results in a scheduled maintenance period of between 50 and 150 days. For simplicity, brake pad wear is not measured continuously. One interesting attempt at monitoring pad wear, wheel bearing temperatures and measurement of axle loading was made using a camera on the track, Preston (1995). This system was able to use image processing techniques to identify and measure pad thickness to within ±1mm. One set of equipment can monitor many trains in a day, without having to remove them from service and the most used trains are tested most frequently.

2.3 *Fault-tolerance on the EMU*

The previous section showed that condition monitoring is well accepted by the rail industry both as a concept and in practice. The EMU concept incorporates many aspects of modern fault-tolerant control theory for safety and reliability. To better understand the usage of fault-tolerance it is useful to first define the terms and describe some of the basic types of fault-tolerance.

2.3.1 Definition of fault-tolerance

A system is fault-tolerant if an 'abnormal event' does not cause the inability of the overall system to continue its original task. Fault-tolerant systems are a way of increasing overall system reliability without increasing the reliability of individual components. A fault-tolerant scheme can only use additional hardware if the cost is justified by the increase in reliability or safety. For a review of the field of fault-tolerance control see Patton (1997).

2.3.2 Types of fault-tolerance

Multiple hardware. This involves the duplication of critical hardware with a simple voting and switching routine to bypass the faulty component. This form of redundancy is common in safety-critical systems, for example the pneumatic brakes on the train or aircraft control surface actuators. However hardware duplication is expensive. The criteria for a multiple hardware fault-tolerant system is simple, there must be multiple hardware, such as the duplication of inverters and motors between powered carriages on the EMU. Reconfiguration is easy to achieve and loss of performance is limited.

Reconfigurable control. This requires that there is some indirect redundancy. For sensor faults *analytical redundancy* which uses a mathematical model to estimate a measurement based on different sensors can be used. For hardware, *functional redundancy* between dissimilar actuators can be used. An example of this is the rudder and ailerons on an aeroplane both of which can alter the aircraft's heading. For reconfigurable control, the system must remain either controllable with one actuator failed or observable with one failed measurement. Unlike multiple redundancy hardware, reconfigurable control requires a separate fault detection algorithm to isolate faults which may not be immediately apparent from the measured data. When a fault is detected the control algorithm will require altering, which may reduce performance. An

important aspect of reconfiguration is the initialisation of new control structures and the stability of systems involving switching.

Robust control. Robust control usually only refers to control which is insensitive to disturbances or model uncertainty, but it can also apply to robustness to faults. In this the controller does not explicitly know that there is a fault but inherently alters its demand to try to maintain the desired output. For example a two element heater under on/off thermostatic control will increase its duty cycle to compensate for reduced heat output when one element fails. For robust control the same controllability and observability criteria have to be met as with reconfigurable control. Alternatively a robust controller can made adaptive to track changes in the system, but may have no way of knowing that these are due to faults. For safety-critical systems it is paramount that any fault-tolerance incorporated into the design must not compromise safety by masking dangerous faults, such as increasing the speed of a fuel pump in response to a fuel leak down line of the pump.

2.3.3 Progressive degradation

An important aspect for fault-tolerant control is that it is not always necessary for the overall system to maintain the same level of performance after a fault as before. The fault-tolerant system may have a number of fall back positions, each one of which will enable the system to continue the primary function with reduced performance and fewer secondary functions. This is demonstrated by the braking system which is safety-critical and already incorporates many features of fault-tolerant control.

2.3.4 An example of fault-tolerance on the EMU, the braking system

Fig. 2.2 shows a state-tree diagram of the braking system, showing the various fault-tolerant methods and the progressive degradation of performance.

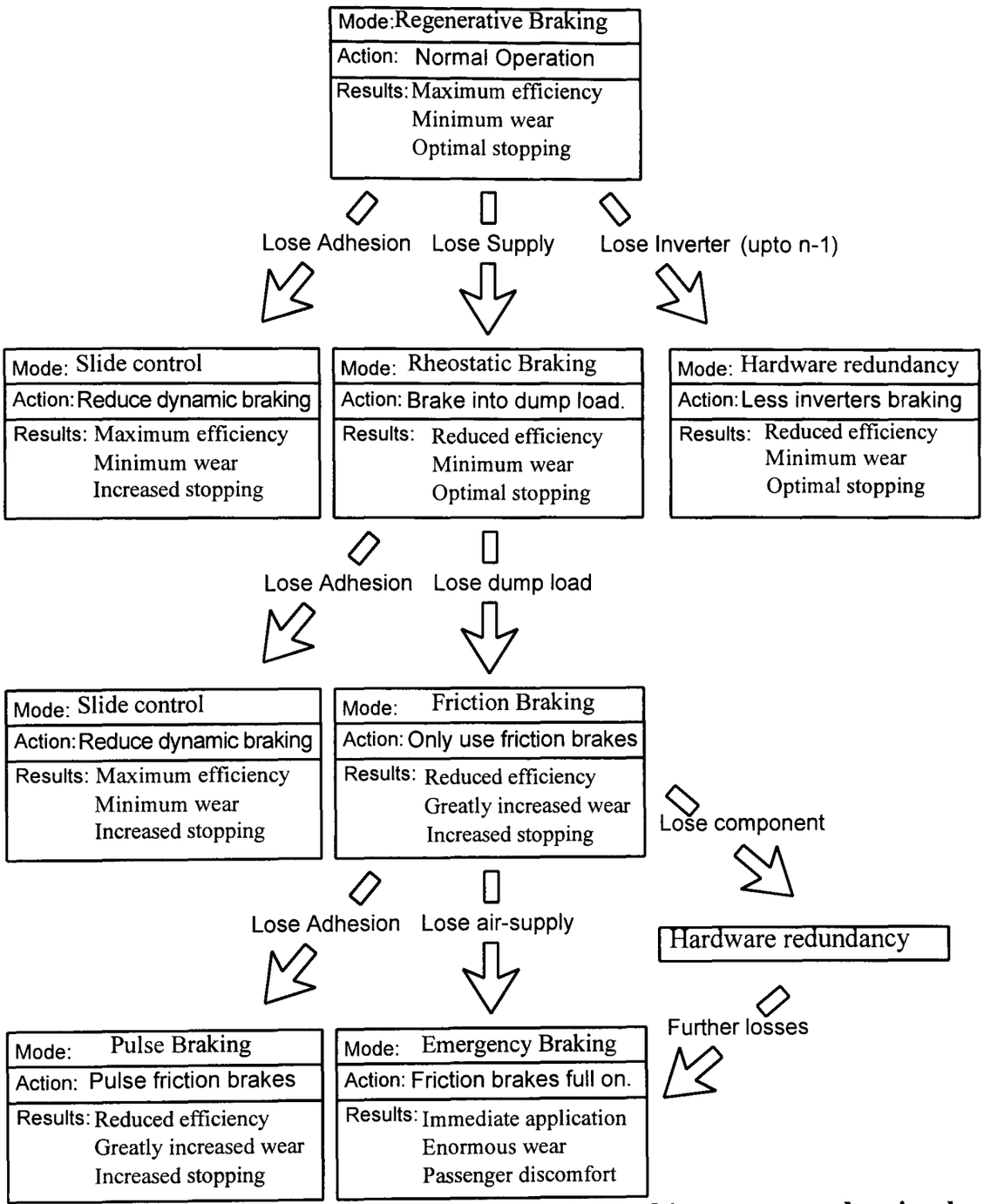

Figure 2.2. State-tree for faults affecting the braking systems, showing how the performance is degraded whilst maintaining some braking function.

The braking system includes examples of all three types of fault-tolerance.

- Reconfiguration between dynamic and friction braking.
- Hardware redundancy in the pneumatic system with duplication of the components.
- Robust control against pad wear, increased pad travel accommodated by more air-flow into the cylinder to reach demand pressure.

2.4 Fault detection method

For both reconfigurable control and redundant control some form of FDI is needed. This section briefly summarises the main methods available, for a more detailed review see Pouliezos & Stavrakakis (1995) and Patton *et al* (1998). Many FDI methods have been developed; some of these are very generic with few practical applications but others are highly specialised and difficult to extend to more general problems. For a review of applications see Isermann & Ballé (1996). The following broad classifications can be applied to the various methods for FDI.

2.4.1 Statistical methods

These are based on analysing the statistics of a measurement or set of measurements, see Pouliezos & Stavrakakis (1994) and Morris & Martin (1997). The simplest form is a limit check on a variable, more sophisticated techniques involve measurement of standard deviation, cross-correllation methods and spectral analysis.

2.4.2 Observer based methods

This general approach exploits the analytical redundancy which is available in a dynamic model of the plant, see Patton *et al* (1995). This is used to generate a residual signal which is used to flag faults. There are many extensions to the basic theory which tackle the problems of disturbance and uncertainty on the model, see Patton & Chen (1993). These techniques will be discussed later in Section 5.4.

2.4.3 Parameter estimation methods

These methods estimate process parameters in an attempt to detect changes in the plant under observation. These include extended observers[2.1] in which a parameter becomes an estimated state of the observer, see Du *et al* (1995) and Atkinson *et al* (1991). Other techniques include parameter identification methods such as recursive least-squares algorithms which develop a best fit of unknown parameters to an *a priori* known model structure, see Isermann (1984) and Isermann & Freyermuth 1991).

[2.1] also called augmented observers

2.4.4 Knowledge based systems

These methods are generally based on the use of tree structure or rule-base evaluation, see Quevedo *et al* (1997). The tree structures can be established using bond-graphs, petri-net, FMEA (failure mode and effect analysis) and causal relations, see Hari-Narayanan & Viswanandham (1986), Blanke *et al* (1997) and Siu *et al* (1997). These techniques are most commonly used on large complex systems with slow dynamics and are often included as part of the design process.

2.4.5 Neural networks

There are two main applications of neural networks to fault detection, see Korbicz (1997). Firstly as model identification, to model the behaviour of an unknown plant, Köppen-Seliger & Frank (1996). The second major application is for the classification of symptoms. A neural network can be trained or can self-learn to classify data sets into clusters which represent normal and abnormal behaviour, Zhang *et al* (1996) and Goode *et al* (1995).

2.4.6 Fuzzy logic

This is more of a tool than a specific fault detection method. It can be used to produce non-linear observer based methods, see Lopez *et al* (1997), rule-based methods and pattern matching for classification methods, see Schneider *et al* (1996) and Goode & Chow (1995).

2.5 Types of traction system fault and existing fault handling methods

The main faults in the traction system can be classified into one of the following three groups; electrical, mechanical and instrumentation faults. The various faults are described in the following section and afterwards the scope for detection and correction is considered.

2.5.1 Electrical faults

The main electrical faults are:-

- Burnt out power devices in the inverter.
- Over current faults due to short circuits in the windings.
- Over voltage conditions on the line.

Because of the high voltages and large currents involved, any fault in the power electronics must be dealt with extremely quickly and safely. For this reason the inverters are protected from over voltage or over current conditions using dedicated circuit breakers. If a fault condition is detected then the inverter is immediately switched off, after a pause it is switched back on again. If the fault condition has not cleared the inverter is shutdown, this is *fault protection.*

Isolating which actual fault occurred is difficult. The actual device which caused the shutdown or the conditions under which it did so may not be obvious. This can cause extra work for repair crews, for example a Gate Turn Off thyristor (GTO) which causes a shutdown due to thermal overload could have been the result of a motor short, a fault in the GTO, a fault in the driver circuit or a fault in the other GTO in the pair.

2.5.2 Mechanical faults

- **Broken rotor bars.** Mechanical stress from excessive high torque starting and vibration combined with material effects such as ageing and overheating can break or crack bars in the rotor cage. The effect of this will be an uneven air-gap flux distribution causing vibration plus additional heating from arcing. This reduces the motor efficiency and increases the risk of further damage. This is more of a problem in cast iron rotors which are more brittle than the modern alloy rotors.
- **Bearing damage.** Excessive vibration, poor maintenance, and stray earthing currents can all damage motor bearings, which will result in increased vibration, with the risk of further damage.

- **Rotor distortion**. Excessive high torque starting can distort the shape of the rotor cage, this is more of a problem in modern motors which use softer alloys.
- **Insulation damage**. Worn bearings and vibration from rotor distortion may cause the rotor to come into contact with the stator, which will wear away the insulation from the stator windings. This causes an increase in stray currents and localised overheating, which will, in turn reduce motor efficiency and in severe cases may burn-out the motor completely
- **Overheating.** Insulation damage, worn bearings and restricted airflow will increase the risk of motors overheating. The control system must be able to cope with an operating temperature range of -20°C at start up on a cold morning to 80°C during prolonged high load operation. Sudden overheating during braking or acceleration may indicate overloading. A generally high temperature may indicate a worn bearing, blocked cooling ducts or stray currents.

At present, the incidence of mechanical faults is lessened by regular scheduled maintenance, which is developed from in-service data about failure rates and the manufacturer's data of reliability and component life. This is a form of *fault prevention.*

2.5.3 Instrumentation faults

The instrumentation is an essential part of the traction system, it measures physical qualities in the motor and the power electronics needed by the control algorithm running in a computer. The controlled variables are torque and flux, neither of which are directly measured. These are estimated using the measured voltages and currents. There are potentially two types of error in the instrumentation, physical sensor faults and estimation errors.

At present, little work is done to validate sensor measurements. Speed sensor faults are handled by comparing multiple sensors, each inverter drives two motors, each with its own speed sensor, the controller takes the highest reading from the two. Current and voltage sensor faults will be detected from the 'mis-behaviour' of the control system, resulting in the inverter shutting down. Intermittent faults may be attenuated by heavy filtering of estimates and slow control loops. One of the aims of the Advanced Traction and Braking Project is to improve the controller design. This will require faster and more precise estimates of torque and flux for which heavy filtering will not be acceptable.

2.6 *Literature review of fault-detection and tolerance for the inverter*

2.6.1 Detection

As stated in Section 2.5 any faults in the power electronics must be detected extremely rapidly. This can be demonstrated using the model described in Chapter 3. The motor is accelerated from 50rad/s to 100rad/s, and after 15.558 seconds one pulse is removed from the PWM voltages. As shown in Fig. 2.3 this corresponds to the high-side GTO on phase A failing to close for the duration of the fault.

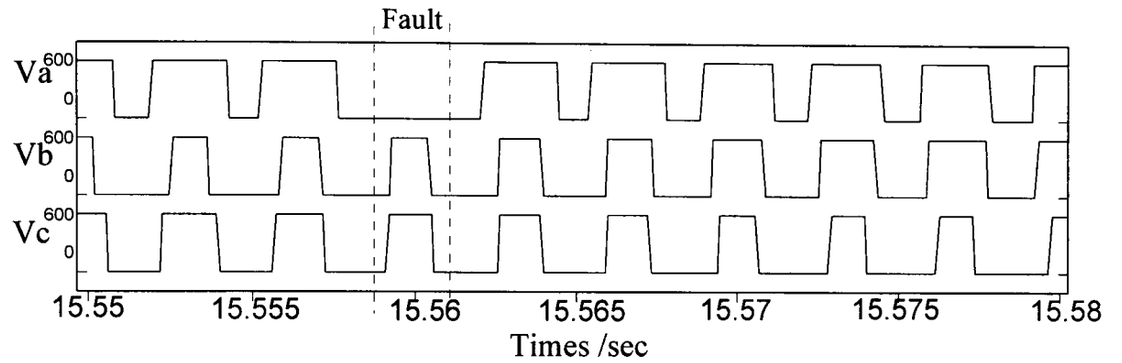

Figure 2.3. Plots showing the inverters output phase-to-ground voltages with one phase of the inverter failing to switch for the duration of a PWM period.

Fig. 2.4 shows the simulated effect of one GTO pair in the inverter failing to switch, on the motor torque and the motor speed. Two cases are shown, the first assuming that the motor is accelerating the whole train mass. In the second case the transient only accelerates the axle, this is more realistic since the wheel would lose adhesion.

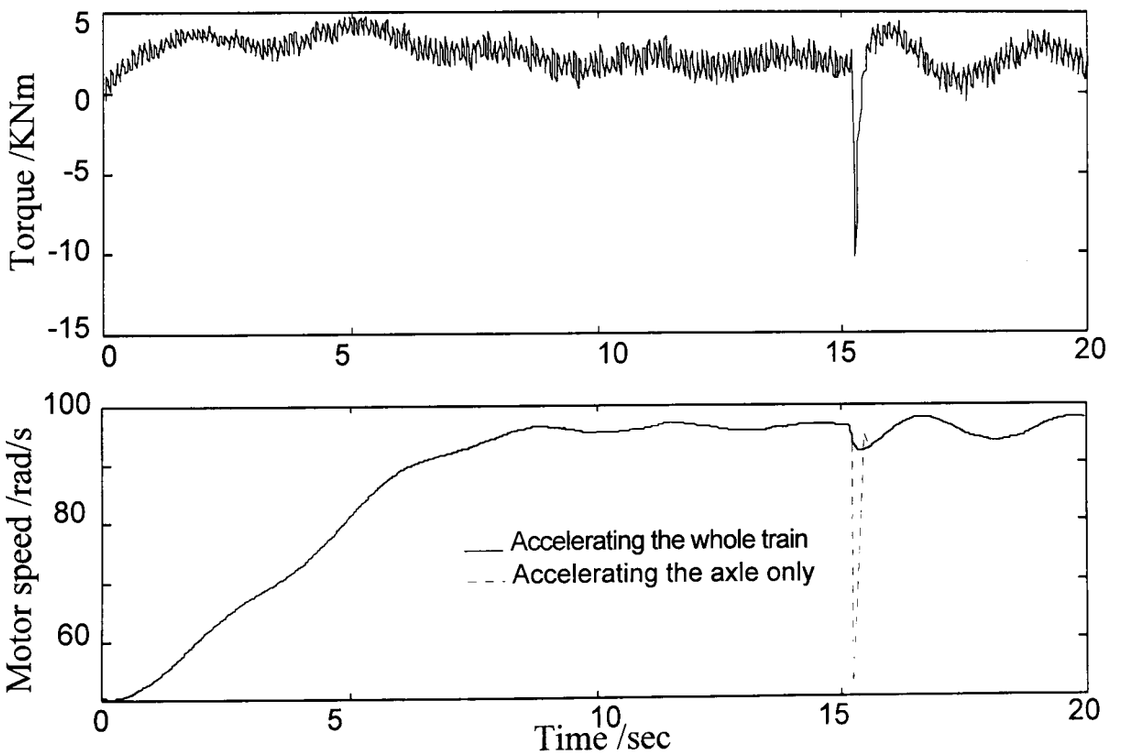

Figure 2.4. Plots of the resulting motor torque and axle speeds.

These results can only provide a limited insight since under such extreme conditions non-linear effects would occur. However, the basic message is clear; that mis-fires in the inverter will result in very rapid and large torque transient. This was highlighted during the early development of insulated gate bipolar transistor (IGBT) inverters for large rail locomotives when device failures would result in broken drive shafts.

On the train systems this sort of inverter fault is intolerable. At the system level inverter mis-fire is difficult to detect without measurements of vibration, since only a brief current surge is produced. The inverter protection system must respond extremely quickly to detect and shutdown the mis-behaving inverter.

The voltage sensors rarely have sufficient bandwidth to enable the comparison of the inverter output to the expected output so faults cannot be detected this way. Noting this Scot-Smith *et al* (1997) proposed a scheme based on monitoring the direction of the measured current vector to detect intermittent mis-fire in the inverter.

For a low power transistor inverter driving a 3HP induction motor Kastha & Bose (1994) have made a systematic study of inverter fault modes and their effects. However, this paper concentrates on improving the design of inverter protection rather than methods for detecting faults in use.

2.6.2 Fault-tolerance

For some types of motor faults and inverter phase faults reconfiguration is possible. Fig. 2.5 shows three possible fault conditions, *phase open* which also corresponds to the IGBT's failing to switch on, *phases shorted* together and *phase shorted to earth* which corresponds to the lower IGBT failing to switch off. A *short to supply* fault is not shown since it is similar to the high-side IGBT failing to switch off.

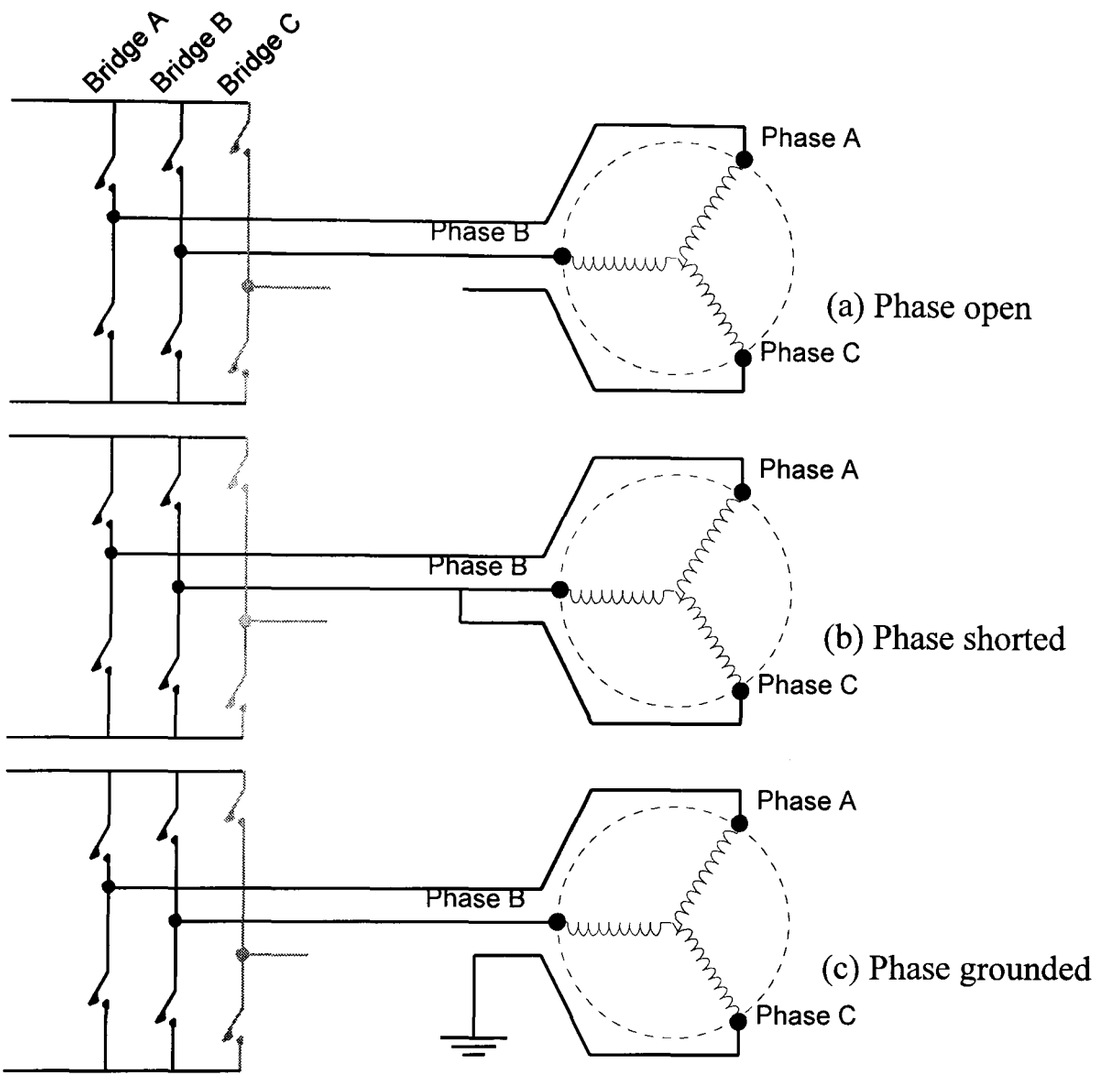

Figure 2.5. Possible single fault conditions for the motor: a; phase open circuit, b; phase short circuit and c; phase shorted to earth.

Any faults which involve shorting will cause the inverter to shutdown due to an over-current trip. The inverter could be restarted, provided that the failed phase can be isolated by both IGBT's in the pair being in the off state. The inverter can continue to drive the motor using just two phases, but at reduced power and torque. With all of the fault conditions the motor is now being operated unbalanced, this will produce increased torque pulsation and internal heating for which the motor must be de-rated.

The effect of the loss of one phase on the induction motor can be considered by simulating it. Fig. 2.6, which shows the harmonic content of the developed torque, for a simulation of the fault phase shorted to earth, using a PWM inverter. The inverter is given a switching frequency of 100Hz [2.2] and the motor is running at a constant 100rads^{-1} (16.6 Hz). A frequency component at the motor speed is present, as one of the windings is not energising.

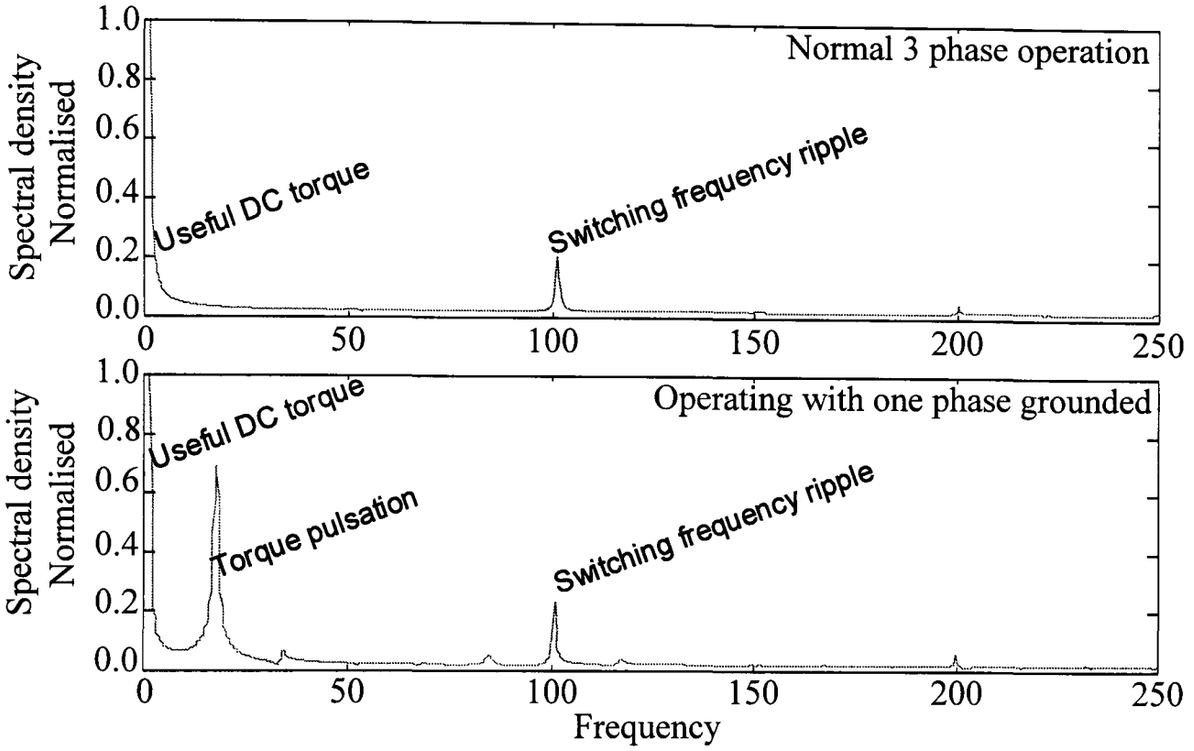

Figure 2.6. Spectral components of motor torque with normal three phase PWM voltages and with two phase PWM after fault.

In this two phase mode the inverter is not able to start the motor from standstill. To understand this consider the voltages which the inverter can supply to a healthy motor. The applied voltages, for a motor driven with 3 phase sinusoidal voltages, will resolve into a continuously rotating vector. With an inverter the applied voltages can only have several combinations, of each motor phase connected either to ground or to the supply voltage. The inverter can only generate six resolved voltage directions, P1,P2,···,P6, as illustrated in Fig. 2.7a. For a fault motor or inverter with one phase, e.g. V_b, isolated the directions are as given in Fig. 2.7b. A complete rotation of the flux vector cannot be created. This is like trying to pedal a bicycle using only one leg or a single cylinder engine; it cannot be guaranteed to produce sufficient torque to complete one rotation of the shaft.

[2.2]. This is set artificially low to demonstrate the relative magnitude of the frequency from the fault and the total inverter output.

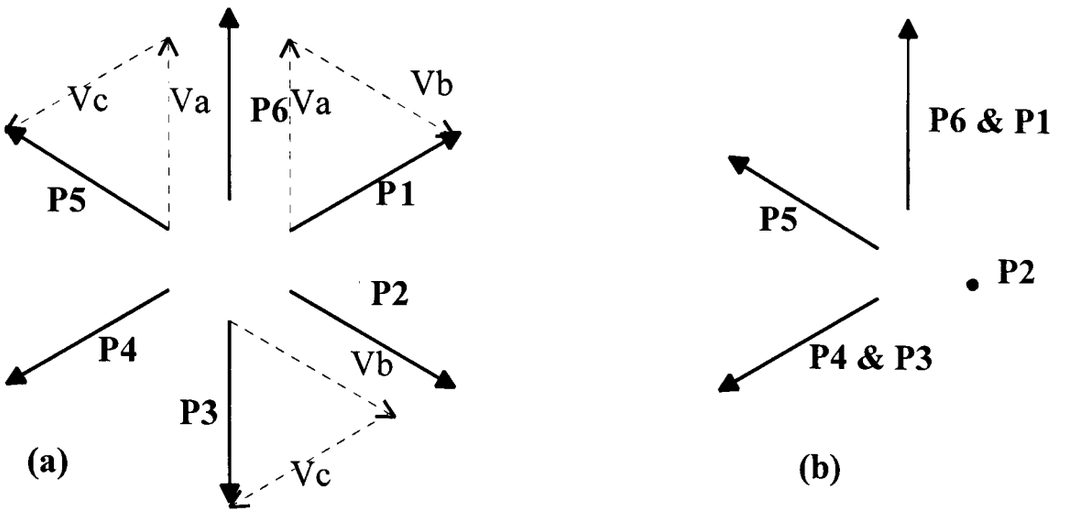

Figure 2.7a Normal directions for applied voltage. b. Direction without B phase.

For train applications the torque pulsation would be unacceptable as it would cause the wheels to judder which, with low adhesion would not produce any useful traction and passenger discomfort would be felt. On the EMU the physical hardware redundancy of multiple inverters and motor sets is the most effective form of redundancy for building a motor-inverter fault-tolerant system.

One extension of the redundant hardware method is given by Jahns (1992). Most induction motors will have many turns on each stator winding and also the inverter will have several GTOs connected in parallel to give sufficient power handling. A fault in any of the devices or shorts in any of the turns in the winding will necessitate a shutdown. By separating the windings into two or more separate coils and driving each one with a single pair of GTOs some hardware redundancy is obtained, Zhao & Lipo (1996). A rotating set of voltages can still be produced with a failure in any one device or turn. The motor can continue to operate but with a reduction in the maximum torque and power achievable.

2.7 Literature review of fault detection for induction motors

A large volume of work has already been published on the various methods for early detection of faults in induction motors. These are many frequency analysis techniques, a few applications of model-based techniques and some specialist techniques.

2.7.1 Frequency Domain Analysis

Most of the techniques in the literature for fault detection and condition monitoring on induction motors are frequency domain analysis techniques. This is a logical approach since the induction motor is a rotary machine. There are many papers on this subject, but in general there are two approaches to frequency analysis. It is possible to model the fault and calculate its frequency signature. Alternatively, it is possible to compare the signature of two machines with and without the fault. For modelling broken rotor bars two main techniques are used, finite element analysis of the rotor with missing bars, Elkasabgy *et al* (1992) and the Fourier transform of the redistributed current in bars adjacent to a broken bar, Kliman *et al* (1988).

A whole range of measurements can be considered as targets for frequency analysis. By using an experimental motor the usefulness of the following measurements were evaluated by Kliman *et al* (1988) for detection of rotor bar faults; air-gap flux, internal and external axial flux, direct torque measurement, radial and azimuthal acceleration, position encoders and stator current sensors. The choice of which signal to analyse must take into account the complexity and reliability of any additional sensors. For example, measurement of the air-gap flux is more than useful the external axial flux but it is much harder to obtain. The phase currents can be used to estimate bearing damage and this has the advantage that no additional sensors are required, Burth & Filbert (1997).

All of the techniques mentioned so far assume a fixed drive frequency and sinusoidal drive voltages. With the use of PWM most measured signals become rich in harmonics. This will make the FDI task harder since some of the harmonic components will interfere or overlap with the fault frequencies. The application of a window function to the sampled signal, before a Fourier transform is taken, has been proposed by Salvator & Trotta (1988) to reduce the effects of PWM harmonics in measured signals. The complications arising from a variable drive frequency can be approached by using a variable sampling rate. With a variable drive frequency and a variable rotor speed there

will be two sets of components which will move independently of each other, producing a complex set of harmonics. For the train traction system all of these techniques are still too undeveloped to be applied, the problems of variable speeds, PWM signals, the excessive vibration levels, the reluctance to add new sensors and the high required computing power make frequency domain techniques unfeasible at present.

2.7.2 Model-based methods applied to induction motors

There is a large range of model-based FDI techniques available, Patton (1995) and Patton *et al* (1998), which have been applied to a variety of applications, Isermann & Ballé (1996). Their application to induction motors has been more limited, this is because of the need for a model that is both simple and accurate. The principle of the induction motor is very simple, see Section 3.2. and for control purposes a reasonably accurate model can be obtained. However, when modelled in more detail the induction motor is an extremely complex and non-linear machine, see Section 8.2.

Parameter estimation is the model-based method most frequently applied to induction motors. The most commonly estimated parameter is rotor resistance, this is because high performance vector control schemes need to be compensated for changes in rotor resistance[2.3]. Chan & Huaqian (1990) select an appropriate reference frame in which the rotor resistance can be obtained from a rearrangement of the electrical equations, Atkinson *et al* (1990) and Wade *et al* (1994) develop extended Kalman filters to estimate the rotor resistance. Pena & Asher (1993) question the reliance of the EKF method on the accuracy of the speed measurement, especially at low speed where the measurement may be poor. Loron & Laiberté (1993) take the EKF design further to estimate both the stator and rotor resistances as well as the magnetising and leakage inductances. Rae-Cho *et al* (1992) propose that rotor faults can be diagnosed from changes in the resistance, but acknowledge that the effect of the fault will be small compared to temperature variations which must be compensated for. By contrast this same fault will cause significant localised changes in the air-gap flux and generate harmonics, which can be detected by frequency analysis. For any parameter identification method it is necessary to fully excite the dynamics of the model. When the motor is running in an unloaded steady-state full parameter identification is not feasible since the rotor circuit and stator

[2.3] Since it alters the rotor time constant.

transient dynamics will not be excited. With a load applied a significant current flows in the rotor, and it is possible to estimate the rotor time constant using an augmented observer, although the convergence rate can be poor. Beilharz & Filbert (1996) propose a method for exciting the motor dynamics significantly by using the flexibility of the PWM inverter to inject additional frequencies in order to excite the dynamics. This approach results in internal heating.

2.7.3 Other Methods

Vibration or mechanical damage to the electrical insulation in the stator winding will alter the performance of the motor and will increase the risk of overheating. When there is a deterioration in the condition of the insulation the 'stray' currents within the motor will increase. These stray currents can be detected with flux leakage sensors, Tavner *et al* (1982), but once again this involves an additional sensor.

The diagnosis of bearings has been widely considered in the frequency domain, see section 2.7.2 for further discussion on this. However most studies do not consider the actual nature of the failure mechanism. A major cause of bearing damage is stray circulating currents caused by earthing faults and damaged insulation. Rather than detecting the damage to the bearing it is more logical to detect the 'stray currents'. The main problem with insulation damage is that it is extremely complex to model and it is almost impossible to predict, Tavner *et al* (1982). It is unlikely that the imbalance current can be measured with sufficient accuracy by the existing phase current sensors, since the imbalance current could be as small as a few milli-amps in a PWM current of several hundred amps. However, it is possible to monitor the imbalance in the three phase currents, with a modified current sensor, Hari-Natarajan & Viswanadham (1989). From this it is possible to detect phase-to-ground and stray phase-to-phase currents. The isolation of insulation faults is harder than mechanical faults. However, from the condition monitoring point of view, is it useful to just be able to detect such faults.

The electrical condition of the motor can also be gauged with chemical analysis of the gases which are produced in the motor, Tavner *et al* (1982). The presence of ozone, nitrous oxides or carbon monoxide in the cooling air will indicate arcing within the motor. This technique requires an extra sensor and would probably only be of value on large motors in excess of a few megawatts, where insulation failures can be catastrophic.

2.8 *Review of instrument fault handling*

The instrumentation is an essential part of the traction system, it measures physical quantities in the motors and in the power electronics which are both needed for the control algorithm. The controlled variables, torque and flux, are not measured directly for reasons of cost and reliability. They are estimated using measurements of the applied voltages and the resulting currents.

Presently the control loops have a low bandwidth due to heavy filtering of the estimates and the control demand. One of the aims of the Advanced Traction and Braking Programme is to improve the controller algorithm. To achieve the rapid and precise torque control needed for slip/slide prevention, the controller bandwidth and gain must be significantly increased. This places greater demands on the quality of the estimates for torque and flux, in respect to the error dynamics and sensitivity to disturbances. The potential danger of intermittent faults can be shown in simulation. Fig. 2.8 shows the result of a brief current sensors disconnection, after 2.4 seconds during a simulated start-up.

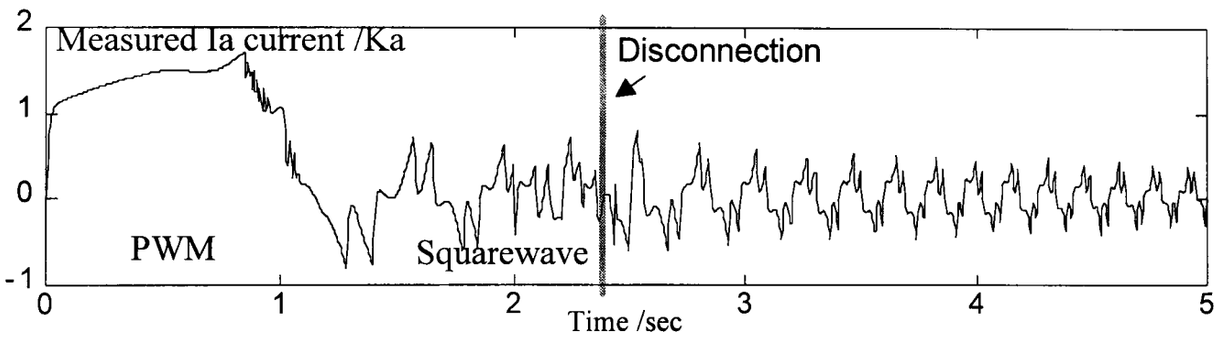

Figure 2.8. Simulated current measurement, with a brief sensor disconnection.

The simulated system consists of the induction motor model from Chapter 3, the existing estimator and the closed-loop controller from the benchmark model. The filtering of the estimates for torque and flux have been reduced and the controller's gain increased slightly. Initially the motor is being driven with PWM waveforms, before switching straight to squarewave. The GTOs have a maximum switching frequency of 300Hz and the estimator is sampling at 1KHz so significant harmonics are present on the measured current. The disconnection is barely visible in the measured current, but the error in the estimated torque is large, as shown in Fig. 2.9. This affects the controller which produces a large transient in the generated motor torque.

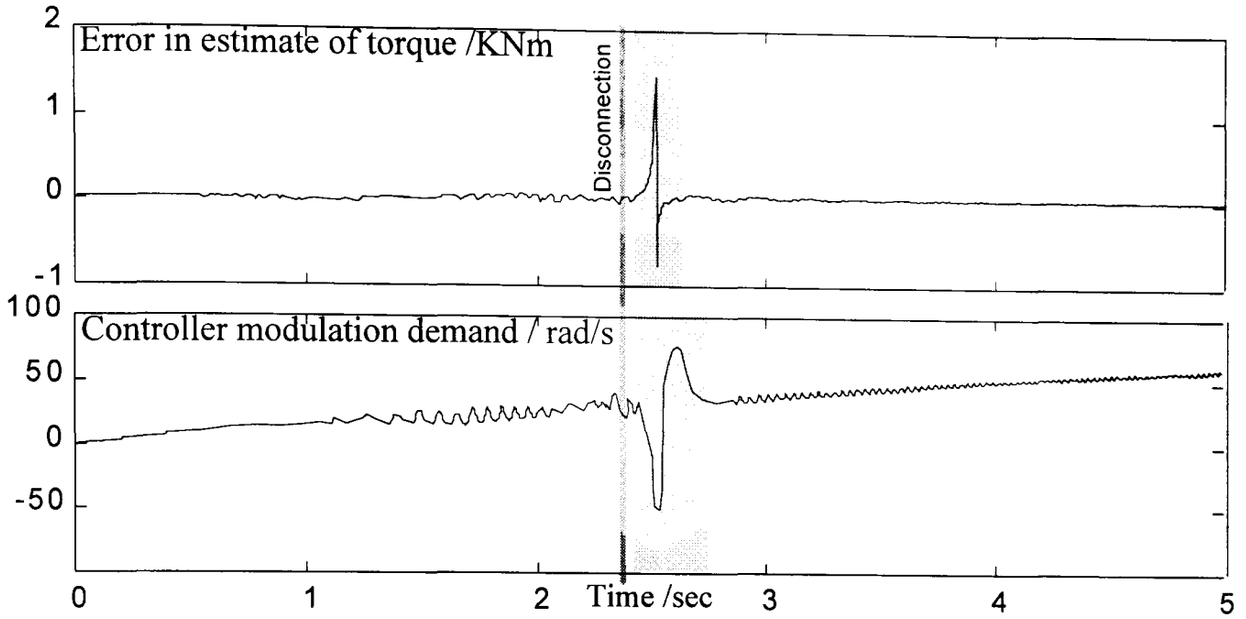

Figure 2.9. Plots of estimated torque and controller demand.

With the simple load model the torque transient does not produce a significant change in speed, as shown in Fig. 2.10. However, in practice this torque transient would cause the wheel to lose adhesion and to spin rapidly, as shown by a dotted line in Fig 2.10.

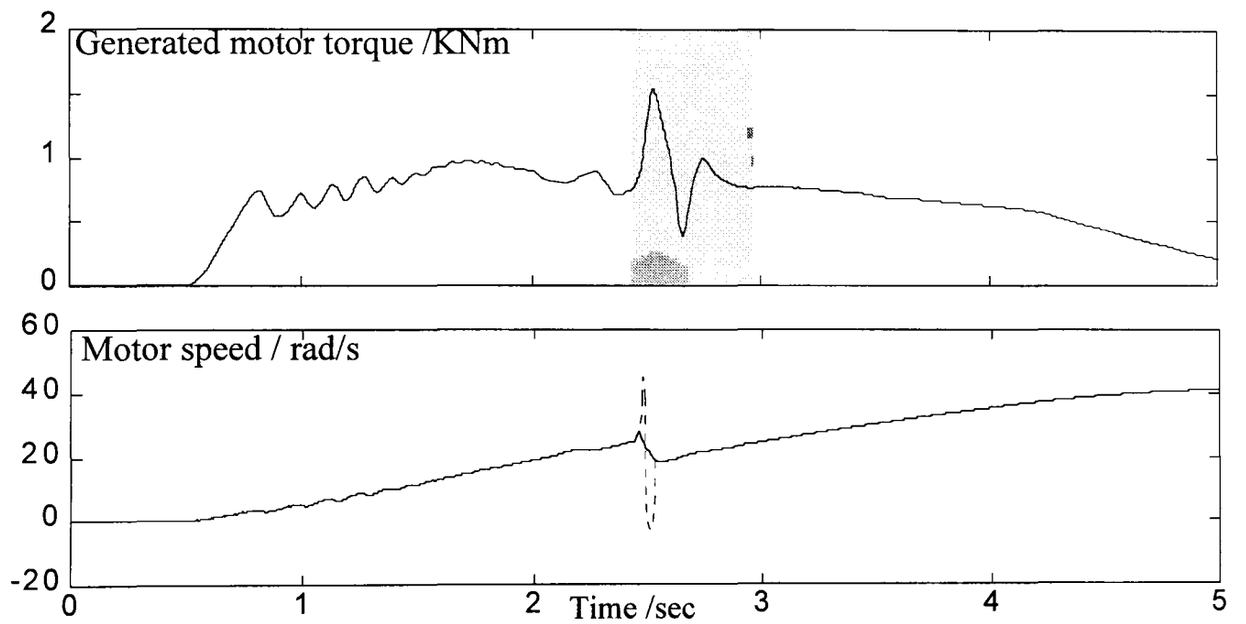

Figure 2.10. Plots of motor torque and wheel speed.

The present estimator design is such that the effect of intermittent faults is filtered out and continuous faults will degrade the performance of the overall inverter such that it shuts down automatically.

The quality of the torque and flux estimates is addressed in Chapter 4 using observers and in Chapter 5 the use of model-based methods for sensor fault handling is considered

2.9 Design factors and operation concerns

There are several factors which a railway operator must balance in order to run a railway. The main three are safety, reliability and cost. These factors are all inter-linked and must be considered throughout the work.

2.9.1 Safety

From a report published by Railtrack in 1994 the target risk for a frequent passenger must be less than a one-in-a-million chance of a fatal accident in a year, Burrage (1995). In order to obtain even this modest level of passenger safety, the safety of individual systems must be very much higher. For example signalling systems are expected to have a mean time between 'dangerous' failures counted in tens of thousands of years, Bailey (1995). For individual components the likelihood of failure must be lower still. For a train the main safety concern is the braking system, which must be fail-safe. Additionally, with an electric train the power electronics must be sufficiently well protected so that the risk of fires is minimised.

2.9.2 Reliability and Availability

The railway environment is extremely harsh and demanding for any system which has to operate within it. There are several additional aspects to reliability which must be considered, the likelihood of failures in service and the length of time spent out of service. It is not uncommon for a train to be in use for up to 20 hours a day, which means faults may not only affect that service but can have a knock-on effect causing rescheduling of other services. A train is only profitable when it is operating. Long down times increase the amount of spare rolling stock which must be held. In general, the Networker class of electric multiple units is considered to be one of the most reliable class of trains in everyday service in the UK, Fry (1995)

2.9.3 Cost

The railway operator must be able to provide a service, at a price which the passenger is prepared to pay, with a level of safety and reliability which the passengers will accept. A failure in service will often result in the need to move additional rolling stock to fill gaps in later services, which is expensive and time consuming. The development of new technology is only practical if it will improve safety or reliability at a realistic price.

2.10 Summary.

The modern EMU is a complex system involving power electronics, pneumatics, mechanical and computer control. The industry practice for fault handling extends little beyond condition monitoring. In the academic community there is already a large range of FDI techniques and much work is now being undertaken in extending their use to fault-tolerant control. The three main methods are identified as hardware redundancy, reconfigurable control and robust control. It is pointed out that the EMU's braking system, which is a safety-critical system, already incorporates examples of the main techniques for fault-tolerance. The traction system has three main types of failure associated with it, electrical, mechanical and instrumentation. On the electrical side the scope for detection is limited by the need to shutdown power devices extremely rapidly, scope for reconfiguration other than multiple-redundancy is also limited. In contrast a range of techniques already exist for detecting motor faults, at a very early stage, before they represent a significant failure. There remains scope for significant new work on the instrumentation side. Sensor fault detection is well developed in theory but few practical applications have been forthcoming, especially in the field of electrical power systems. Sensor fault detection and tolerance will form the basis of the work in this thesis. Any further work must be done with regard to the safety, reliability and cost constraints of the modern railway industry.

Chapter 3:

Modelling the traction system

Chapter 2 has shown the scope for work on model-based methods for sensor fault detection and on improving the estimator design. For either of these topics models are an important part of the design and the testing. This chapter develops a simple model of the traction system.

A simplified over-view of the real traction system is used as a starting point. The model has four main components, the induction motors, the inverter, the control loops and the physical dynamics of the train. For each of these an appropriate level of model detail is identified and then a suitable model produced. The completed model is then validated against key performance data from the real traction system.

3.1 The operation of the traction system

Fig. 3.1 shows a block diagram of the main components in the traction system and the inner control loop. The driver is responsible for regulating the train speed, using a speedometer[3.1] and a four position lever for the traction system's power demand. The driver's selection, called *notch* setting, is translated into a torque and flux demand for the traction system. The traction system itself consists of PI loops for torque and flux. The controlled variables torque and flux cannot be measured directly and are estimated from the measured currents and voltages. The controller produces a frequency and amplitude demand for the inverter. The inverter modulates a DC supply to produce the 3 phase waveforms to drive the induction motors.

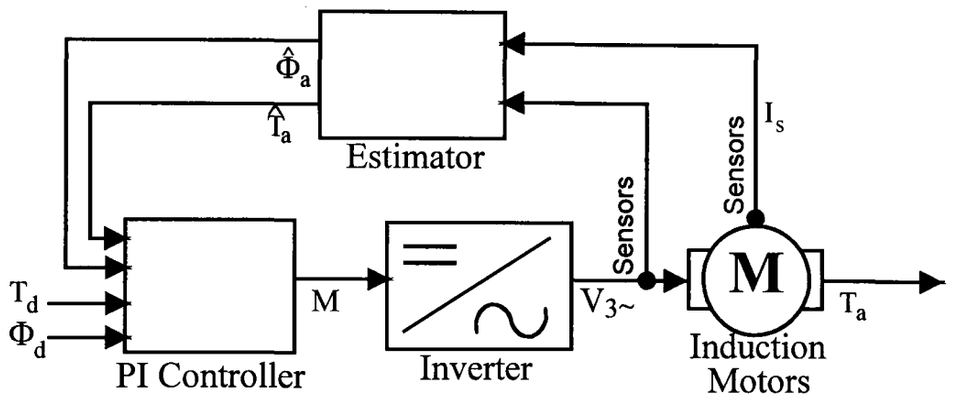

T_d Torque demand — I_s 3 phase stator currents — M Modulation demand
Φ_d Flux demand — T_a Motor torque achieved — $\hat{T_a}$ Estimated motor torque
$V_{3\sim}$ 3 phase drive voltages — $\hat{\Phi_a}$ Estimated motor flux

Figure 3.1. The traction system.

The PI controller coefficients are gain-scheduled to take account of changes in the motor dynamics with speed, tuned to prevent the excitation of resonances in the suspension and to limit harmonics which might interfere with the signalling system.

3.1.1 Developing a simple model for the traction system

In order to work on the traction system, a simple model is required, which consists of an inverter, an induction motor and a load driven open-loop as shown in Fig. 3.2. The controller converts the driver's notch setting into a frequency and amplitude demand for the inverter. The inverter chops the DC supply to produce the three phase voltages to drive the motor.

[3.1] Except when stated otherwise the use of the term 'speed' refers to the rotational speed of the motor, in rads^{-1}, rather than the train's speed along the track. See appendix D for conversion between the two.

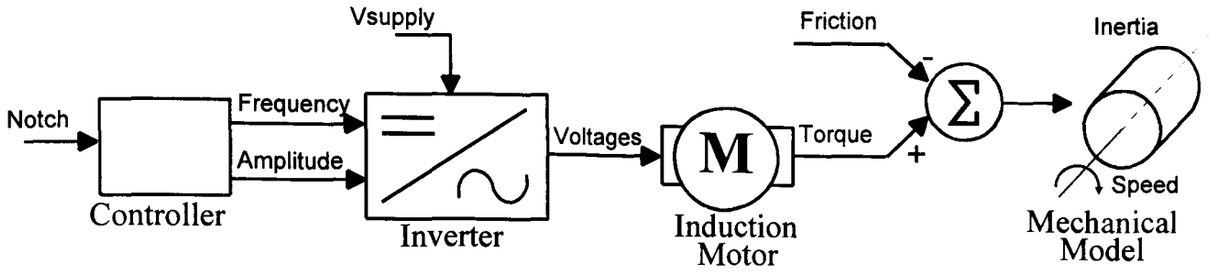

Figure 3.2. The simplified model of the traction system for open-loop simulation.

3.2 AC squirrel cage induction motors

The motors used in the traction system are 3 phase AC squirrel cage induction motors. Their basic construction is shown in Fig. 3.3a. The rotor is made of metal bars held by end-rings to form a cage. The stator consists of windings for each phase. When supplied with 3 phase voltages these produce a rotating magnetic field. If this field rotates faster than the rotor then currents are induced in the rotor bars. These currents produce an attractive force causing the rotor to rotate in the same direction as the stator field, see Fig. 3.3.b.

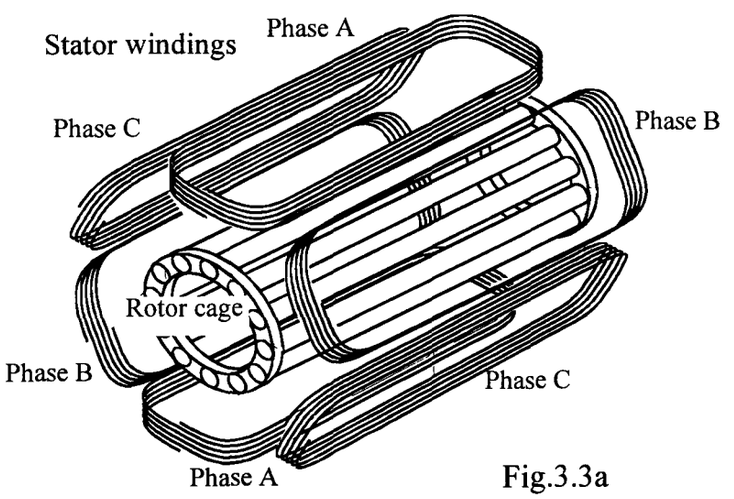

Fig.3.3a

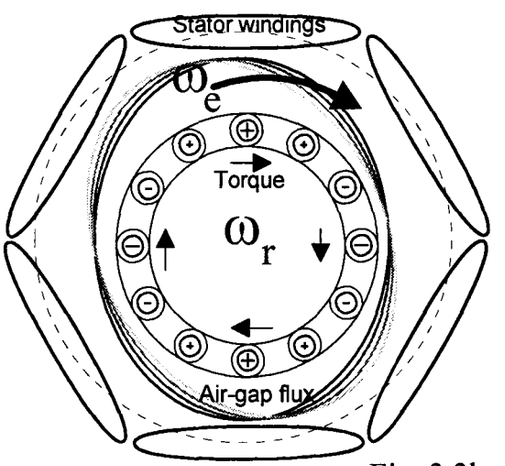

Fig. 3.3b

Figure 3.3a. Electrical construction of an induction motor.
3.3b. Rotating magnetic field which induces a torque producing currents in the rotor.

3.2.1 Level of modelled motor detail

The principle of the induction motor is extremely simple, however the physical motor is a very complex and non-linear machine. To model the air-gap flux accurately a detailed spatial model is needed, this is usually done using finite element analysis to model the magnetic field patterns, as used by Parkin & Preston (1993) and Williamson & Ralph (1983).

The model can be simplified by assuming an *ideal air-gap flux distribution* and a *linear magnetisation characteristic.* These conditions can be created by using *'volts-per-Hertz'* control to limit the flux level and prevent excessive saturation or hysteresis. This is explained in Section 3.5. Using these assumptions a relativity simple state-space model can be developed. This is standard procedure, summarised in Sections 3.2.2 to 3.2.6, which can be found in any good textbook on induction motor drives, for example Bose (1986). The validity of this model is considered in Chapter 8.

3.2.2 Constant power 3 phase to 2 axis transformation

For modelling purposes the 3 phase motor is transformed into a two axis notation. The currents and voltages are resolved into two orthogonal directions, called direct and quadrature. This is done using a *power invariant transform*, where the winding impedances are altered so that the total power generated by the motor remains constant for a given set of applied voltages, details of this transform are given in appendix A.

3.2.3 Reference frame

The currents flowing in the rotor bars are rotating at the mechanical speed of the motor. There are two commonly used methods for represented this in the model.

In the **stationary axis frame** the currents and voltages are resolved into two axes which coincide with the direct and quadrature directions of the stator. A DC current flowing in the rotor would appear as a sinusoidal in the stationary frame axes as the rotor turns.

In the **synchronous axis frame** the currents and voltages are resolved into two axes which rotate at the electrical frequency of the supply. In this way the AC current flowing in the rotor will appear as DC currents in the synchronous frame axes as the rotor rotates. The input voltages must also be transformed, a sinewave drive voltage will appear as a DC input to the synchronous reference model.

3.2.4 Electrical equations

Initially ideal magnetic behaviour, air-gap flux distribution and constant temperature are assumed, the validity of these assumptions is considered in Section 8.2. Using two axis notation the electrical circuit for each axis is shown in Fig. 3.4. For both the stator and rotor the total inductances, L_r and L_s respectively, have two components. The portion of the stator and rotor windings through which the same flux flows is called the

magnetising inductance, L_m. The portion of a winding through which only the flux generated by itself flows is called the self inductance, L_{ls} and L_{lr} for stator and rotor respectively. R_s and R_r are the stator and rotor resistances.

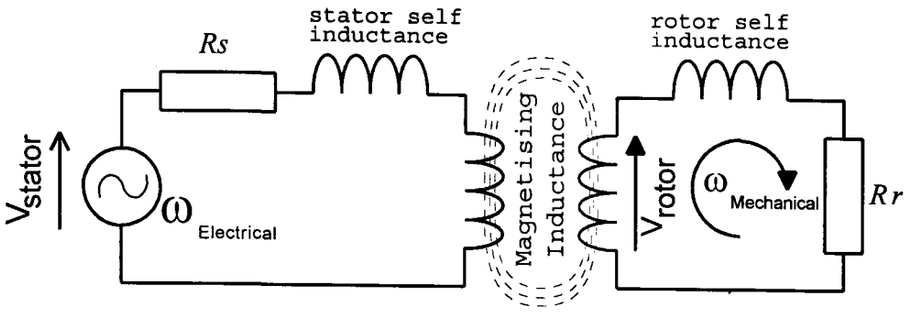

Figure 3.4 Electrical circuit for each axis.

By equating the currents through the impedances to the voltages a set of equations is obtained in Ohm's law form, as given by Eq. 3.1, where a vector of voltages equals a matrix of impedances[3.2] multiplied by a vector of currents.

$$\begin{bmatrix} V_{sD} \\ V_{sQ} \\ V_{rD} \\ V_{rQ} \end{bmatrix} = \begin{bmatrix} R_s + s(L_s) & 0 & sL_m & 0 \\ 0 & R_s + s(L_s) & 0 & sL_m \\ sL_m & \omega_r L_m & R_r + s(L_r) & \omega_r(L_r) \\ -\omega_r L_m & sL_m & -\omega_r(L_r) & R_r + s(L_r) \end{bmatrix} \begin{bmatrix} I_{sD} \\ I_{sQ} \\ I_{rD} \\ I_{rQ} \end{bmatrix} \tag{3.1}$$

3.2.5 Model parameters

The 2 axis electrical parameters, in Fig. 3.5, were supplied by GEC-Alsthom for a generic traction motor with an approximate power rating of 100kW. Note that, since each inverter drives two motors in parallel the parameters supplied by GEC-Alsthom are actually for two motors lumped.

Parameter	Symbol	Value
Stator resistance[1]	R_s	0.017Ω
Rotor resistance[1]	R_r	0.0125Ω
Stator leakage inductance	L_{ls}	96μH
Rotor leakage inductance	L_{lr}	164μH
Magnetising inductance[2]	L_m	3.8mH

[1] At operating temperature.[2] At 65% of maximum rated load.

Figure 3.5. Table of motor parameters.

[3.2] s is the Laplace operator

3.2.6 State space model

In Eq. 3.1. V_{rD} and V_{rQ} are both zero since no voltage is applied to the rotor. The impedance matrix can be separated into terms involving the Laplace operator and those not, given as A_2 and A_1 respectively. This gives the general form of Eq. 3.2.

$$\underline{V} = (A_1 + sA_2)\underline{I} \tag{3.2}$$

Taking $\underline{I}$ as the state vector, Eq. 3.2 is rearranged into a state-space form:

$$\dot{\underline{I}} = -A_2^{-1}A_1\underline{I} + A_2^{-1}\underline{V} \tag{3.3}$$

Note that the state dynamics are a function of motor speed, this gives rise to a bilinear system[3.3] as a function of rotor speed, as given in the general form of Eq. 3.4

$$\begin{aligned} \dot{\underline{x}} &= (A + N\omega_r)\underline{x} + B\underline{u} \\ \underline{y} &= C\underline{x} \end{aligned} \tag{3.4}$$

where:-

ω_r is the mechanical speed of the rotor
$\underline{u}$ is a vector of inputs, direct and quadrature components of the applied stator voltages.
$\underline{x}$ is a vector of states, direct and quadrature components of stator and rotor currents.
$\underline{y}$ is a vector of the outputs, the measurable stator currents.

Therefore $C = \begin{bmatrix} 1 & 0 & 0 & 0 \\ 0 & 1 & 0 & 0 \end{bmatrix}$

This gives the motor electrical state space equation as:

$$\begin{bmatrix} \dot{I}_{sD} \\ \dot{I}_{sQ} \\ \dot{I}_{rD} \\ \dot{I}_{rQ} \end{bmatrix} = \underbrace{\begin{bmatrix} -L_rR_s & \omega_rL_m^2 & R_rL_m & \omega_rL_rL_m \\ -\omega_rL_m^2 & -L_rR_s & -\omega_rL_rL_m & R_rL_m \\ R_sL_m & \omega_rL_sL_m & -L_sR_r & -\omega_rL_rL_s \\ -\omega_rL_sL_m & R_sL_m & \omega_rL_rL_s & -L_sR_r \end{bmatrix}}_{L_rL_s - L_m^2} \times \begin{bmatrix} I_{sD} \\ I_{sQ} \\ I_{rD} \\ I_{rQ} \end{bmatrix} + \underbrace{\begin{bmatrix} L_r & 0 \\ 0 & L_r \\ -L_m & 0 \\ 0 & -L_m \end{bmatrix}}_{L_rL_s - L_m^2} \times \begin{bmatrix} \underline{V}_D \\ \underline{V}_Q \end{bmatrix} \tag{3.5}$$

[3.3] Justification of terminology, Quadratic or Bilinear system. During the course of this work the use of the term *bilinear* has been the cause of some discussion. The state space motor model, given by Eq. 3.4 is not strictly bilinear since ω_r is not a controllable input, however when considered from the point of view of an observer the systems may be called bilinear.

$$\underbrace{\dot{\underline{x}} = A\underline{x} + N\underline{x}\omega_r + B\underline{u}}_{\text{Quadratic system}} \quad \Leftrightarrow \quad \underbrace{\dot{\underline{x}} = A\underline{x} + \Sigma_{i=1}^{n} N_i\underline{x}\upsilon_i + B\underline{\upsilon}}_{\text{Bilinear system}} \text{ where } \underline{\upsilon} = \begin{bmatrix} \underline{u} \\ \omega_r \end{bmatrix}$$

3.2.7 Motor dynamics

The motor model is non-linear, its dynamics alter as a function of the motor speed. This means that the poles of the motor's dynamics are a function of speed. The loci of the poles with speed are plotted in Fig. 3.6. Note that the motor dynamics are relatively poorly damped at speeds in the range 10-50 rads^{-1}.

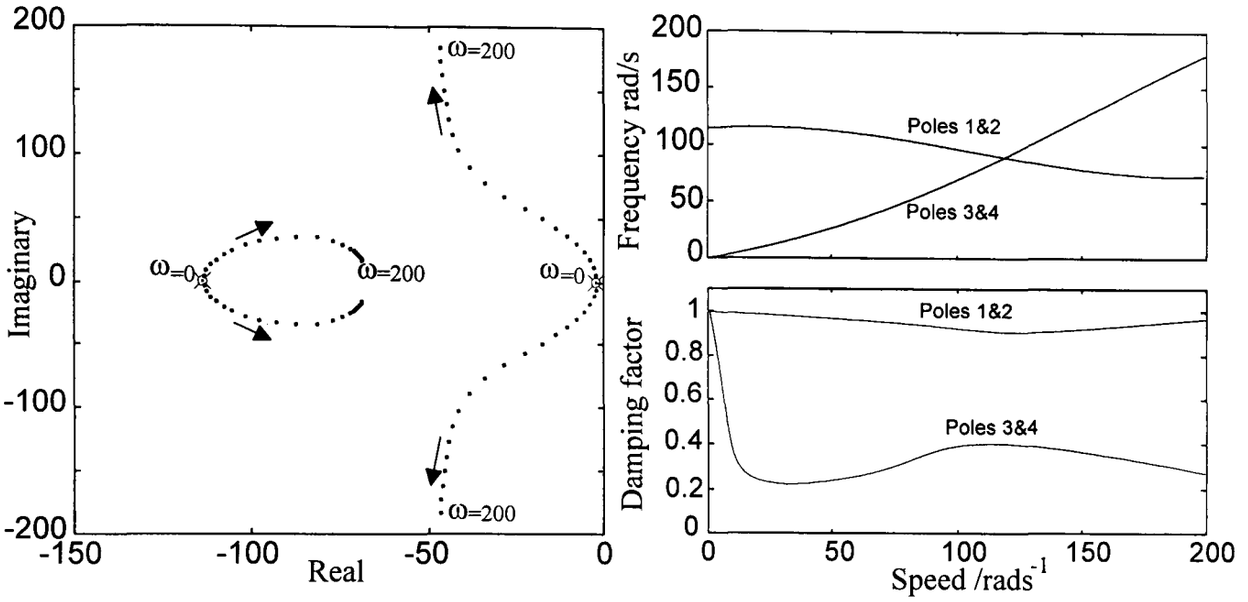

Figure 3.6. Plot of poles with speed and plot of damping and frequency with speed.

3.2.8 State space model for synchronous reference frame

The state-space model for the synchronous reference frame can be derived in the same way to give:

$$\begin{bmatrix} \dot{I}_{sD} \\ \dot{I}_{sQ} \\ \dot{I}_{rD} \\ \dot{I}_{rQ} \end{bmatrix} = \begin{bmatrix} \frac{-L_r R_s}{L_r L_s - L_m^2} & -\omega_e - \frac{\omega_r L_m^2}{L_r L_s - L_m^2} & \frac{R_r L_m}{L_r L_s - L_m^2} & \frac{\omega_r L_r L_m}{L_r L_s - L_m^2} \\ \omega_e + \frac{\omega_r L_m^2}{L_r L_s - L_m^2} & \frac{-L_r R_s}{L_r L_s - L_m^2} & \frac{-\omega_r L_r L_m}{L_r L_s - L_m^2} & \frac{R_r L_m}{L_r L_s - L_m^2} \\ \frac{R_s L_m}{L_r L_s - L_m^2} & \frac{\omega_r L_s L_m}{L_r L_s - L_m^2} & \frac{-L_s R_r}{L_r L_s - L_m^2} & -\omega_e - \frac{\omega_r L_r L_s}{L_r L_s - L_m^2} \\ \frac{-\omega_r L_s L_m}{L_r L_s - L_m^2} & \frac{R_s L_m}{L_r L_s - L_m^2} & \omega_e + \frac{\omega_r L_r L_s}{L_r L_s - L_m^2} & \frac{-L_s R_r}{L_r L_s - L_m^2} \end{bmatrix} \times \begin{bmatrix} I_{sD} \\ I_{sQ} \\ I_{rD} \\ I_{rQ} \end{bmatrix} + \frac{\begin{bmatrix} L_r & 0 \\ 0 & L_r \\ -L_m & 0 \\ 0 & -L_m \end{bmatrix}}{L_r L_s - L_m^2} \times \begin{bmatrix} V_D \\ V_Q \end{bmatrix} \tag{3.6}$$

3.2.9 Torque and Flux equations

The electrical torque and the magnitude of the air-gap flux are given by Bose (1986) as:

$$T_e = \tfrac{3}{4} P \times L_m \times (I_{sQ} I_{rD} - I_{sD} I_{rQ}) \tag{3.7}$$

where P is the number of pole pairs per motor.

$$\Phi_{air\text{-}gap} = L_m \sqrt{(I_{sD} + I_{rD})^2 + (I_{sQ} + I_{rQ})^2} \tag{3.8}$$

The air gap flux is the magnitude of the flux generated in the mutual inductance from both the rotor and stator currents.

3.2.10 Torque characteristic

For the work covered in this thesis detailed consideration of the motor torque characteristic, Eq. 3.9, given by Bose (1986), is not necessary. The difference between the motor rotational frequency and the electrical drive frequency is called the *slip frequency.* Alternatively this is can be defined as *fractional slip* which is the slip frequency divided by the drive frequency.

$$T_e = 3\left(\frac{P}{2}\right)\frac{R_r}{S\omega_e} \times \frac{V_{supply}^2}{\left(R_s+\frac{R_s}{S}\right)^2+\omega_e^2(L_s+L_r)^2} \tag{3.9}$$

where p is the number of pole-pairs and S is the fractional slip.

The traction motor's torque characteristic for a fixed drive frequency is plotted in Fig. 3.7 for a motor speed range -10 to 40 Hz. There are three distinct regions.

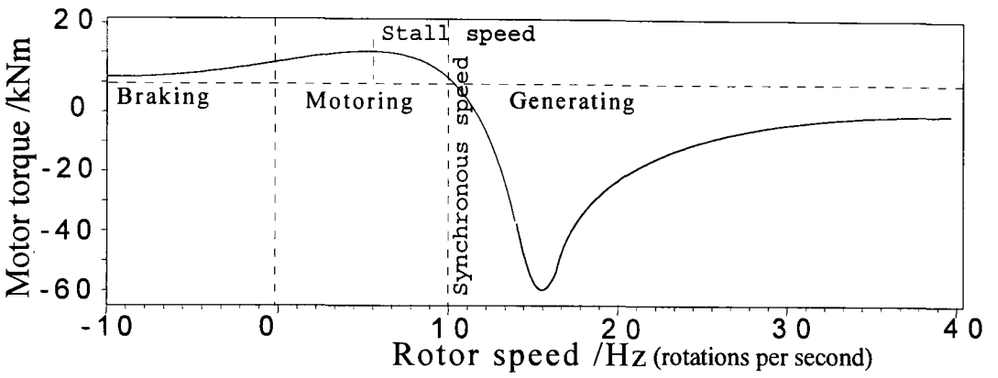

Figure 3.7. Graph of motor torque characteristic for fixed electrical frequency.

Braking, also called plugging, when the motor is being rotated in the reverse direction to the field. The direction of the motor torque opposes the rotation. Energy from the load is being dissipated into the motor, care must be taken to avoid excessive overheating. In this region the motor can be used as a rheostatic brake.

Motoring when the rotation is in the same direction but slower than the field. Energy flows though the inverter from the supply into the load. On the boundary between motoring and generating, at zero slip, the motor's speed is equal to the drive frequency, this is called the *synchronous speed* [3.4]. At this speed no torque is produced.

Generating. Beyond the synchronous speed the motor is being rotated faster than the field and the motor torque is now opposing the direction of rotation. As long as the inverter can handle it, energy flows from the load, through the motor, the inverter and back into the supply. In this region the motor can be used as a regenerative brake.

[3.4] For a 2 pole-pair motor the synchronous speed is half the drive frequency since two complete supply cycles are needed for each full rotation of the rotor.

3.3 Inverter model

3.3.1 The physical construction of the inverter

To control the motor's torque and flux, the inverter has to produce three phase voltages with both variable frequency and variable amplitude. The inverter consists of six switches arranged in three pairs, called *bridges*. These 'chop' a DC supply to produce pseudo-sinusoidal waveforms. On the Networker the switching devices are GTOs. Each bridge can switch to either line or ground, as shown in Fig. 3.8. For the EMU the inverter supply voltage is nominally 600V DC but may vary rapidly between 450-850 volts, depending on other loads on the line.

The inverter controller generates reference waveforms for each of the phases and produces the switching signals. On the practical side the controller has to deal with floating gate drive voltages and inserting time delays to protect the devices during turn-off, see Section 6.2.2.

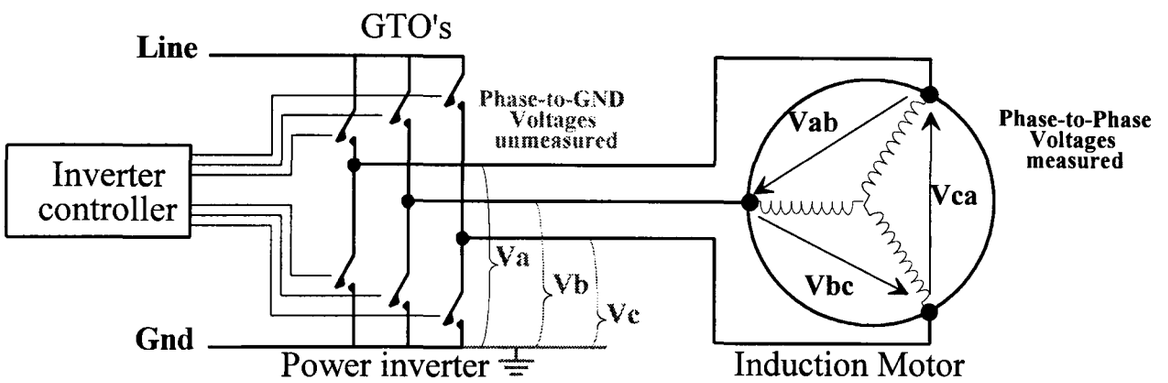

Figure 3.8. Diagram of basic inverter.

The motor has no neutral connection to the centre of the three phases, it is balanced. The voltage monitoring devices (VMD) on the real train measure the phase-to-phase voltages V_{ab}, V_{bc} and V_{ca} to avoid reference problems associated with earthing, rather than the phase-to-ground voltages V_a, V_b and V_c. The inverter model produces the phase -to-ground voltages, the phase-to-phase voltages can be readily generated from these. More details of the various voltage and current measurements and the associated transformations are given in Appendix A.

3.3.2 Inverter operating modes

Squarewave is the simplest mode, the output is a squarewave of the same frequency as the required sinewave. The drawback of this method is the high harmonic content of the resulting currents, see Fig. 3.10.b. Some of the harmonics generate a negative torque and

increase internal heating. Squarewave drive is only acceptable at high frequencies where the harmonics generated are significantly attenuated by the motor. It is not possible to control the amplitude of the squarewave and therefore separate flux control is not possible, see Section 3.5.

Asynchronous PWM has a fixed pulse rate with the mark-space ratio altering, see Fig. 3.9. This has a broad spectrum centred around the pulse frequency, sees Fig 3.10a. It is not possible to use asynchronous PWM for all drive frequencies because the high power GTO's used on the EMU's inverter have a maximum switching frequency of 300Hz.

Synchronous PWM has a fixed number of pulses per cycle. This is used as a transition between asynchronous PWM and squarewave, since slower switching rates are required than the asynchronous PWM but the harmonic content is lower than the squarewave. For the thesis this mode is ignored since it is complex to produce and is only used over a small frequency range.

The EMU's inverter uses asynchronous PWM at low drive frequencies, as the frequency increases it switches to short sequence synchronous PWM until eventually at high frequencies squarewave is adopted.

3.3.3 Generating asynchronous PWM

Asynchronous PWM is generated by comparing the required sinewave reference against a fixed frequency triangular 'carrier' wave. If the sinewave reference is less than the instantaneous value of carrier the PWM output is high, otherwise it is low. This is shown graphically in Fig. 3.9. A Simulink block diagram of the inverter is given in appendix B.

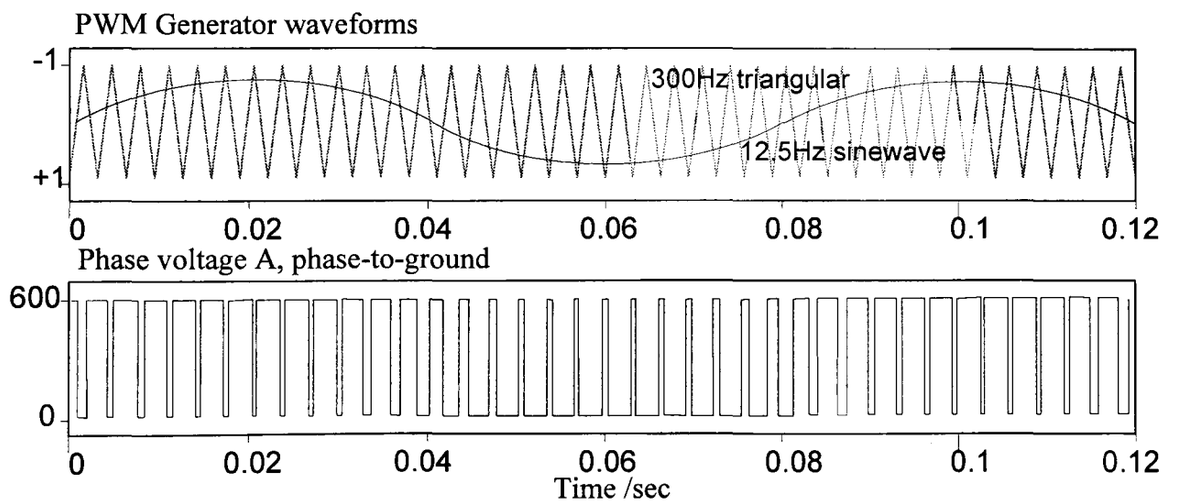

Figure 3.9. Waveforms for generating asynchronous PWM. A 12½Hz sinewave modulated at a switching frequency of 300Hz.

This form of PWM requires a simulation with very accurate time resolution, typically $\Delta T<0.01$ms in order to obtain the cross-over points accurately. The use of variable step simulations is not recommended since the routine can 'skip over' short PWM pulses.

Fig. 3.10a, shows the major spectral components of a 20Hz PWM sinewave with a 300Hz switching frequency. Fig. 3.10b shows the spectral components of a squarewave 20Hz of equivalent amplitude in the required frequency. This is the spectral content of the phase-to-ground voltages generated by the inverter.

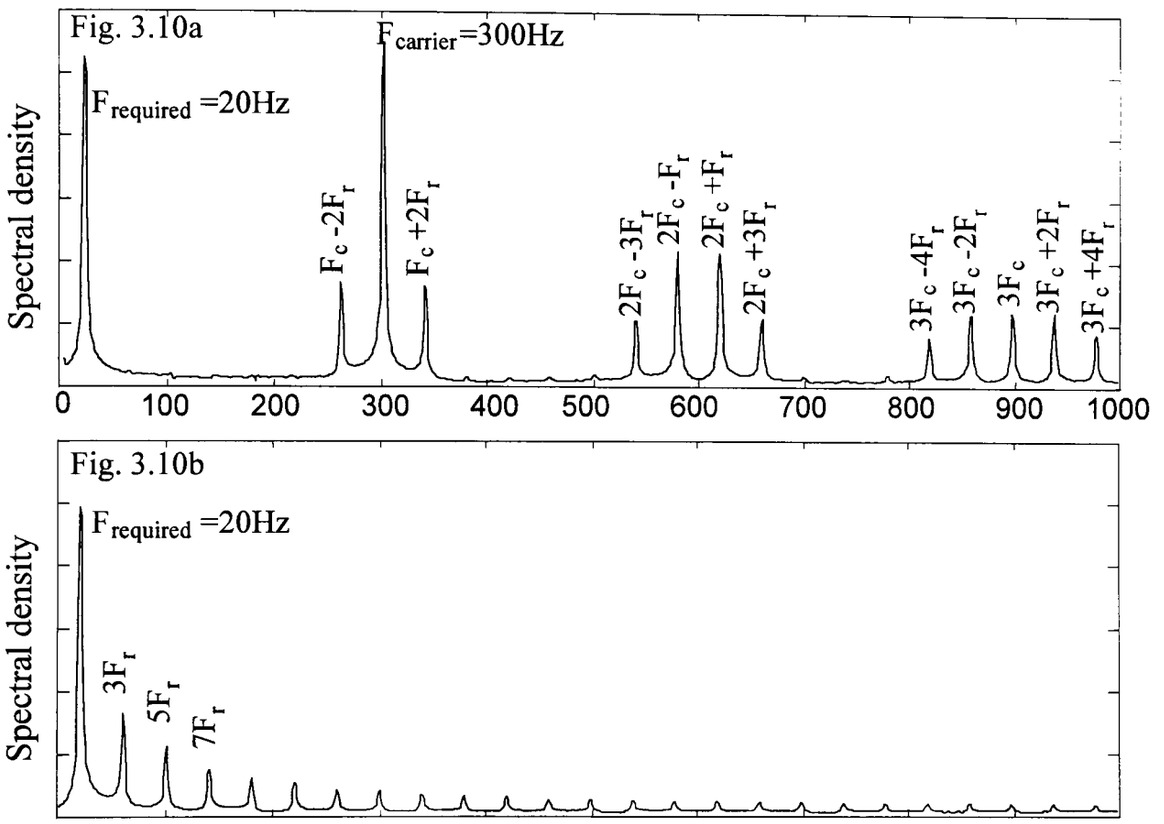

Figure 3.10a Spectral components of the phase A phase-to-ground voltage, for 20Hz required sinewave on a PWM switching at 300Hz.
3.10b Spectrum of equivalent 20Hz squarewave.

The major unwanted frequency components in the PWM waveform are the carrier frequency with sidebands of twice the required frequency. These components are sufficiently high that the inductance of the motor will heavily suppress them. In the case of squarewave drive the unwanted harmonics are odd multiples of the required frequency. Only at high speeds will these harmonics be of sufficiently high frequency that they will be attentuated.

3.4 Mechanical load model

3.4.1 Train dynamics

For the detailed model of the EMU system developed and used by the Advanced Traction and Braking project, the following major mechanical effects were included to produce a realistic benchmark to study the dynamics of the whole train.

- **Carriage momentum.** The carriage mass will be variable with the number of passengers.
- **Motor suspension.** The wheel bearings are mounted onto the bogie. The motors are hung upon spring-loaded arms. The arm moves as the motor rotates around the wheel, which couples the spring dynamics back into the traction system. This system resonates at around 4Hz, the design of the motor controller must be tuned so that it does not excite this.
- **Carriage suspension.** The bogie is isolated from the carriage by air bag suspension. The carriage is free to bounce up and down when forces are applied from the neighbouring carriages or from the wheels but any twisting movement is heavily damped.
- **Rail-wheel interface.** The adhesion between the metal wheel and a metal track is an extremely complex subject which has been studied both empirically by Nagase (1988) and theoretically by Kalker (1991). The available adhesion depends on the track condition, the relative speed between the wheel and rail, called creep and the axle loading. Within the industry it is acknowledged that the best that can be obtained is simple generic curves of adhesion against creep.
- **Wheel-axle inertia**. This effect is small compared with the mass of the train, unless the train is in a slip / slide condition, in which case the motor torque will only be accelerating the wheelset.
- **Friction.** The rolling friction of a metal wheel on a metal rail is very low compared to that of road haulage. The major source of friction is aerodynamic losses.

For work on the torque and flux estimator most of these affects are not important. A simple inertial mass with losses with be sufficient to produce realistic speed and load behaviour on the motor model.

3.4.2 A simple rotating mass model with speed dependent losses

For simulations involving the motor, the effects of the carriage and wheel-rail interface are not important. A simple mechanical model is proposed, as in Fig. 3.11, consisting of an inertia plus speed-dependent losses.

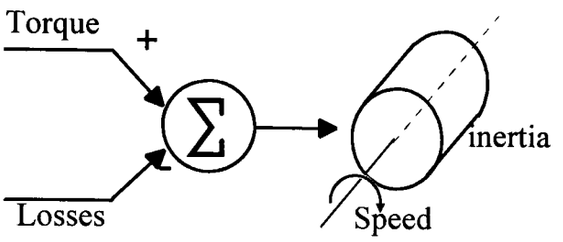

Figure 3.11. Simple mechanical model.

A typical 4 unit EMU has two powered cars each with 4 motors, a total mass of 70 ton plus a 4 ton equivalent mass from the inertia of the rotating components. This model will consider one bogie which accelerates a quarter of the total mass.

$$V_{train} = \int \frac{F_{tractive} - \Sigma F_{retarding}}{M} dt \text{ km/h} \tag{3.10}$$

Both the tractive and retarding forces are variable; the tractive force varies with train speed and supply voltage and the retardation will vary with speed and gradient.

$$F_{tractive} = \frac{T_m \times N}{R_w \times G_r} \tag{3.11}$$

Where T_m is the motor torque, N is the number of motors, R_w is the wheel radius = 0.4m (will reduce slightly with wear) and G_r is the gearbox ratio 1:6.93, approximately seven turns of the motor gives one turn of the axle.

From data supplied by GEC-Alsthom, the retarding forces are given as:

$$\Sigma F_{retarding} = K_c + K_v \times V_{train} + K_a \times V_{train}^2 \text{ kNm /per motor} \tag{3.12}$$

Where K_c=0.26, K_v=0.00048 and K_a=0.000078 for a fully laden train.

For simplicity the K_v term is neglected, since at low speed $K_c >> K_v V_{train}$ and at high speed $K_a V^2_{train} >> K_v V_{train}$.

For later work the motor speed in rads^{-1} is more useful than carriage speed in km/h.

$$\omega_r = \frac{V_{train} \times (2\pi)}{R_w \times (2\pi) \times G_r} \times \frac{1000}{3600} \text{ rads}^{-1} \tag{3.13}$$

Combining equations 3.10-13 gives the simple mechanical model as:-

$$\omega_r \approx \int (1.2 \times 10^{-4} T_m - 5.9 \times 10^{-3} \text{sign}(\omega_r) - 6.4 \times 10^{-7} \omega_r^2) dt \tag{3.14}$$

3.5 Controller design

The methodology behind the controller used in current versions of the Networker class is based on PI loops for torque and flux. In order to obtain acceptable performance from the induction motors which are non-linear and avoid suspension and supply resonances, the control loops are gain-scheduled and tuned. The controller shown in Fig. 3.1 has two PI loops for torque and flux. The loop gain, between torque error and frequency demand, must be variable to take account of Eq. 3.9. The flux loop controls the amplitude demand to maintain constant air-gap flux. In practice it is not possible to fully decouple these two loops and other constrains such as harmonic interference and resonant frequency further complicate the controller design used on the EMU. For the simplified model a basic open-loop controller is proposed which gives near maximum torque for full demand whilst restricting the air-gap flux to limit saturation effects.

3.5.1 Basic open loop controller

A simple controller is designed so that at notch 4 the motor produces close to the maximum torque for the current speed. For a given motor the torque characteristic is a 2D surface described by Eq. 3.9. The maximum torque, for any given electrical frequency, will occur at a slip S_m. This is found by differentiating Eq. 3.9 with respect to slip to find the maximum.

$$S_m = \pm \frac{R_r}{\sqrt{R_s^2 + \omega_e^2 (L_s + L_r)^2}} \tag{3.15}$$

Substitute Eq. 3.15 into Eq. 3.9 to find maximum torque T_m.

$$T_m = \frac{3}{4}\frac{P}{\omega_e} \times \frac{V_s^2}{\sqrt{R_s^2 + \omega_e^2 (L_s + L_r)^2 + R_s}} \tag{3.16}$$

The controller is implemented by means of a lookup table relating motor speed to optimum slip, as given by Eq. 3.15. Fig. 3.12 gives the results in tabular form for a range of speeds. For example at a speed of 13rads^{-1} a drive frequency of 20rads^{-1} will give maximum torque.

ωe /rads^{-1}	2	5	10	20	50	100	200	500
S_m%	73.5	73.3	72.6	70.3	58	40.2	22.8	9.5
$\frac{1}{2}S_{freq}$ /rads^{-1} [3.5]	0.7	1.8	3.63	7	14.6	20.1	22.5	23.8
ωr /rads^{-1}	1.3	3.2	6.4	13	35.4	79.9	177.5	476.2

Figure 3.12. A table of values of slip and slip frequency against motor speed for maximum torque.

At high slips and low speed the air-gap flux in the motor will be relatively high, causing saturation and severe internal heating. To overcome this, the amplitude of the applied voltage must be reduced at low frequency. This is done by making V_s linearly proportional to ω_e, up to the maximum inverter voltage. This is known as *volts-per-Hertz* control. The amplitude of the sinewave is altered to give a constant voltage to frequency ratio, reaching the maximum supply voltage at 150rads^{-1}. At low speed a small constant amplitude is used, else very little torque is produced at start-up and the motor model can not overcome the static friction.

The controller inputs are the motor speed and the demand notch setting, it outputs the required electrical frequency and amplitude demand for the inverter. Fig. 3.13 shows the *Simulink* block diagram for the controller and inverter combined.

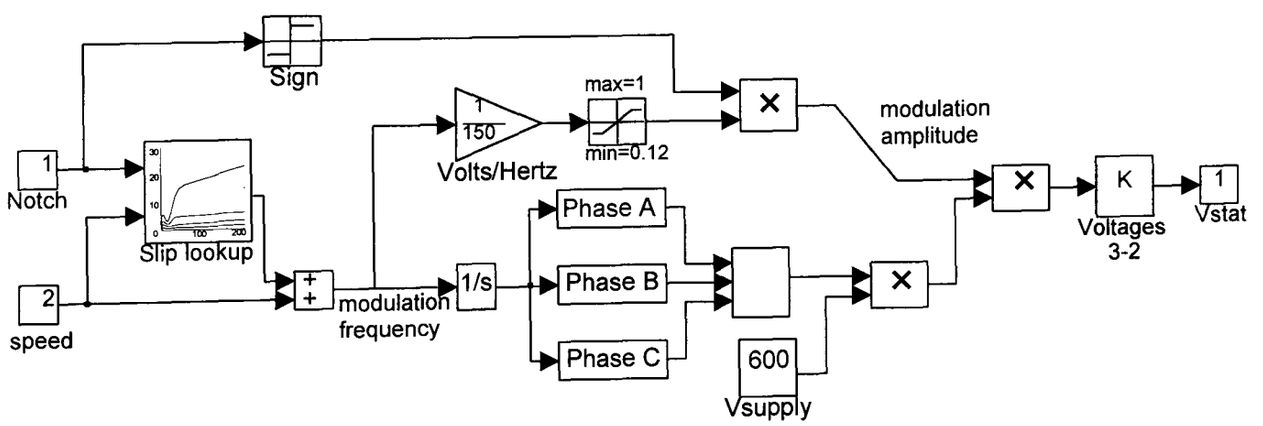

Figure 3.13. Simulink block Diagram of controller and sinewave inverter model.

[3.5] The induction motor has two pole-pairs and therefore the synchronous speed is half the applied electrical frequency. There the required slip frequency is half the calculated maximum.

This section will demonstrate the importance of the volts-per-Hertz control. Fig. 3.14a shows the time response of the motor speed and air-gap flux for a notch four start-up after 1 second. Note that the constant volts-per-Hertz control below 25rads^{-1} limits the air-gap flux. Fig. 3.14b shows the same start-up but full inverter amplitude is used. Note that the gain around 15rads^{-1} had to be considerably reduced to prevent an oscillation occurring. This is because the motor is more oscillatory between 10-30rads^{-1}, as shown in Fig.3.6. Without volts-per-Hertz control the motor can accelerate slightly faster at low speeds, but there is a large increase in the air-gap flux, this will cause saturation and internal heating in the motor.

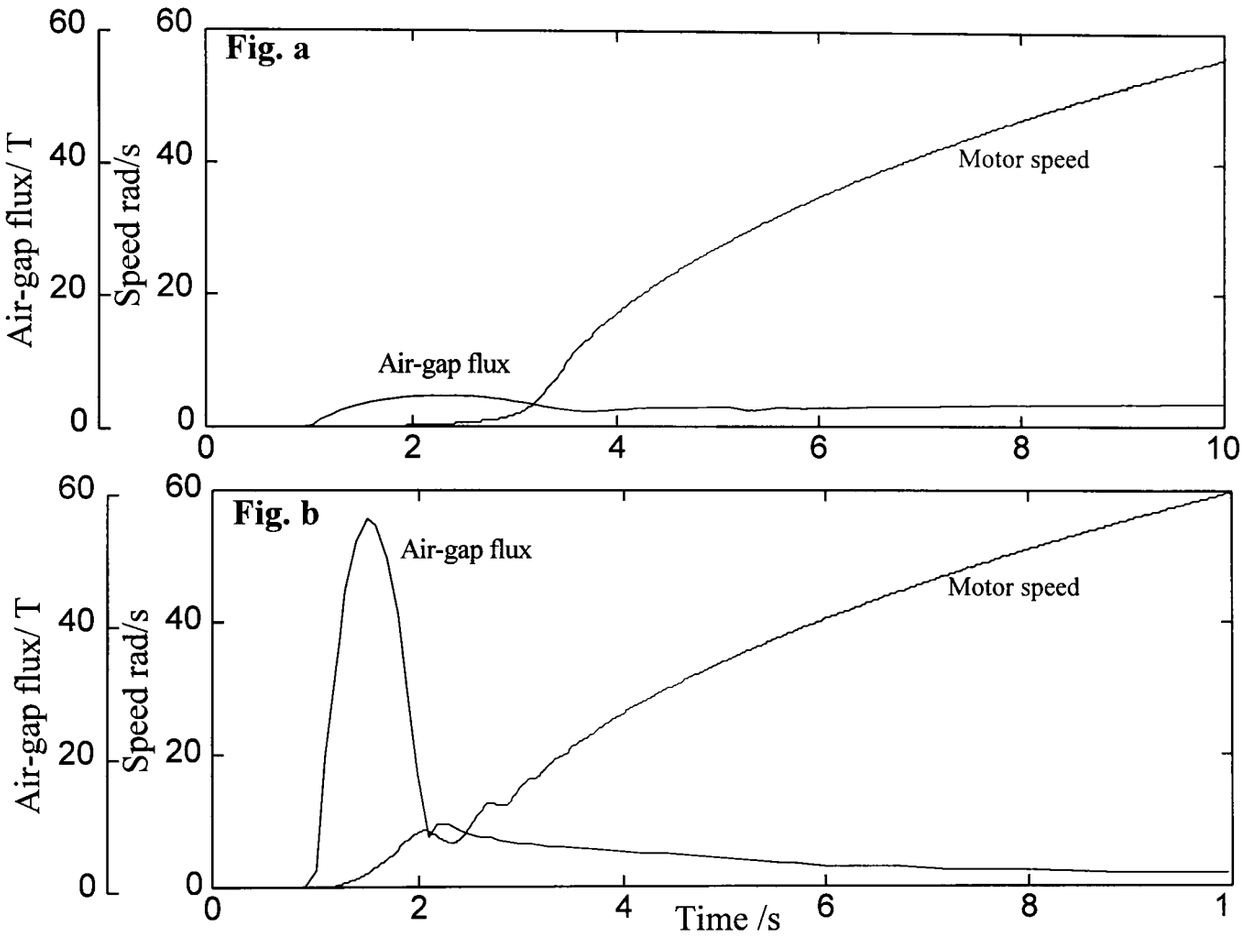

Figure 3.14a. Motor speed and flux during a notch four start-up after 1 second, with constant volts-per-Hertz control below 25rads^{-1}.
3.14b. Motor speed and flux during a notch four start-up after 1 second, at full inverter amplitude.

The simulated air-gap flux shown in Fig. 3.14b will not correspond to the actual flux in a real motor under the same conditions because the model does not include saturation which would limit the flux. However, this simulated example does demonstrate the importance of volts-per-Hertz control in keeping the motor operating in the linear part of the magnetic characteristic.

3.6 *Testing the simulation*

3.6.1 Comparison of stationary and synchronous reference frames

The simulation model developed can be used to demonstrate the key features of the stationary and synchronous reference frames, described in Section 3.2.3. To do this two sets of identical motors and loads were simulated in parallel, in the stationary and synchronous reference frames. The motors were accelerated with a ramp in slip frequency and constant volts-per-Hertz amplitude. An ideal sinewave generator is used. The resulting voltages, currents, torque and speeds are shown in Fig. 3.15 below.

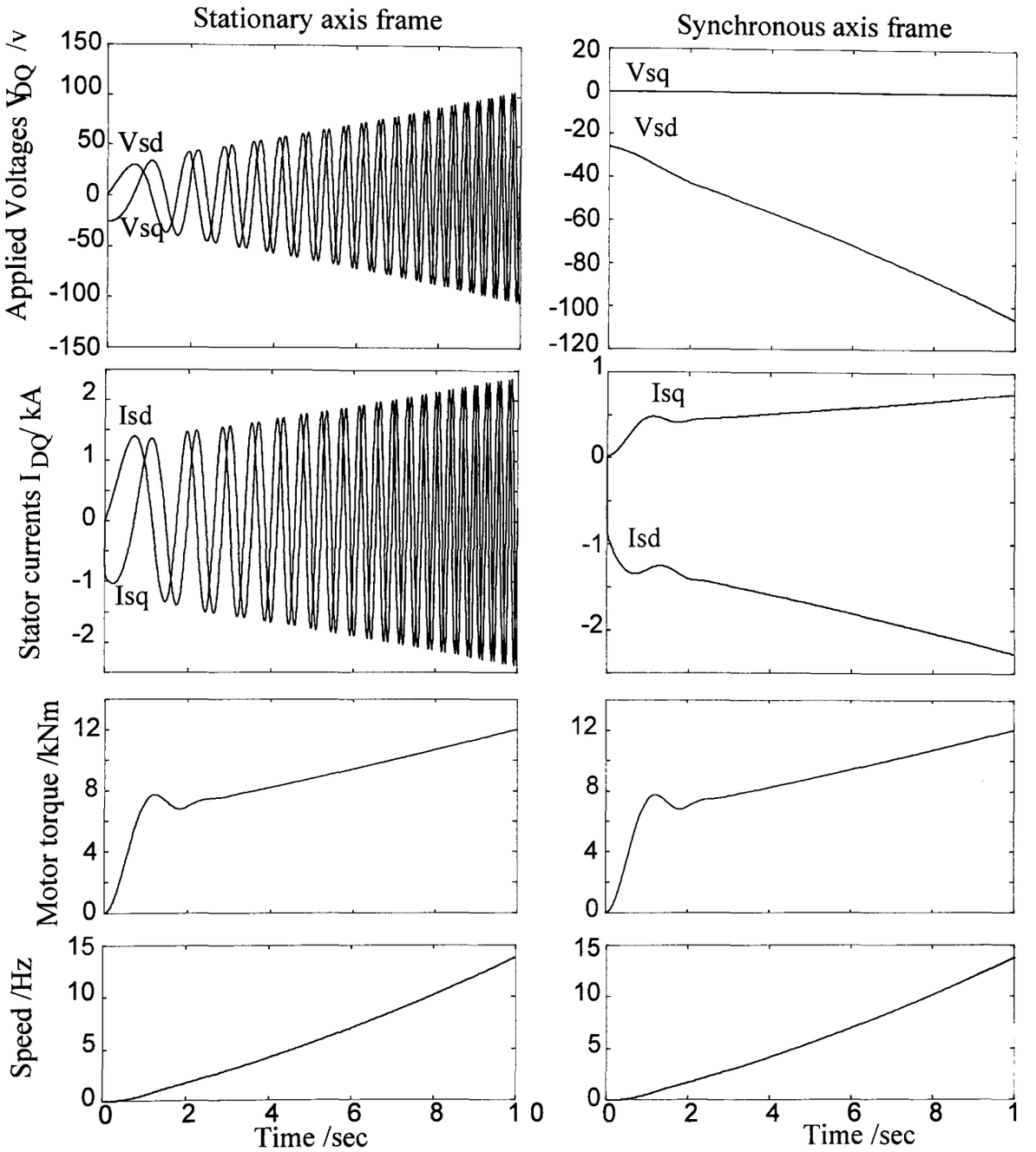

Figure 3.15. Plots of voltage, current, torque and speed for a simulated start, in both stationary and synchronous reference frames.

The main advantage of the synchronous reference frame is that under steady state conditions the currents are DC. The consequence of this is that the model is easier to linearise and larger time-steps can be used in simulating it. The disadvantages are that there is a second bilinear input to the model, the electrical speed, and it is harder to visualise the nature of complex transients in the synchronous frame.

3.6.2 Typical operating cycle

In later chapters the simple model developed in this chapter will be used to evaluate and compare new estimator designs under realistic conditions. The simplified model is validated by being put through a simulated start-up and key features are compared against data supplied by GEC-Alsthom. The model is not expected to match the real system completely because many assumptions were made for the model and the real traction system is under closed-loop control. This section shows the results of running the model through a typical operating cycle. Figure 3.16 shows the driver's notch selection and the train's speed. Initially notch 2 is used to move the train away from the platform before applying full power to accelerate up to the line speed. Using the speedometer in the cab the driver is responsible for maintaining the train speed. In this case notch three is re-applied briefly to maintain the speed.

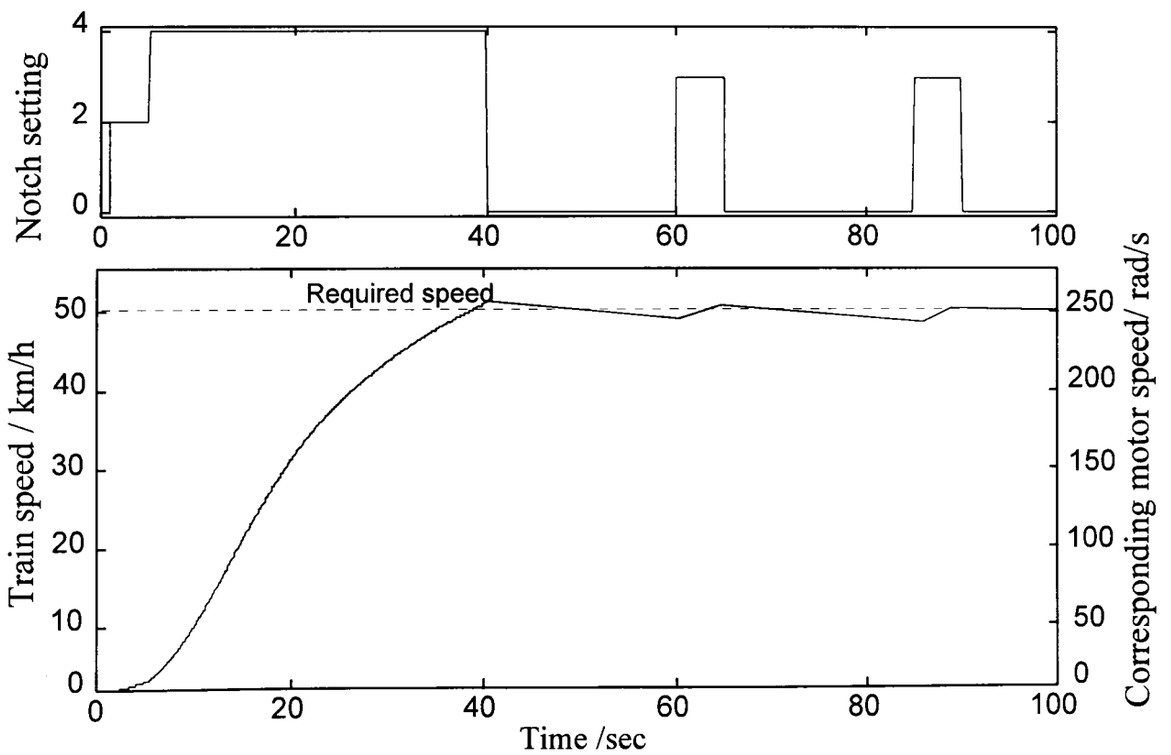

Figure 3.16. Graphs showing driver selection and train speed.

Fig. 3.17 shows the phase current in the motor. The maximum RMS phase current should be 1000 Amps, the current shown is for two motors. This current is slightly higher than expected, this is due to the lack of saturation in the model which would limit the motor current.

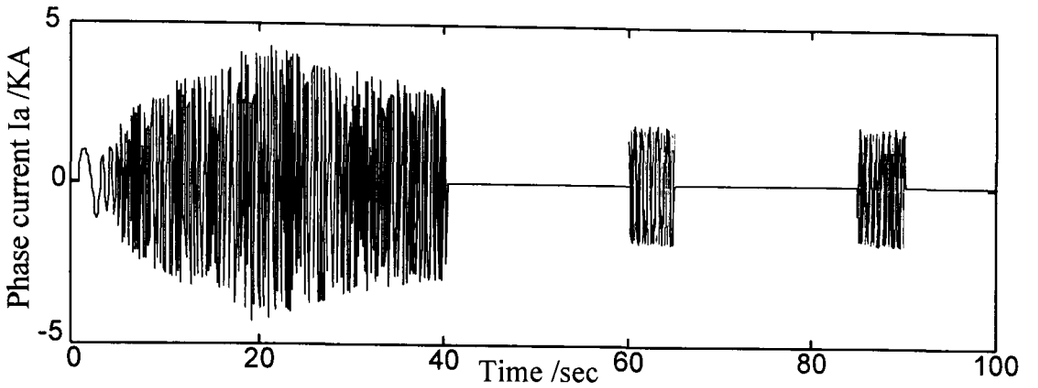

Figure 3.17. Graphs of the A phase current during simulated train operation.

Fig. 3.18. Shows the motor torque and air-gap flux during the simulation. The maximum rated motor torque is 2500Nm and the maximum air-gap flux is 1.5T.

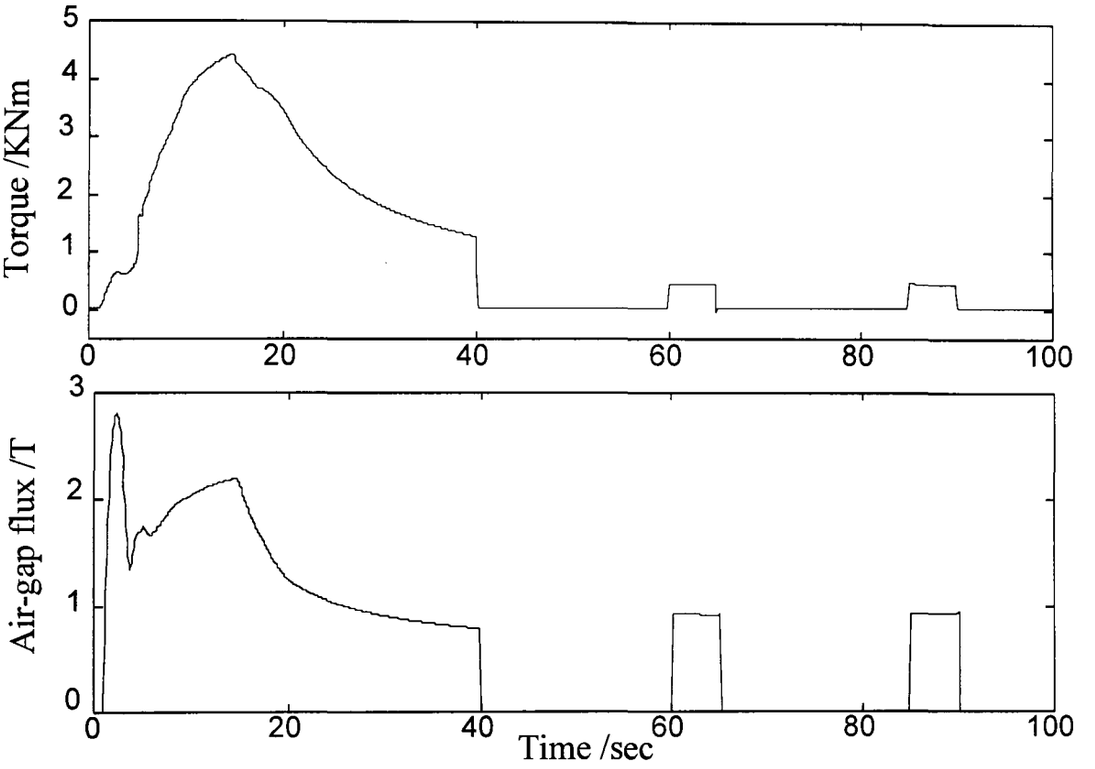

Figure 3.18. Plots of torque and flux from the simulation.

The real system operates under closed-loop control and hence gives smoother and flatter torque and flux control. The simulation is for a pair of motors and hence both torque and flux should be halved before comparison against the manufacturer's data for a single motor. The simplified model gives sensible results for speed, current, torque and flux and is sufficient to allow its use for testing new estimators under realistic conditions.

3.7 Summary

The first task for the advanced traction and braking project was to develop a model of the complete benchmark train of which the traction system is a part. For this thesis the complete benchmark model is too detailed. The starting point was to develop a simplified model of the main traction system components which could be used to evaluate new estimator designs and instrument FDI schemes as quickly as possible. This chapter has discussed the development a simplified model of the traction system for use in the work described in this thesis. Each of the main components in the traction system model is described and suitable assumptions are made to produce a simplified model with sufficient detail for the required application.

The four main components are:

The induction motors. The basic principle of the induction motor is extremely simple though the physical machine is very complex and non-linear. Making appropriate simplifications a bilinear space-state model for the motor can be obtained, with parameters supplied by GEC-Alsthom.

The inverter. The high power and available technologies limit the flexibility of the real inverter and hence three separate operating modes are used on the EMUs. These are discussed, the model is simplified by assuming that the inverter always operates in PWM mode.

The mechanical model. For more detailed studies of the dynamics of the whole EMU the model must include many different effects. For the work required in this thesis an inertia plus losses model is developed.

The controller. On the real hardware closed-loop control is used with PI loops which are gain scheduled to cope with the motor non-linearities and tuned to prevent unwanted resonances. For this work a simple open-loop controller is proposed.

The complete model is programmed in Simulink. It is run through a simulated operation cycle to validate it against data supplied by GEC-Alsthom. The model produces similar levels of flux and torque as the real EMU would in service. The most important single point in this chapter is the importance of the volts-per-Hertz control to limit the air-gap flux, this avoids saturation and keeps the model linear.

Chapter 4:

Torque and Flux estimation

As highlighted in Chapter 2 there is scope for work on the design of the torque and flux estimator used by the traction system. This chapter explains the limitations of the existing estimator. As a means of improving the estimation of state variables the use of error feedback is a widely established technique to achieve better estimation. The main body of this chapter reviews the available designs for state observers for induction motors and proposes some novel designs. The chapter ends by considering the merits of the estimation techniques. This chapter considers the merit and limitation of a range of designs and shows the tools by which they can be analysed.

4.1 The need to estimate control variables

The scalar control scheme on the EMU requires accurate knowledge of motor torque and air-gap flux. From discussions with GEC-Alsthom Traction, direct measurement of torque and flux, whilst technically possibly, is considered to be impractical or unreliable. Both these quantities can be calculated from the complete state vector of motor currents. However, to measure the rotor currents would require the sensors to rotate with the rotor. The motors are very compact and when operating in a harsh environment such a rotary connection would be unfeasible. It is necessary to estimate the unmeasured torque and flux from the measured currents and voltages.

4.1.1 Methods for estimation of control variables

The heart of any estimation routine is prior knowledge about the system, thus to estimate motor torque and flux a model of the motor is required. Methods for estimating torque and flux split into two types, those based on an open-loop model and those which use feedback to force a model to track the real plant, shown in Fig. 4.1. In the context of inductor motors these two types are commonly referred to as estimator and observer approaches, respectively[4.1].

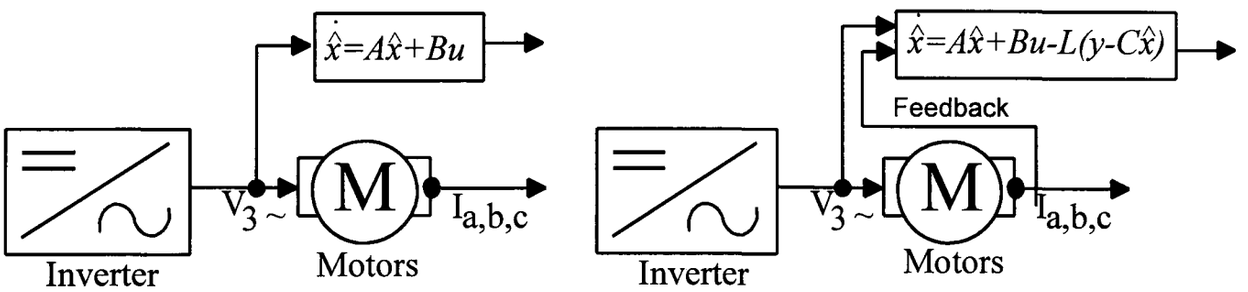

Figure 4.1. Block diagram of open-loop estimator and closed loop observer.

4.2 Open-loop methods, estimators

Jansen & Lorenz (1994) give two open-loop estimators which are derived from the electrical equations for current and flux given as Eq. 4.1 though in complex vector form rather than separate direct-quadrature components. This is because the complex notation is a more compact notation in which to write the electrical equations, as described in appendix C. In this model the fluxes in the rotor and stator windings are considered separately, rather than the air-gap flux common to them both.

[4.1] As distinct from the control theory definition of an estimator relating to stochastic techniques and observer for deterministic methods.

$$\begin{aligned} \underline{V}_{dq} &= R_s \underline{I}_{Sdq} + s\underline{\Phi}_{Sdq} \\ 0 &= R_r \underline{I}_{Rdq} + (s - j\omega_r)\underline{\Phi}_{Rdq} \end{aligned} \tag{4.1}$$

where the fluxes are defined as $\underline{\Phi}_{Sdq} = L_s \underline{I}_{Sdq} + L_m \underline{I}_{Rdq}$ and $\underline{\Phi}_{Rdq} = L_s \underline{I}_{Rdq} + L_m \underline{I}_{Sdq}$ (4.2)

By re-arranging Eq. 4.1 into state space form two equations are derived which can be used as estimators, Eq. 4.3 and 4.4.

4.2.1 Current model estimator

Using the rotor equation of the state-space form of Eq. 4.1 the estimator Eq. 4.3 is obtained, again in complex vector notation. This is an open-loop estimator and is referred to as the *current model estimator*.

$$s\hat{\underline{\Phi}}_{Rdq} = \frac{R_r L_m}{L_l} I_{sdq} - \left(\frac{R_r}{L_r} - j\omega_r\right)\hat{\underline{\Phi}}_{Rdq} \text{ [4.2]} \tag{4.3}$$

Jansen *et al* (1994) shows that this equation is very sensitive to changes in the parameters R_r and L_m. This form of estimator is especially suited to low-cost inverters where voltage sensors are often omitted to reduce the cost.

4.2.2 Voltage model estimator

By using the stator equation of the state-space form of Eq. 4.1 and Eq. 4.2 the estimator Eq. 4.4 is obtained. This is an open-loop estimator and is referred to as the *voltage model estimator*.

$$\hat{\underline{\Phi}}_{Rdq} = \frac{L_r}{L_m} \int \left(\underline{V}_{Sdq} - R_s \underline{I}_{Sdq}\right) - \left(\frac{\sigma}{1-\sigma}\right) L_m \underline{I}_{Rdq} \tag{4.4}$$

Unlike the current model form Eq. 4.4 contains a pure-integration term which is sensitive to offset errors and drift. The advantage of this method is that a speed measurement is not required, unlike the current model. This means that all the sensors can be internal to the inverter.

[4.2] Has the general state-space form of $\dot{\Phi} = A\Phi + Bi$, with flux as the state and current the input.

4.3 Analysis of the existing estimator

The existing torque and flux estimator on the traction system has been highlighted as one of the areas of interest for further study. In order to better understand the reasons for this, its design and limitations are considered.

The estimator is implemented from Eq. 3.1 for electrical behaviour of the stator, this is a voltage model method, note the flux being estimated is the air-gap flux, common to both the stator and rotor rather than the rotor flux as in Section 4.2.

$$V_{sD} = (R_s + s(L_s + L_m))I_{sD} + sL_m \times I_{rD} \quad \text{for the direct component.} \tag{4.5}$$

The required estimate is the flux across the magnetising inductance, L_m, which is caused by both the rotor and stator currents. This is called the linkage flux or the air-gap flux as given by:

$$\Phi_D = L_m \times I_{sD} + L_m \times I_{rD} \tag{4.6}$$

From Eq. 4.6 and by rearranging Eq. 4.5 an expression for the direct component is obtained as

$$\hat{\Phi}_D = \int (V_{sD} - R_s I_{sD})dt - L_s I_{sD} \tag{4.7}$$

Similarly for the quadrature component:

$$\hat{\Phi}_Q = \int (V_{sQ} - R_s I_{sQ})dt - L_s I_{sQ} \tag{4.8}$$

The scalar control system only requires the magnitude of the air-gap flux given as:

$$\hat{\Phi}_{GAP} = \sqrt{\Phi_D^2 + \Phi_Q^2} \tag{4.9}$$

An estimate of motor torque is obtained from Eq. 3.7 as:

$$\hat{T}_e = I_{sQ}\hat{\Phi}_D - I_{sD}\hat{\Phi}_Q \tag{4.10}$$

4.3.1 Practical implementation of the estimator

The estimator equations contain a pure-integration term, see Fig. 4.2a, which is likely to yield an unstable estimate in practice. Therefore to stabilise the estimator the integrator is replaced by a *leaky integrator*[4.3]. As this introduces a phase lag into one path a compensator is added to the other, see Fig. 4.2b. This technique is often referred to as *cancellation,* Jansen & Lorenz (1994).

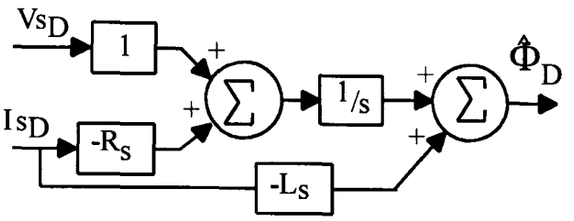

Figure 4.2a.
Based on the stator equations.

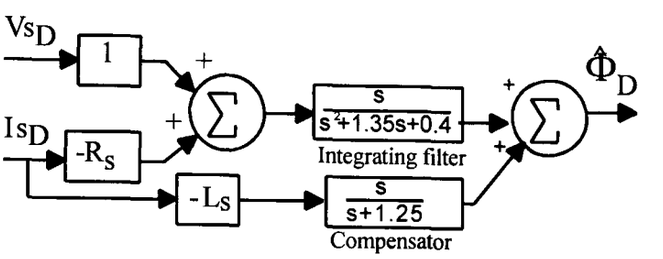

Figure 4.2b.
Without a pure-integration term.

The addition of the filter and compensator gives the estimator different dynamics from the plant model. There will therefore be an estimation error between the actual and estimated flux. As the states of the estimator are not the same as those of the model it is not possible to derive an expression for the state error, but the output error can be considered instead. The expression for the error in the air-gap is complex. The stability of this can be inferred from the two sub-expressions for the flux error in each axis. This sub-expression also appears in the equation for torque.

The error is given by the difference between the actual and estimated flux:

$$E_{fluxD} = \Phi_D - \hat{\Phi}_D \tag{4.11}$$

This is just the error resulting from the difference between the ideal estimator given by Fig. 4.1a and the actual implementation used given by Fig 4.1b with no initial condition error present. The error for each axis is the sum of two transfer functions driven by the applied voltage and measured current, given as Eq. 4.12.

$$E_{fluxD} = \left[\frac{1.35s + 0.4}{s^3 + 1.35s^2 + 0.4s}\right] Vs_D - \left[\frac{0.0001s^3 + 0.0231s^2 + 0.0355s + 0.0085}{s^4 + 2.6s^3 + 2.0875s^2 + 0.5s}\right] Is_D \tag{4.12}$$

Both these transfer functions approximate to integrators, with infinite DC gain but by 10rads^{-1} their gains are less than -40dB. The steady state error in the estimates of torque and flux are only significant at low speeds. The transient behaviour of the estimator is considered in Section 5.3.

[4.3] Leaky integrator: $H(\omega) = \frac{s}{s^2+as+b}$ such that $H(\omega \to \infty) = {}^1/_s$ and $H(\omega \to 0) = 0$.

Only at low speeds does the error in the estimate become significant, for example at 5rads^{-1} the error in the air-gap flux estimate is 3.5%. Note that Eq. 4.12 gives only the error between the ideal motor and the estimator, any noise, disturbance or initial conditions will excite a separate transient error, this is shown later by Fig. 5.4.

Using the model developed in Chapter 3, a simulated start-up in notch 2 is used to demonstrate the error dynamics of the overall estimator. The estimated torque and flux are compared against values from the motor simulation. The motor speed and resulting error in the torque estimate are shown in Fig. 4.3. From a mathematical point of view, the response to a step input would be more useful. However, on the practical side this represents an unrealistic test. Such a large step change in frequency would never be applied to motors of this size since an excessively large torque surge would be produced which could damage the rotor.

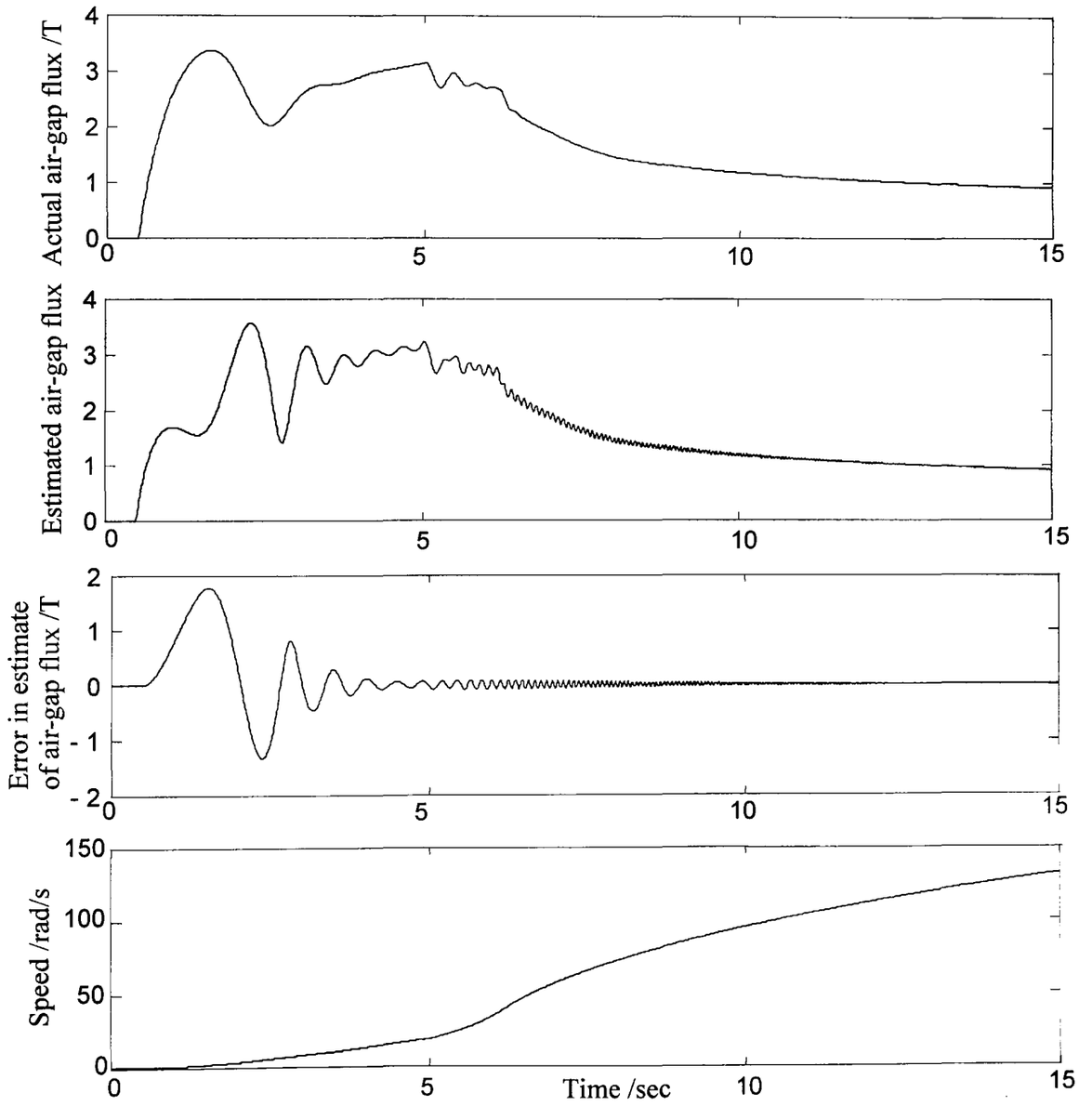

Figure 4.3 Graph of estimator error dynamics.

The estimation error becomes small as the motor speed increases. At low speed the estimator has a large steady state error. However, at high speed the estimator becomes very accurate as expected from Eq. 4.12. The error in the flux estimate appears at first to be decaying with time, like a transient, however as shown by Eq. 4.12 the error is a speed-dependent function of the motor current and applied voltage. The error decays as the motor's speed increases.

In order to limit harmonics and other 'stray' frequencies in the system high order filtering is added to both the inputs and outputs of the estimator. The final estimator becomes computationally intensive. The mathematics for the estimator are very simple but to obtain a practical estimator is rather more complex.

4.3.2 State space form of the estimator

The existing estimator is a reduced order parallel plant model, it can be represented as a state space system as given by Eq. 4.13

$$\begin{aligned} \dot{\underline{z}} &= A\underline{z} + B\underline{u} + L\underline{y} \\ \hat{\underline{\Phi}} &= C\underline{z} + D\underline{y} \end{aligned} \tag{4.13}$$

where $A = [0]^{2\times2}$, $B = [I]^{2\times2}$, $L = -R_s \times [I]^{2\times2}$, $C = [I]^{2\times2}$ and $D = -L$

This state space form for the estimator is not particularly useful because the estimator's own states do not directly correspond to the actual motor states. In the practical implementation of the estimator given by Eq. 4.1b the matrix A is replaced by one corresponding to the filter dynamics.

4.4 Closed loop methods, observers

The main body of this chapter considers the uses of closed-loop observers to estimate the motor states.

4.4.1 Observers for a linear system

An observer has two components, a model of the plant and error feedback of the outputs which is used to force the observer's model to track the plant.

For a linear plant given in state space form as Eq. 4.14

$$\begin{aligned} \dot{\underline{x}} &= A\underline{x} + B\underline{u} \\ \underline{y} &= C\underline{x} \end{aligned} \tag{4.14}$$

a linear observer can be produced as in Eq. 4.15.

$$\begin{aligned} \dot{\hat{\underline{x}}} &= A\hat{\underline{x}} + B\underline{u} + L(\underline{y} - \hat{\underline{y}}) \\ \hat{\underline{y}} &= C\hat{\underline{x}} \end{aligned} \tag{4.15}$$

The state estimation error, $\underline{e} = \underline{x} - \hat{\underline{x}}$ in the observer will decay with dynamics determined by the matrix (A-LC) as given by:

$$\dot{\underline{e}} = (A - LC)\underline{e} \tag{4.16}$$

4.4.2 Observer design for an induction motor

For the induction motor the model may be in either the stationary or synchronous reference frame and may use all the currents or the stator currents with air-gap fluxes as states. The observer does not have to be of the full order, a reduced order observer can be used to estimate the fluxes or rotor currents on their own. Observers have the advantage that the error feedback will give faster convergence between the model and the plant. It can also prevent small discrepancies in dynamics causing the state estimate to diverge. The induction motor is non-linear and therefore a large range of observer designs can be considered.

4.5 *Linear feedback observers*

For a practical application the design should be as simple as possible. This section shows the limitations of linear feedback to explain why more complex methods are required.

4.5.1 Fixed gain observers

It is easy to assign error dynamics for a fixed drive frequency, since the plant is effectively linear for small changes in speed. The problem in the design of a state space observer occurs with variable frequency drives because of the speed dependency of the motor dynamics. Beginning by assuming a fixed operating speed a state space observer is proposed of the form given by Eq. 4.17. Feedback of the measurable motor state is used to force a parallel model to track the plant, from which the unmeasurable states are estimated. The observer feedback gain is calculated for a fixed motor speed.

$$\begin{aligned} \dot{\hat{\underline{x}}} &= (A + N\omega)\hat{\underline{x}} + LC(\underline{x} - \hat{\underline{x}}) + B\underline{u} \\ \hat{\underline{y}} &= C\hat{\underline{x}} \end{aligned} \tag{4.17}$$

Fig. 4.5. shows the loci of the poles of the observer's error dynamics with speed, when the feedback gain is calculated at two different fixed speeds, 0 and 200rads^{-1}.

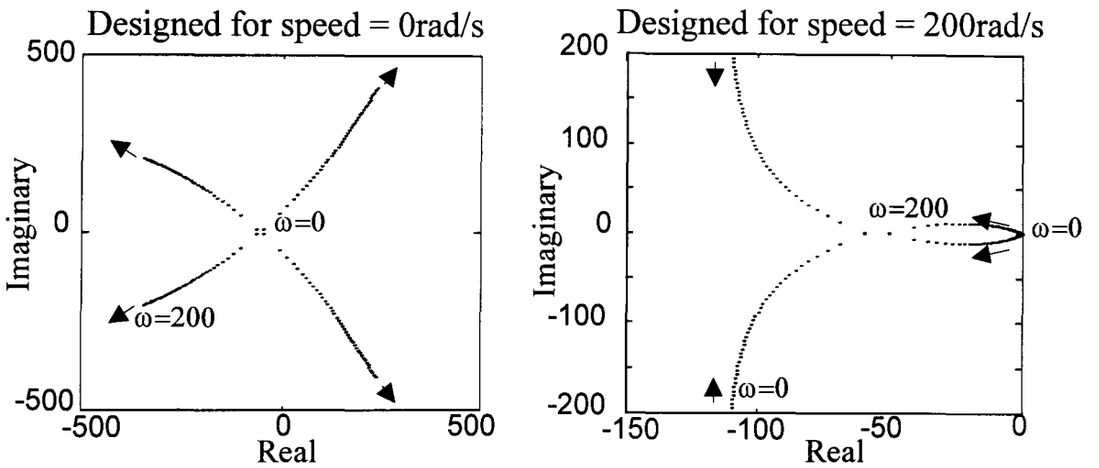

Figure 4.5. The loci of the eigenvalues of the error dynamics with speed for two assumed design speeds.

With the eigenvalues placed for zero speed, as the speed increases they move out in a 'star-burst' fashion, two of the eigenvalues cross into the right-hand half plane. In order for an observer to remain stable over the complete operating range of speeds the eigenvalues need to be placed far enough left of the origin. The moving eigenvalues make the observer's error dynamics variable with speed. With the eigenvalues placed for a model speed of 200rads^{-1} the observer is stable across the whole operating range.

However, at low speeds the eigenvalues are close to the origin and the observer would be slow to converge.

This observer implementation has a gain which is independent of speed but it still requires a speed input for the bilinear term. The error dynamics of both these approaches are undesirable, as would be expected with the changing dynamics.

4.5.2 Bilinear decoupled observers

A more rigorous approach to fixed gain observer design for bilinear system is obtained by considering the bilinear terms as unknown inputs. The observer is then designed to decouple the unknown inputs from the error dynamics. For more details on unknown input observer see Chen *et al* (1996). This general approach has become known as the bilinear decoupled observer method, Shields & Yu (1995), Yu & Shields (1995) and Hou & Pugh (1997).

Using the method proposed by Hac (1992) but ignoring the additional disturbance input that is included for robustness:-

Starting with the general form of a bilinear system given by Eq. 4.18,

$$\begin{aligned} \dot{\underline{x}} &= A\underline{x} + B\underline{u} + \sum_{i=1}^{k} N_i u_i \underline{x} \\ \underline{y} &= C\underline{x} \end{aligned} \tag{4.18}$$

Where $\underline{u} \in \Re^{\kappa}$ is a vector of k inputs, u_i i=1,2···k which have linear or multiplicative effects on the state vector, through matrices B and N.

An observer of the form given in Eq. 4.19 is proposed by Hac (1992).

$$\begin{aligned} \dot{\underline{v}} &= H\underline{v} + L\underline{y} + J\underline{u} + \sum_{i=1}^{k} G_i u_i \underline{v} + \sum_{i=1}^{k} E_i u_i \underline{y} \\ \underline{z} &= \underline{v} + P\underline{y} \end{aligned} \tag{4.19}$$

The corresponding observer error dynamics are:

$$\dot{\underline{e}} = (H + \sum_{i=1}^{k} G_i u_i)\underline{e} + (MA - HM + LC)\underline{x} + \sum_{i=1}^{k} (E_i C + MN_i - G_i M)u_i \underline{x} + (J + MB\underline{u}) \tag{4.20}$$

where $M = (PC - I_n)$

This can be reduced to $\dot{\underline{e}} = H\underline{e}$ if the following conditions are met.

$$\begin{aligned} &i) && G_i = 0 && i = 1...k \\ &ii) && E_i C + (PC - I)N_i = 0 && i = 1...k \\ &iii) && H(PC - I) - (PC - I)A - LC = 0 \\ &iv) && J = -(PC - I)B \\ &v) && H \text{ must be stable} \end{aligned} \tag{4.21}$$

Hac (1992) has outlined a set of tests to determine if the conditions 4.21 i-v can be satisfied for a specific bilinear system and if so it outlines the design procedure.

For the bilinear motor model it is possible to meet condition (ii) but conditions (iv) and (v) require that the pair $(I_n\text{-}PC)A,C$ is detectable. This is not the case for the induction motor, the rank of the observability matrix is 2, the system order is 4 and the eigenvalues of $(I_n\text{-}PC)A$ are zero. Using a symbolic design it has been shown that this will be the case for any motor, see appendix E. However Shield & Yu (1996) considers several generalised designs for bilinear observer for fault detection and gives a formal condition for the existence of a stable observer in each case. The conditions cannot be met for any motor, since there are too many bilinear terms to decouple with the available design freedom, irrespective of the type of states or the rotation of the reference frame.

4.5.3 Bellini's observer

One of the first uses of a bilinear model for an induction motors was by Bellini *et al* (1979) who considered a simple design for a reduced order observer from a bilinear representation. In this case the motor equations were in terms of stator currents and air-gap flux, as given in Eq. 4.22.

$$\begin{bmatrix} V_{sD} \\ V_{sQ} \\ 0 \\ 0 \end{bmatrix} = \begin{bmatrix} R_s + s(L_s - L_m) & 0 & s & 0 \\ 0 & R_s + s(L_s - L_m) & 0 & s \\ R_r - s(L_s - L_m) & -\omega(L_r - L_m) & \dfrac{R_r + sL_r}{L_m} & \dfrac{\omega L_r}{L_m} \\ \omega(L_r - L_m) & R_r - s(L_s - L_m) & -\dfrac{\omega L_r}{L_m} & \dfrac{R_r + sL_r}{L_m} \end{bmatrix} \begin{bmatrix} I_{sD} \\ I_{sQ} \\ \Phi_D \\ \Phi_Q \end{bmatrix} \tag{4.22}$$

This is then rearranged into the state space form. The intermediate equations at this stage are rather cumbersome and have not been included. A state transformation T is then applied which gives the following space state system.

$$\dot{\underline{z}} = (A_b + N_b\omega)\underline{z} + B_b\underline{u} \tag{4.23}$$

where $\underline{z}=T\underline{x}$ and the transformation matrix is:

$$T = \begin{bmatrix} 1 & 0 & 0 & 0 \\ 0 & 1 & 0 & 0 \\ -L_s + L_m & 0 & 1 & 0 \\ 0 & -L_s + L_m & 0 & 1 \end{bmatrix} \tag{4.24}$$

giving the transformed model as Eq. 4.25.

$$\dot{\underline{z}}=\underbrace{\begin{bmatrix} -\frac{L_rR_s+R_rL_s}{L_rL_s-L_m^2} & -\omega & \frac{R_r}{L_rL_s-L_m^2} & \frac{\omega L_r}{L_rL_s-L_m^2} \\ \omega & -\frac{L_rR_s+R_rL_s}{L_rL_s-L_m^2} & -\frac{\omega L_r}{L_rL_s-L_m^2} & \frac{R_r}{L_rL_s-L_m^2} \\ -R_s & 0 & 0 & 0 \\ 0 & -R_s & 0 & 0 \end{bmatrix}}_{\text{Bilinear}} \underline{z} = \begin{bmatrix} \frac{R_r}{L_rL_s-L_m^2} & 0 \\ 0 & \frac{R_r}{L_rL_s-L_m^2} \\ 1 & 0 \\ 0 & 1 \end{bmatrix} \underline{u} \qquad (4.25)$$

Bellini *et al* (1979) then derive a reduced order observer, which implements the state equation:

$$\begin{aligned} \dot{\underline{p}} &= (T_1 + T_2\omega)\underline{p} + (T_3 + T_4\omega)\underline{y} + T_5\underline{u} \\ \hat{\underline{x}} &= L_1\underline{y} + L_2\underline{p} \end{aligned} \qquad (4.26)$$

Where $\underline{p}$ are the unmeasurable states, $\underline{y}$ are the measurable states, $\underline{u}$ are the inputs and $\underline{x}$ is the complete state vector. T_n and L_n are matrices to be designed.

$\underline{p}$ is a reduced state vector obtained by a linear transform C' on the complete states $\underline{x}$

where $C' = [H\ I]$

H is a design matrix $\begin{bmatrix} -h_1 & h_2 \\ -h_2 & -h_1 \end{bmatrix}$ selected with prior knowledge of the motor structure.

The L matrices are defined by $\begin{bmatrix} C \\ C' \end{bmatrix}^{-1} = \begin{bmatrix} L_1 & L_2 \end{bmatrix}$ (4.27)

The T matrices are defined as:

$T_1 = C'A_bL_2$, $T_2 = C'N_bL_2$, $T_3 = C'A_bL_1$, $T_4 = C'N_bL_1$ and $T_5 = C'B_b$ (4.28)

Bellini states that the eigenvalues of this observer are given by Eq. 4.29.

$$\lambda_{(1,2)} = -(h_1A_{12} + h_2N_{12}\omega) \pm j(h_1N_{12}\omega + h_2A_{12}) \qquad (4.29)$$

By making h_1=0 and h_2=-L_s+L_m the eigenvalues are constrained in the complex direction and move with speed from the origin further into the left-hand half plane. Note that this observer is at the limit of stability for zero speed. Once set up and simulated the observer has a favourable performance and under practical conditions the error converges to zero.

The two poles of the reduced order observer are located at -ω±3.14*i*, for the induction motor. The observer is set up and simulated at two fixed motor speeds, with an initial condition error, Fig. 4.6 shows the resulting error transient.

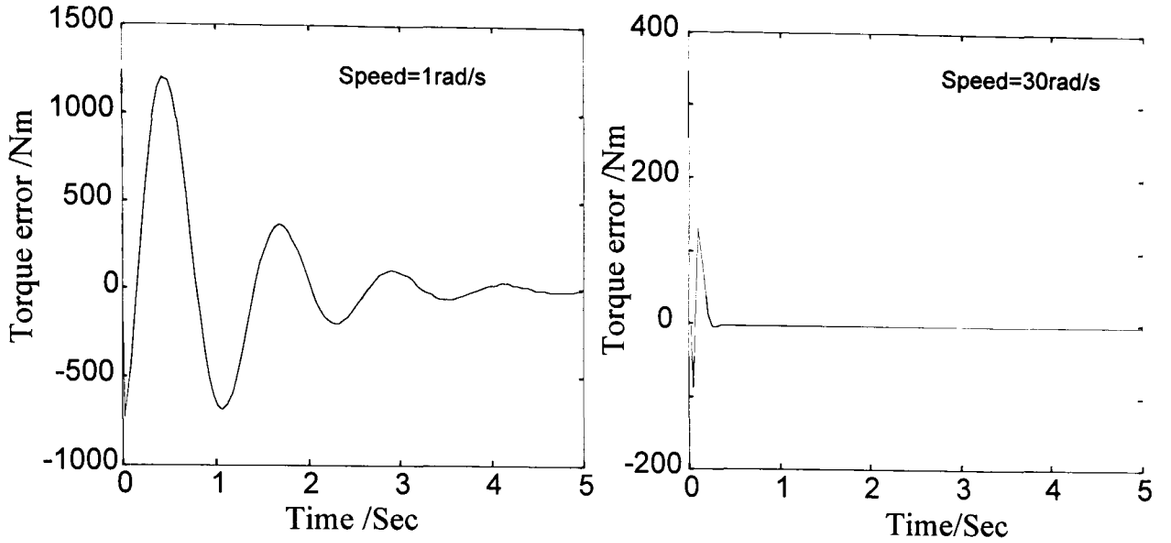

Figure 4.6. Error in the torque estimate with a difference in initial conditions between the observer and the model, for the rotor speed fixed at 1rads^{-1} and 30rads^{-1}.

At low speeds the observer's error dynamics are slow to converge and very oscillatory. At higher speeds the error decays more rapidly and is less oscillatory, as would be expected from the eigenvalue locations. At zero speed the eigenvalues have zero real value and as a result the error will not decay.

This specific observer design method for induction motors is very similar to the general method of Hac (1992) for bilinear systems. It is the arbitrary choice of H that relaxes the conditions given in Eq. 4.21 and causes the eigenvalues to become functions of speed.

4.6 State observers using speed-dependent feedback

The use of a fixed gain has been shown to be impractical since the error dynamics become a function of speed. Whilst stable observers can be produced the design lacks the freedom to make the observer performance desirable at all operating speeds. Since the motor model is speed-dependent several methods which use speed-dependent feedback will be considered in the following sections.

4.6.1 On-line recalculation of gain

Ben-Brahim & Kawamura (1992) and Bottura *et al* (1993) consider observers which re-calculate feedback gains on-line to assign observer dynamics in real-time. Regardless of the method employed the computational load of re-calculating the observer at each update becomes very high. A better approach would be either gain scheduling with observer gains for speed stored in a look-up table or pre-calculating a gain matrix as a mathematical function of speed.

The rest of this section considers work which has been done on the development of a non-linear observer using gain scheduling. The design process described in the following section is circular. The initial aim was to obtain, as a function of speed, a feedback matrix $L(\omega)$ which fixes the eigenvalues for all speeds then to implement this as an equation on-line, rather than using look-up tables which are memory intensive. This is shown to be impractical, never-the-less it is useful to consider the entire design process.

4.6.2 Obtaining the feedback matrix as an explicit function of speed

The observer has the following closed-loop form.

$$\begin{aligned} \dot{\hat{\underline{x}}} &= (A + N\omega)\,\hat{\underline{x}} + L(\omega)\left(\underline{y} - \hat{\underline{y}}\right) + B\underline{u} \\ \hat{\underline{y}} &= C\hat{\underline{x}} \end{aligned} \tag{4.30}$$

The observer gain matrix is a function of speed so that the observer eigenvalues remain fixed with speed. This method involves obtaining an expression in terms of speed such that the observer's gain matrix can be dynamically re-calculated to fix its eigenvalues. The Matlab Symbolic Toolbox is a powerful extension to Matlab based on the software package Maple. Using a parametric approach to design the feedback matrix described by Wang *et al* (1993), it was possible to write a Matlab script file which would produce a gain matrix $L(\omega)$.

Using the parametric approach, $L(\omega)$ is given by Eq. 4.31.

$$L(\omega) = W^{-1}Q \tag{4.31}$$

where W is a matrix of left eigenrows, $W = \begin{bmatrix} w_1 & w_2 & w_3 & w_4 \end{bmatrix}^T$ obtained from Eq. 4.32.

$$w_i = q_i^T C(A + N\omega - \mathrm{I}\lambda)^{-1} \tag{4.32}$$

λ_i are the desired eigenvalues and $Q = \begin{bmatrix} q_1 & q_2 & q_3 & q_4 \end{bmatrix}^T$ is an arbitrarily design matrix.

By using the Symbolic toolbox for Matlab it is possible to get an expression for the gain matrix in terms of speed. This involves two matrix inversions and the complexity of the calculation will grow rapidly if care is not taken to simplify the calculation and to manipulate the intermediate results.

4.6.3 The functions for the feedback gain

The $L(\omega)$ is a 4×2 matrix where the terms L_{11} and L_{22} are constant: L_{12} and L_{11} are linear with speed and the other four are order 10 polynomials of speed. The eight plots in Fig.4.7 show how the terms of the gain matrix alter with speed, for pairs of eigenvalues at -50 and -10. Appendix F shows that the symbolic expression is too sensitive to numerical errors and the resulting gain matrix has to be stored in a look-up table.

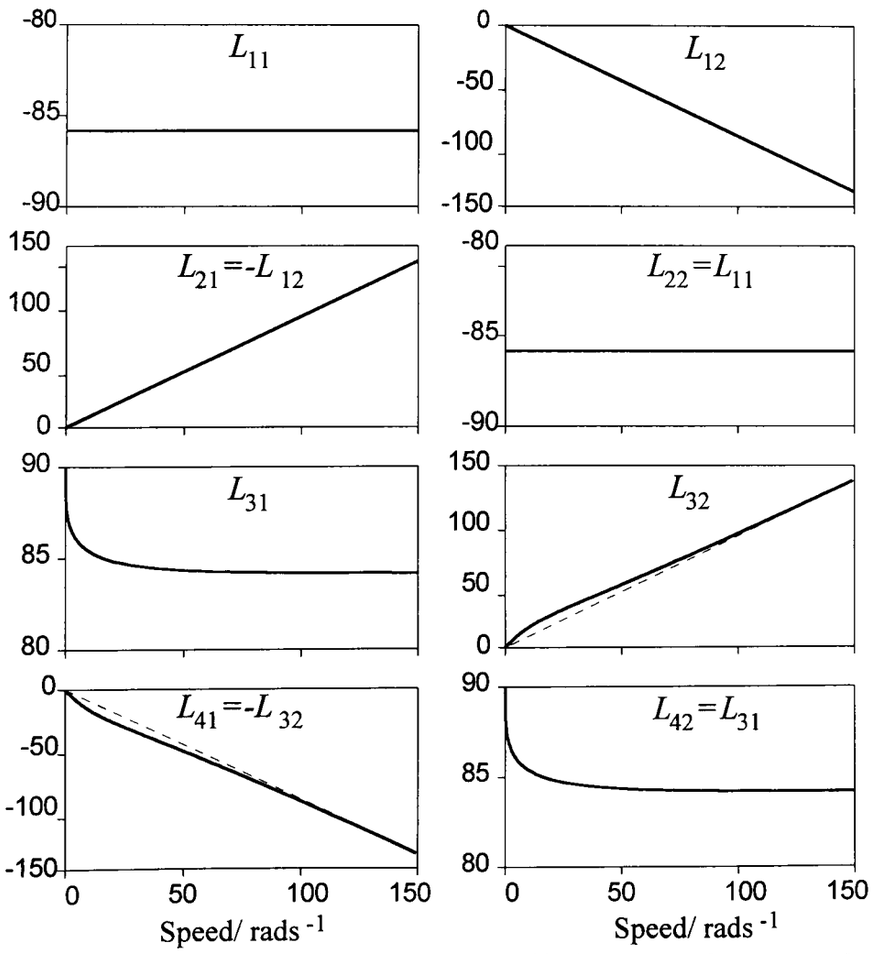

Figure 4.7. The gain matrix co-efficients against speed.

The eigenvalues were initially placed in pairs to simplify the design. This can be done because two linearly independent eigenvectors can be found for the repeated poles. However, the likely effect of this is to increase the sensitivity of the observer and there is no reason why they cannot be placed individually.

Since it is necessary to store the gains in a look-up table there is freedom to use other pole assignment routines, for example the Matlab '*place*' function. This gives full freedom to assign the observer's error dynamics. Section 7.2.3 shows that relatively few points actually need to be stored, typically twenty over the motor's operating range.

Bird & Zelaya-dela-Parra (1996) plot graphs of gain against speed for an observer design in a state space form, using stator current and flux as the states. These gains are assigned using the Matlab 'place' function. These are then approximated to give an observer which can be implemented without a look-up table; the eigenvalues of the error dynamics are nolonger fixed.

4.7 A Bilinear observer

This section describes another attempt at obtaining the feedback as an explicit function of speed by exploiting the structure inherent in the motor model to develop a novel observer using bilinear feedback.

The matrices can be represented in partitioned form.

$A = \begin{bmatrix} A_{11} & A_{12} \\ A_{21} & A_{22} \end{bmatrix}$ where each term is a constant, a_{xx}, multiplied by the matrix $I = \begin{bmatrix} 1 & 0 \\ 0 & 1 \end{bmatrix}$

$N = \begin{bmatrix} N_{11} & N_{12} \\ N_{21} & N_{22} \end{bmatrix}$ where each term is a constant, n_{xx}, multiplied by the matrix $J = \begin{bmatrix} 0 & 1 \\ -1 & 0 \end{bmatrix}$

The observer is of the same form as the non-linear observer.

$$\begin{aligned} \dot{\hat{\underline{x}}} &= (A + N\omega)\,\hat{\underline{x}} + L(\omega)\left(\underline{y} - \hat{\underline{y}}\right) + B\underline{u} \\ \hat{\underline{y}} &= C\hat{\underline{x}} \end{aligned} \tag{4.33}$$

where, $L(\omega) = L_1 + L_2\omega$ gives a bilinear feedback of the state error.

The matrix L_1 is designed such that it cancels the linear terms in the observer's error dynamics, ((A+Nω)-LC) and adds two eigenvalues. The matrix L_2 is designed to cancel the speed dependent terms..

If $A = \begin{bmatrix} A_{11} & A_{12} \\ A_{21} & A_{22} \end{bmatrix}$ let $L_1C = \begin{bmatrix} -A_{11} + \Lambda & 0 \\ -A_{21} & 0 \end{bmatrix}$ where $\Lambda = \begin{bmatrix} \lambda_1 & 0 \\ 0 & \lambda_2 \end{bmatrix}$

and $N = \begin{bmatrix} N_{11} & N_{12} \\ N_{21} & N_{22} \end{bmatrix}$ let $L_2C = \begin{bmatrix} -N_{11} & 0 \\ -N_{21} & 0 \end{bmatrix}$

It can be shown that the eigenvalues of the observer's error dynamics are λ_1, λ_2 and $a_{22} \pm \omega v_{22} i$. For the bilinear motor model there are two fixed assignable eigenvalues and two unassignable eigenvalues, given by -48.5±ω15.4*i*. This observer has stable eigenvalues for all steady state operating speeds, but at high speed they become increasingly oscillatory. For the traction motor the poles become too oscillatory for practical use. However for the test-rig motor, used in Chapter 7, the poles of the error dynamics are -298±ω6*i* which are significantly less oscillatory. Consideration of a_{22} and n_{22} show that the bilinear observer is best suited to small induction motors where $R_r >> L_r$., see Appendix G.

The observer for the traction motor is set up in Simulink and simulated for an error in initial conditions. Fig. 4.8a shows the decay of this error for two different assignable

eigenvalue locations and speeds. The motor speed is held constant by using a very large inertia in the mechanical model.

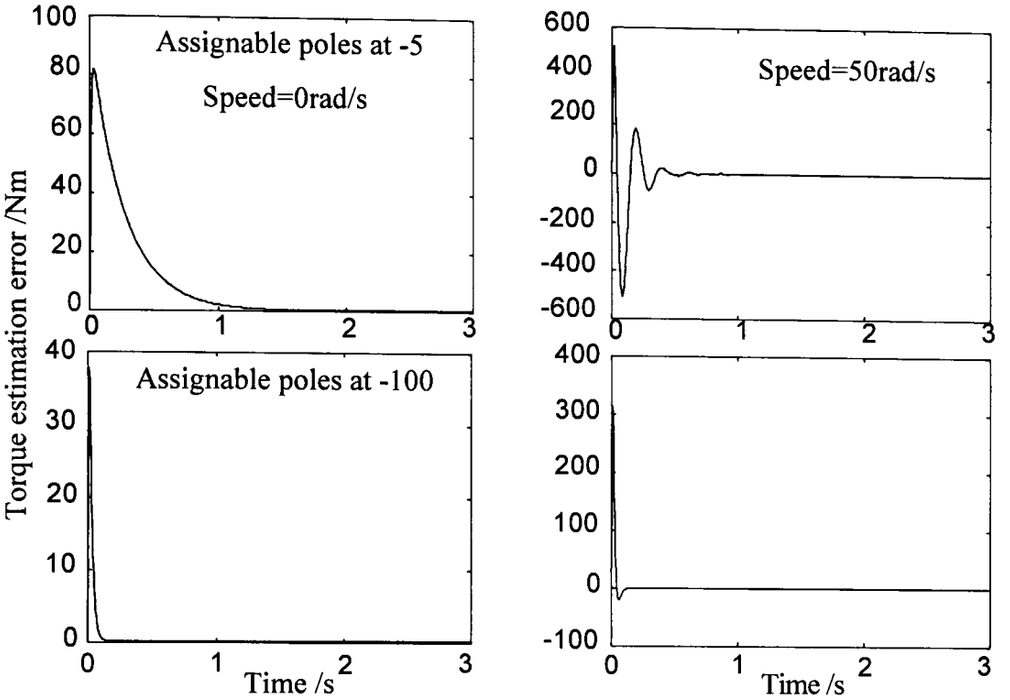

Figure 4.8. The transient response of the observer with the assignable poles in pairs at -5 and -100 at two different speeds

4.7.1 Observer stability

For a time-varying observer, negative eigenvalues are a necessary but not sufficient condition for stability and a more rigorous proof of stability is required. To prove that the bilinear observer is stable for all operating conditions it must be shown to be locally stable for all operating speeds.

In the error dynamics, there is no feedback-coupling between the stator and rotor states, therefore the stability problem reduces to proving the stability of the submatrix $[a_{22}I+\omega n_{22}J]$. This can be achieved using Lyapanov's second method which states that a non-linear function $f(x)$ is locally stable if when linearised about the point x it is positive definite and the derivative $\dot{f}(x)$ is negative definite, see Franklin *et al* (1995).

A Lyapanov function is chosen in terms of the state error as:

$$V = e^T e \tag{4.34}$$

where the observer's error dynamics are:

$$\dot{e} = (A + N\omega)e \tag{4.35}$$

This is chosen such that, by definition, it is always positive definite. To prove the stability of V and hence of $f(x)$ it must be shown that $\dot{V}$ is negative definite for all possible conditions.

Differentiating Eq. 4.34 with respective to time yields:

$$\begin{aligned}\dot{V} &= \dot{e}^T e + e^T \dot{e} \\ &= e^T\left(A_{22}^T + A_{22} + (N_{22}^T + N_{22})\omega\right)e\end{aligned} \tag{4.36}$$

It can be seen that $N_{22}^T = -N_{22}$ and $A_{22}^T = A_{22}$

$\therefore N_{22}^T + N_{22} = 0$ and $A_{22}^T + A_{22} = 2A_{22}$

The stability property is now independent of speed and solely depends on A being negative definite, which it is if $a_{22}<0$. Since a_{22} is always negative, stability is guaranteed for any motor. In this case stability could have been assumed since the real parts of the error dynamics are independent of the bilinear input which changes much more slowly than the states.

4.7.2 Using bilinear feedback in other reference frames

Using the current-flux states model, as in Section 4.5.3, the real value of the unassignable poles would be zero. Using the synchronous reference frame, as described in Section 3.2.3, the error dynamics are a function of both the rotor speed and the electrical drive frequency. For the traction motor they approximate to $-0.1\pm i\omega_e$ which is stable but very slow to converge and still become oscillatory.

This method is opportunist; it exploits the general structure of an induction motor and the numerical properties of the specific motor. Its main advantage is that it involves minimal on-line calculations and does not require memory to store a look-up table.

4.8 Sliding mode observers for the induction motor

Sliding mode control has attracted much interest in recent years because of its low sensitivity to noise and modelling errors. As with linear feedback there is a duality between controller and observer design. However it is only recently that sliding mode observers have been developed.. Utkin (1992) presented the basic design for a sliding mode observer, where discontinuous feedback is used to force a model onto a sliding mode to track a plant. More recently, Walcott *et al* (1987) and Edwards & Spurgeon (1994) have proposed designs where linear feedback is use to obtain an asymptotically stable observer and switching is then added to reject matched uncertainty or disturbances.

Sliding mode control for induction motors has attracted interest, Shyu & Shieh (1995) and Sabanovic & Izosimov (1981), this is because the switching inherent in an inverter lends itself more readily to a switching scheme than many other linearly controlled plants. However, on the observer side only one paper by Jezernik *et al* (1993), has been located which mentions sliding techniques for observer designs on induction motors. In this paper a fixed gain is used, despite the speed measurement being required for the model. This ignores the potential advantage of optimising the observers dynamics by scheduling the gain for different speeds.

4.8.1 The basic theory for a sliding mode observer

For a system whose outputs are a subset of the actual states, the state equations can be rewritten in submatrix form as:

$$\begin{aligned} \dot{\underline{y}} &= A_{11}\underline{y} + A_{12}\underline{x}_2 + B_1\underline{u} \\ \dot{\underline{x}}_2 &= A_{21}\underline{y} + A_{22}\underline{x}_2 + B_2\underline{u} \end{aligned} \tag{4.37}$$

where $\underline{y}$ are the measured states and $\underline{x}_2$ the unmeasured states.

Utkin (1992) proposed an observer of the form:

$$\begin{aligned} \dot{\hat{\underline{y}}} &= A_{11}\hat{\underline{y}} + A_{12}\hat{\underline{x}}_2 + B_1\underline{u} - \underline{\upsilon} \\ \dot{\hat{\underline{x}}}_2 &= A_{21}\hat{\underline{y}} + A_{22}\hat{\underline{x}}_2 + B_2\underline{u} + K\underline{\upsilon} \end{aligned} \tag{4.38}$$

$\underline{\upsilon}$ is vector of components, $\upsilon_i = Msgn(\hat{y}_i - y_i)$ i=1.2···m, where m is the number of outputs. $K \in \Re^{n\text{-}m}$ is a design matrix, where n is the number of states.

$$sgn(x) = \left\{ \begin{array}{l} = 1 \text{ if } x \geq 0 \\ = -1 \text{ if } x < 0 \end{array} \right\} \tag{4.39}$$

The error between the actual and estimated states are $\underline{e}_y = \underline{\hat{y}} - \underline{y}$ and $\underline{e}_2 = \underline{\hat{x}}_2 - \underline{x}_2$

$$\begin{aligned} \dot{\underline{e}}_y &= A_{11}\underline{e}_y + A_{12}\underline{e}_2 - \underline{\upsilon} \\ \dot{\underline{e}}_2 &= A_{21}\underline{e}_y + A_{22}\underline{e}_2 + K\underline{\upsilon} \end{aligned} \tag{4.40}$$

Consider the transform $T_s = \begin{bmatrix} I_p & 0 \\ K & I_{n-p} \end{bmatrix}$ such that $\begin{bmatrix} y \\ x_2' \end{bmatrix} = T_s \begin{bmatrix} y \\ x_2 \end{bmatrix}$ (4.41)

The error in the system when transformed into the new co-ordinates becomes

$$\begin{aligned} \dot{\underline{e}}_y &= A'_{11}\underline{e}_y + A'_{12}\underline{e}'_2 - \underline{\upsilon} \\ \dot{\underline{e}}'_2 &= A'_{21}\underline{e}_y + A'_{22}\underline{e}'_2 \end{aligned} \tag{4.42}$$

With a large enough switching gain, M, a sliding motion can be set up on $\underline{e}_y$ and after this time the error is reduced to zero, therefore the observer's error dynamics reduce to:

$$\begin{aligned} \dot{\underline{e}}_y &= 0 \\ \dot{\underline{e}}'_2 &= A'_{22}e'_2 \end{aligned} \tag{4.43}$$

where $A'_{22} = A_{22} + KA_{12}$.

By a suitable choice of the gain, K, the observer can be made stable. The convergence of the measured states is dependent on M, which determines how long it takes to reach a sliding mode. The convergence of the unmeasured states is determined by the selection of K.

4.8.2 Extension of Utkin's observer for the induction motor problem

The Section considers how it has been possible to extend the basic Uktin observer for linear systems to a bilinear plant. For the induction motor problem the two key matrices in this sliding mode observer design, A_{22} and A_{12}, now contain bilinear terms.

Consider first the design of K for the induction motor.

$$A_{22} = \begin{bmatrix} a_4 & \omega n_4 \\ -\omega n_4 & a_4 \end{bmatrix}, \quad A_{12} = \begin{bmatrix} a_2 & \omega n_2 \\ -\omega n_2 & a_2 \end{bmatrix}$$

Using *a prior* knowledge about the motor the gain matrix is assumed to have the form:

$$K = \begin{bmatrix} k_1 & k_2 \\ -k_2 & k_1 \end{bmatrix}$$

Therefore, the important dynamics in the new axis are given by:

$$A'_{22} = \begin{bmatrix} a_4 + k_1 a_2 - k_2 n_2 \omega & n_4\omega + k_1 n_2 \omega + k_2 a_2 \\ -n_4\omega + k_1 n_2 \omega + k_2 a_2 & a_4 + k_1 a_2 - k_2 n_2 \omega \end{bmatrix} \tag{4.44}$$

Using a symbolic mathematics package, such as *Maple*, an expression for the eigenvalues can be produced. However, the result is a large expression which is not easy to work with. This can be simplified by further constraining the gain matrix.

Assuming the gain matrix has the form $K = \begin{bmatrix} k & 0 \\ 0 & k \end{bmatrix}$

the eigenvalues of A'_{22} are then given by:

$$\lambda_{(e_2)} = a_4 + a_2 k \pm \sqrt{-(n_4 + n_2 k)^2 \omega^2} \tag{4.45}$$

For any k there will be a complex conjugate pair with a fixed real part, but with an increasingly large imaginary part, as speed increases. By choosing $k = -\frac{n_4}{n_2}$ the speed-dependent term can be cancelled. This however results in the real part become numerically almost zero, and hence the observer is very slow to converge.

Taking a gain k=0.1, in Eq. 4.45, and using the values for the traction motor the eigenvalues are $\lambda_{(e_2)} = -43.8 \pm i3.72\omega$.

The extended sliding mode observer is set up in Simulink and run through a simulated start-up. An initial condition error is introduced between the plant and observer states, to excite the error dynamics of the sliding observer. Fig. 4.9 below shows the error in the state I_{sD} and the motor speed, with a small initial condition error. The observer is given a gain M=100 and k=0.1

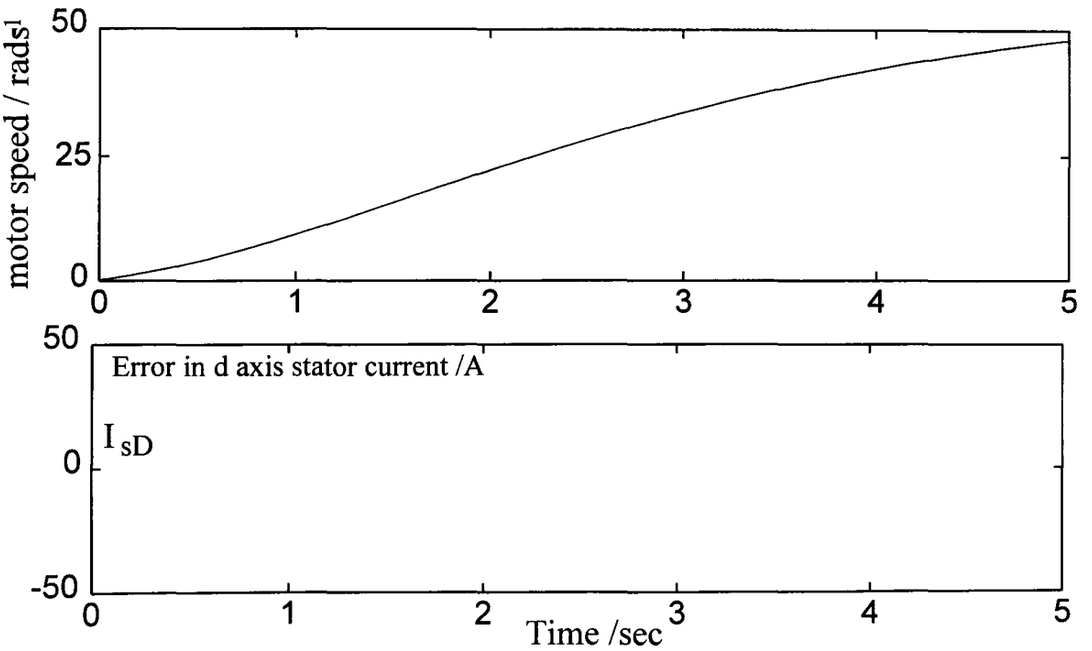

Figure 4.9. Plots of the error in the sliding mode observer's estimates of the direct component of the stator current and speed during a simulated start up.

Fig. 4.9. shows how the error in the state estimate initially decays to zero, following a sliding mode. However, as the speed increases a limit cycle oscillation is established which increases with speed. This behaviour is shown more clearly in the state trajectory diagram in Fig. 4.10. This observer is stable but at high speed it converges to a speed-dependent limit cycle.

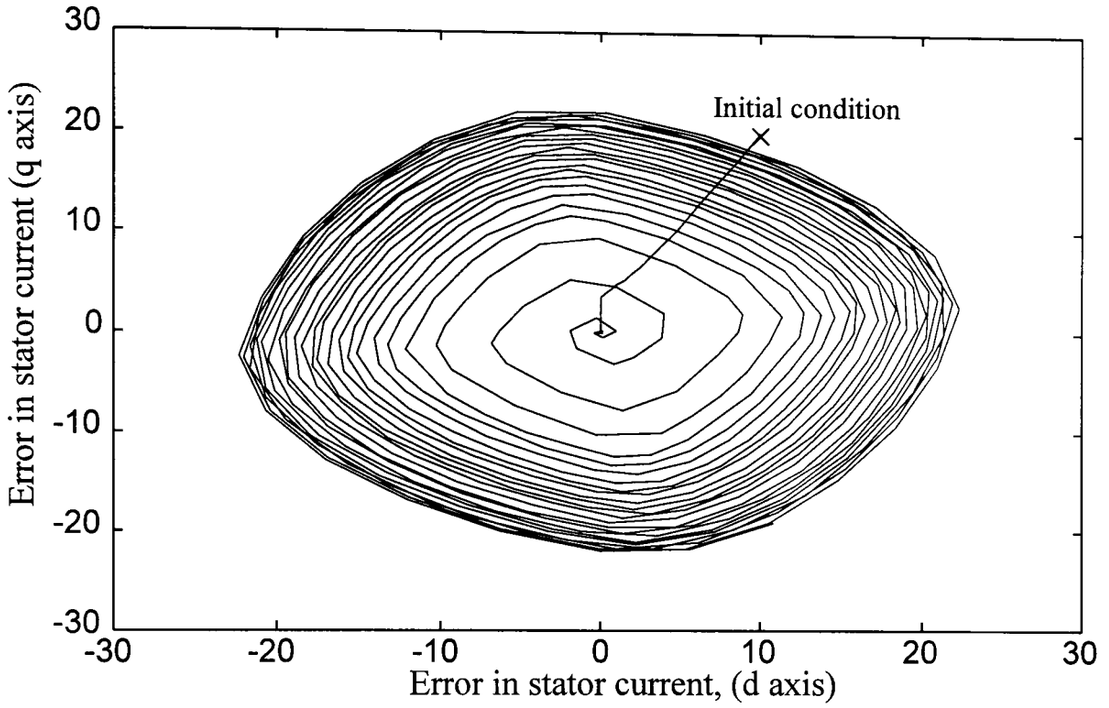

Figure 4.10. State transition diagram showing limit cycle.

4.8.3 Preventing the occurrence of limit circle at high speed

The limit cycle in Fig. 4.10 can be shown to occur as a result of trying to design a sliding mode observer with oscillatory eigenvalues, see Appendix H. Therefore it is necessary to find a gain matrix K which does not give oscillatory eigenvalues to the observer's error dynamics at high speed.

The one possible speed independent case for the observer gain, $K=\begin{bmatrix} k & 0 \\ 0 & k \end{bmatrix}$, has been shown to be unsuitable, because the resulting oscillatory poles cause a limit cycle to occur.

Consider then $K=\begin{bmatrix} 0 & k \\ -k & 0 \end{bmatrix}$, chosen with some prior knowledge about motor's structure.

This results in pole locations of :

$$\lambda = a_{22} \pm \sqrt{k^2\omega^2 n_{12}^2 - \omega^2 n_{22}^2 + k^2 a_{12}^2} \tag{4.46}$$

by equating the expression under the square root to zero the poles can be fixed.

This gives an expression for k as a function of speed:

$$k = \frac{n_{22}\omega}{\sqrt{n_{12}^2\omega^2 + a_{12}^2}} \tag{4.47}$$

Using speed-dependent feedback the poles can be fixed at $\lambda=a_{22}$, which for the traction motor is approximately -64.

Fig. 4.11 shows the error dynamics both in the time-domain and as state trajectories for a range of gains, M=1000, 100 and 10, obtained from simulation with an initial condition error.

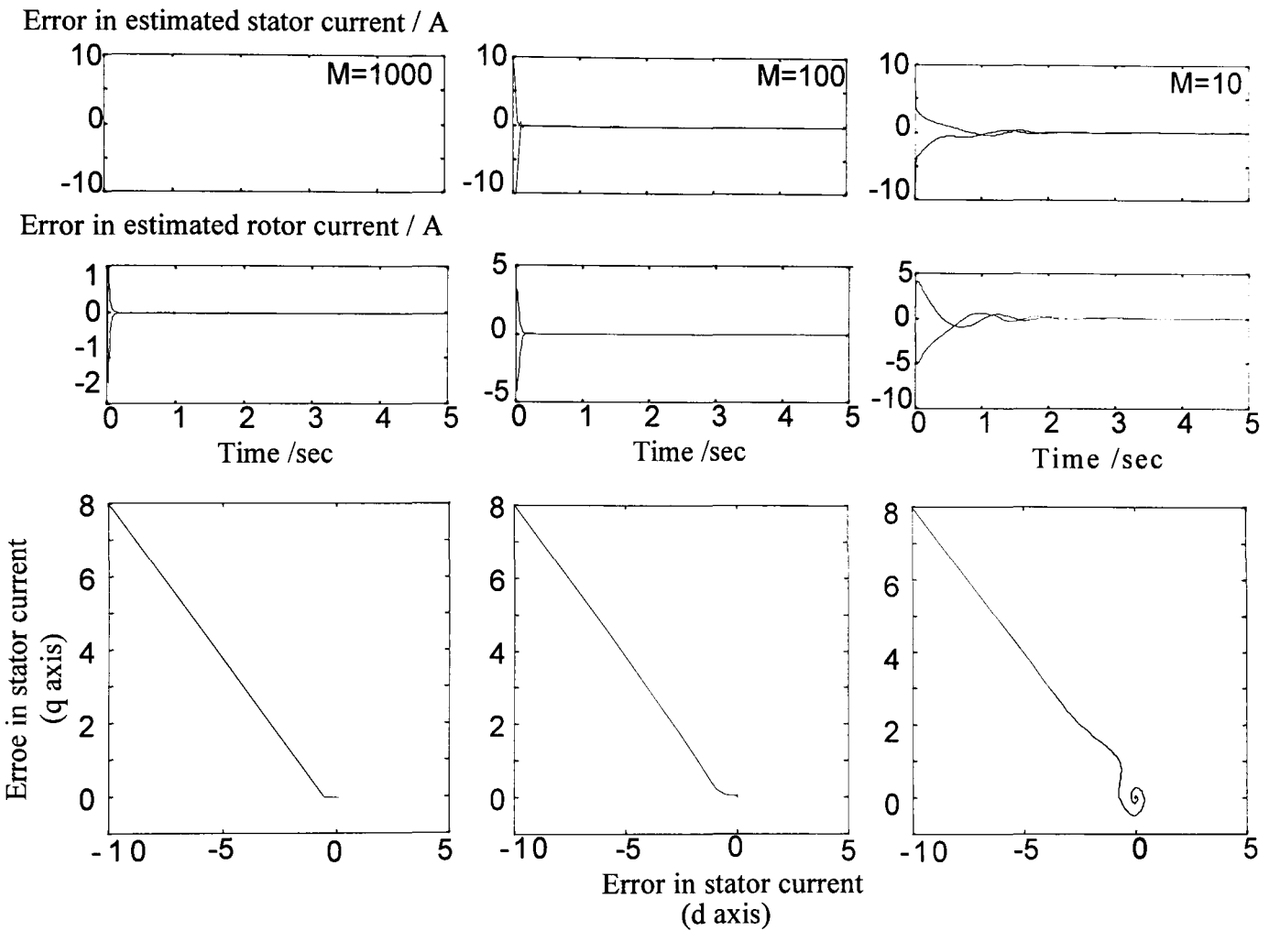

Figure 4.11. Plots of error dynamics and state-trajectories for different switching gains.

The greater the switching gain the stronger the attraction to sliding. If the gain becomes too small the states nolonger follow the sliding surface. However, high gains require small time steps and greater resolution in the simulation because of high-frequency chattering.

4.8.4 Comparison of sliding mode observer and parametrised observer

One of the most commonly stated advantages of sliding mode techniques is the ability to reject noise. To consider this, the sliding mode observer is compared, in simulation, with the parametrised observer with Guassian noise, 20A rms on the stator currents, 2000A rms. Fig. 4.12. shows the results.

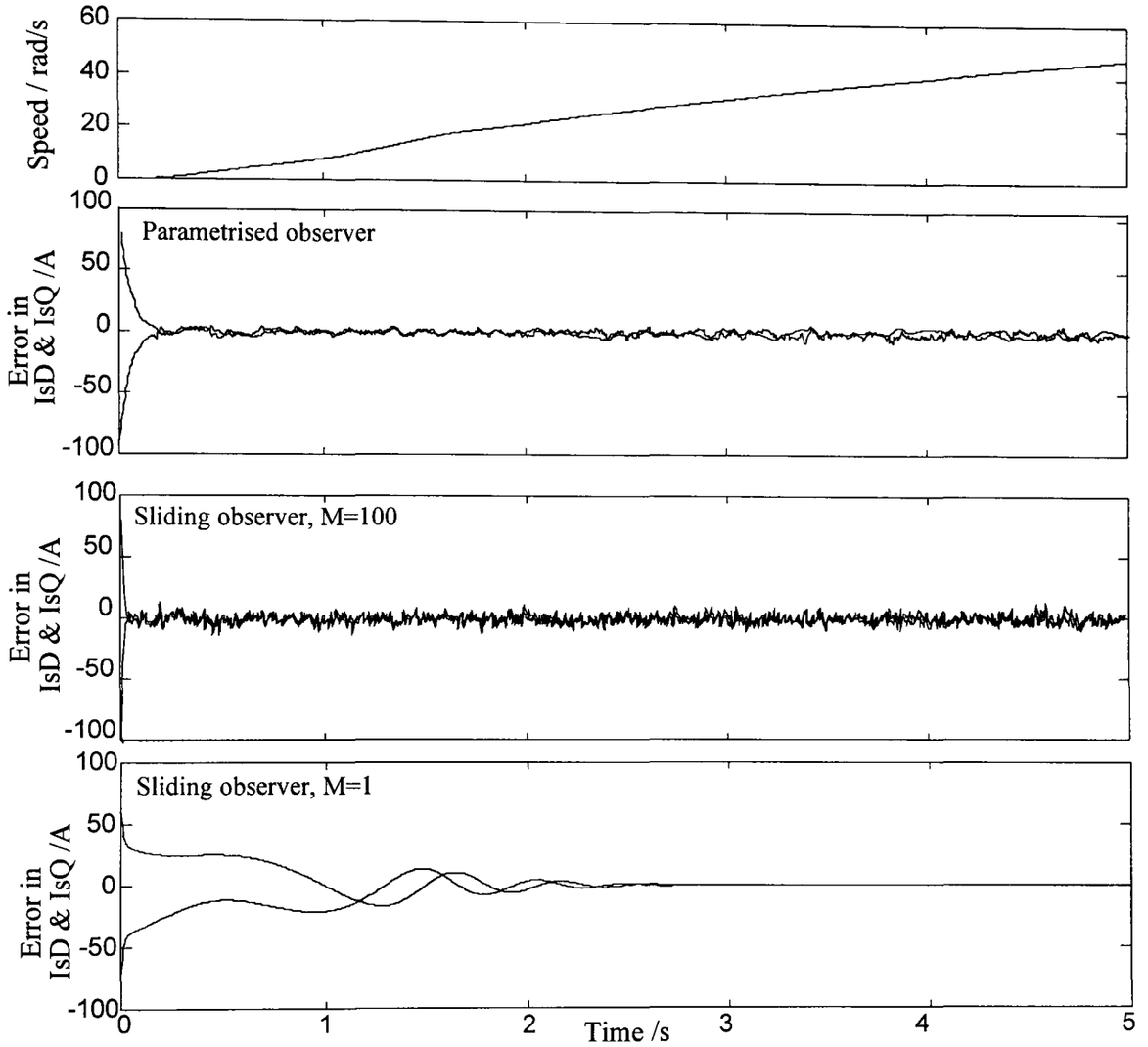

Figure 4.12. State estimation error for the sliding mode observer.

The greater the gain on the switching function the faster the sliding observer converges, but its sensitivity to noise is increased. With the low gain the observer's noise rejection is far better than the parametrised observer but the error convergence is slow. An analysis of the sliding observer is significantly more complex than that of Luenberger observers. The sliding mode observer uses a full order model, Eq. 4.38, but once it is sliding the system becomes a reduced order observer, Eq. 4.43. Dorling & Zinober (1983) compare the robustness of the sliding mode observer to noise and parameter changes against both the full and reduced order Luenberger observers. The sliding mode observer has a comparable sensitivity to parameters as the reduced order Luenberger observer, which

has a significantly lower performance than the full order observer. When noise is include however, the sliding mode observer is comparable with the full order method. The basic sliding mode observer does not produce a more robust design. It can however be extended by using linear feedback to stabilise the observer and then using the switching feedback to accomplish other objectives, Slotine *et al* (1987). Edwards & Spurgeon (1994) describe a design which uses the switching feedback to decouple matched uncertainty from the states. This work was later extended to detect faults, Edwards *et al* (1997). However using this design procedure it is not possible to produce a stable observer for the induction motor over the complete speed range.

4.8.5 A continuous implementation by approximating the switching function

The problem of high frequency chattering and the need for small time-steps are major limitations for sliding mode observer techniques. A common method of implementing a switched mode controller is to replace the hard switch with a soft switching function as given by Eq. 4.48. This can be extended to the observer design.

the switching function *sgn* is replaced with $\upsilon = \begin{cases} = 1 & \text{if } k\underline{u} \geq 1 \\ = k\underline{u} & \\ = -1 & \text{if } k\underline{u} \leq -1 \end{cases}$ (4.48)

The effect of the transition slope (k), can be shown by considering two extremes. Fig. 4.13 shows the state trajectories with an initial condition error for k=1 and 10000.

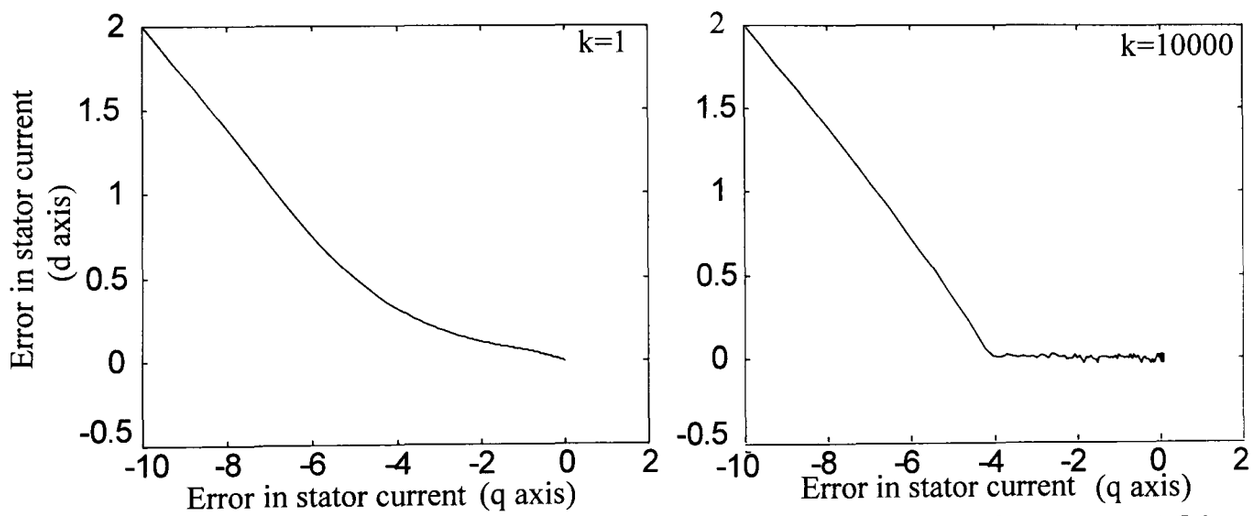

Figure 4.13. Error trajectory diagrams for the sliding observer with *soft* switching.

If the value of k is too small the feedback remains in the linear (transition) region giving a linear observer. Too high a value of k and the feedback jumps across the linear region giving discontinuous feedback, which 'chatters' about zero error, like the 'pure' sliding mode observer.

4.9 Other observer techniques

Several other closed-loop methods for induction motor state estimation have been discussed in the literature and are summarised below for completeness.

4.9.1 Multiple-model fuzzy observers

Lopez *et al* (1997) present a fuzzy observer scheme, which uses TS[4.4] fuzzy models to represent the bilinear motor model. This consists of a set of models, covering a range of speeds, for each of which an observer is designed. This is done using a LMI[4.5] framework to ensure that when the outputs from the observers are combined the overall estimate is stable. This is able to constrain the error dynamics to a bounded region which becomes smaller as the number of models increases. The disadvantage of this technique is the computational burden involved in the use of the multiple observers when a similar design can be obtained by gain scheduling as proposed in Section 4.6.3. The computational load of this fuzzy technique cannot be justified unless it adds something of value which cannot be obtained otherwise. The advantage of this technique is that the formal design procedure guarantees stability.

4.9.2 Kalman filter techniques

The Kalman filter is a special case of an observer. It is designed to give optimal estimates of a plant's states in the presence of noise of a known distribution. Noise or disturbance signals are modelled as Gaussian or coloured noise on the states or outputs, with the distribution given in two co-variance matrices, Q for the plant and R for the measurements. The algorithm then calculates the feedback to minimise the effect of the noise on the estimated states. Atkinson *et al* (1991) consider a Kalman filter design for the induction motor; look-up tables are used to limit the amount of on-line calculations.

Much discussion has centred on assigning the co-variance matrices for the noise in the measurements and the process, which remains largely arbitrary. It is important to understand from the outset what the design is trying to achieve, whether it is noise rejection on the outputs or robustness to model uncertainty. For the motor state estimation the largest co-variance is normally assigned to the process to reflect the uncertainty in model parameters, especially winding resistances.

[4.4]Takagi-Sugeno. Takagi & Sugeno (1985)

[4.5] Linear Matrix Inequality. Boyd *et al* (1994)

The Kalman filter method is restrictive in that it constrains the convergence rate of the error dynamics. Luenberger observers have the same problem balancing the conflicting needs of fast convergence and low sensitivity to noise, as discussed in Section 4.14.

The basic Kalman filter design is computationally very intensive since it involves a matrix inversion or Ricatti equation solution. The calculation can be simplified by means of a look-up table of steady state gains against speed, but this means the filter is only optimal in steady state conditions. For the traction motor this would mean that during rapid transients such as the onset of wheel spin, the estimates are likely to be inaccurate. This is precisely the situation which must be avoided.

4.10 Extended observers

It is possible to augment the basic state-space model, given by Eq. 3.5. Using the dynamic equation for the load, Eq. 3.14 and the equation for the motor torque, Eq. 3.7 the motor speed and torque can be made states of the model. The resulting state equation given by Eq. 4.49 is extremely non-linear, containing multiplications of states with states. The reason for wanting to 'augment' the states to include speed is that it can then be estimated. In practice the motor will be driving a load, so there will be an unknown load torque, T_L by assuming that this load torque is constant, $\dot{T}_L = 0$, it too can be augmented as a state. The resulting state equations are given as:

$$\begin{bmatrix} \dot{I}_{sD} \\ \dot{I}_{sQ} \\ \dot{I}_{rD} \\ \dot{I}_{rQ} \\ \hline \dot{\omega}_r \\ \dot{T}_L \end{bmatrix} = \left[\begin{array}{cccc:cc} & & & & & \\ & & [A(\omega_r,\omega_e)] & & & [0] \\ & & & & & \\ \hline -\beta I_{rQ} & \beta I_{rD} & 0 & 0 & 0 & -\alpha \\ 0 & 0 & 0 & 0 & 0 & 0 \end{array}\right] \left[\begin{array}{c} I_{sD} \\ I_{sQ} \\ I_{rD} \\ I_{rQ} \\ \hline \omega_r \\ T_L \end{array}\right] + \left[\begin{array}{cc} & \\ [B] & \\ & \\ \hline 0 & 0 \\ 0 & 0 \end{array}\right] \begin{bmatrix} V_{sD} \\ V_{sQ} \end{bmatrix} \qquad (4.49)$$

Where α and β are constants relating the torque to speed, from Eq. 3.14 and $A(\omega_r,\omega_e)$ represents the state-space model in the appropriate form.

The basic principle of the extended observer as described by Birk & Zeitz (1988) is simple. A local linearisation is performed about the present states. The model is differentiated about the present states to give a perturbation model. Next an observer is designed for the perturbation model. This is used to calculate the change in the states. The change is added to the previous states to give the updated values for the states. The feedback may be calculated using either a Kalman filter or Luenberger observer technique. This gives either the extend Kalman filter, Kataoka *et al* (1993) or Loron & Laiberté (1993) or the extended Luenberger observer as Brdys & Du (1991) or Orlowska-Kowalska (1989). Du *et al* (1995) point out that for Kalman filter based approaches poor selection of the co-variance matrix will result in bias errors and Ljung (1979) shows that the stability can only be guaranteed for a limited range of systems and inputs. The problem for these approaches is that the states are changing relatively rapidly. This makes assigning gains difficult since the linearisation is not always stable. The numerical complexity of extended observers is highlighted by the attempts at practical evaluation which have to be done off-line using recorded data, Du *et al* (1995).

4.11 Comparison of methods

The table in Fig.4.20 summarises the significant methods for induction motor state estimation, both from the literature and the new methods considered in this chapter.

Name	Axis	States	Feedback	Comments
Current model	Synch.	Is & Φr	Open-loop	Simple, does not require voltages, sensitive to R_r and L_m.
Voltage model	Synch.	Is & Φr	Open-loop	Simple, does not require speed sensor, contains pure-integral term.
Compensated Voltage model	Synch.	Is & Φm	Open-loop	Has steady state error which is significant at low speed.
Linear	Either	Any	Linear	Only useable over small range of speeds.
Bilinear	Synch	Is & Ir	Bilinear $L_1+L_2\omega$	Oscillatory eigenvalues give undesirable behaviour at high speed, but very simple to implement
Bellini	Synch.	Is & Φm	Fixed	Reduced order, slow convergence at low speed.
Parametrised	Synch.	Is & Ir	Non-linear function	Fully assignable error dynamics. To avoid numerical accuracy problem, gain matrix stored in lookup table.
Sliding-Mode.	Synch.	Is & Ir	Switching.	Good noise rejection, requires short time-step.
Kalman-filter	Synch.	Various	Stochastic	Can be optimised to reject noise on measurements or uncertainty in plant.
Extended	Synch.	Is & Ir plus R_r, ω_r or T_l	Linear about a local linearisation.	Computationally intensive, stability hard to prove since convergence can't be guaranteed.
Fuzzy.	Synch.	Is & Ir	Multi-model with fuzzy 'selection'	Functionally equivalent to the speed parametrised observer, but computationally very intensive to implement.

Figure 4.14. Table summarising various methods for estimating torque and flux.

The open-loop current and voltage model methods are both simple electrical models of either the rotor or the stator circuits. The voltage model has the advantage of not requiring a speed measurement. The problems associated with the integral term in this method can be overcome for all but slow speeds, the compensated voltage model is used on the existing generation of EMU traction system.

For fixed frequency drives, the model is linear and standard linear techniques can be applied without problems. As long as the slip remains below a few percent, the observer's error dynamics will not alter significantly and any steady state error will remain small.

The method developed by Bellini was one of the first applications of state-space observer designs to variable speed drives, but this observer has slow error dynamics at low speed and is on the limit of stability at start up.

The use of extended observers, either Kalman or Luenberger, has been much reported in the literature. Attempts to duplicate such work for this thesis has shown that much more work is needed since a method which guarantees convergence has not yet been demonstrated for all speeds.

Fuzzy observers do not presently offer any significant advantage to compensate for their higher computational load.

The sliding mode observer is an extension of Utkin's original linear sliding mode observer. The feedback is characterised by a switching action, the computational load is relatively small but the timing of this is not periodic. To simulate the observer a very small time step is needed around the switching points. In Simulink this is not a problem since an integration routine with a variable time step can be used. For a real time implementation, however rather than using a fixed sampling time of the algorithm an 'event' implementation would need to be adopted, in which the observer algorithm would be calculated in response to a zero crossing of the error.

Three of the most promising methods, the bilinear observer, the parametrised observer and the Kalman filter, will be considered further using test-data from a real motor on test. The bilinear observer is the simplest and has the smallest memory requirement of the three methods, but its sensitivity to noise may preclude its use in anything other than simulation. The parametrised observer, by storing gains pre-calculated for speed, has full freedom for pole assignment whilst the Kalman filter techniques can be optimised for either measurement noise or process uncertainty.

4.12 Validation against test-rig data

To validate the observers it is necessary to consider some variable which is a function of both the measurable states and the unmeasurable rotor states. Rotor currents are not easy to measure and neither is flux, so it is convenient to use torque. The induction motor test-rig built for this thesis, whose development is described in Chapter 6, does not include a torque measurement and so cannot be used to validate the torque estimate. However, through a collaboration with Aalborg University in Denmark, a limited set of hardware test-rig runs were made available to be used for validation. The test rig consisted of a Danfoss inverter driving a 4kW induction motor loaded with a DC load-machine. Whilst torque is not directly measured the torque load produced by the DC machine is controlled.

The data supplied from Aalborg is a set of load steps for use in off-line analysis. It includes supply voltage, frequency demand, motor speed, the three phase currents and load machine torque demand. The validation is limited to steady-state since only the demand load torque is known, not a dynamic measurement. The Aalborg rig does not include phase voltage measurements so they have to be reconstructed from the supply voltage, frequency demand and modulation index, as shown in Fig. 4.15. The data is also sampled and in each case initial conditions have to calculated for the observers, to limit the initial transient error caused by mis-match in initial conditions.

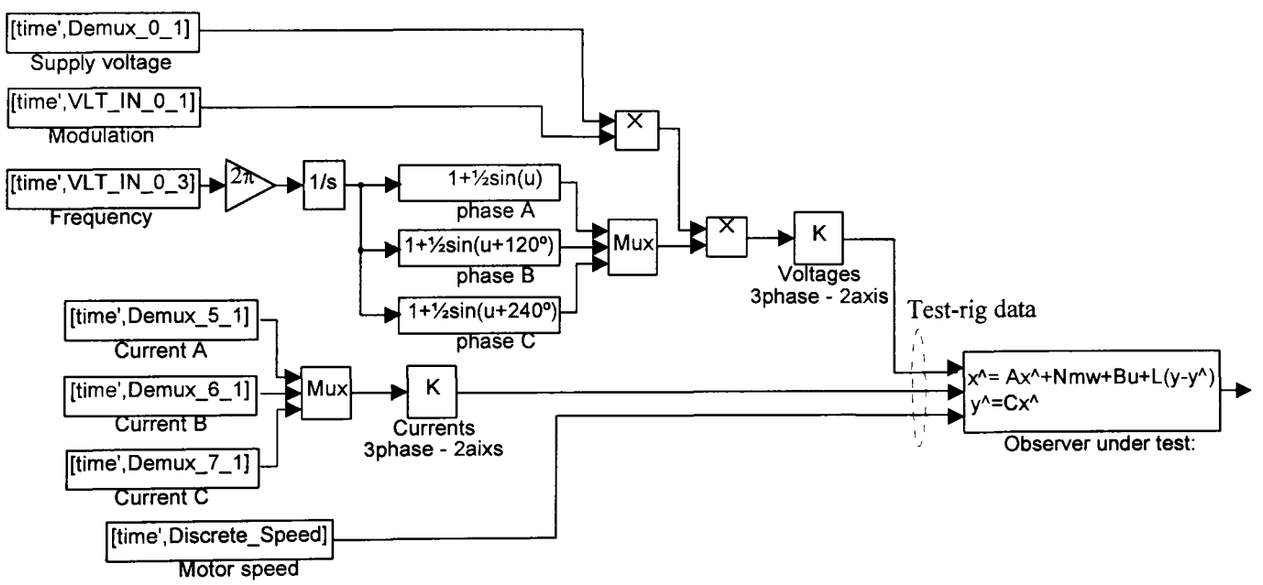

Figure 4.15. Simulink diagram for off-line analysis of observers on real motor data including reconstruction of the unmeasured voltages.

0.8 seconds of data are available with a load step from 0 to 5Nm applied at 0.2seconds. The motor is driven with an electrical frequency of 50Hz, giving a synchronous speed of 25Hz because it is a 4pole machine. The measured motor speed is shown in Fig. 4.16

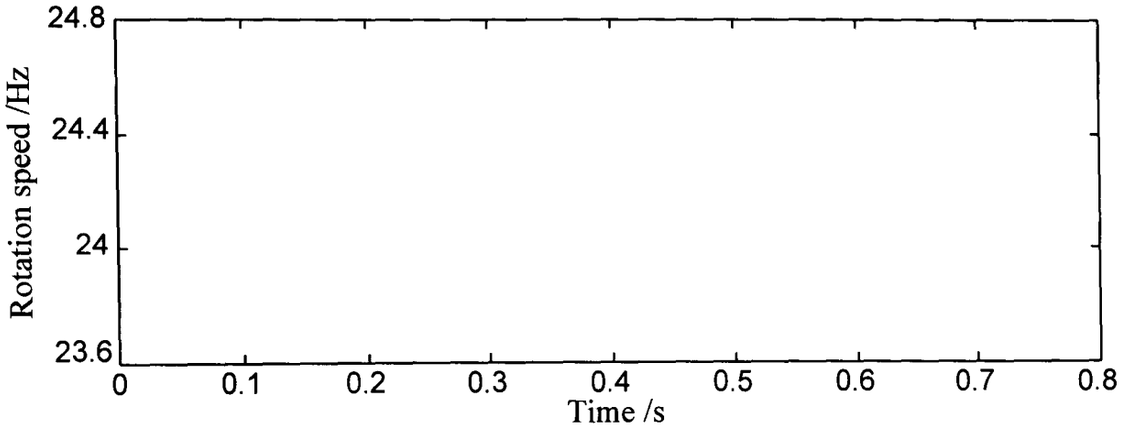

Figure 4.16. Plot of motor speed during test.

The following motor parameters were given for the motor on the test-rig.

1.5kW 3phase AC induction motor 380V/50Hz,

$R_s = 5.14\Omega$; $R_r = 4.2\Omega$; $L_{ls} = 0.010$H; $L_{lr} = 0.012$H; $L_m = 0.314$H at 120°C;

Number of poles pairs 2 and nominal magnetising current 2A.

The observer methods to be considered are the most promising of those outlined in this chapter, the bilinear observer, the Kalman filter and the parametrised observer.

4.12.1 Lookup table observer

The parametrised observer allows maximum freedom in assigning the Eigenvalues of the observer. For these tests two different observer poles locations are compared, two pole-pairs at -100 and -30 with -2000 and -200. The observers are set up in parallel using the reconstructed voltages, measured currents and measured speed. The estimated torque is shown in Fig. 4.17.

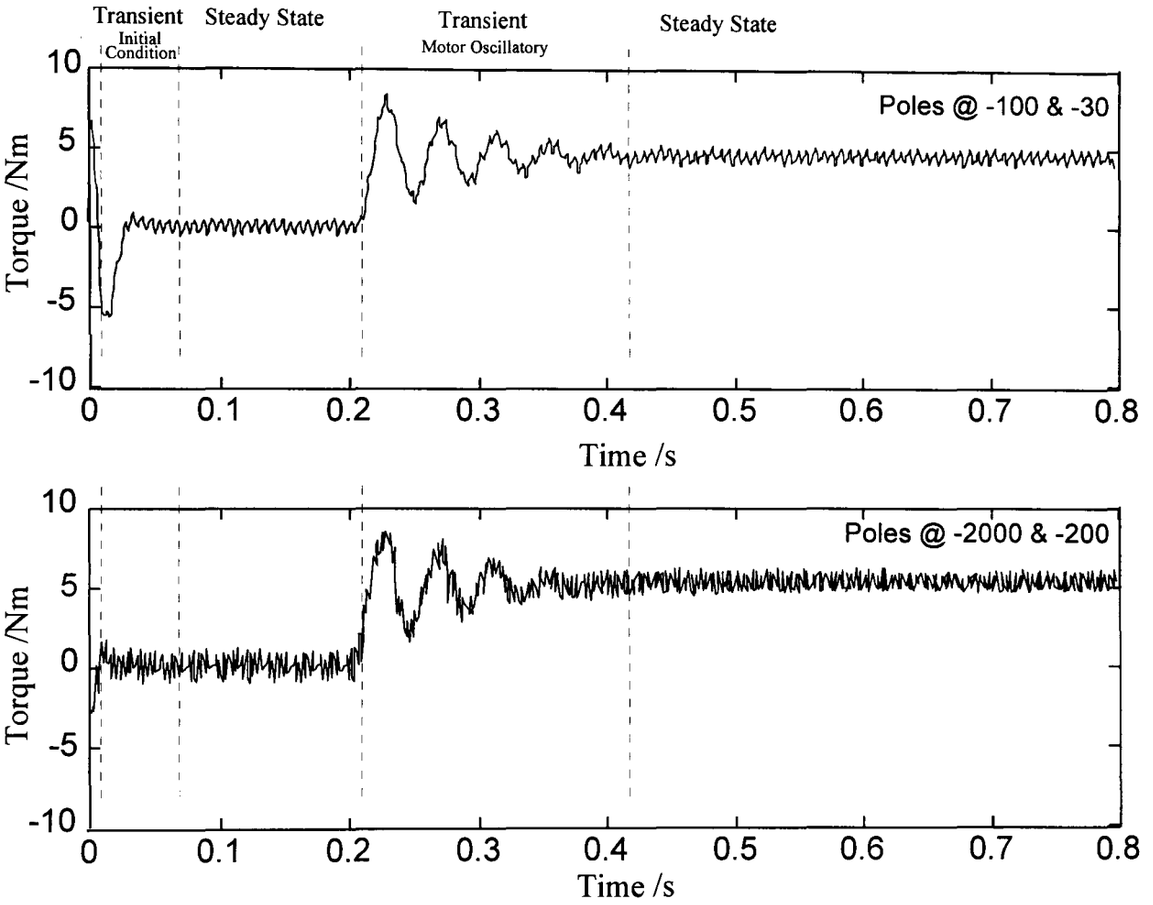

Figure 4.17. Estimated torque for two different pole locations using the parametrised observer on real test data.

The observer with the faster poles produces a smaller initial transient which decays much quicker, but it is more sensitive to noise, as expected. Both observers are able to track the underlying torque accurately, the oscillatory behaviour after the step is due to the DC load motor and the induction motor oscillating when the step in load torque is applied.

4.12.2 Bilinear observer

The bilinear observer is set up in Simulink, as shown in Section 4.7. It has two unassignable poles at $-200\pm i10\omega_r$ and the assignable are placed at -2000 to compare with the second case of Section 4.12.1.

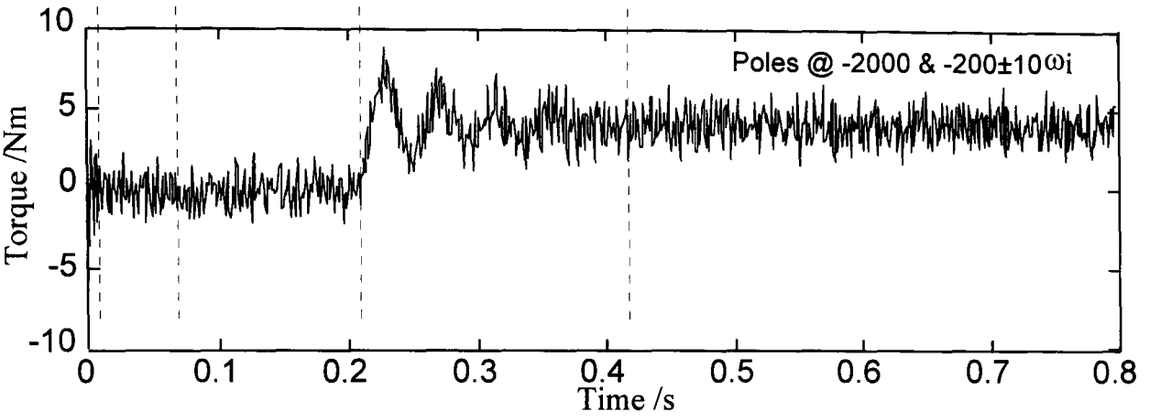

Figure 4.18. Estimated torque using the bilinear observer on real test data.

The bilinear observer has a rapid decaying initial transient, which can just be seen to be oscillatory. This is because the motor is already rotating at 25Hz at the start of the available data and the observer poles are much more oscillatory than the parametrised observer. This observer is noticeably more sensitive to noise than the parametrised observer, this is discussed in detail in Section 4.13.

4.12.3 Kalman filter

The Kalman filter algorithm is set-up in Simulink for evaluation on the test-data. The data is sampled at 1kHz which limits the Kalman filter algorithm to the same rate. The two co-variance matrices Q for the process and R for measurements, give the distribution of the noise and disturbances to the states. Two cases are considered with Q very much greater than R and vice-versa. Fig. 4.19 shows the torque estimates produced in each of the two cases.

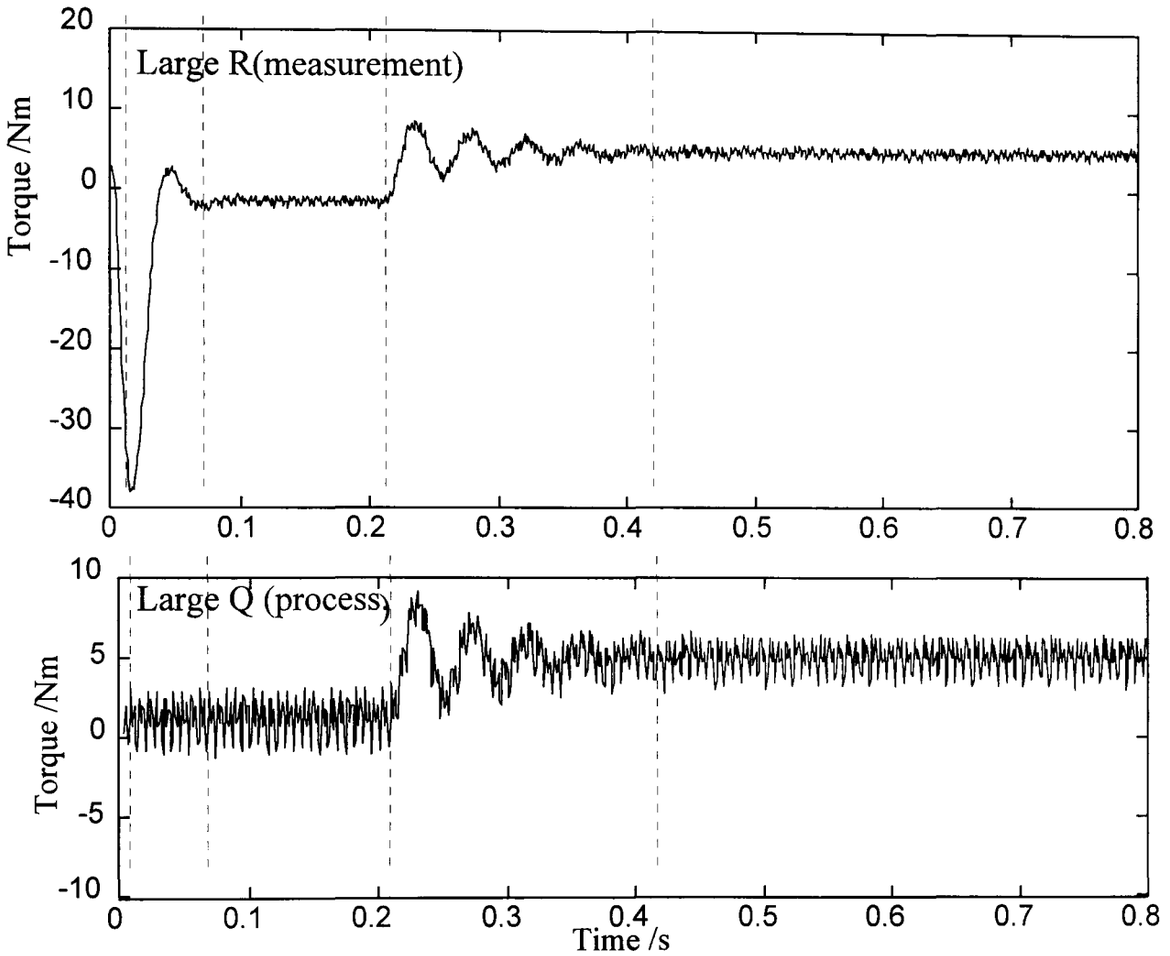

Figure 4.19. Estimated torque for two case of co-variance matrices using the Kalman filter approach to estimate the states from real test data.

By making the process co-variance matrix Q large the Kalman filter tracks the underlying torque characteristic with a minimal initial transient. However, it is clear that most of the noise in the system is associated with the measurements since the noise on the high Q case is very significant. As expected, by making R large the noise is strongly rejected but the dynamics become slow and there is a large initial transient.

4.13 Effect of gain matrix on sensitivity to noise and model uncertainty

Assuming the motor model to be in the form given by Eq. 4.50

$$\begin{aligned}\dot{\underline{x}} &= (A + N\omega)\underline{x} + B\underline{u} \\ \underline{y} &= C\underline{x}\end{aligned} \tag{4.50}$$

Consider the effect of measurement noise, model uncertainty, and speed sensor errors, on an observer. Eq. 4.51 shows the time domain representation of measurement noise given by $\underline{n}$, a modelling uncertainty represented by the matrix ΔA, and an offset $\Delta\omega$ on the speed sensor measurement.

$$\begin{aligned}\dot{\hat{\underline{x}}} &= \left(A + N(\omega + \Delta\omega) + \Delta A \right)\hat{\underline{x}} + B\underline{u} + L\left(\left(\underline{y} + \underline{n}\right) - \hat{\underline{y}} \right) \\ \hat{\underline{y}} &= C\hat{\underline{x}}\end{aligned} \tag{4.51}$$

The error dynamics for this observer will become

$$\dot{\underline{e}} = (A + N\omega - LC)\underline{e} + \Delta A\underline{x} + L\underline{n} + \Delta\omega N\underline{x} \tag{4.52}$$

Eq. 4.52 gives the time domain expression for the error dynamics and driving terms.

4.13.1 Noise

Consider now the error equation in the frequency domain initially just for noise.

$$\begin{aligned}e_{(s)} &= (sI - A + N\omega - LC)^{-1} L n_{(s)} \\ &= G_n(\omega)_{(s)} n_{(s)}\end{aligned} \tag{4.53}$$

Where $G_n(\omega)_{(S)}$ gives the coupling between the state error and the measurement noise on the currents in transfer function form. This is also a function of speed. Figure 4.20. shows the gain of the terms in $G_n(\omega)_{(s)}$ for the traction motor at three fixed speeds for both the parametrised and bilinear observer feedback. The poles of the parametrised observer are placed in pairs at -500 and -48. These have the same real values as the poles of the bilinear observer.

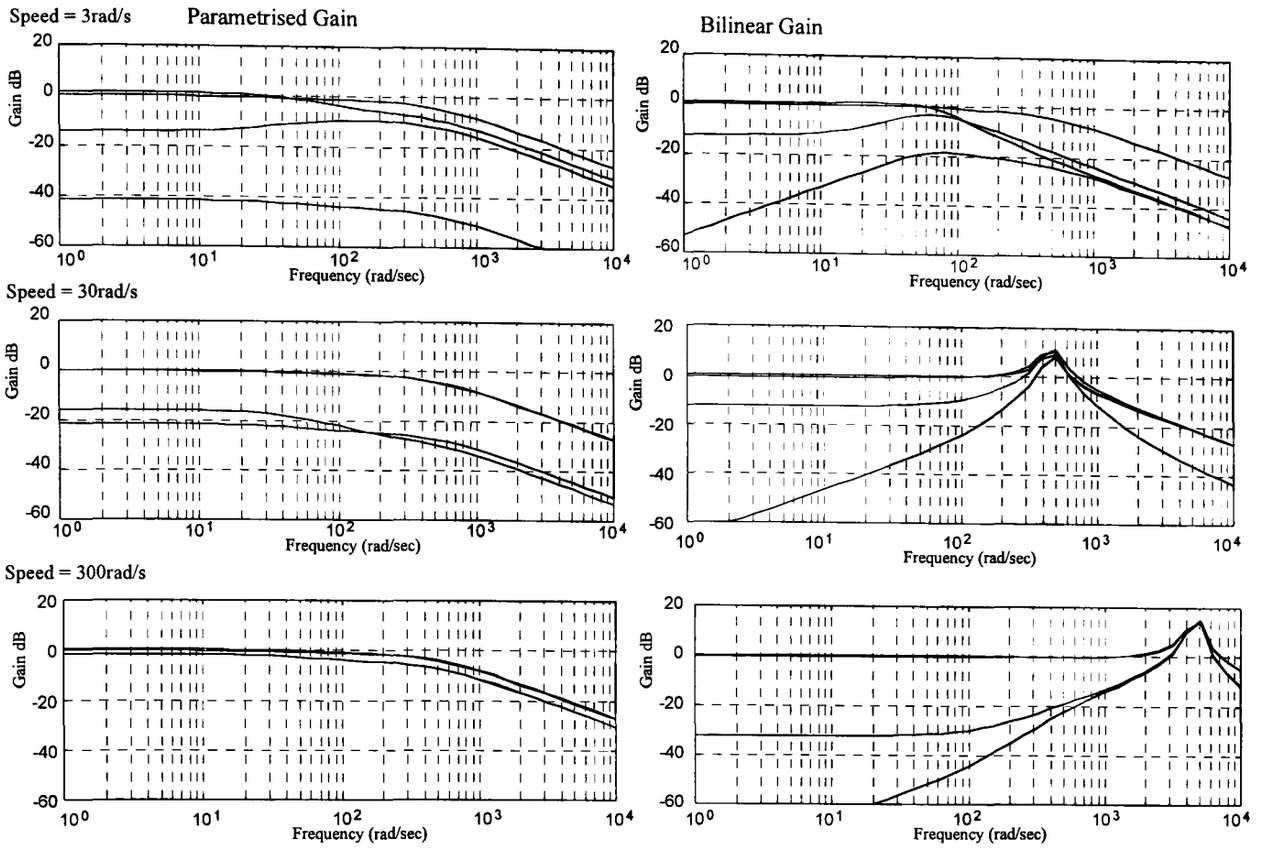

Figure 4.20. Gain plots for the transfer functions between noise and the state errors, for parametrised and bilinear feedback at speeds 3, 30 and 300rads^{-1}.

The problem with the bilinear observer's sensitivity to noise, highlighted in Section 4.12.2, is clearly demonstrated by the increasingly higher peak in $G_n(\omega)_{(s)}$ as the speed increases, whilst the sensitivity of the parametrised observer rolls off. It is also possible to consider the effect of bias on the current sensors by considering the DC gain of $G_n(\omega)_{(s)}$, from which is can be seen that there is no difference between the two observer designs.

The location of the observer poles will also have an influence on the noise sensitivity. Fig. 4.21 shows the gain of the coupling matrix of sensor noise to the state error, for two different sets of observer poles in the parametrised observer.

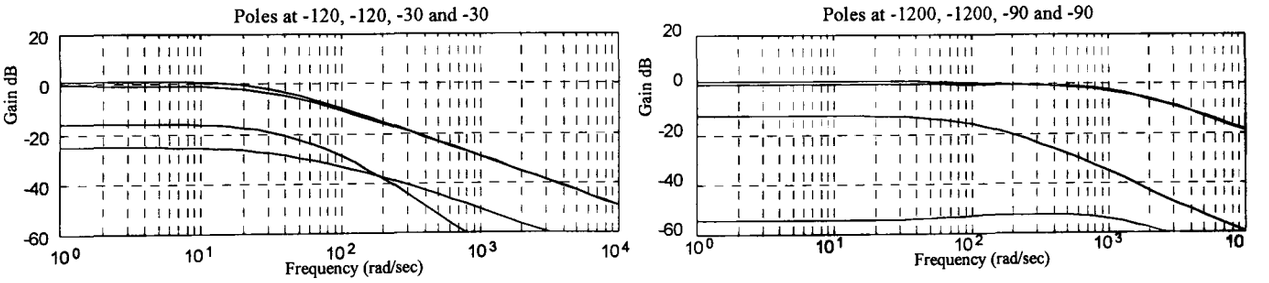

Figure 4.21. Plots showing the noise sensitivity of the observers for two different pole locations.

For the faster poles the coupling between sensor noise and the states is increased.

4.13.2 Speed sensor errors

The state error for a small change in the speed signal is given by

$$\begin{aligned} e_{(s)} &= (sI - A + N\omega - LC)^{-1} N\Delta\omega x_{(s)} \\ &= G_{\Delta\omega}(\omega)_{(s)} x\Delta\omega_{(s)} \end{aligned} \qquad 4.54$$

For speed sensor errors and also modelling uncertainty, (which is considered in more detail in Section 4.13.3, the error is a multiple of the states. The error will always be sinusoidal at the same frequency as the applied voltage. This means that the gains of the coupling terms are only of interest at the frequency of the applied drive[4.6]. Since the motor has two pole-pairs the applied drive is twice the motor speed. Two possible speed sensor faults are considered. An offset error, by making $\Delta\omega$ constant and a gain error, by making $\Delta\omega$ a multiple of speed. The magnitude of the terms in $G_{\Delta\omega}(\omega)_{(s)}$ are plotted in Fig.4.22a, this shows the magnitude of the error in the observer states for a 1rads^{-1} offset on the speed sensor. The magnitude of the terms in $\omega G_{\Delta\omega}(\omega)_{(s)}$ are plotted in Fig.4.22b, this shows the magnitude of the error in the observer states for a speed sensor which is reading double the correct value.

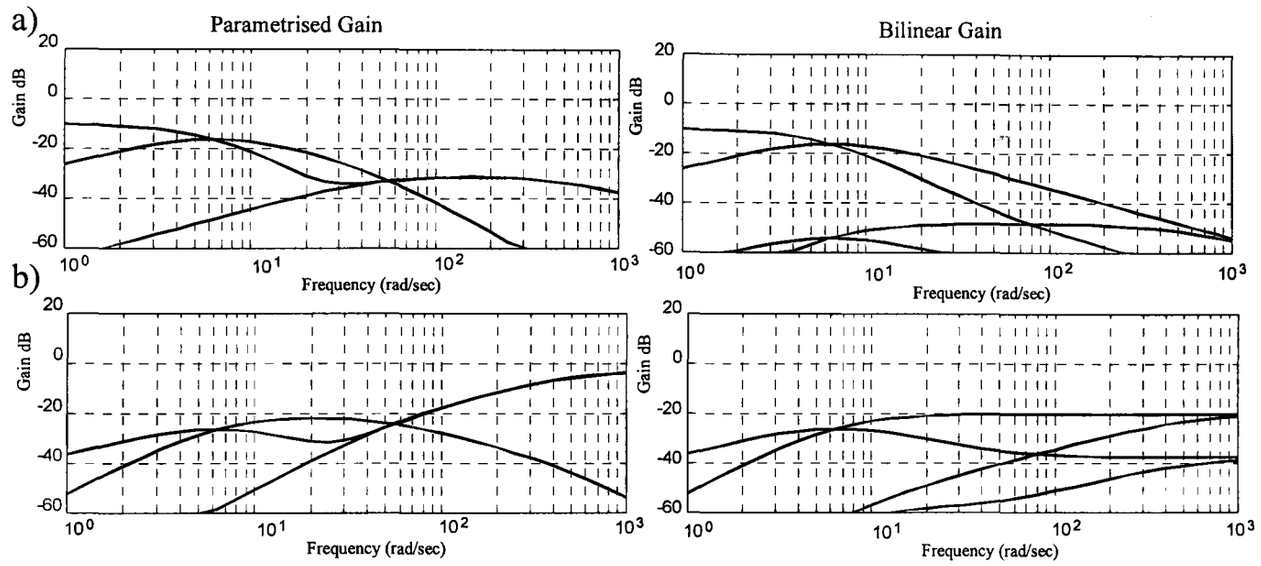

Figure 4.22 Gain plots showing the error in the observer states for a speed sensor fault, with parametrised and bilinear feedback in the speed range 1-1000rads^{-1}.

At low speeds, both observers are equally affected. At a drive frequency greater than 100rads^{-1} the bilinear observer is less affected by errors in the speed sensor measurement.

To demonstrate this the two observers are simulated in parallel using the model for the traction system with the speed sensor reading 10% too high. Fig. 4.23 shows the motor speed, the motor currents and the errors for the observers during a simulated startup.

[4.6] Ignoring harmonics.

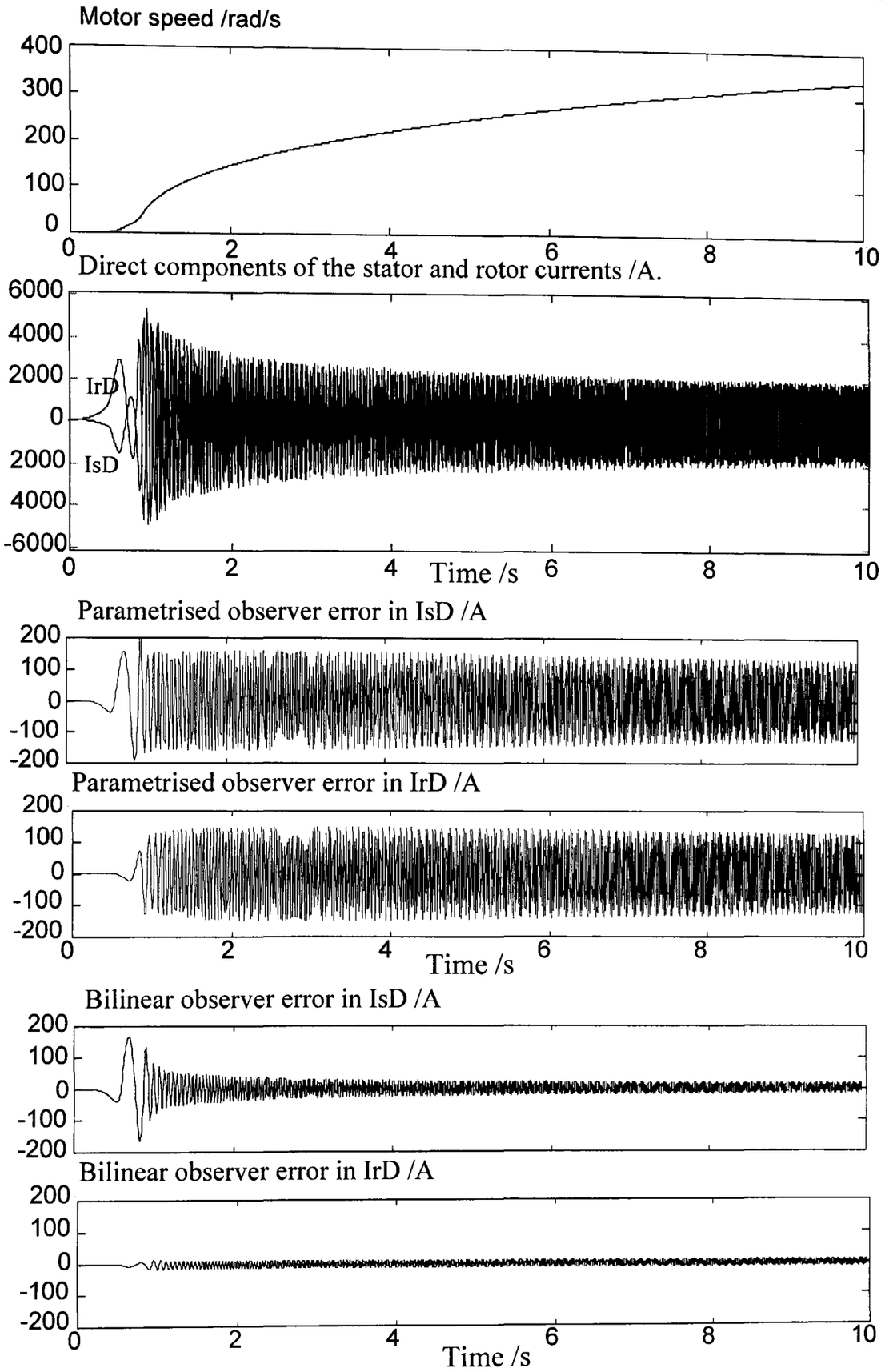

Figure 4.23. States error for parametrised and bilinear observer with an error of 10% on the speed sensor measurement.

At low speeds both observers have similar performance. As the speed increases, the error for the bilinear observer is roughly a fifth of that of the parametrised observer. These results agree with the frequency domain sensitivity analysis shown.

4.13.3 Model uncertainty

Up to this point model uncertainty has just been represented by the term ΔA. The actual form of this matrix is dependent on the source of the error, it is unlikely that the ΔA would simply be a multiple of A since it is the motors electrical parameters which changes. The two parameters most unlikely to change are resistance with temperature and magnetising inductance with saturation. Changes in the leakage-inductances would normally indicate a fault, but are likely to be very small even for significant faults.

Considering the resistances first. Eq. 4.55 gives an expression for ΔA in terms of changes for the stator and rotor resistances.

$$\Delta A = \begin{bmatrix} L_r\Delta R_s & 0 & L_m\Delta R_r & 0 \\ 0 & L_r\Delta R_s & 0 & L_m\Delta R_r \\ L_m\Delta R_s & 0 & L_s\Delta R_r & 0 \\ 0 & L_m\Delta R_s & 0 & L_r\Delta R_r \end{bmatrix} \frac{1}{L_sL_r - L_m^2} \tag{4.55}$$

For example, assuming a 20% increase in both the resistance parameters this gives:

$$\Delta A = \begin{bmatrix} -13.4 & 0 & 9.5 & 0 \\ 0 & -13.4 & 0 & 9.5 \\ 12.9 & 0 & -9.7 & 0 \\ 0 & 12.9 & 0 & -9.7 \end{bmatrix}$$

The observer state error resulting from a change ΔA is given by Eq. 4.56.

$$\begin{aligned} e_{(s)} &= (sI - A + N\omega - LC)^{-1}\Delta A x_{(s)} \\ &= G_{\Delta A}(\omega)_{(s)}\Delta A x_{(s)} \end{aligned} \tag{4.56}$$

Fig. 4.24 shows the gains for the transfer functions between the actual states and the observers error, for both the parametrised and bilinear observers.

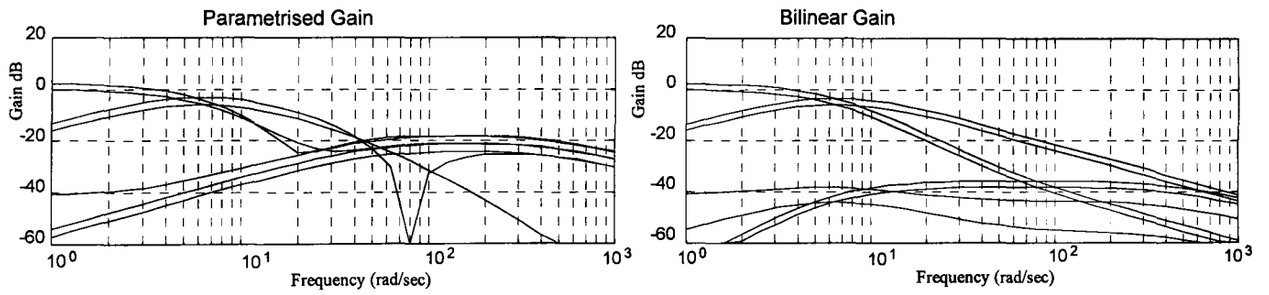

Figure 4.24. Gain plots for the transfer functions between changes in resistance and the state errors, parametrised and bilinear feedback for speeds 1-10000rads^{-1}.

There is a significant difference between these two observer methods when faced with a change in resistance due to a temperature change. Initially, at low speeds the bilinear observer is slightly better. Beyond a drive frequency of 10 rads^{-1} the bilinear observer is significantly better and remains so across the full range of operating frequencies shown.

These results can be verified using the simulation. The observers were set up in parallel in Simulink with the motor resistances increased in magnitude by 20%. The resulting motor currents, speed and the state errors for the two observers are shown in Fig. 4.25.

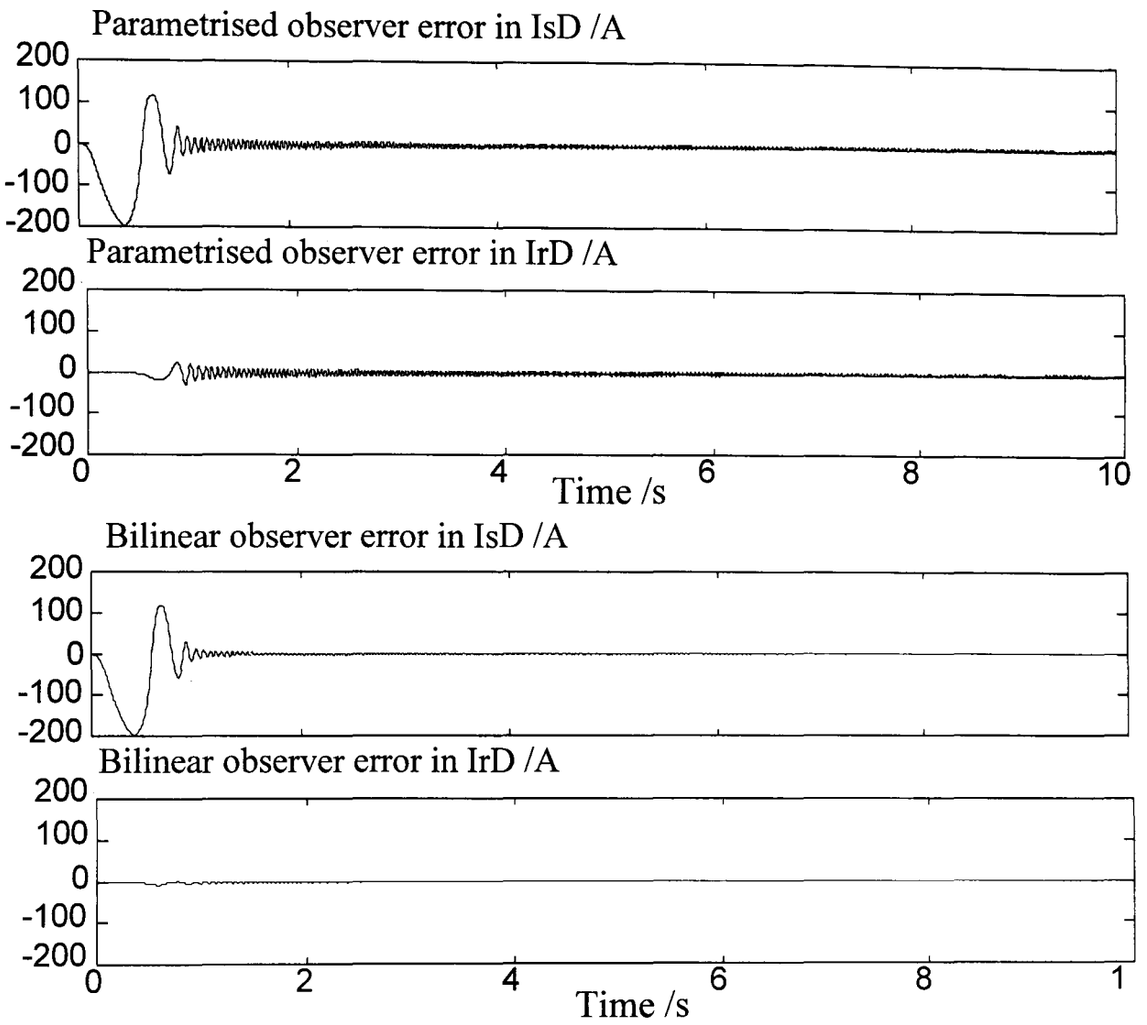

Figure 4.25. Error in estimated states for the parametrised and bilinear observers with a 20% increase in R_s and R_r.

Both observers are sensitive to changes in resistance at low speeds. At high speed the bilinear observer is less sensitive than the parametrised observer, but both have generally good performance. Fig. 4.26 shows that altering the pole locations has little effect on the low speed sensitivity.

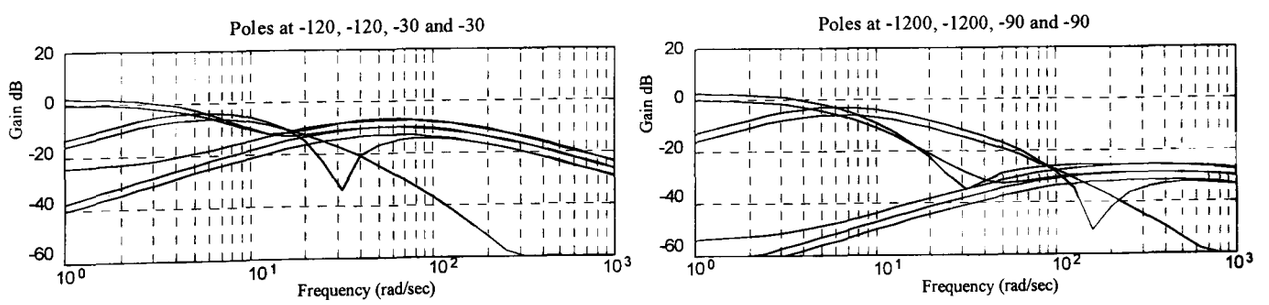

Figure 4.26. Plots showing the sensitivity to changes in resistance for the parametrised observer with two different pole locations.

For magnetising inductance, ΔA is a much more complex function of ΔL_m. Hence, rather than trying to find a symbolic expression it is evaluated numerically for a 1% change in L_m. Also the input matrix B is a function of the electrical parameter L_m and will therefore add a second driving term to Eq. 4.56.

$$\dot{\underline{e}} = (A + N\omega - LC)\underline{e} + \Delta A\underline{x} + \Delta B\underline{u} \tag{4.57}$$

$$\Delta A = \begin{bmatrix} 0.0171 & 0.01461\omega & 0.0074 & 0.01461\omega \\ -0.01461\omega & 0.0171 & -0.01461\omega & 0.0074 \\ 0.01 & -0.01461\omega & 0.0043 & -0.01461\omega \\ 0.01461\omega & 0.01 & 0.01461\omega & 0.0043 \end{bmatrix} \text{ and } \Delta B = \begin{bmatrix} 1 & 0 \\ 0 & 1 \\ 0.59 & 0 \\ 0 & 0.59 \end{bmatrix}$$

It is desirable to attempt some form of simplification before proceeding. At low speeds (<20rads^{-1}) ΔB will be significantly larger than ΔA. However, the applied voltage, $\underline{u}$, will be small compared with the currents, $\underline{x}$, because of the volts per Hertz control, making $\Delta A\underline{x}$ predominant. At speeds greater than 20 rads^{-1} the speed-dependent terms in ΔA will dominate, so only these will be considered.

$\dot{\underline{e}} \approx (A + N\omega - LC)\underline{e} + \Delta A\underline{x}$ where $\Delta A = \text{sgn}(N)\omega$ if $\omega > 10$ with volts-per-Hertz control.

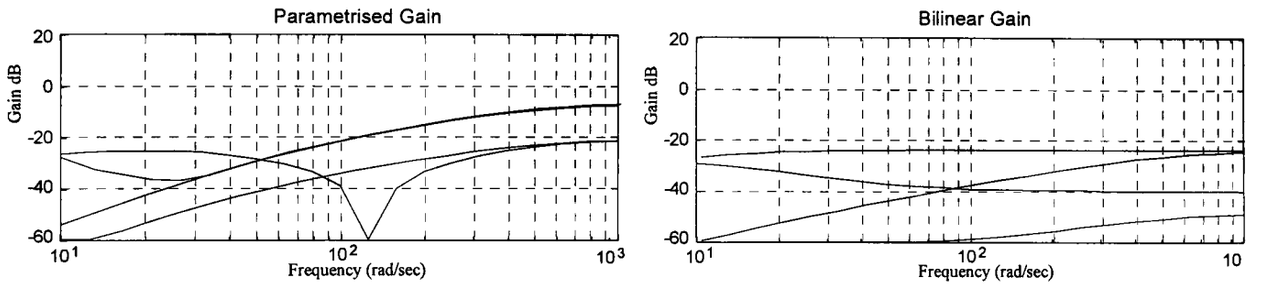

Figure 4.27. Gain plots for the transfer functions between errors in the parameter L_m and the state errors, for parametrised and bilinear feedback in the speed range 10-1000rads^{-1}.

These results suggest that at high speeds the error in the parametrised gain observer caused by a change in the magnetising inductance is greater, whilst at low speed the parametrised observer is slightly better. These comparisons of course, rely on the validity of the assumptions made for ΔA and ΔB. This can be verified more easily in the time domain. Both the observers were simulated with the L_m term increased by 10%. The resulting motor currents, speed and the state errors for the two observers are shown in Fig. 4.28.

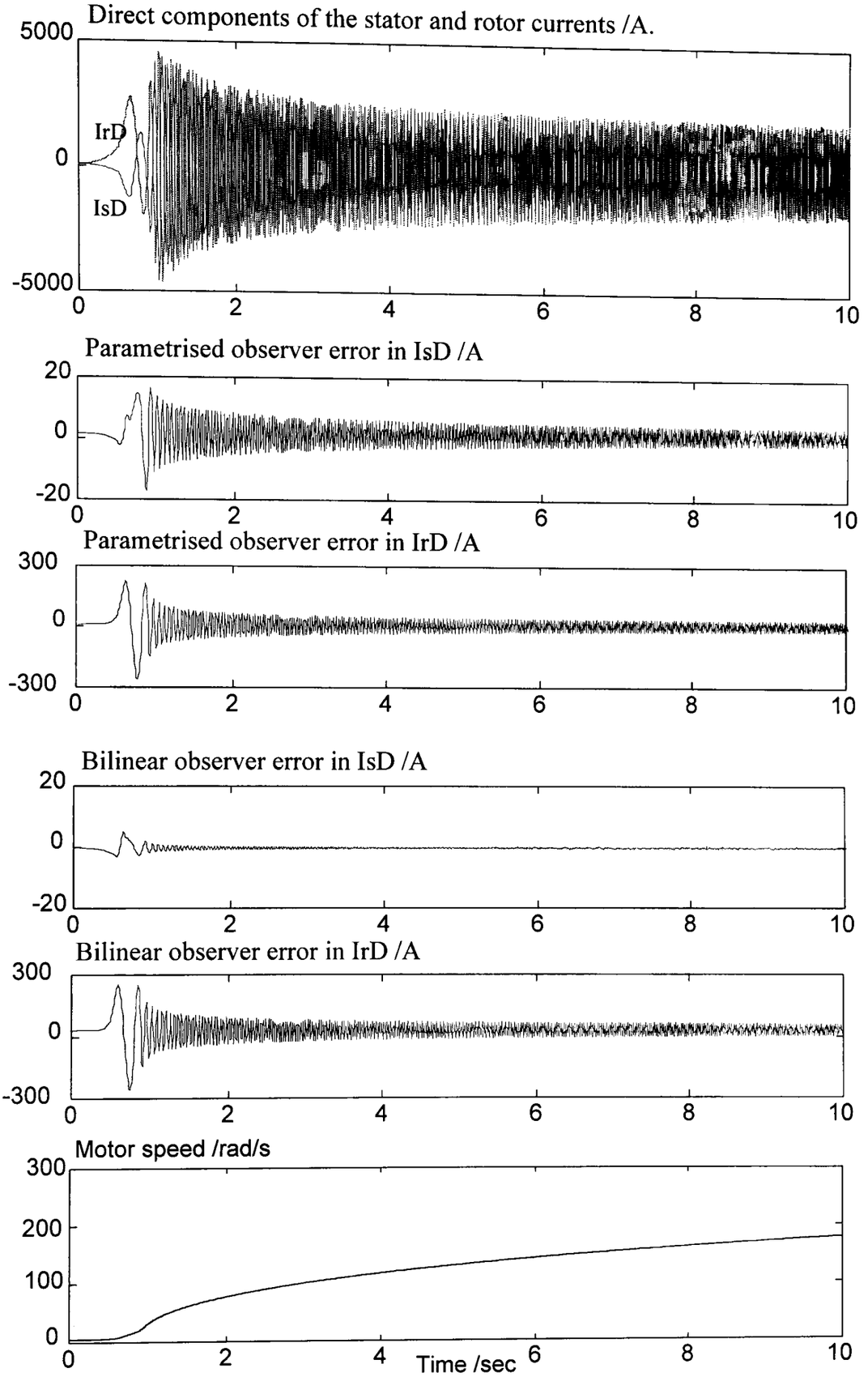

Figure 4.28. Error in estimated states for the parametrised and bilinear observers with a 20% increase in L_m.

There is little apparent difference between the estimation errors two observer types. This is not expected from the frequency domain results. This suggests that the assumptions made were over simplifying what is in fact a very complex phenomenon. The relevance

of these results is not important enough to justify further exploration, as the sensitivity being considered here is the sensitivity only to mis-identification of the non-saturated magnetising inductance and not the effect of saturation in operation. This is further explained in Section 8.3, but in summary the effect of saturation cannot be modelled by simply altering the magnetising inductance as a function of the flux, Brown *et al* (1983).

4.14 Observer design for state estimation

For estimation a high gain observer is generally required. This combines fast convergence of the state estimates with low sensitivity to model uncertainty. The drawback of high feedback gain is that the observer becomes sensitive to noise on the measurements. For most applications the model mis-match is more of an issue than measurement noise. A commonly used compromise for this is to assign the eigenvalues of the observer's error dynamics to be three times the real parts of the motor poles, Bird & Zelaya-dela-Parra (1996).

For the induction motor the observer design is complicated by the speed-dependent dynamics of the model. The motor model is strongly bilinear, therefore to obtain desirable dynamics the feedback gain must be altered with the motor speed. To get the maximum flexibility the feedback matrix can be pre-calculated and stored in a lookup table for a range of speed.

4.15 Summary

For the traction system the two controlled variables of torque and flux are not direct measurements and have to be estimated. Initially, open-loop estimators, which are usually used in practise, are considered. Open-loop estimators are based on electrical circuit equations for the induction motor. Using a bilinear state-space model for the motor modern control theory can be applied. Bellini was one of the first to apply state feedback to design a state observer for an induction motor. This chapter reviews several other observers from the literature and proposes several novel designs which exploit the structure of the bilinear model, the characteristics of the various methods are summarised.

The three most practical methods are identified as the Bilinear feedback observer, the parametrised feedback observer and the Kalman filter. Using off-line data from an induction motor test rig the three methods are compared. From this it is obvious that there is a trade-off between the conflicting requirements of high feedback gain to give low sensitivity to model-mismatch and low gain to give high noise rejection. This is either in the pole location of the observer or in the relative magnitudes of the co-variance matrices for the Kalman filter. Only a limited amount of test data was available so detailed evaluation of the observers on real hardware is limited. The chapter ends by developing frequency domain sensitivity analysis for the observers with respect to noise, speed sensor errors and parameter changes. The result of this analysis is supported by time domain simulation.

This final Section has presented two basic methods for comparing observer designs, calculating the coupling between noise and uncertainty to the state estimation error in the frequency domain and time domain simulation. In each case the sensitivity is effected by the motor speed and the location of the observer poles. In selecting the 'best' observer design knowledge of the actual application must be included so that a compromise between the various conflicting requirements can be made. This section has shown the methods necessary to made such an evaluation.

Chapter 5:

Sensor fault detection

The aim of this chapter is to develop techniques for sensor fault-tolerant estimation of torque and flux. The first topic considered is the type of faults which a sensor may be subject to. There are three types of sensors in the traction system to consider, current, voltages and speed. Initially, simple parity equation methods are considered for both continuous and intermittent faults. Since the control system requires an observer to estimate unmeasured states the use of observer based fault detection techniques is a logical progression. The main focus of this chapter is the use of model-based methods for sensor fault detection. From the diverse range of model based FDI techniques the most suitable methods are selected and developed. These are demonstrated in simulations and their sensitivity to faults is assessed to enable comparison on the grounds of complexity, capacity and sensitivity. The chapter ends by considering methods which can be applied to the speed sensor.

Any practical control system will rely on sensors which in simulation are normally considered to be ideal. Earlier sections of this thesis have described simulations in which physical values are just connections on a Simulink block diagram. In practical applications sensors are physical devices which will have limitations on range and bandwidth and also will be subject to faults. Sensor fault detection has been identified as one area of the traction system in which there is scope for further work.

5.1 Types on sensor faults

A generic sensor may be subject to disconnection, changes in gain and bias, clipping or slew-rate limits and noise and interference, see Fig. 5.1.

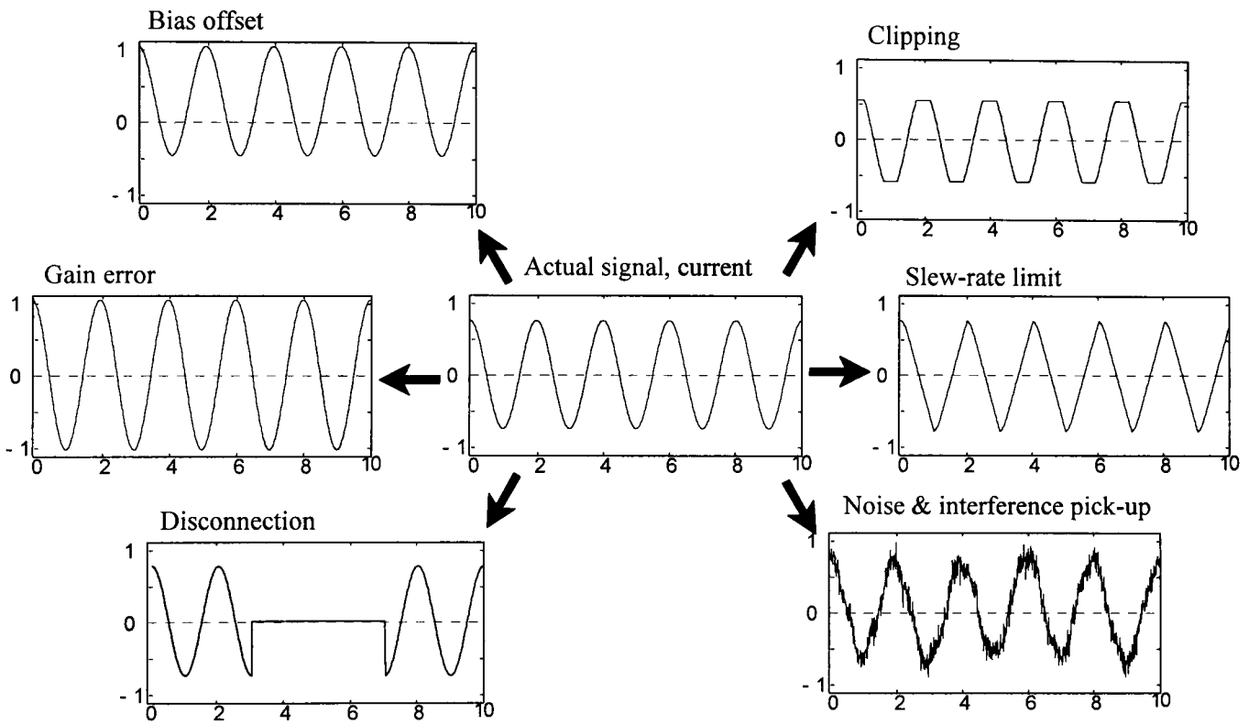

Figure 5.1. Types of sensor faults for a generic sensor.

A specific sensor may have fault modes unique to its physical construction, such as the speed sensor. The speed sensor is a toothed wheel pick-up and may suffer from missing teeth or disk eccentricity, as illustrated by Fig. 5.2.

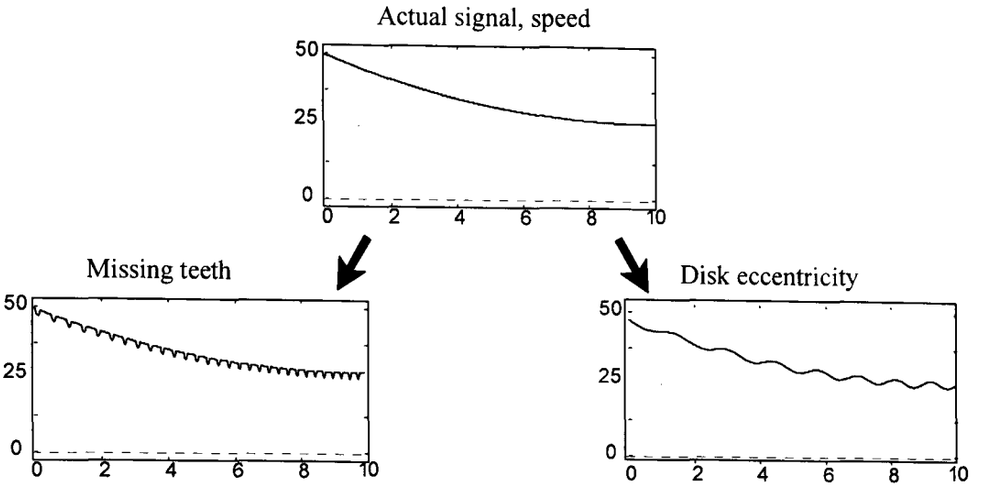

Figure 5.2. Types of sensor fault specific to the speed sensor.

5.2 Simple sensor checks

For disconnection a simple threshold detection could be applied. For the traction sensors this may prove unreliable because of the variable amplitude of the measurements and the PWM waveforms. Detection of intermittent disconnection would also be difficult. Other methods such as peak detection and taking the mean of a sliding window could be used to detect gain and bias changes. Whilst these methods can be used for fault detection, the problem of fault correction would still remain. Some of the limitations of these simple methods are demonstrated in Section 5.3. It is possible to consider the use of analytical redundancy within the measurement set to ensure that a valid measurement or estimate is always available, wherever possible. To exploit the analytical redundancy in the measurements, model-based techniques are discussed in Sections 5.4-5.6.

5.3 *Parity equation method*

The induction motor must obey Kirchoff's laws, the sums of the three phase voltages and the sums of the three phase currents must be zero at all times. There is no connection to the centre of the windings the conditions given by Eqs. 5.1 and 5.2 must hold.

$$I_a + I_b + I_c \equiv 0 \tag{5.1}$$

$$V_{ab} + V_{bc} + V_{ca} \equiv 0 \tag{5.2}$$

A fault can be detected by a non-zero sum of the measured currents[5.1] or voltages. By comparing the mean value of the three sensor outputs a fault can be isolated (uniquely located). Any imbalance in the fault-free system will be small compared with the peak current. The effect of a sensor fault, once isolated, can be corrected by estimating the faulty sensor measurement from the other two. For example an estimate for a current can be obtained from rearranging Eq. 5.1

$$\hat{I}_a = I_b + I_c \tag{5.3}$$

5.3.1 *A sensor fault-tolerant torque and flux estimation scheme*

Fig. 5.3 shows a simple single sensor fault detection and correction scheme which would be situated between the measurement and the estimator in front of the estimator, to perform a parity check on the sensor data. Each sensor output is compared against the mean peak value of all three outputs. If any one deviates by more than a few percent it is deemed to have failed. The sensor's actual measurement is then replaced by an estimate generated from the other two sensors.

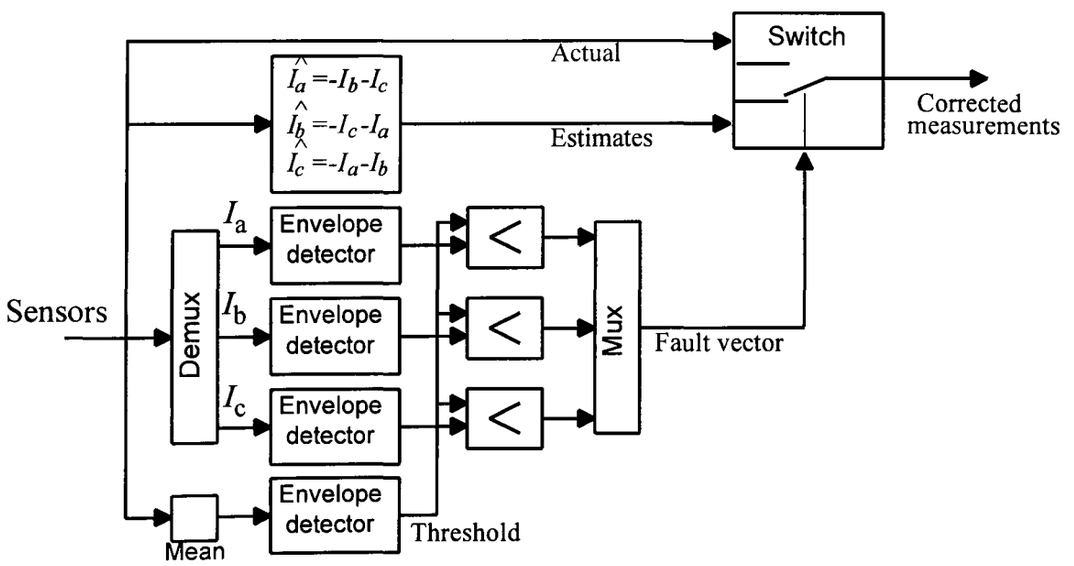

Figure 5.3. Block diagram of single sensor fault correction scheme.

[5.1] This assumes that there are no significant leakage currents, which is reasonable since any leakage currents will be small compared with the phase currents.

This scheme is set-up in Simulink. Fig. 5.4 shows the effect of the correction scheme on the torque error during a one second disconnection of the Ia sensor. For comparison both the bilinear observer and the estimator responses are shown.

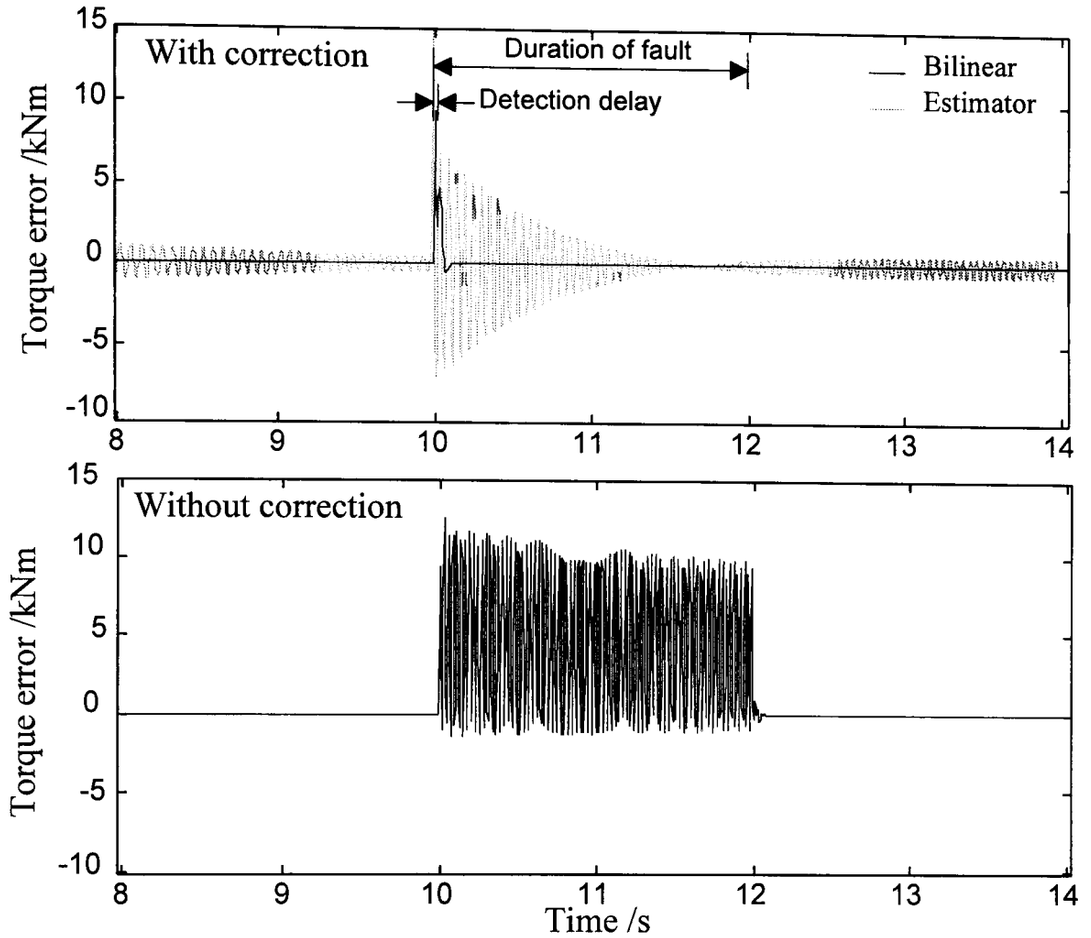

Figure 5.4. Plots of torque error with and without parity equation sensor correction, also showing difference between estimator and observer.

There will be a delay in detecting the sensor fault because the residual has to be envelope detected, as described in Appendix I. This results in an error being passed to the observer which excites its error dynamics. Once this transient decays the effect of the sensor fault is removed from the estimate of torque and flux. Without correction, the torque estimate is meaningless during a fault. The existing estimator has significant transient dynamics which are excited by the error being passed to it during the detection delay. Replacing the estimator with the bilinear observer improves the situation significantly. If the fault is intermittent then this would continually re-excite the transient making the estimate unusable.

This section has shown the parity equation method applied to current sensors, for voltage sensors the methods and results are similar and are therefore not shown.

5.4 *Model-based methods for sensor fault detection*

Since the induction motor has already been modelled it is logical to consider the use of model-based techniques for fault detection.

5.4.1 Types of faults acting on a plant

There are three main types of fault which can affect a system under feedback control:

- **Actuator faults** which directly affect the input to a plant.
- **Sensor faults** which directly affect the measured output from a plant.
- **Process faults** which alter the plant dynamics.

The classical state-space fault model has the structure shown in Fig. 5.5.

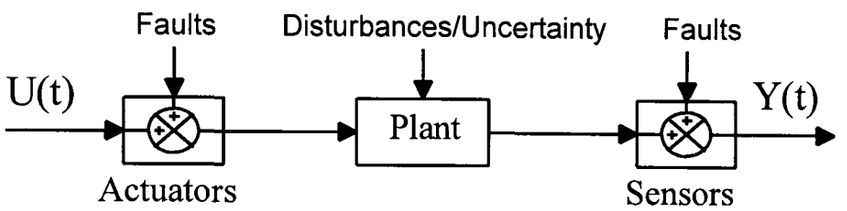

Figure 5.5. Block diagram of the classic state-space fault model.

Within this classification the three types of traction system faults mentioned in Section 2.5 are clearly distinct. The power electronic faults correspond to *actuator faults*, the induction motor and mechanical faults are effectively *plant faults* and the instrumentation faults are *sensor faults*.

5.4.2 Current and voltage sensors

The current sensors are standard output sensors as given in the classic FDI structure in Fig. 5.5. The voltage sensors have a different interpretation in the state-space model; they are sensors measuring the inputs to the plant, as shown in Fig. 5.6. The controller output is a modulation demand for the inverter. Since the inverter is not modelled, the drive voltages which are actually applied to the motor must be measured.

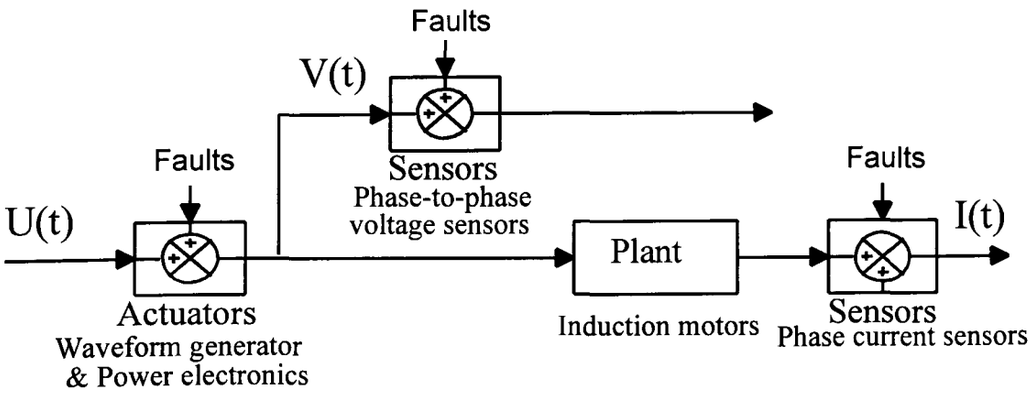

Figure 5.6. The difference in type between the current and the voltage sensors.

5.4.3 Model based fault detection

There are a range of model-based techniques, Patton (1997, *et al* 1998). The two largest groups are parameter identification and observer based methods. Parameter identification attempts to estimate plant variables whose change would be indicative of a fault. Observer methods use error feedback to force a model to track the plant; any divergence between the plant and the model is used to indicate a fault. Observer methods are better suited to sensor and actuator faults which cause erroneous feedback or inputs to the parallel model. The parameter identification method is more suited to plant faults, or parameter deviations. In both methods, further processing is often needed to isolate a fault once it has been detected. Since an observer is already required in the traction system the use of observer based techniques is a logical next step.

With observer-based fault detection the idea is to generate a set of residual signals which are non-zero in the presence of a fault and zero in the fault-free case.

$$r(t) = \begin{cases} 0 \text{ if system fault free} \\ \neq 0 \text{ in the presence of faults.} \end{cases} \tag{5.4}$$

The classic FDI residual generation structure is shown in Fig. 5.7 as given by Patton *et al* (1989).

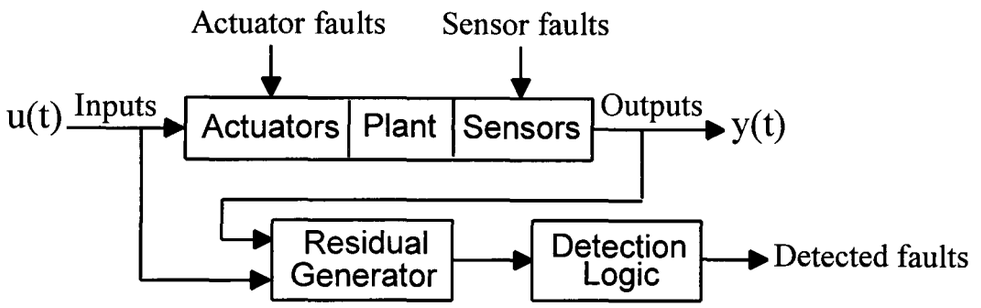

Figure 5.7. Block diagram of model based faults detection.

Estimates from the observer are compared against measurements from the plant to generate the residual signals. Faults can then be isolated by applying simple logic to the residuals. Ideally, the residuals will be sensitive to a single fault and insensitive to noise and uncertainty. There is a large range of design techniques to achieve better isolation, rejection of disturbances and insensitivity to modelling uncertainty, Patton & Chen (1993). Most of the techniques are only suitable for linear systems. For the bilinear induction motor problem many of these techniques would become much harder to apply.

The simplest scheme is called the *Dedicated Observer Scheme* (DOS), Clark (1978) This comprises a bank of observers each driven by just one sensor. If a fault occurs on the dependent sensor then the residual becomes non-zero. If a fault occurs on a non-dependent sensor the residual is unaffected. The main advantage of this scheme is that the *fault isolation* is easily achieved. However, as shown in Section 5.10 and 7.8 the DOS method has several drawbacks. The robustness of the scheme is poor and the fault sensitivity is relativity low, since much of the design freedom is used in isolating residuals.

A more sophisticated technique is called the *Generalised Observer Scheme*, (GOS), Frank (1991). This uses feedback from a subset of sensors for each observer making them independent of a subset of faults. This increases the work which is involved in isolating faults but leaves more design freedom to accomplish other aims. Both of these methods will be considered in this chapter.

5.5 A dedicated observer scheme for current sensors

For this method a bank of observers is designed with each one using feedback from only one sensor. If a fault occurs on the dependent sensor then the residual generated by the observer will become non-zero. If the fault occurs on a non-dependent sensor there will be no effect on the residual. This scheme, whilst being less robust than other more generalised schemes, does give residuals which are dependent on a single fault. However most of the available design freedom is used in decoupling the faults.

For the induction motor this will require three observers, one for each phase current sensor. The motor model has to be altered slightly so that the outputs are the three phase currents in the phase-to-ground orientation, see Appendix A, for derivation of transform.

$$\begin{bmatrix} I_a \\ I_b \\ I_c \end{bmatrix} = C_{abc} \begin{bmatrix} I_{sD} \\ I_{sQ} \end{bmatrix} \text{ where } C_{abc} = \begin{bmatrix} 0.8165 & 0 & 0 & 0 \\ -0.4082 & 0.7071 & 0 & 0 \\ -0.4082 & -0.7071 & 0 & 0 \end{bmatrix}$$

The input voltages must also be transformed from three phase-to-phase voltage into the two axis phase-to-ground voltages, using the transform given in Appendix A.

5.5.1 *Designing an observer with single sensor feedback*

Two possible observer feedback designs will be considered. The bilinear design which offers a simple implementation and the parametrised design which gives more freedom for pole placement.

Bilinear feedback. The feedback is designed using the same technique as Section 4.7 the observer is of the form given by Eq. 5.5

$$\begin{aligned}\dot{\hat{\underline{x}}} &= (A+N\omega)\,\hat{\underline{x}} + L(\omega)C_a(\underline{x}-\hat{\underline{x}}) + B\underline{u} \\ \hat{\underline{y}} &= C_a\hat{\underline{x}}\end{aligned} \qquad (5.5)$$

where C_a=[0.8165 0 0 0] and $L(\omega)=L_1+\omega L_2$

With only one sensor there are insufficient degrees of freedom to assign all the observer poles. At zero speed the rank of the observability matrix is 2, which means that only two poles can be assigned arbitrarily. Fortunately, the other two poles are stable, so the detectability condition is met. By choosing the feedback matrix to fix one of the poles for all speeds the resulting behaviour of the second assignable pole must be accepted.

The error dynamics of the observer are given by Eq. 5.6:

$$\dot{\underline{e}} = (A+N\omega - L_{(\omega)}C_a)\underline{e} \qquad (5.6)$$

Using the same observer design technique as in Section 4.7 the feedback gain matrix L is chosen to cancel the first column of these. The observer poles are a function of speed. For the traction motor one eigenvalue is fixed at -60, a second is constrained along the real axis between -113 and -65 and two break out into a complex pair of $-48\pm i3.92\omega$.

Parametrised observer. This observer has the same form as Eq. 5.5. However the gain matrix $L(\omega)$ is pre-calculated for a range of speeds using the Matlab *'place'* command and stored in a look-up table. As mentioned previously, with only one sensor being used for feedback the observability matrix is rank deficient at zero speed, with only two poles freely assignable. For all non-zero speeds all four poles are fully assignable. Observer poles are chosen as -210,-200,-48,-49. With only one output measurement being used it is not possible to place poles in pairs. As the observability matrix is rank deficient at zero speed the gain matrix at $\omega=0$ is calculated for a small positive value, $\omega=0.0001\text{rads}^{-1}$. Using this gain at zero speed results in pole locations -211,-199, -48±0.2i, which is only a small deviation.

Fig. 5.8. shows the terms in the parametrised gain matrix $L(\omega)=[L_1,L_2,L_3,L_4]^{\text{Transpose}}$.

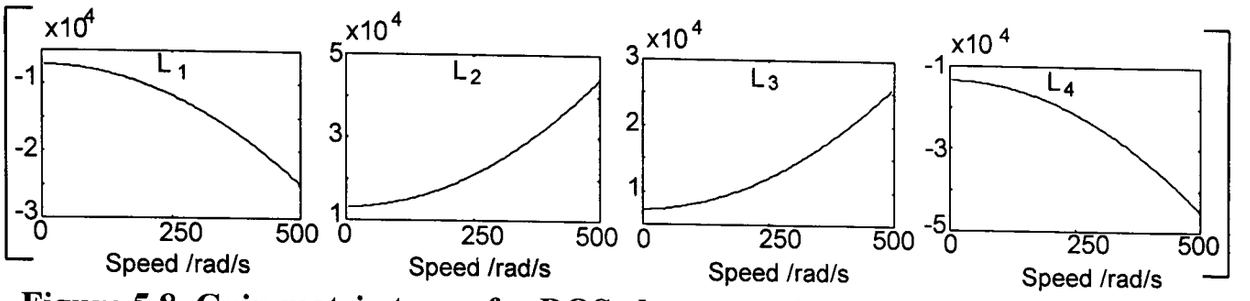

Figure 5.8. Gain matrix terms for DOS observer using parametrised feedback.

5.5.2 Residual generation and isolating faults

The residual signal is required to be zero in the fault-free case and non-zero in the presence of a fault. Consider the observer which only uses the A phase current sensor for feedback. The observer uses the sensor I_a to estimate a complete state vector from which it calculates currents $\hat{I}_a, \hat{I}_b$ and $\hat{I}_c$ as well as a residual signal $R_a = I_a - \hat{I}_a$. For the three possible sensor faults the residual signals are shown in the table in Fig. 5.9.

Fault	Residual
I_a=0	$R_a = -\hat{I}_a$
I_b=0	R_a=0
I_c=0	R_a=0

Figure 5.9. Table of residual values for disconnection of each sensor.

By subtracting the estimate from the A dependent observer from the measured value of the A sensor a residual signal is generated. If the dependent sensor becomes disconnected the residual will be predominantly a sinusoidal signal. By amplitude detection of the residual a fault can be detected, as shown in Fig. 5.10.

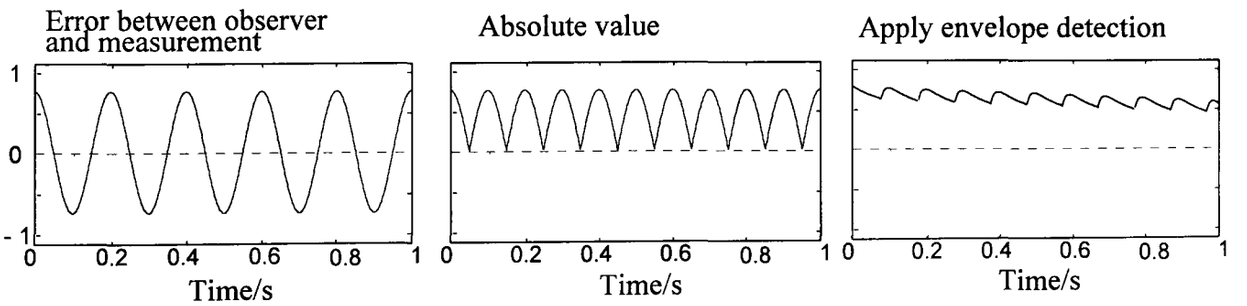

Figure 5.10. Plots showing how the error signal is converted into a residual.

Three further observers are needed with each using a different sensor for feedback. In this way faults on each phase can be detected and isolated. Fig. 5.11 shows the residual signature for each sensor fault using three observers.

Residual / Error	R_a	R_b	R_c
I_a=0	≠ 0	0	0
I_b=0	0	≠ 0	0
I_c=0	0	0	≠ 0

Figure. 5.11. Table of residuals for each possible sensor disconnection.

Two further observers have to be designed each using just one of the I_b or I_c sensors.

5.5.3 Setting up the other two observers

Rather than trying to design the gain matrices for C_b=[0.8 -0.4 0 0] to produce suitable locations for both the assignable and the unassignable poles, a transform of the problem will be used. The directions of the D and Q axes with respect to the A, B and C phases of the motor are totally arbitrary. By rotating the D and Q axes by 120° the B sensor can be rotated to make it independent of Q, as shown in Fig. 5.12. This means that the same gain matrix can be used so that each observer has the same error dynamics.

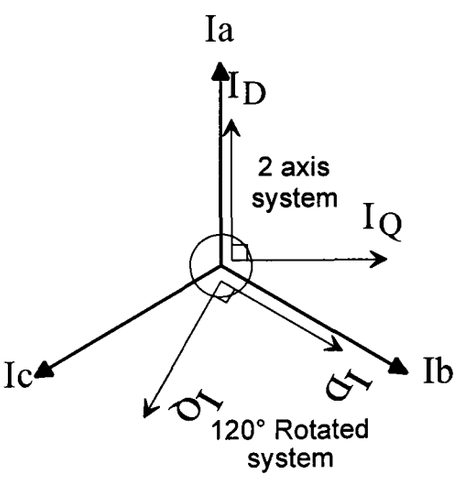

Figure. 5.12. The rotation of the reference axes to make the B sensor independent of the Q axis.

The input voltages have to be rotated using the transform in Eq. 5.7.

$$\begin{bmatrix} V_D \\ V_Q \end{bmatrix}_{120} = \begin{bmatrix} \cos(120) & -\sin(120) \\ \sin(120) & \cos(120) \end{bmatrix} \times \begin{bmatrix} V_D \\ V_Q \end{bmatrix}_{ref} \tag{5.7}$$

The output states have to be rotated back, using the inverse transform of Eq. 5.7.

The Simulink model of the rotated axis observer for the B current sensor is shown in Fig. 5.13. This method has the advantage that the error dynamics of each observer will be the same. Likewise a rotation of 240° is used to make the observer for the C sensor.

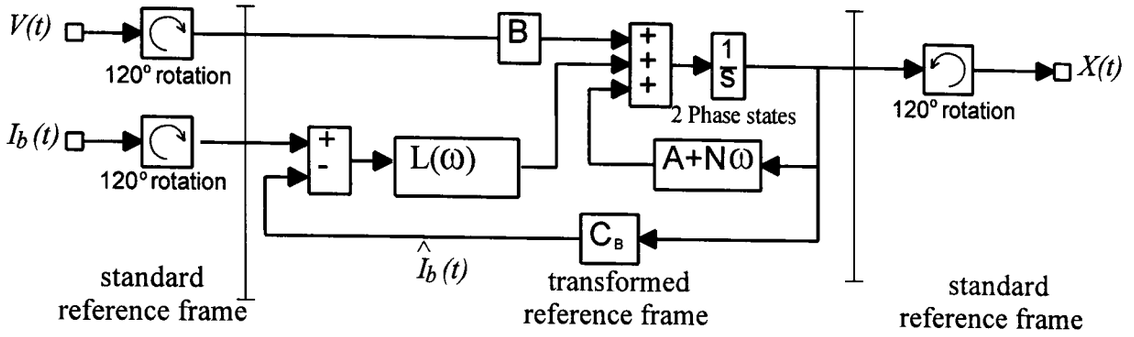

Figure 5.13 Simulink block diagram of B sensor dependent observer.

5.5.4 The complete scheme

Each observer estimates a complete state vector. Whilst this is unnecessary for fault detection it is convenient for correcting the sensor faults. A phase current sensor fault can be corrected by replacing the measured value by an estimate from by one of the other observers, which are independent of the faulty sensor.

The aim of this work is not just to detect defective sensors, since this can be done simply using a parity equation. The aim is rather to obtain fault-free estimates of torque and flux in the presence of sensor faults. To achieve this, the estimates of torque and flux are calculated from the state vector of the observers which is independent of the faulty sensor. Initially, the scheme uses the A sensor observer to generate the required motor state estimates. If it fails the system switches to the B observer and if this also fails the system switches to the C observer. The complete Simulink model for the dedicated observer scheme correction method is shown in Fig. 5.14. This is then subjected to a sequence of multiple faults on the current sensors.

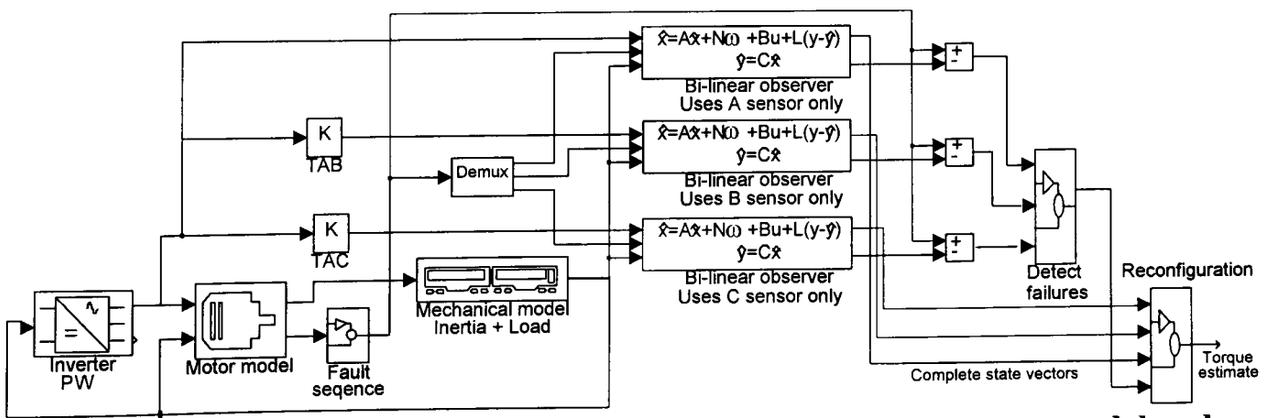

Figure 5.14. The Dedicated observer scheme applied to the motor model and problem of estimating torque and flux with current sensor faults.

Fig. 5.15 shows the torque error during a sequence of simulated current sensor faults. Each sensor malfunctions individually, then sensor malfunctions in pairs and finally all three malfunction together.

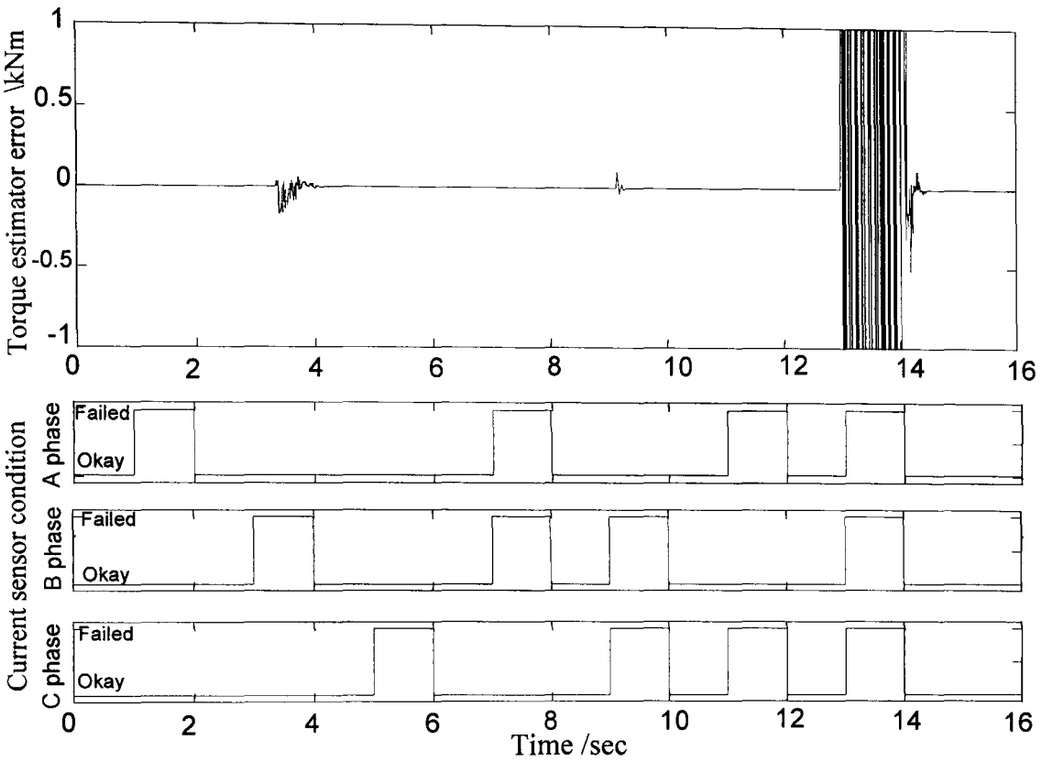

Figure 5.15. Plot showing the torque error using the DOS method for current sensors for a sequence of multiple faults.

With the DOS method, when a disconnection occurs, the system switches to another observer which is independent of the faulty sensor. When the sensor returns to normal operation, the dependent observer has a large error in its estimation which takes time to decay. If the system switches back to this observer too quickly then an error occurs in the estimate, as shown in the Fig. 5.4. The solution to this is to select the estimates from the observer whose residual has the smallest value. The DOS method applied to the induction motor is able to detect faults on all three sensors and correct for any two. This is unlike the parity equation scheme which can only detect and correct single faults.

5.5.5 *Comparison of DOS method and simple parity scheme*

Intermittent faults are difficult to 'see' in the sensor measurements because of the switching noise from the PWM signals or harmonics from squarewave drive. However, they still affect the controller. To compare the DOS method with the simple parity equation approach the two schemes are subjected to a string of rapid intermittent disconnections on multiple sensors. The resulting error in torque estimate is shown in Fig. 5.16.

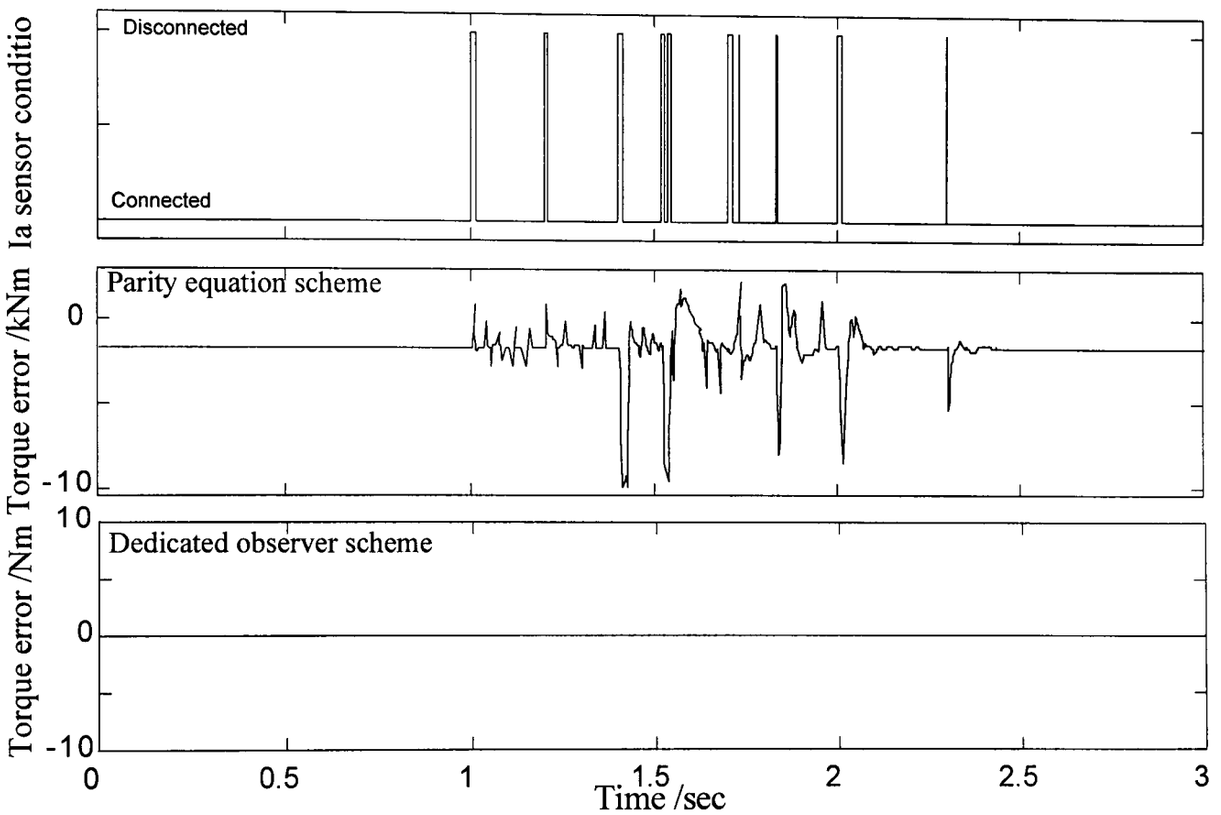

Figure 5.16 Plots of the measured Ia phase current, the sequence of intermittent faults and resulting torque estimation errors from the two schemes.

The DOS method is able to cope with the intermittent faults since within a few sample periods, the estimates are switched to an unaffected observer. The resulting error in torque is extremely small, less than 10^{-3} Nm, this is using the observer with the minimum residual for the estimate of the complete state vector. The parity equation method has a large error which is passed to the estimator each time a fault occurs. The DOS method would encounter difficulty with multiple intermittent failures on multiple sensors, since each individual observer takes a finite time to converge sufficiently after a fault on the dependent sensor. If intermittent faults occur on all sensors within this time then no reliable estimation of the torque is available. If the intermittent faults are constrained to two observers then there is no minimum separation time.

5.6 *The unknown input observer for voltages sensors*

For each sensor in turn the other voltage sensors can be treated as unknown inputs, the observer will estimate the motor states. If there is an error between the estimate and the actual measured output then there is a fault on the voltages sensor upon which the observer is dependent. The unknown input observer is a well developed technique, Chen *et al* (1996), the problem in this case is again the bilinear nature of the model.

5.6.1 Design of an Unknown Input Observer for linear model.

Initially, consider the design of Chen & Zhang (1991) for a linear state-space plant with the unknown disturbance input $d(t)$ but with a known distribution to the states E.

The state space equation for this is given by Eq. 5.8.

$$\begin{aligned} \dot{\underline{x}}(t) &= A\underline{x}(t) + B\underline{u}(t) + E\underline{d}(t) \\ \underline{y}(t) &= C\underline{x}(t) \end{aligned} \tag{5.8}$$

The observer proposed by Chen *et al* (1991) has the general form.

$$\begin{aligned} \dot{\underline{z}}(t) &= F\underline{x}(t) + TB\underline{u}(t) + K\underline{y}(t) \\ \hat{\underline{x}}(t) &= \underline{z}(t) + H\underline{y}(t) \end{aligned} \tag{5.9}$$

The estimation error in this observer is given as.

$$\begin{aligned} \dot{\underline{e}}(t) &= \dot{\underline{x}}(t) - \hat{\dot{\underline{x}}}(t) \\ &= (A - HCA - K_1C)\underline{e}(t) + [F - (A - HCA - K_1C)]\underline{z}(t) \\ &\quad + [K_2 - (A - HCA - K_1C)H]\underline{y}(t) + [T - (I - HC)]B\underline{u}(t) + (HC - I)E\underline{d}(t) \end{aligned} \tag{5.10}$$

This will reduce to $\dot{\underline{e}}(t) = F\underline{e}(t)$ if the following conditions are met.

$$\begin{aligned} &\text{i} \quad (HC - I)E = 0 \\ &\text{ii} \quad T = I - HC \\ &\text{iii} \quad F = A - HCA - K_1C \\ &\text{iv} \quad K_2 = FH \end{aligned} \tag{5.11}$$

The design procedure can be summarised as:

For condition i if CE is non-square then use the left pseudo-inverse

$$H = E(CE)^{+}$$

where $(\ )^{+}$ denotes the left pseudo-inverse, such that

$$(CE)^{+} = \left[(CE)^{T}(CE)\right]^{-1}(CE)^{T} \tag{5.12}$$

Condition i can be met if rank(CE) = rank(E).

- With H now determined to meet condition i, T can be calculated.

• Substitute $T=I-HC$ into condition iii.

$$F = A_1 - K_1 C \tag{5.13}$$

where $A_1 = TA$ and K_1 can be found using a pole placement routine.

• K_2 can be calculate from F and H.

$$K = K_1 + K_2 \tag{5.14}$$

The residual generator is obtained by subtracting the observer's estimate of the measured states from the actual measured states. The Simulink block diagram for the residual generator is shown in Fig. 5.17.

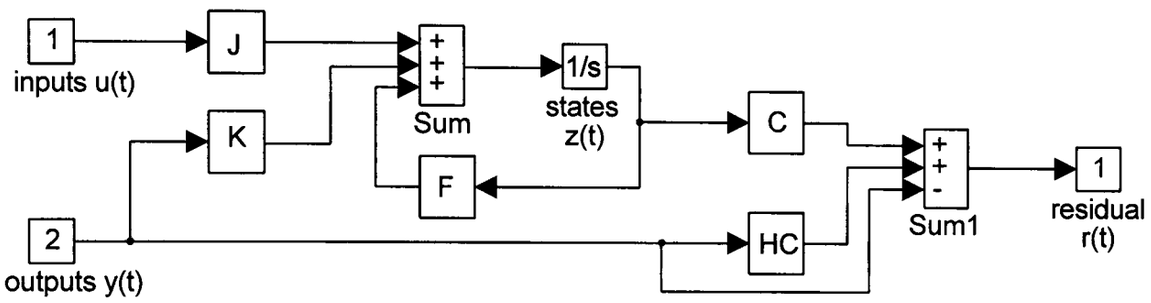

Figure. 5.17. Simulink block diagram of the residual generator observer.

5.6.2 Extending to the Bilinear Model

The unknown input observer design must be extended to account for the bilinear terms in the induction motor model. The matrix A_1 in Eq. 5.13 becomes $A_1=T(A+N\omega)$. The gain matrix K_1 is found using bilinear feedback to cancel the first two columns in the error dynamics as used in Section 4.7.

The feedback K_2 is also now bilinear and is calculated from F and H as before.

For this specific design example there is an advantage in using the Phase-to-Ground reference plane. This alters the state input B matrix which relates the three phase voltages in phase-to-phase form to the observer states which are 2 axis currents in phase -to-ground orientation. See Appendix A for details of the transformations.

$$B=10^3\begin{bmatrix} 1.6123 & 0 & -1.6123 \\ 0 & 2.7925 & 0 \\ -1.5456 & 0 & 1.5456 \\ 0 & -2.677 & 0 \end{bmatrix}$$

Note that the first and third columns lie in the same direction but have opposite sign[5.2]. By making this the distribution of the unknown input it is possible to decouple two input sensors with a single unknown input.

[5.2] Assuming that the motor is balanced, so the quadrature components of V_{ab} and V_{ca} cancel.

The unknown input vector becomes.

$$E=10^3\begin{bmatrix} 1.6123 \\ 0 \\ -1.5456 \\ 0 \end{bmatrix}$$

As $A_1=T(A+N\omega)$ and the closed-loop observer matrix is given by $F=A_1-K_1C$, this means that speed-dependent feedback is needed to stabilise the observer. Again either parametrised or bilinear feedback can be use. Using bilinear feedback the gain matrix K_1 is given as:

$$K_1 = L_1 + L_2\omega \tag{5.14}$$

$$\text{where } L_1 = TA_{(1:4,1:2)} - \lambda\begin{bmatrix} 1 & 0 \\ 0 & 1 \\ 0 & 0 \\ 0 & 0 \end{bmatrix} \text{and } L_2 = TN_{(1:4,1:2)}$$

The F and K matrices in the observer, shown in Eq. 5.9, now have the bilinear structure:

$$F = (TA - L_1C) + (TN - L_2C)\omega \tag{5.15}$$

$$K = (TAH - L_1CH + L_1) + (TNH - L_2CH + L_2)\omega \tag{5.16}$$

The eigenvalues of this observer are not fixed, but remain in the stable left hand plane. With λ=-50 the loci of the observer's poles with speed are a fixed pair at -50 and a moving pair mirrored in -25.8 which form a complex conjugate pair beyond ω=7. At high speed these tends towards $25.8\pm i3.92\omega$, using the parametrised feedback method both F and K would have to be pre-calculated and stored in look-up tables. However, all four poles would be fully assignable.

The method is now the same as the DOS observer for current sensors, three observers are set up each using one voltage sensor to produce a residual. By rotating the axes of the d-q two phase system by 120° it is possible to make an unknown input observer which is dependent on V_{ca} only. A further 120° rotation and the observer is dependent on V_{ab} only. This has produced a set of three observers each only dependent on one sensor. Each observer has the same dynamics. The complete scheme as implemented in Simulink is shown in Fig. 5.18. The state estimates used to calculate torque and flux are taken from the observer with the smallest residual. Note that this scheme does not actually reconstruct the value of the failed sensors, which the DOS method did for currents, this may be a limitation if the phase-to-phase voltages are needed elsewhere in the control systems.

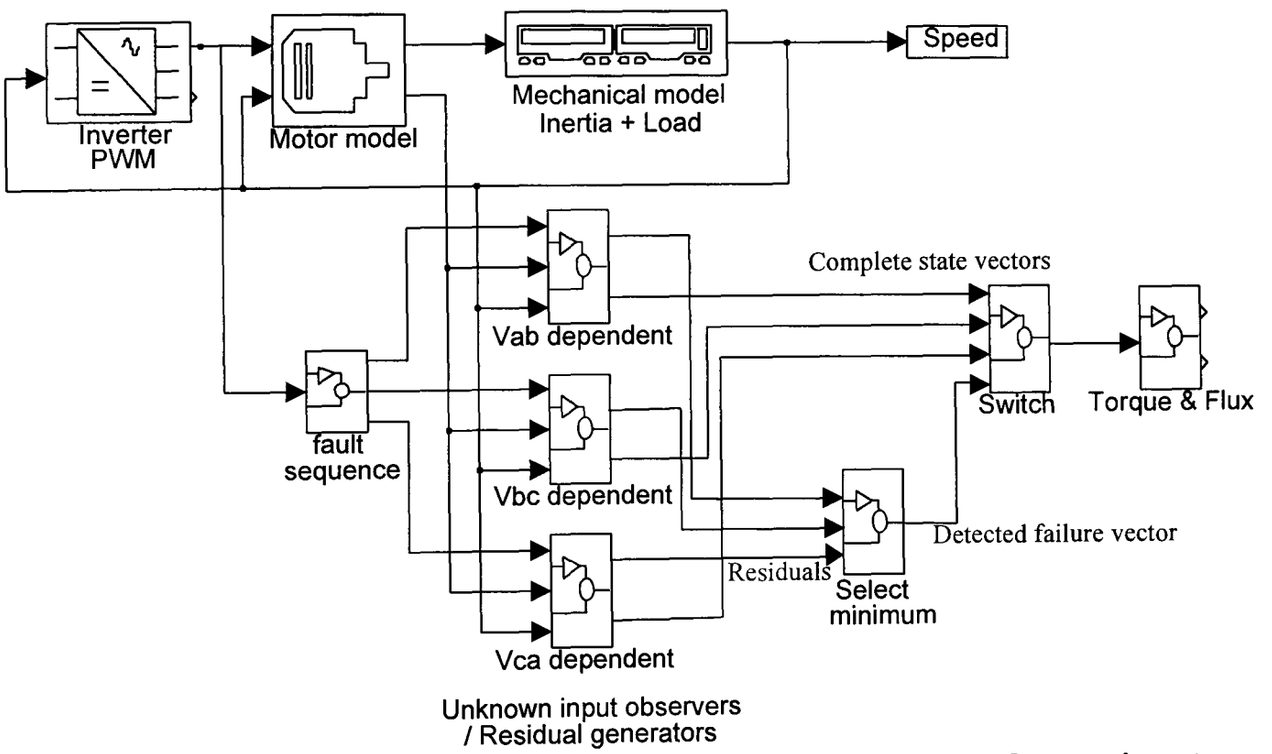

Figure 5.18. Top level Simulink block diagram of the three unknown input observers and the failure correction scheme.

5.6.3 Testing the unknown input based voltage sensor fault detection scheme

The three observers were set up in Simulink and tested. Each voltage sensor was made to malfunction in turn, then in pairs and finally all three together. This was done during a simulated start-up with the train accelerating from rest, Fig. 5.19 shows the detected faults and the error in the torque estimate.

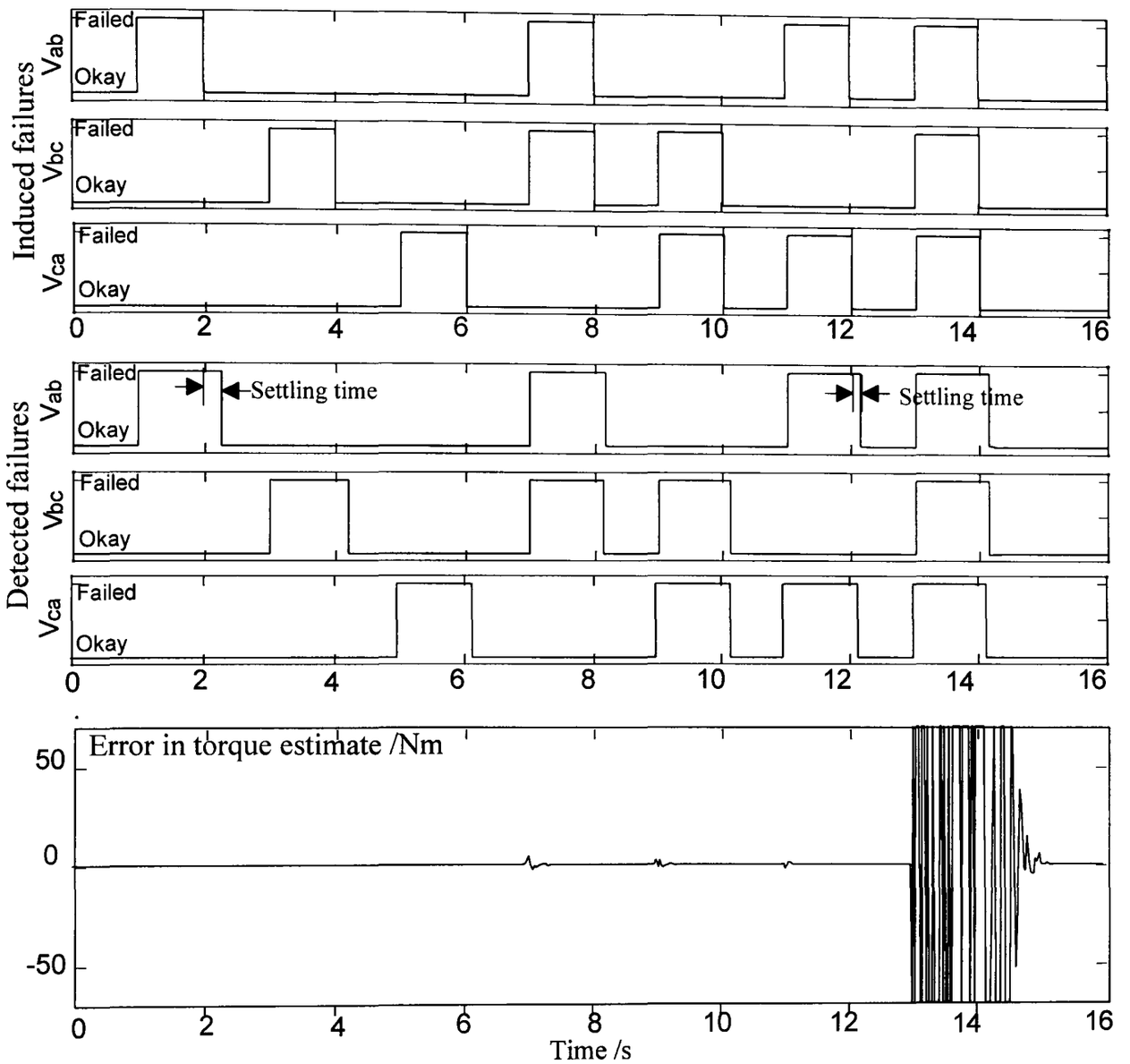

Figure 5.19 Plots of faults induced, faults detected and the error in torque estimate.

At low speeds one of the observer's eigenvalues is slow. Hence the initial fault on the A sensor takes longer to clear than the later ones which occur at higher speeds. Note the settling time marked on Fig. 5.19 for the fault on Vab.

For estimating torque and flux this scheme can be made tolerant to up to two voltage sensor failures by simple switching to a functioning observer. Regenerating the correct sensor value is harder. For one sensor fault this could be done by the use of Kirchoff's

law as before. In the present Networker control system the voltages are only used by the estimator, therefore this is not a significant limitation. As with the current sensor scheme intermittent faults can be corrected, although at low speed the time taken for the observer errors to settle down again is relatively long, typically 0.1s.

5.6.4 Other applications of the DOS methods

During a meeting with engineers from a major traction equipment manufacturer, the following question was raised 'many of our systems have proven reliability but the market is very competitive, can we use DOS methods to reduce the cost of instrumentation ? '

The DOS methods are less robust and more sensitive to noise, this has been demonstrated in Section 5.10. and Section 7.8. The test-rig results show that for a small motor the DOS method is not suited to FDI since its sensitivity to faults is also low. However, this does not prevent its use for control estimates, since for low cost equipment, performance is less important. For simple control loops requiring a measurement of torque, the DOS method, although sensitive to noise, has limited transient errors. However the effect of the reduced robustness would have to be considered for the specific application.

5.7 *Generalised Observer Scheme for current and voltage sensors*

The DOS for current sensors and UIO method for voltage sensor faults are limited in that for each method it is assumed that one set of sensor is fault free. This section considers a method which combines the fault correction for current and voltage sensors.

Using the GOS method, three observers are designed, each using two out of the three voltage and current sensors and the speed dependent feedback method for an observer. For the induction motor problem Kirchoff's laws can be applied to produce an observer which is independent of one of each type of sensor. No special observer design is needed, this method could be used with any of the observers outlined in Chapter 4. However for simplicity the bilinear observer is considered.

Using Eq. 5.1 and 5.2 one sensor from a set can be estimated from the others. For example by estimating I_a and V_{ba} an observer is made independent of faults on these sensors.

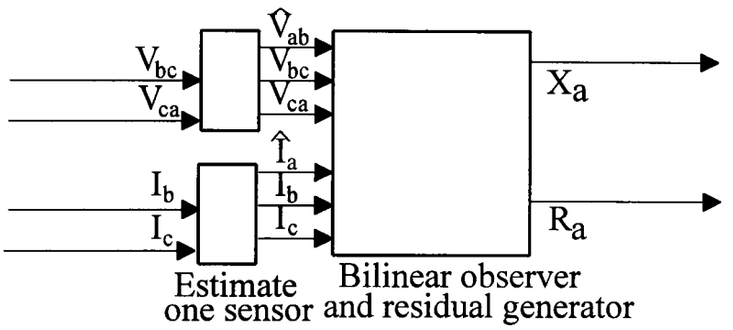

Figure 5.20. Diagram of single observer made independent of two sensors.

Sensors I_b and I_c are used to generate an estimate of I_a called $I_a est$, the observer generates an estimate of the complete state vector from which the sensor estimates $\hat{I}_a, \hat{I}_b$ and $\hat{I}_c$ are produced and the residual signal is $R_a = I_a est - \hat{I}_a$. The table in Fig. 5.21 shows the six possible faults and their residual signals.

Error	$I_a est$	$\hat{I}_a$	R_a
I_a=0	I_a	I_a	0
I_b=0	$-I_c$ *	$\neq I_a$	$\neq 0$
I_c=0	$-I_b$ *	$\neq I_a$	$\neq 0$
V_{ab}=0	I_a	I_a	0
V_{bc}=0	I_a	$\neq I_a$	$\neq 0$
V_{ca}=0	I_a	$\neq I_a$	$\neq 0$

* From Kirchoff's law, $I_a est = -I_b - I_c$

Figure 5.21. Table of residuals for the six possible single sensor disconnections.

With two more observers, using estimates of I_b plus V_{bc} and I_c plus V_{ca} respectively, an estimate of the state vector and unique set of residuals can be obtained in the presence of any single fault, see Fig. 5.22. The complete scheme contains a block of signal processing logic, which selects the state estimate from the observer with the smallest residual. The block diagram for this complete scheme is shown in Fig. 5.23.

Residual / Error	R_a	R_b	R_c
I_a and or V_{ab}	0	$\neq 0$	$\neq 0$
I_b *and* or V_{bc}	$\neq 0$	0	$\neq 0$
I_c and or V_{ca}	$\neq 0$	$\neq 0$	0

Figure 5.22. Table of residual signatures for the six possible single sensor disconnections.

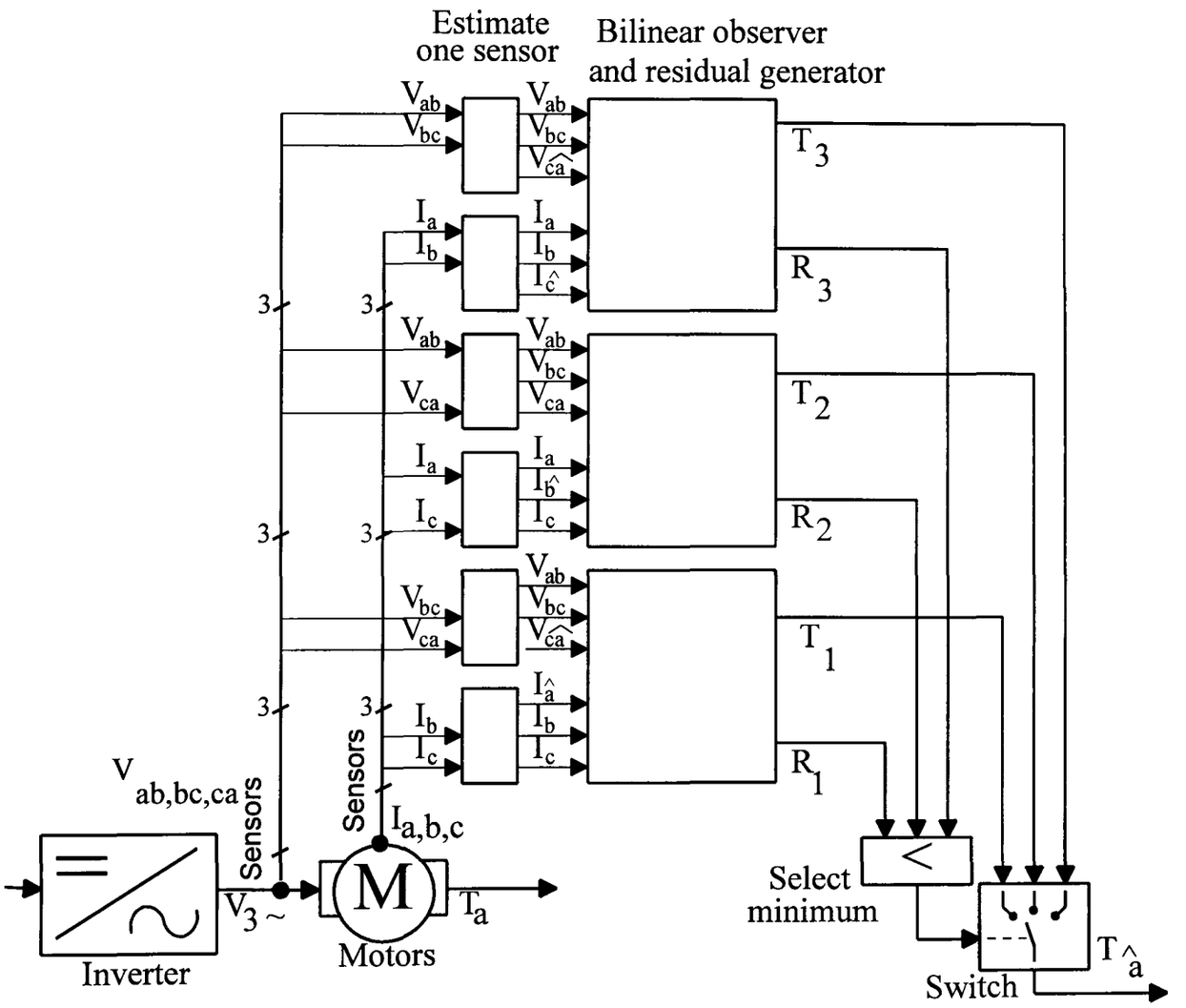

Figure 5.23. Block diagram of Generalised Observer Scheme for detecting and correcting sensor faults.

The traction system is subjected to a simulated sequence of disconnections on each sensor, this is shown in Fig. 5.24 with the resulting error in the torque estimate.

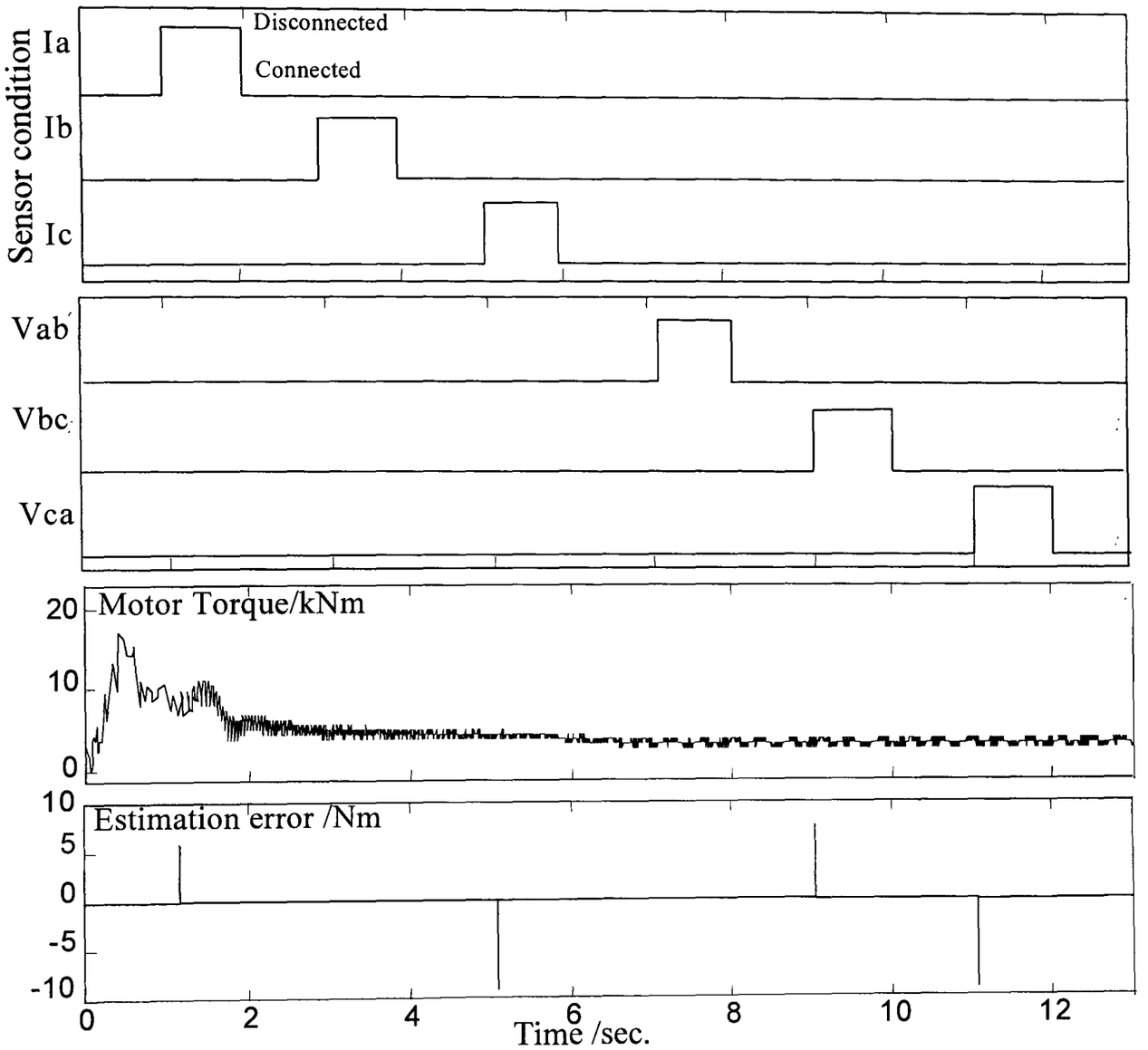

Figure. 5.24. Diagram of fault sequence and resulting error in torque estimate.

Note that there is a small glitch when a sensor malfunctions. There is no transient induced because, as soon as the fault is detected the torque estimate is switched to another unaffected observer. What is not shown here is the time taken for an affected observer to reconverge after the fault disappears. If sensor faults occur on different sensors the observers will not have reconverged. For the faults occurring with 1 second separation, as in Fig. 5.24, there is no problem. The graph in Fig. 5.25 shows the transient error in torque as the separation decreases.

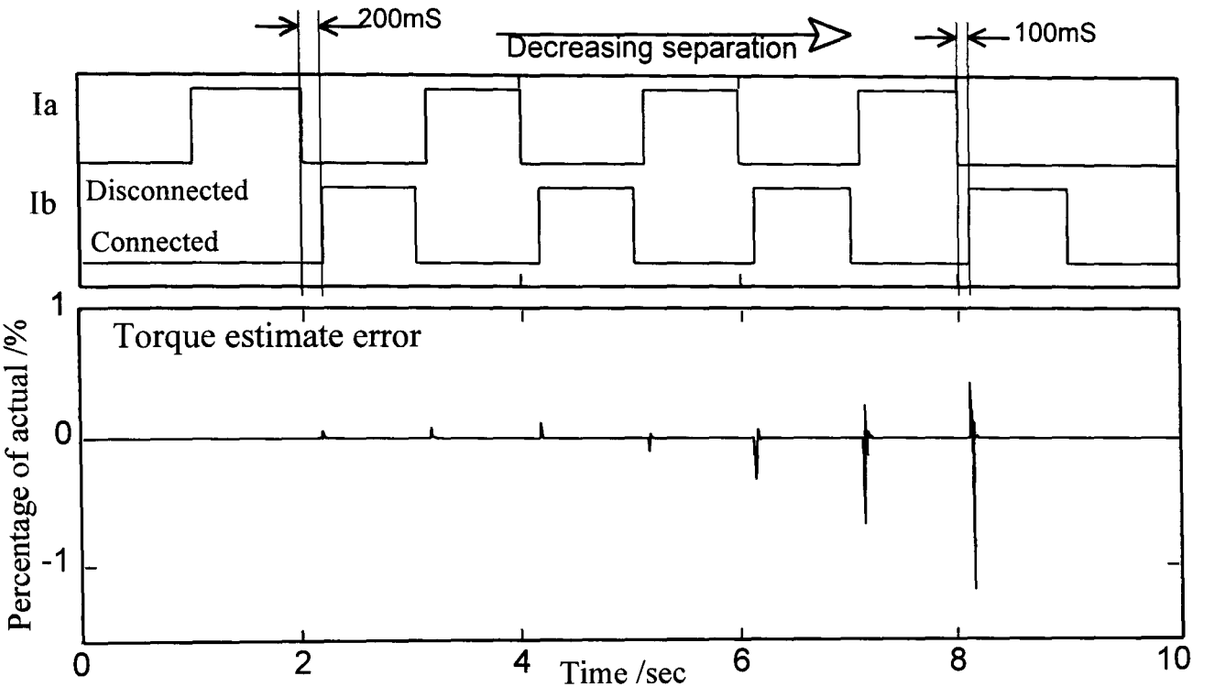

Figure 5.25. Diagram showing the effect of minimum separation between failure on different sensors.

5.8 Multiple sensor techniques

Whilst it is possible to produce an observer which uses only one current and one voltage sensor this is not practicable since the observer would have very complicated error dynamics. This would make an observer dependent on just two sensors. Using nine observers in a bank up to two pairs of failed sensors could be corrected.

By using two sensors to estimate the third measurement it is possible to make an observer which is independent of a pair of either sensor types and one of the other. This gives several possibilities; using three observers a scheme can be set up which is able to correct any one sensor failure, with six observers any two sensor failures and with eighteen observers any three sensor faults[5.3]. However, this final scheme is clearly impractical on the grounds of computational load. Each observer would generate a residual, this would then be passed to a block of logic to select the state from the one with the minimum residual.

[5.3] excluding three sensors of the same type, ie all three current sensors.

5.9 State trees scheme

As suggested in Section 5.8 the capacity exists to tolerate faults on 'two of one and one of the other' for voltage and current sensors. The overall scheme is impractical. However by assuming that only one sensor fault can occur at a time then it is not necessary to detect all combinations of faults. At any given time the instrumentation system is said to be in a '*state*', when a sensor fails or returns to normal this results in a *transition* which takes the system to another state. Initially, with all sensors functioning it is only necessary to monitor for a single voltage or current sensor fault. In the general case it is necessary to monitor for a current sensor failing or voltage sensor failing or returning to normal operation. At any given moment upto five possible transitions need to be monitored for.

For each state there are several possible transitions which can occur after an event. An event is defined as a sensor failing or returning. Fig. 5.26 shows a 'state-transition tree' for the fault diagnosis problem. Depending on the state of the system different observers will be needed. In any given state the observer must provide three functions, correct estimation of the state, detection for any new failures, and monitoring to check for the return of prior failed sensors.

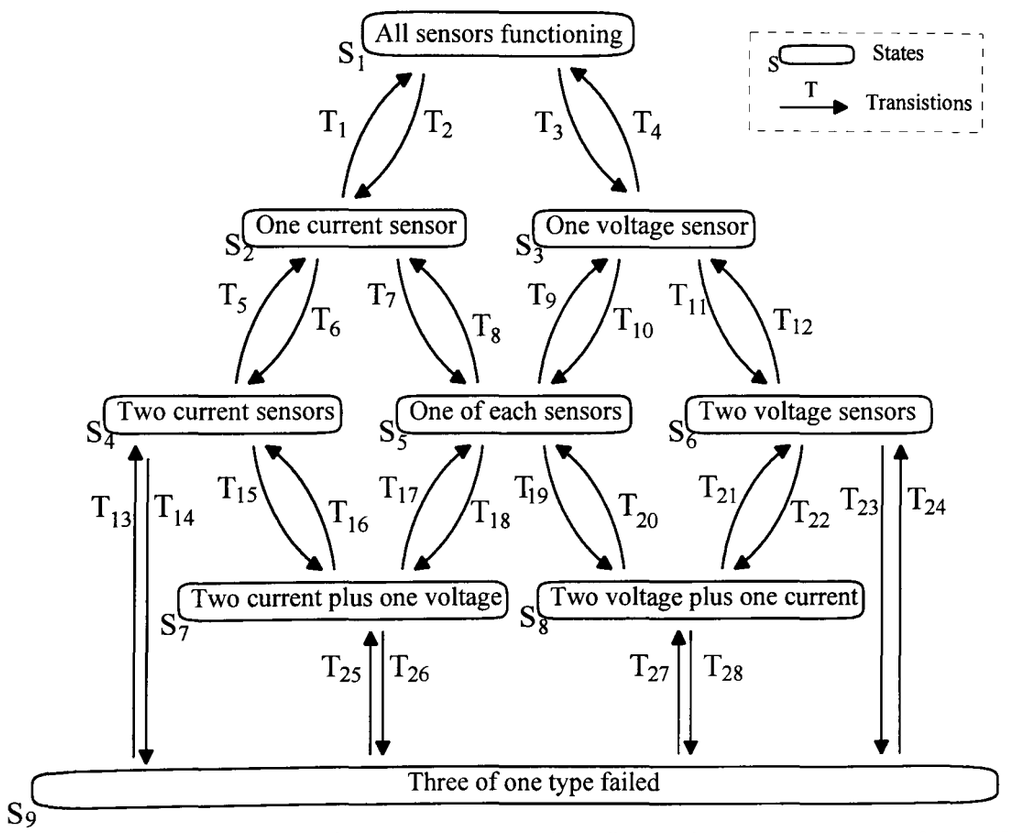

Figure 5.25. State transition diagram for detecting and correcting all possible combination of sensor faults.

It is not intended to show the complete design since this would be repetitive. This scheme is overly complex for the application, but it does represent an important aspect of the theory of fault-tolerance, reconfiguring with the usage of the last-known good states and the timing problems this encompasses

Consider the initial starting condition, with all the sensors functioning

State: S_1 All sensors functioning.
Task: Monitor all sensors for fault.
Observer required: R_1: Dependent on I_a, V_{ab}, & V_{bc}
R_2: Dependent on I_b, V_{bc}, & V_{ca}
R_3: Dependent on I_c, V_{ca}, & V_{ab}

	Resid. 1	Resid. 2	Resid. 3	Transitions.
Fault on Ia	≠0	0	0	T_1
Fault on Ib	0	≠0	0	T_1
Fault on Ic	0	0	≠0	T_1
Fault on Vab	≠0	≠0	0	T_2
Fault on Vbc	0	≠0	≠0	T_2
Fault on Vca	≠0	0	≠0	T_2

State: S_2 One current sensor failed (I_c)
Task: Monitor for return of failed current sensor.
Monitor remaining sensors for another failure.
Observer required: R_1: Dependent on I_a, V_{ab}, & V_{bc}
R_2: Dependent on I_b, V_{bc}, & V_{ca}
R_3: Dependent on I_b, V_{ca}, & V_{ab}
R_4: Dependent on I_c, V_{ca}, & V_{ab}

	Resid.1	Resid.2	Resid. 3	Resid.4	Transition
Fault on Ia	≠0	0	0	≠0	T_6
Fault on Ib	0	≠0	≠0	≠0	T_6
Return of Ic	0	0	0	0	T_3
Fault on Vab	≠0	0	≠0	≠0	T_7
Fault on Vbc	≠0	≠0	0	≠0	T_7
Fault on Vca	0	≠0	≠0	≠0	T_8

And so on, for the various states.

Each state will have a different set of observers depending on which sensors are available and which of the already faulty sensors are being monitored. This scheme will require two different types of observer, the DOS and UIO methods, and up to five observers in parallel, (two monitoring and three following functioning sensors). The basic scheme will have a bank of observers which can be reconfigured depending upon the present tasks for the current state. A reconfigurable observer is shown in Fig. 5.27, with all the necessary gains to form either of the observers given by Eq. 5.13 or 5.17, in any rotation.

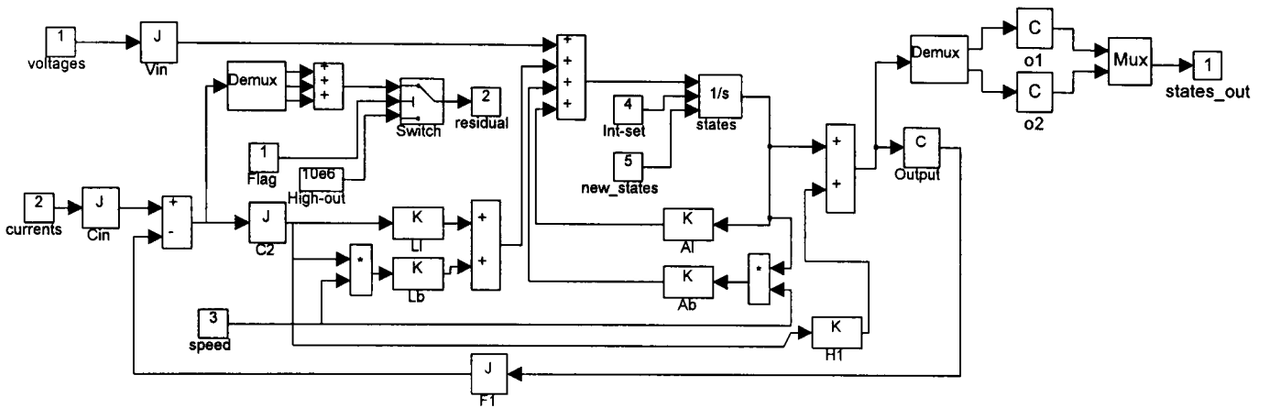

Figure 5.27. Diagram of reconfigurable observer.

The complete scheme requires five reconfigurable observers. Each observer generates a complete estimated state vector and a residual. This residual is passed through an envelope detector and the minimum selected. A function called 'process' then selects the appropriate transition or not to change. The function called 'reconfigure', when a transition occurs, gives the appropriate commands to reconfigure the observers, reset the integrators to the last known accurate estimate and change the function 'process' to detect a different set of faults. Any unused observers are set to give a large positive residual so that they are discounted from the selection process. Fig. 5.28 below shows the resulting Simulink structure.

The Matlab command *set_param* is used by the function *reconfigure* to change the values of the matrices whilst the simulation is running. Since, when a fault occurs not all the residuals are affected at the same time, a block called 'deglitcher' is needed. Once a change is detected there is a short delay before the scheme is allowed to reconfigure to ensure that the correct action is taken. During this time correct estimates are still available from the observers but no other fault can be catered for.

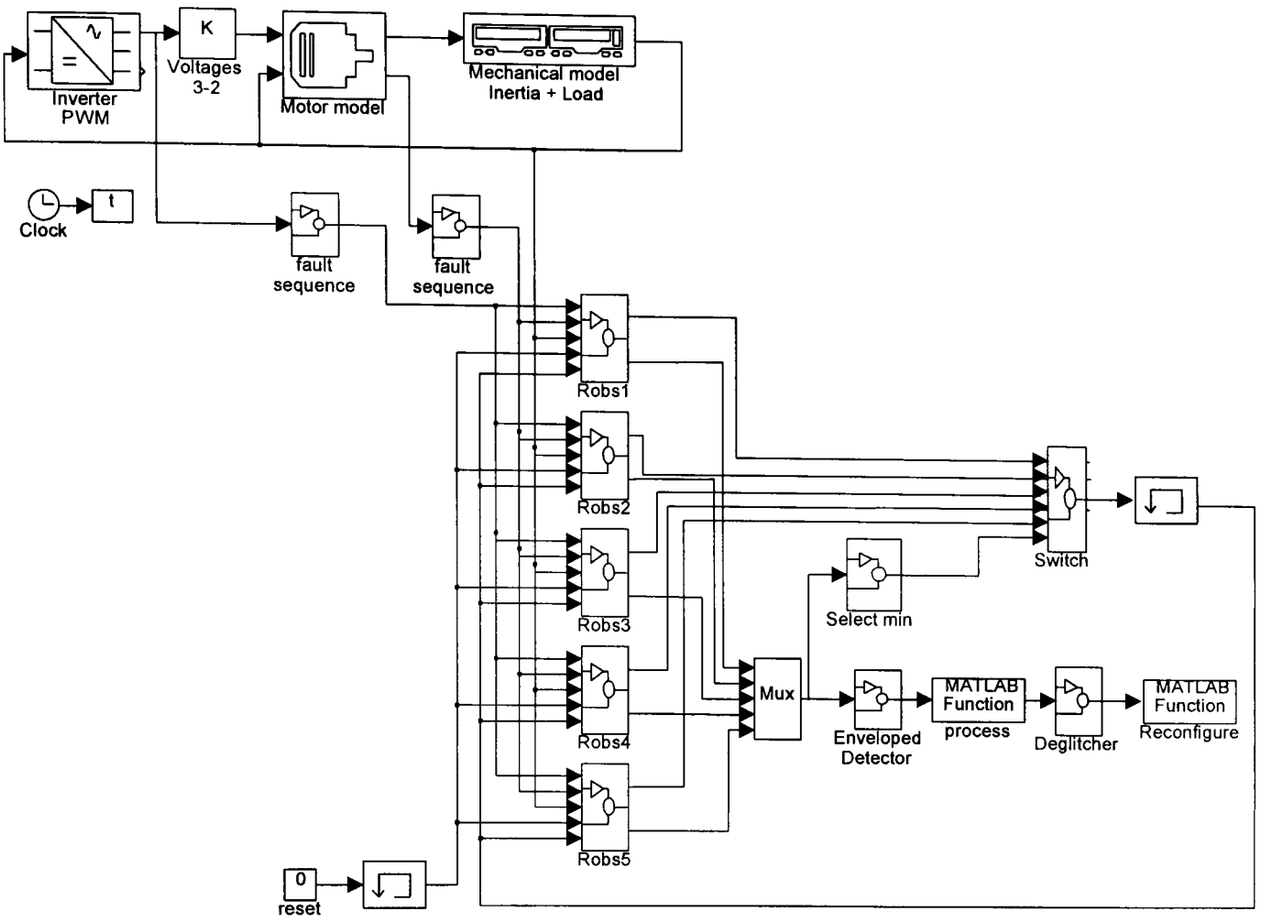

Figure 5.28. Simulink block diagram of complete systems.

5.10 Comparison of residual fault sensitivity for DOS and GOS methods

This section compares the two main methods discussed in this chapter, DOS and GOS, for sensor fault tolerance. The two methods do not necessarily have the same sensitivity to faults. Using simulation it is possible to obtain a relationship between the sensor fault and the size of the residual as a function of motor speed.

5.10.1 Current sensor disconnections

The DOS and GOS methods are simulated in parallel and run through a notch four start up. For both observers one of the dependent current sensors is disconnected. The resulting residuals are plotted in Fig. 5.29.

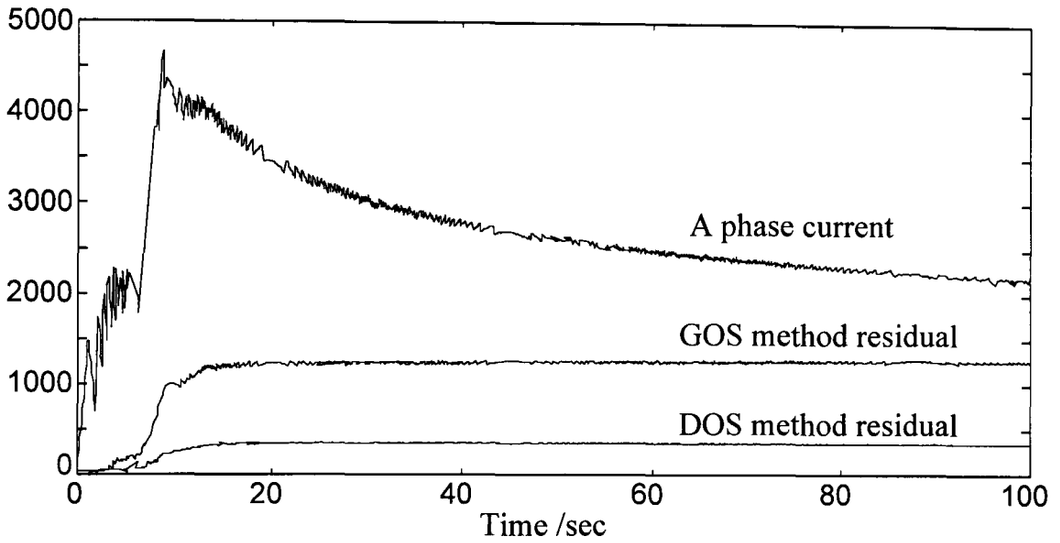

Figure 5.29. Plots of A phase stator current and the residuals for the GOS method and the DOS method for a sensor disconnection on Ia.

A more useful measure of the residual's sensitivity to sensor faults is to normalise the residual by dividing it by the magnitude of the phase current and then plotting the result against speed, as shown in Fig. 5.30.

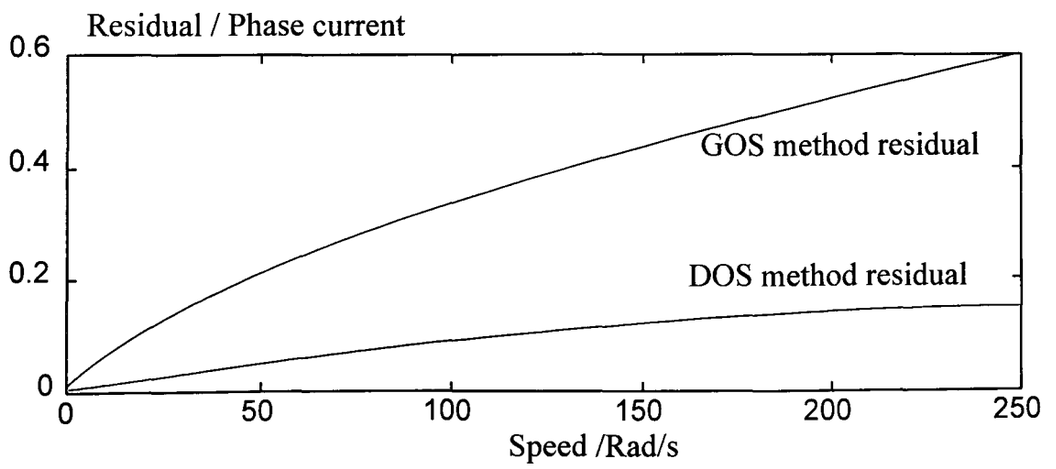

Figure 5.30. Plots of normalised residuals against motor speed for the GOS and DOS methods.

The DOS method has lower sensitivity to sensor faults, for comparable convergence rates for the error dynamics. This is be to expected since most of the available design freedom is used in isolating the fault, so that each observer is only sensitive to one fault.

The observer sensitivity to a particular fault is likely to be a function of the pole locations. To demonstrate this the tests were repeated with three different sets of poles. The resulting residuals are shown in Fig. 5.31 normalised for current.

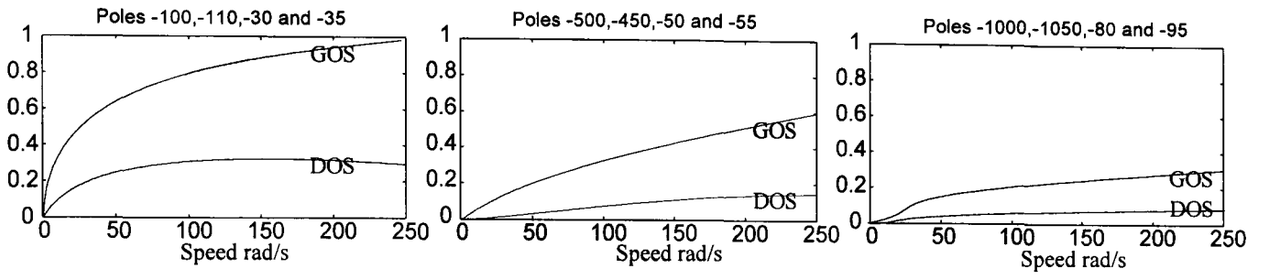

Figure 5.31. Plots showing the relative sensitivity of the DOS and GOS methods to sensor faults for different observer poles locations.

As the poles of the observer's error dynamics become increasingly fast the sensitivity of the observer is reduced.

It is also possible to compare the use of bilinear and parametrised feedback. The results for the GOS method using the two types of feedback and based upon the same real pole locations for the observer dynamics, -500,-500,-48 and -48, are shown in Fig. 5.32.

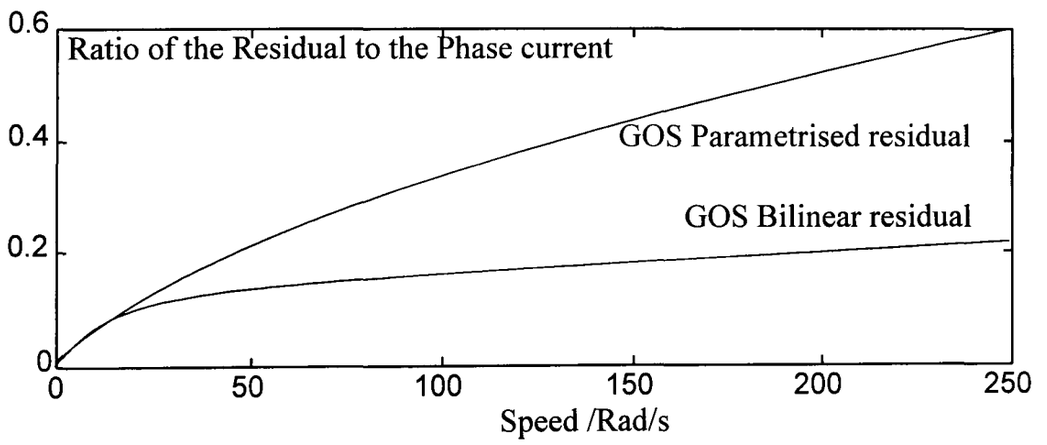

Figure 5.32. Plots showing the relative sensitivity to sensor faults for different observer feedback methods.

At low motor speeds the two schemes have similar sensitivity. At higher speeds the parametrised observer is more sensitive. For fault detection low gains are desirable or else the error feedback is sufficient that the observer is forced to track the fault, which reduces the residual. For example consider the DOS residual given by:

$$R_a = I_a - \hat{I}_a \tag{5.17}$$

If there is a sensor disconnection on the dependent sensor, making I_a=0 the residual reduces to $-\hat{I}_a$. If the observer has sufficient gain, the feedback will force the estimate of I_a to track I_a and the residual will then tend towards zero.

It is not sensible to compare the two methods for their sensitivity to faults alone. In simulation the GOS method is clearly more sensitive to faults. However, for a real application it is the difference between the magnitudes of the fault and the fault-free residual which enables a fault to be detected. For example, to compare both schemes in the presence of noise on the measurements, the noise sensitivity of the observers must be considered. Using the method outlined in Section 4.13.1 the noise sensitivity of the GOS and DOS observers using parametrised feedback are plotted, in Fig. 5.33, for a fixed speed of 200rad/s.

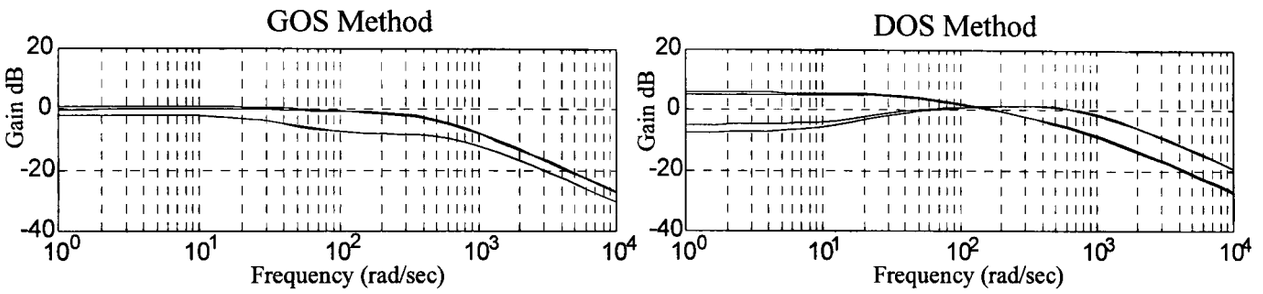

Figure 5.33. Plots for the magnitude of the coupling between measurement noise and observer error against frequency for fixed speed of 200rad/s.

The DOS observer is significantly more sensitive to noise on the current sensors. The DOS method for fault detection is worse than the GOS method for two reasons. Firstly, smaller residuals are generated for comparable faults, secondly greater fault-free residuals combine to make the detection problem harder. This is illustrated in Fig. 5.34.

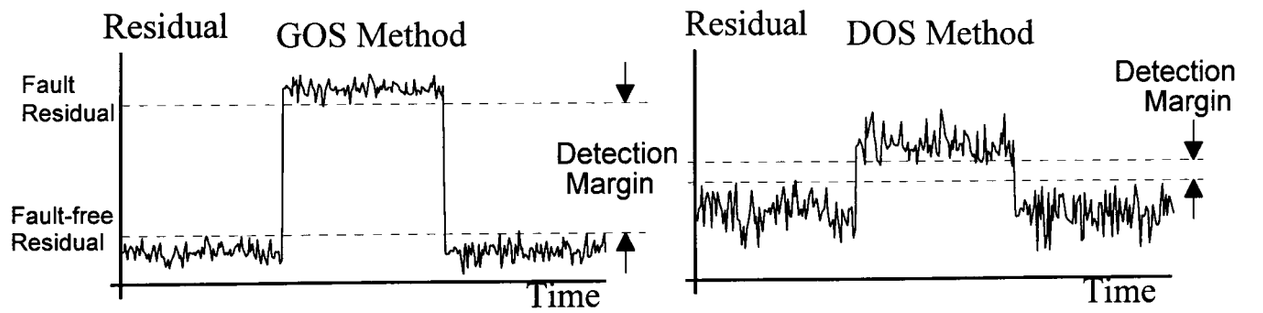

Figure 5.34. Sketch comparing the GOS and DOS methods when faced with noise on the measurements. Illustrating how greater sensitivity to noise and lower sensitivity to faults of the DOS method makes detection much harder.

5.10.2 Voltage sensor disconnections

The GOS method and the UIO for voltage sensors can be compared in the same way as previously used for current sensor disconnections.

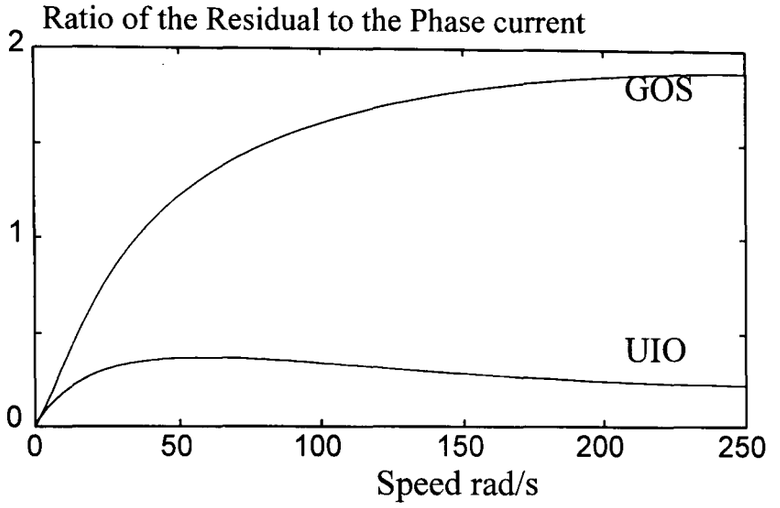

Figure 5.35. Relative magnitude of residuals for GOS and UIO methods.

The GOS method is much more sensitive than the UIO method for voltage sensor faults. Again the same issues of pole location and observer sensitivity would need to be considered before making any definitive comparison.

The very low sensitivity of the UIO to voltage sensor faults is clearly demonstrated in practice on the test-rig in Section 7.8, where the fault residual is barely greater than the fault-free residual.

5.11 Summary of current and voltage sensor fault detection methods

	GOS	DOS	Combined	State-tree
Capacity	Single fault on either type of sensor	Two faults on one type of sensor	6 observers at least any two 3 observers at least any one	Two plus one of other.
Advantages	Guaranteed stability	Makes better use of available redundancy in the motor model	Able to cope with simultaneous faults.	Only five observers are needed
Drawbacks	Minimum separation time between failures (though very short)	Poor fault detection performance due to lower sensitivity to faults and greater sensitivity to noise.		Implementation very complicated Cannot handle simultaneous disconnections
Suitability	Occasional faults.	Only one type of sensor subject to faults	Heavy intermittent faults on multiple sensors	Continuous loss of multiple sensors

All four methods allow a choice of bilinear or parametrised observer feedback. The bilinear method is easy to implement and requires minimal memory and computation, but for comparable poles, it is less sensitive to faults and more sensitive to noise.

The GOS method is simply a bank of three identical observers preceded by estimation of a sensor measurement. This method can be used with any of the observer designs in Chapter 4, and has subsequently been done using fuzzy observers, Lopez *et al* (1997).

The DOS methods make better use of the available redundancy in the motor model to decouple two of either type of sensor. However, the DOS method is significantly less sensitive to faults and more sensitive to noise making detection harder. The three observers needed to be designed using three rotated sets of axes, to give each observer identical error dynamics.

The DOS and GOS methods can be combined to give better capacity but the number of observers required increases as the number of failures allowed increases. In order to limit the number of observers it is possible to use a state-tree of reconfigurable observers to monitor for changing sensor conditions. Both of these methods are probably too complex for the application in this study.

5.12 Observer design for fault-detection

The choice of observer feedback not only affects the convergence rate, noise and parameter sensitivity, it can also be used to accomplish other design goals. The unknown input observer has similar error dynamics but is designed to completely reject a single disturbance direction. This produces an observer for fault detection which is independent of two out of the three voltage sensors. Similarly a fault detection observer for current sensors can be designed by using a single sensor for feedback. However, both these designs have been shown, in Section 5.10, to be less sensitive to faults and much more sensitive to noise than the standard observer. There is a limited amount of flexibility in the feedback design which can be used to obtain a desired objective, but this is at the expense of performance in other areas.

For fault detection a high observer gain is shown to be undesirable, since it forces the observer to track the fault condition. This considerable reduces the magnitude of the fault residual. There is a fundamental conflict between the design requirements of observers for estimation, discussed in Section 4.14, and those for fault detection.

5.13 Tolerance to speed sensor faults

5.13.1 Incorporating the speed sensor into a state-space FDI scheme

So far two types of sensors have been introduced, voltage sensors which measure the inputs and the current sensors which measure the outputs of the plant, see Section 5.4. The speed sensor is of a third type since it is supplying measurements of the bilinear input, ω_r in the model given by Eq. 3.4, see Section 3.2.5. To make a fault detection observer for the speed sensor would require an observer which is independent of the sensor. It is possible to design feedback for an observer which is independent of speed, as discussed in Section 4.5. However, the observer itself is dependent on speed since there are still speed terms in the model. The following sections discuss several methods for handling of speed sensor fault .

5.13.2 Detecting faults in the speed measurements

Since the speed measurement should change relatively slowly it could be threshold detected for disconnections, or statistical techniques used to detect intermittent disconnections. As mentioned in Section 5.1 the speed sensor is subject to two specific types of faults, missing teeth and eccentricity. To detect these faults. frequency domain techniques (spectral analysis) can be considered. Whilst setting up the test-rig, described in Chapter 6, the speed sensor was damaged, this provided an opportunity to observe the effect of this in both the time and frequency domains. The opto-wheel had been accidentally bent whilst fitting it to the motor shaft. Fig. 5.36 shows both the time domain signal and spectral content of the resulting speed measurement, with the motor driven at 30Hz, giving a motor speed of $89 rads^{-1}$. To evaluate the effect of missing teeth the damaged disk was straightened and then 8 of the 512 slots were covered with masking tape, Fig. 5.37 shows the results of doing this.

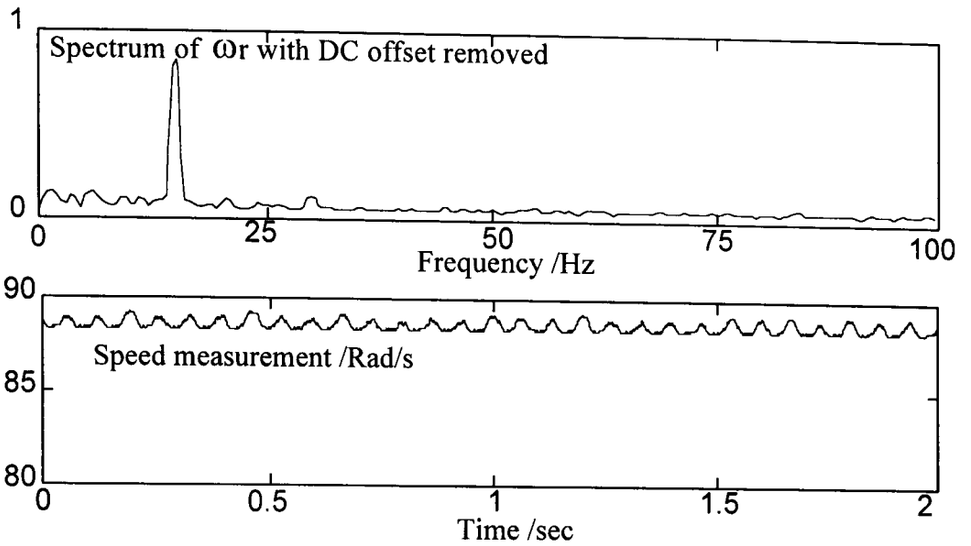

Figure 5.36. Spectral components of speed measurements with opto-wheel 'bent'.

The bent disk gives a predominantly sinusoidal disturbance around the correct speed. The total count per revolution is unchanged and therefore the 'mean' of this signal will be the correct value. The exact spectrum of the speed measurement is dependent on the physical nature of the distortion of the disk and the effect of the spacing of the slots.

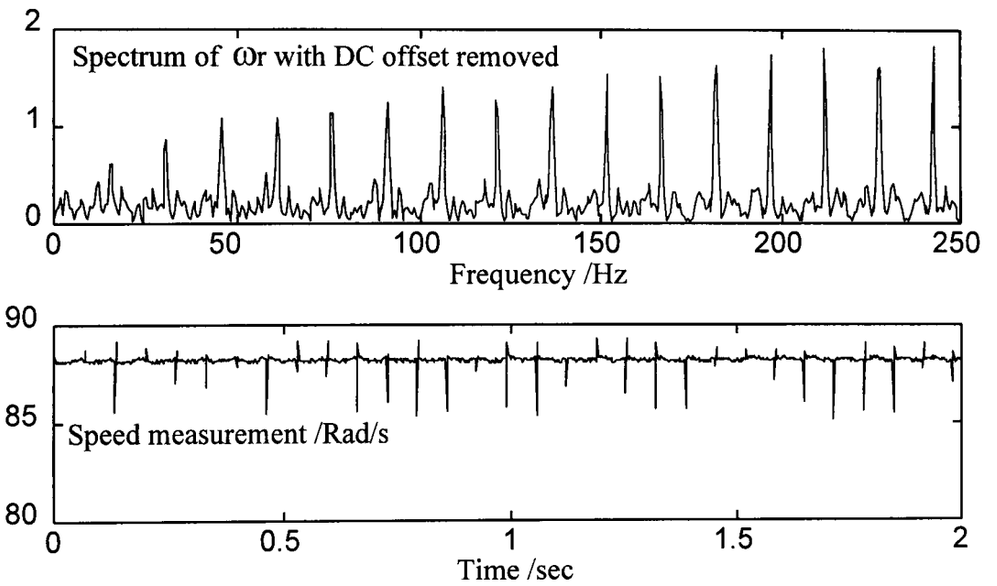

Figure 5.37. Spectral components of speed measurements with ten slots on opto-wheel covered.

With missing slots, the measured speed stays at the correct value with drop-outs only when the missing slots pass through the detector. The measurement can be corrected by considering a window of samples and ignoring any samples which significantly deviates from the mean. The spectrum of this has a high harmonic content and hence the two types of faults can be distinguished.

5.13.3 Hardware redundancy

On the traction system, redundant speed sensors are available. It is necessary here to describe the layout of the EMU's traction equipment in slightly more detail than that given previously in Section 2.1. For a typical four carriage EMU two carriages will be powered. Each of these has two bogies and each with two motors and powered axles. The two motors on each bogie are powered from the same inverter. Under good adhesion conditions the two motors are mechanically locked together by the rails and their speeds will be the same. Each motor has its own speed sensor which gives some hardware redundancy to handle errors. At present the highest reading is used as the measurement, because the nature of the sensors is such that most common faults give low readings. This gives no protection against two sensors reading low or one spinning due to dirty wheels or inefficient braking. It is therefore useful to consider how the speed sensor fault can be detected. The GOS method for voltage and current sensors can be extended to include the speed sensor, by using different speed sensors for different observers.

5.13.4 Estimation of speed

To incorporate fault detection of the speed sensor with only one sensor available it is necessary to consider ways to estimate the speed measurement.

Open-loop estimators. Several papers detail the design of speed estimators, the basic principle is given by Sathiakumar *et al* (1996). This is based on the open-loop estimator equations described in Section 4.2. By using the voltage model to estimate the direct and quadrature components of flux it is then possible to substitute flux into the current model equation to obtain speed. This method is subject to problems arising from the pure integration term in the voltage model. Shirsavan & McCulloch (1996) rearranges the state-space motor equation to obtain speed as the solution of a quadratic equation of the motor states. Yoo & Ha (1996) presents a more complex method based on the estimation of flux, without pure integration by exploiting a novel polar co-ordinate frame. Zamora and Garcia-Cerrada (1996) considered the sensitivity of these estimator methods to changes in motor parameters and presents practical results from field tests.

Extended observers. Du & Shields (1993) considers an extended observers which is augmented to make the motor speed a state variable. The use of extended observers has already been discussed, they are computationally very intensive and convergence conditions for the induction motor case are not guaranteed, see Section 4.10 for discussion of this.

Frequency domain methods. Using the model in the two axes bilinear form, as described in Section 3.2 there are no harmonics of the motor speed present in the stator currents, only harmonics of the drive frequency. The physical construction of the rotor with the bars will give rise to an air-gap flux concentrated near to the bars, called the '*slotting effect*'. As the rotor rotates, the stator currents will have harmonics of the *slot frequency* from air-gap flux distribution induced onto them as a function of speed. These harmonics have a very low magnitude compared to the drive frequency and PWM harmonics. Brudny & Rogers (1995) describes a method of isolating the motor speed from the measured current only. The required frequency is extracted with a phase-locked loop but very high measurement resolution is needed. Ferrah *et al* (1993) considers the use of an additional sensor to obtain a better measure of the slot frequency. This method is based on incorporating a measurement from an axial flux leakage sensor, which is a coil mounted concentrically on the motor shaft, with an improved method of obtaining the frequency spectrum, rather than the discrete Fourier transform, to obtain the slot frequency. These methods require relatively high resolution measurements and are computationally intensive.

5.13.5 Using the estimate of speed

On detecting a fault in the speed sensor the estimates of torque and flux can be switched to those from an open-loop estimator. The controller bandwidth would need to be reduced to attenuate any undesirable transient dynamics. In this way the system could continue to operate with reduced performance until maintenance can be arranged. The various methods of sensor fault tolerance can be combined into a single scheme which when subjected to faults progressively degrades the control performance, whilst making the best use of available measurements.

5.14 Sensor fault tolerance in the traction system

The traction system function is not defined as safety-critical, although safe operation is essential because of the potential hazards of the high power and voltages. The scheme shown, in Fig. 5.38, would make use of the available redundancy in the traction system's instrumentation. For current or voltage sensors analytical redundancy can be used to estimate the motor torque and flux in the presence of faults. For speed sensors, hardware redundancy can be used initially. A fault in the second sensor would be handled by estimating the speed, to handle the poorer quality of the estimate the controller bandwidth would have to be reduced.

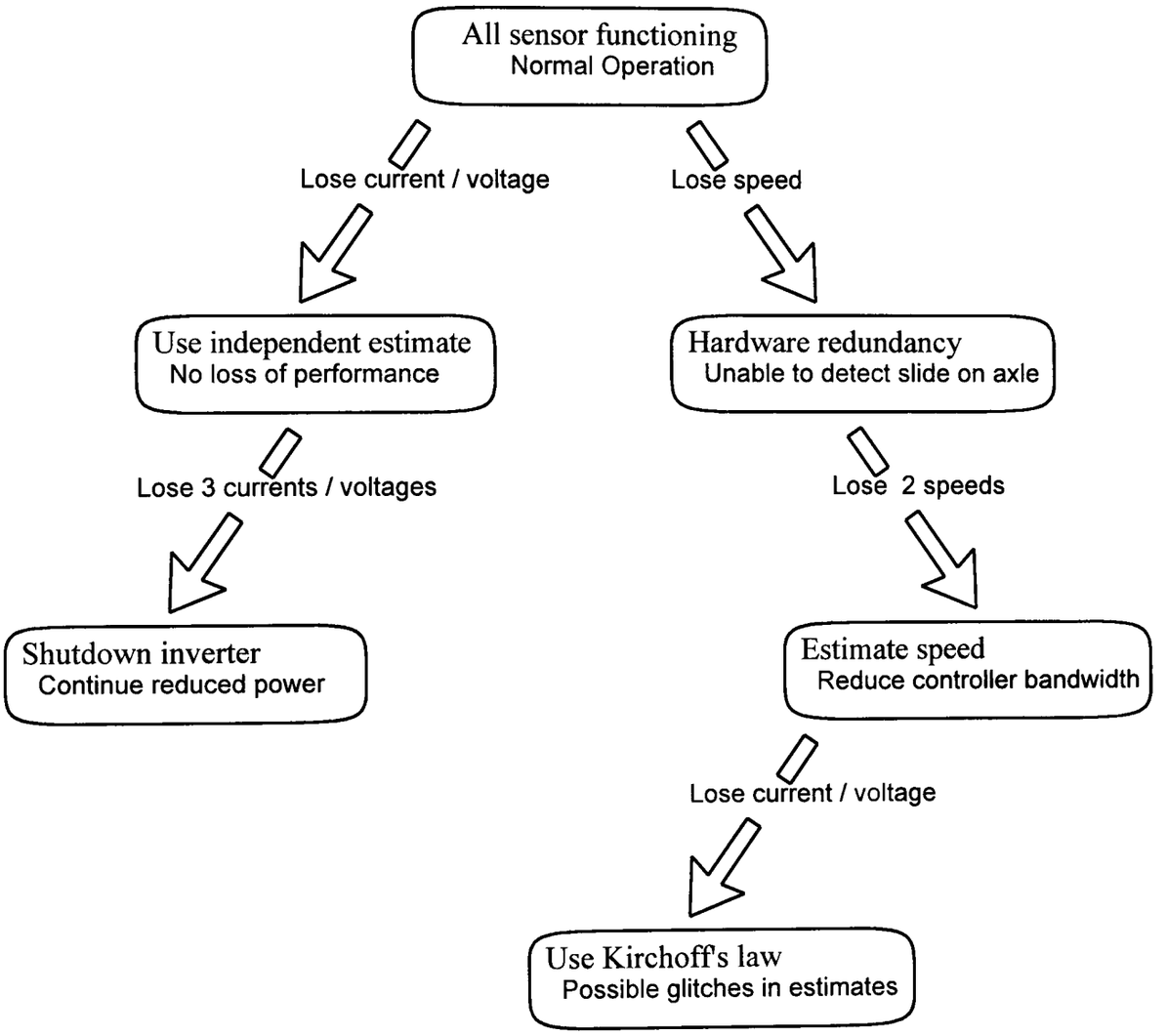

Figure 5.38. Fault tree for sensor faults, with progressive degradation of control systems

5.15 Summary

This chapter focuses on sensor disconnections which whilst abrupt, and hence should be easy to detect, can be very brief in duration or intermittent. Initially simple parity equation methods are detailed. These have significant limitations when faced with intermittent faults. Model-based methods are a much reported technique for sensor fault detection and isolation. Since observers have been proposed as a means of improving the estimation of control variables the use of a observer based fault detection scheme is a logical progression.

Firstly methods based on the dedicated observer scheme (DOS), are considered. These use a bank of observers each with feedback from a single sensor to make isolation simple when a fault occurs. The current and voltage sensors are shown to be different types of sensors in the classical state-space fault model, different methods have to be used for the two types. These methods have the limitation that they assume the other type of sensor to be fault free.

Using Kirchoff's laws a current or voltage sensor output can be estimated from the other two of that type. This enables an observer to be made independent of two sensors to produce a generalised observer scheme, (GOS). This consists of a bank of observers, each of which uses a different subset of the available sensors.

The capacities and relative merits of the approaches are compared along with some possible hybrid schemes. From the methods covered in this chapter several possible application areas are covered.

The GOS method is best suited to general applications, where single sensor fault-tolerance is needed.

The DOS method has greater capacity for detecting multiple sensor faults but is more sensitivity to noise. A possible application for the DOS method is to reduce the number of sensors on a low-cost low-performance drive.

The reconfigurable observer method is computational complex but offers the greatest scope for reconfiguration. It's application area would be for systems where maintenance is not possible and the need to maintain some level of functionality exists.

This chapter shows how residual sensitivity can be analysed and combined with the observer sensitivity results from Chapter 4 to make comparisons between methods under more realistic conditions.

Attention then shifts to the speed sensor which is shown to be of a third type since it supplies a measure of the bilinear terms in the model. The chapter ends by discussing how the speed sensor can be incorporated into the generalised observer scheme or how a progressive degrading scheme could make use of an estimate of speed.

Chapter 6:

Building a hardware test-rig

This chapter outlines the setting up of a hardware demonstrator to go beyond simulation to explore the practical implementation of the model-based techniques. The choice of hardware has been limited, but the use of a powerful DSP card and real-time workshop for Matlab has enabled the setting up with minimal effort on the software side.

The main body of this chapter concentrates of two aspects, building the additional electronics and identifying the model parameters for the motor. The power electronics for the inverter and the instrumentation have to be designed and built. This must fully exploit the capabilities of the available DSP card and overcome the limitations of it. Secondly the motor model must be identified and validated.

6.1 Demonstrating model based fault detection techniques

So far the sensor fault-tolerant observer techniques developed in Chapter 5 have only been demonstrated in simulation. However, there are various factors which mean that whilst something may be possible in simulation it cannot be achieved in practice. For example noise on measurements, uncertainty in model parameters, finite computing power and sampling.

Implementation of the techniques developed in this study of the traction system is not immediately possible, firstly due to lack of resources and secondly due to the safety aspect of the high power systems. An important intermediate step was considered to be the design and construction of a small scale hardware test-rig. It was first necessary to generate sufficient interest to secure funding for this stage of the project.

Model-based techniques are not new but they have not been readily taken up by industry. A possible reason for this is that much of the work has focused on the limitations of such techniques, namely the reliance on the model. Consequently, a lot of theory has been developed to tackle this, see Section 5.4 for further discussion, most of which is mathematically very complex. Industry is reluctant to take the more complex methods onboard without a demonstration of the basic concepts.

To explain model-based FDI several presentations were given with results presented in the form of graphs as in Fig. 5.15. The major problem with this format of presentation is the time it takes to assimilate what these graphs represent, how the signals shown were generated and the basic theory of the underlying method. To overcome this problem a 'live' demonstration was developed in the form of a graphical front-end to the Simulink simulation. This consisted of a schematic diagram of the inverter output and motor showing the sensor locations, a block diagram of the FDI method, residual traces and the switching to select the best set of estimates. The graphics where produced using the Matlab *handle graphics* features. A typical screen shot is shown in Fig. 6.1. After using this demonstration several times in presentations, the response from industry became more positive. Limited resources were then made available to build a hardware prototype. This shows the importance of exploiting modern computer tools to produce interactive demonstrations for both teaching and demonstrating academic work.

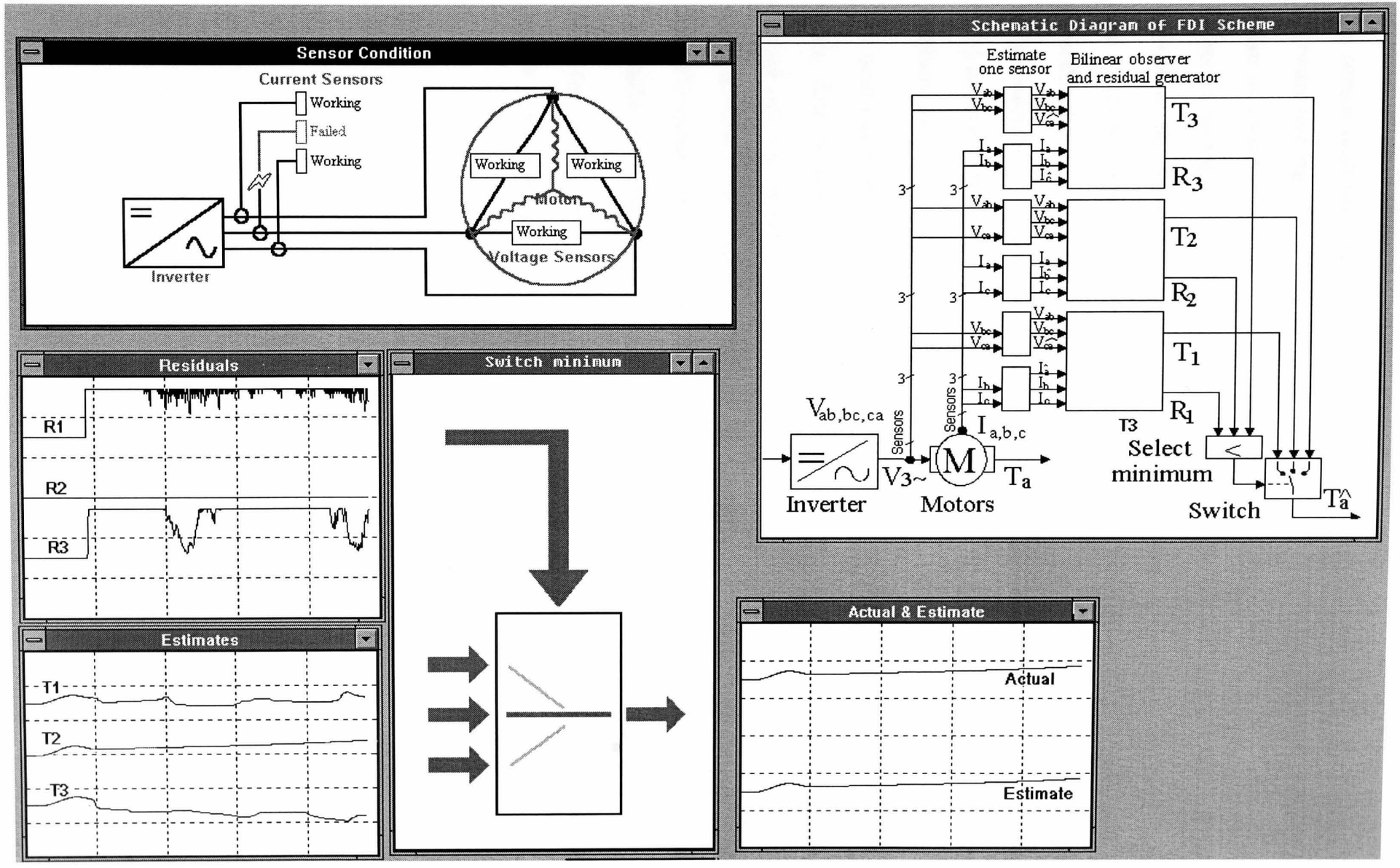

Figure 6.1. Screen-shot showing demonstration program.

6.2 The hardware

The sensor fault-tolerant algorithm is run in real-time using measurements taken from a hardware test-rig. The test-rig consists of a three phase AC induction motor driving a DC motor as a load. The 3 phase voltages are supplied from a PWM inverter. The first major choice in setting up the test-rig is that of the required scale. By using a low power motor the rest of the design is simplified and the cost keep to a minimum. The motor selected was a 0.2kW 3 phase 4 pole induction motor manufactured by ABB Motors Ltd. This is considered to be very small for 3phase induction motors. It is not practical to use a motor of the same level of power rating as the real traction motor, such motors are typically rated at several hundreds of kilowatts. With this in mind it seemed logical to choose the smallest possible motor.

The next major decision was the choice of the computing hardware. This has three main tasks, data acquisition, running the algorithm and output of results. These must be carried out within the limited time between samples. A DSP kit and Matlab real-time toolbox were made available for use. These contained a DSP and support hardware on an IBM-PC expansion card, made by the German firm D-Space GmbH with software tools compatible with Matlab.

With the motor and computer chosen this finalised much of the overall design. The outline of the test-rig is shown in Fig. 6.2.

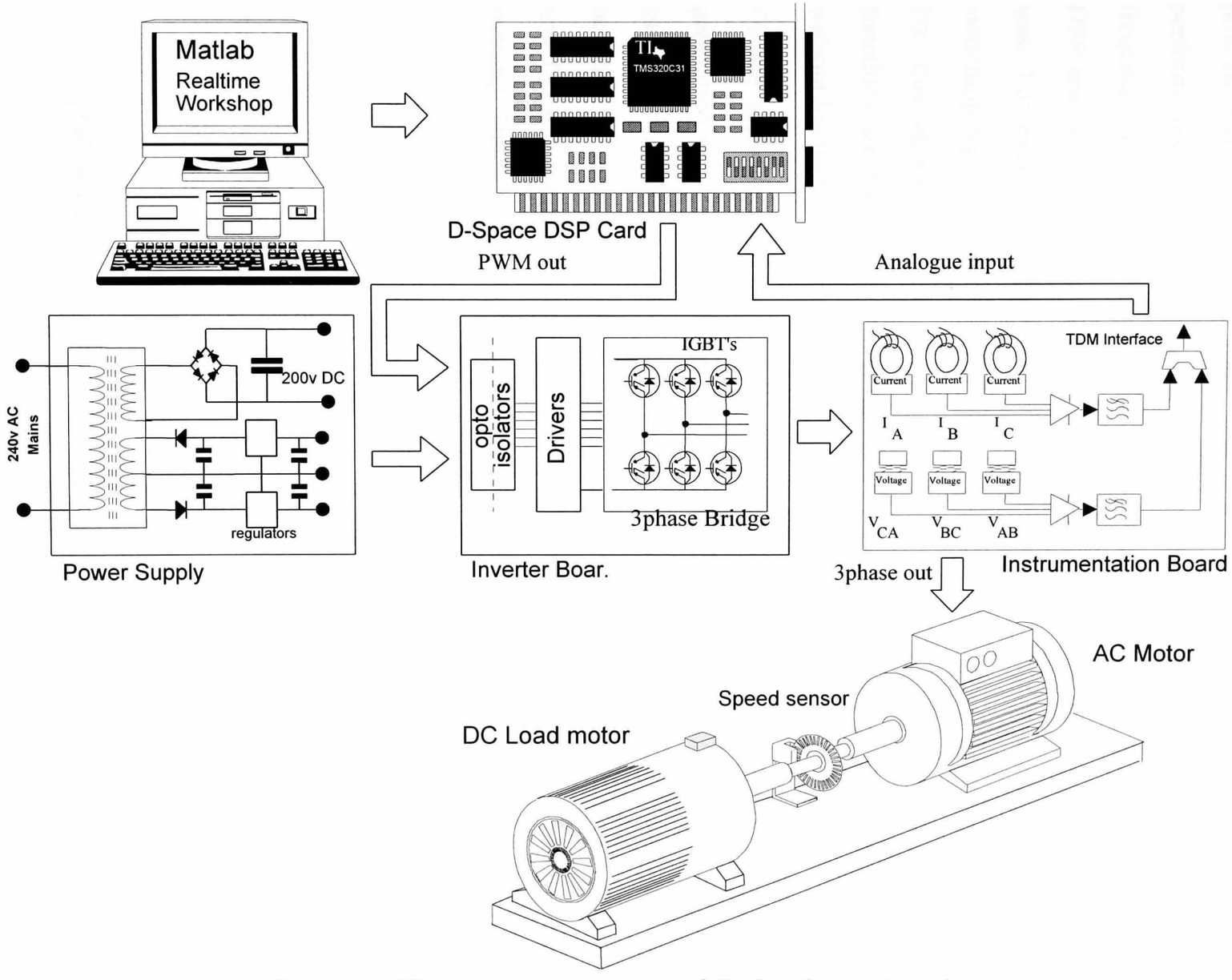

Figure 6.2. The major components of the hardware test-rig

6.2.1 The D-Space Real-time Toolbox and DS1102 DSP development board

The DSP hardware consisted of a Texas Instrument TMS320C31 single precision floating point DSP on an IBM-PC expansion card with additional onboard hardware. This provides four analogue inputs and four analogue outputs, a 16 bit digital IO port plus an auxiliary DSP. This 'slave' DSP is a TMS320P14, which can be programmed to perform 'intelligent' IO functions such as PWM generation, position encoding and frequency measurement or synthesis. It operates at a clock rate independent of the main DSP and so can implement functions rapidly without placing an overhead on the main task. For example, a 100Hz motor control loop can run on the main DSP with the switching signals for a 10kHz PWM being produced independently by the slave DSP. For this application, the PWM generation waveforms and opto-encoder decoding functions are handled by the slave which significantly reduces the external hardware without loading the main task.

On the software side, the *Real-time Toolbox* provides two levels of code generation, generation of C language code from a Simulink block diagram and then compiling to assembler and linking the object files with a real-time core and IO handling routines before downloading onto the DSP. The toolbox also provides two programs called *Trace* and *Cockpit* which enable data to be read from and passed to the DSP whilst it is running. The toolbox functionality is shown in Fig. 6.3.

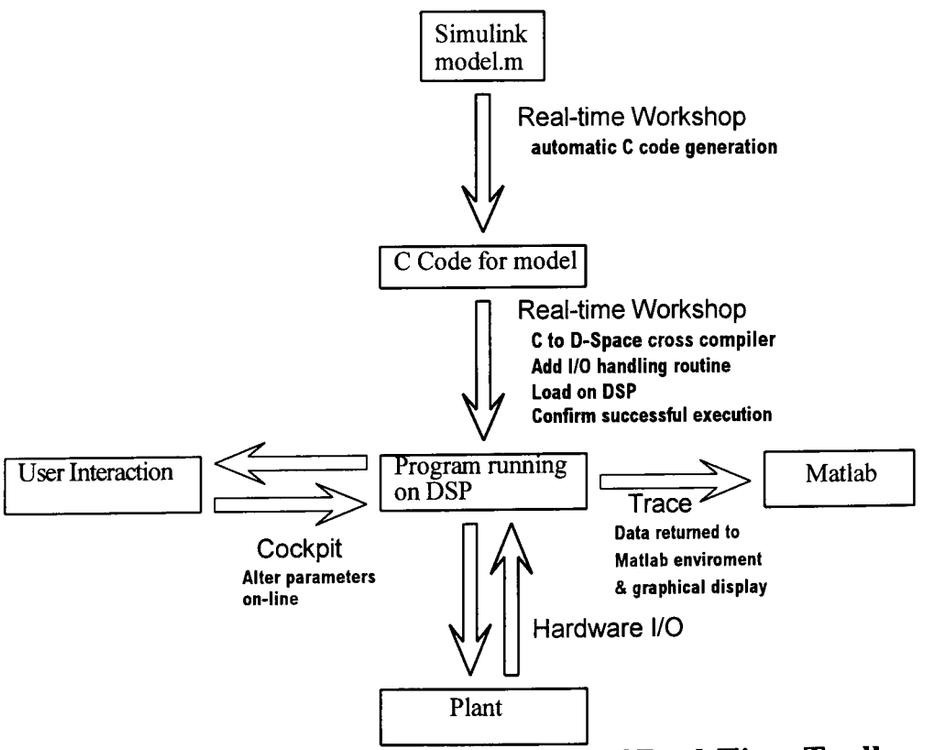

Figure 6.3. Diagram showing components of Real-Time Toolbox software.

6.2.2 The dedicated hardware

The 3 phase inverter. The inverter consists of some decoding logic, the switches, the necessary drivers and the protection circuits. The basic inverter layout is shown in Fig. 6.4, a schematic circuit diagram is included in appendix H. The switching devices on the traction inverter must be able to handle switching currents in excess of 1kA and block voltages greater than 1kV. But for the low power required for the test-rig three types of switching device are available: power MOSFETs, GTOs and IGBTs[6.1]. The latter were chosen since they most closely approximate ideal switches, as the gate drive is easy to operate and they offer the fastest switching rate.

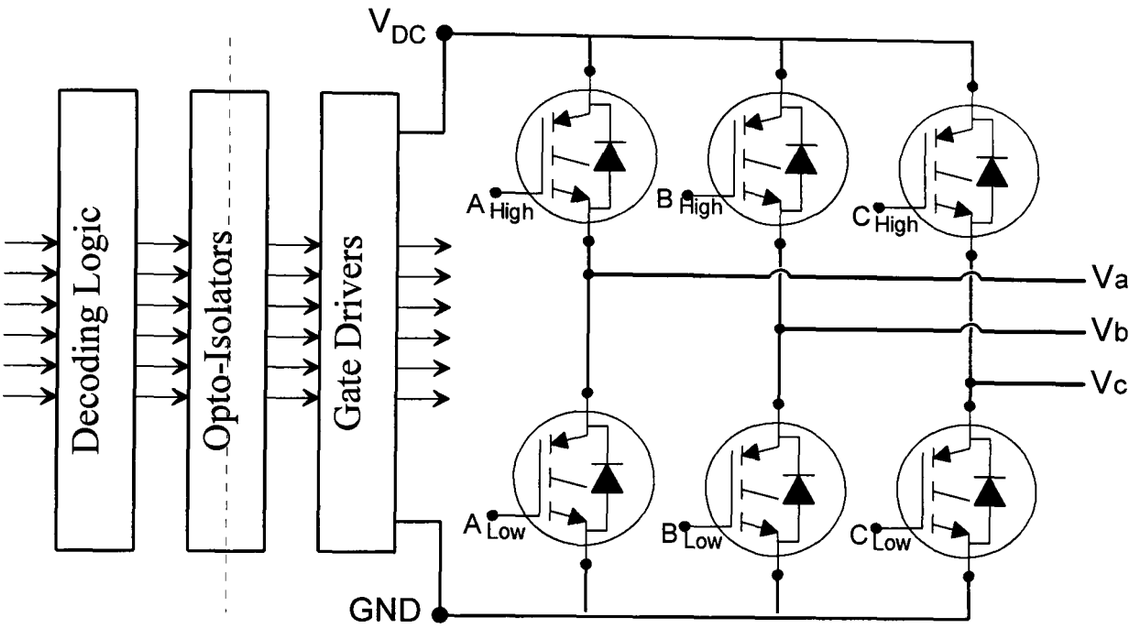

Figure 6.4. Block diagram of inverter components.

The devices can be turned on with a 15volt gate voltage and turned off when the voltage is returned to zero. For the high-side IGBT this must be floating, since the gate will switch between the two rails. IGBT's have a considerably faster *switch on time* than *switch off time*. In order to prevent both low and high side devices being in conduction simultaneously it is necessary to insert a guard-time between switching one off and the other on. The three IGBT bridges can be controlled by a single chip, the IR3031, which provides the floating voltages from a single grounded supply and inserts the guard-time. It also provides over-current and under-voltage protection and prevents simultaneous conduction state for series IGBTs, see IR Application note 985B. Opto-isolators are used between the DSP outputs and the inverter inputs for safety.

[6.1] When this project was started the most advanced ultra-high power semiconductors available were GTO's. This limited the switching frequency to 300Hz. Presently IGBT's can obtain the same level of power switching and are used on locomotive drives at switching frequencies upto 2000Hz.

As the IGBTs switch extremely fast, very large current transients are generated in the leads around the devices. Even the small inductance of the wiring around the devices is sufficient to give significant voltage transients. A snubber is needed to limit the voltage swing across the device and to dissipate some of the energy contained in the transient. This consists of a low inductance capacitor and a resistor across each IGBT pair in the bridge as shown in Fig. 6.5. The design of the snubber was fine-tuned from observations[6.2]. The switching transient is still the most significant source of noise effecting the instrumentation, see Section 8.1 for discussion of the effect of this.

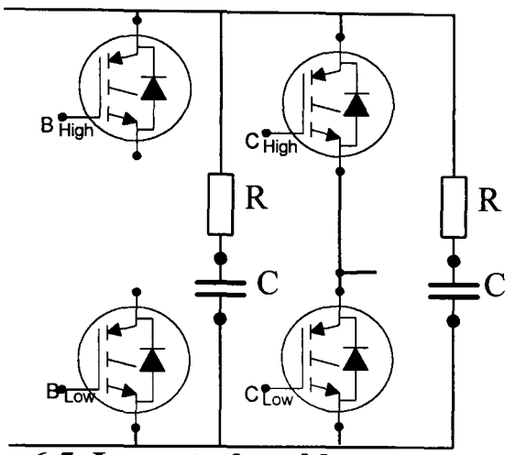

Figure 6.5. Layout of snubber components.

Instrumentation. The current and voltage sensors are both based on Hall effect devices. These are expensive and represent the largest single hardware cost. However, these sensors reflect the hardware of the full scale application and provide electrical isolation for the DSP. Their outputs are anti-alias filtered and sampled. Because only four analogue inputs are provided on the DSP card the six measurements are *time division multiplexed* (TDM) using some additional timing logic. This is possible since there are no filters on the DSP card before the ADCs. This technique is limited by the settling time of the analogue switches used, however it has been demonstrated successfully at frequencies of up to 10kHz with the hardware used.

The speed sensor is a 2 phase opto-encoder wheel. Its outputs are fed directly into the DSP card and decoded in software. The slave DSP counts the incoming pulses which is then differentiated, using the backward difference numerical method, to give speed.

The complete schematic diagram of the hardware is shown in Appendix J and photographs of the hardware in Appendix K.

[6.2] By experiment with the snubber, a voltage transient of 50volts rise in less than 2nS on the supply rail was damped to 20volts in 20nS

The Slave DSP produces *pulse position modulation* (PPM) rather than *pulse width modulation*. Using two PPM channels the required PWM can be generated as shown in Fig. 6.6. The signal is inverted for the other IBGT in the pair.

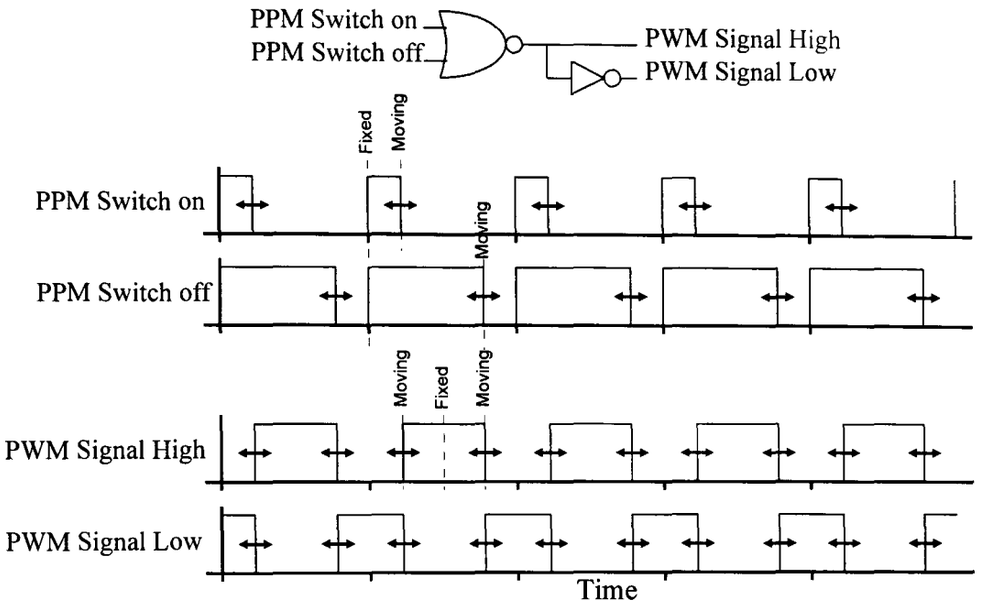

Figure 6.6. Diagram showing conversion between pulse position modulation and pulse width modulation.

6.2.3 Software

Apart from the algorithm, described in Section 7.2, the software must generate the inverter control signals and split the TDM sensor data back into two separate channels. The top level Simulink block diagram of the basic software is shown in Fig. 6.7.

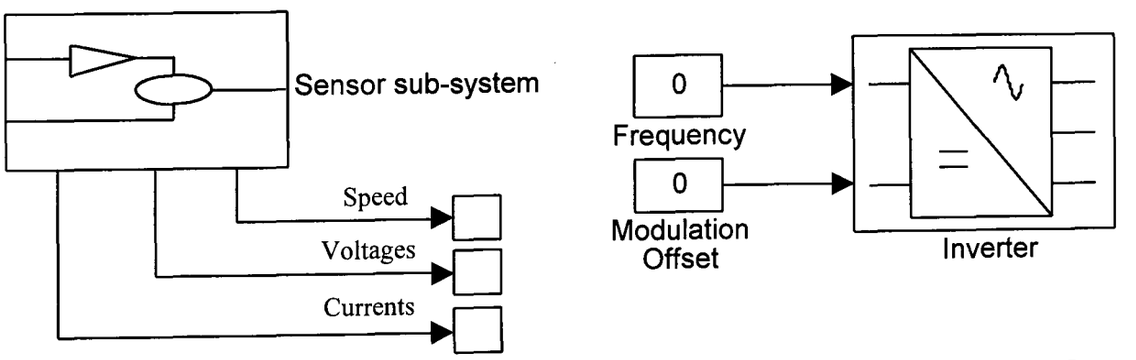

Figure 6.7. Simulink block diagram showing top level of software, with the sensor and inverter subsystem.

Within the inverter subsystem the reference sinewaves of the demand frequency and amplitude are generated, as described in Section 3.3.3. From these the two separate PPM signals are produced and fed to the slave DSP. For the instrumentation the timing signals for the TDM interface must be generated and fed out. The incoming TDM signals from the ADC must be separated back into the two channels and latched. For both of these functions the complete Simulink block diagram is included in Appendix L.

6.3 *Parameter identification*

Traditionally this has been done using the locked-rotor and no-load tests, Say (1963). This involves large currents and potentially damaging step changes in torque, the accuracy of the model can be poor since the test conditions generate large flux densities. Though time consuming stand-still frequency response test are currently regularly used, Willis *et al* (1989). More recently boardband excitation methods have been developed, these are computationally demanding and can be used whilst the motor is running normally, Beilharz & Filbert (1997). A simpler method can be developed by considering the electrical equation in one phase.

Rasmussen *et al* (1996) have extended a technique suggested by Schierling (1988) based on exciting a single phase of the motor only. This requires no special reconfiguration when used with modern three phase inverters. Rasmussen used a star connected motor whilst the induction motor on the test-rig has been connected in delta configuration, this means the method must be altered slightly to take account of this. The applied voltages on phases B and C are driven with the same voltage, which effectively shorts out one winding. For positive voltages B and C are grounded with the demand applied to A. For negative voltages A is grounded and the demand applied to B and C. The connection is shown in Fig. 6.8, note that the impedances identified will be halved since two windings are in the parallel. In this configuration the motor does not generate torque which eliminates the problems of potentially harmful abrupt torque changes. The motor is modelled in the rotor flux oriented reference frame, the rotor self-inductance has been referred back to the stator side. Parameters in this new model are denoted by an apostrophe, for example the rotor resistance in the new frame is written as R_r'.

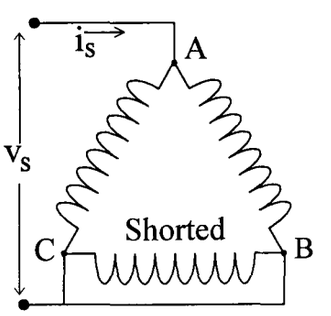

Figure 6.8. Voltages applied to three motor phases to give no torque.

This method consists of three tests; steady-state, a high frequency excitation and a step test. For these tests a simple PI controller, shown in Fig. 6.9, is needed to enable the fast control of the stator current required to impress the signals onto the motor. This is set-up on the DSP system and tuned using Ziegler-Nichols closed-loop method, Franklin *et al* (1995).

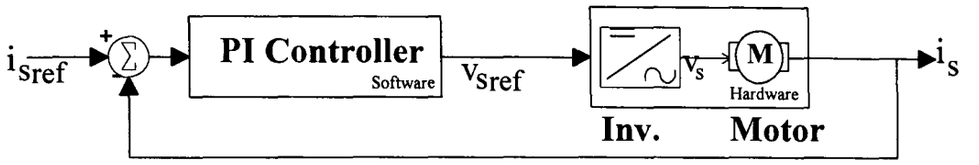

Figure 6.9. The fast PI current control loop.

Using only a proportional term, the gain is increased until the loop begins to oscillate. The gain at which this occurs is called the *ultimate gain*, K_u, and the period of the oscillation the *ultimate period*, T_u.

For the stator current PI controller, K_u=4.18 and T_u=0.0133s and from these the PI parameters can be found as:

$$K=0.45K_u = 2.16$$

$$T_i = T_u/1.2 = 0.011\text{s}$$

6.3.1 DC tests

This simply involves Ohm's law to obtain stator resistance from measured currents and voltages. However, a steady state gain for the inverter can also be found from the demanded voltages and actual voltages produced as a function of current. This represents a useful way to model the non-ideal characteristic of the inverter, caused by device resistance and guard-time, in steady-state operation.

The stator resistance is given by:

$$R_s = \frac{V_{measured}}{I_{measured}} \tag{6.1}$$

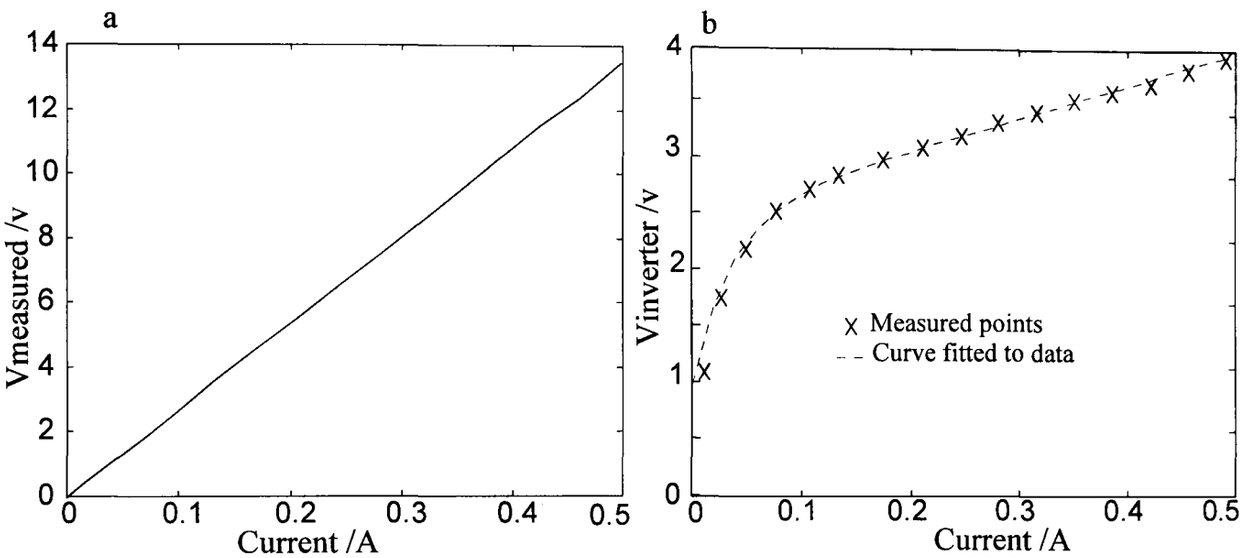

Figure 6.10 a. Plots of measured voltage against current to find resistance.
b. Plots of volt drop across inverter against current.

The inverter voltage drop as a function of current is given by:

$$f_{inv}(i) = V_{demand} - V_{measured} \tag{6.2}$$

The results are plotted in figure 6.10a.

For later use an empirical fit is made to this data to approximate the inverter function.

$$f_{inv}(i) = 2.4 - 1.4e^{-28i} + 2.8i \tag{6.3}$$

This represents an 'acceptable' fit to the data rather than prior knowledge of a model for the non-linearity.

6.3.2 High frequency test to find the referred stator inductance

The magnetising current has relatively slow dynamics. The aim of this test is to hold the magnetising current constant, whilst applying a high frequency squarewave onto the stator current to measure the much faster leakage inductance dynamics.

The TDM interface is not fast enough to enable the DSP to make the measurements necessary to perform these tests, so a digital storage scope is used instead. The controller is set to generate a DC current $i_{s\text{-}ref}$ which corresponds to the nominal magnetising current. For these test 300mA was used, this will be shown later to be too low. On top of this a fast square-wave is super-imposed, this is done by adding ±d to the $v_{s\text{-}ref}$ demand for the inverter, shown in Fig. 6.9. If the period (h) is too large then the magnetisation current cannot be assumed to remain constant. A suitable frequency for the square-wave has either to be found by experiment or from assumptions. The following equality for the selection the period is shown by Rasmussen *et al* (1996) to hold true:

$$h << L'_s(R_s + R'_r) \tag{6.4}$$

It is possible to make assumptions for the parameters to set h beforehand or to check this inequality afterwards and repeat where necessary. The period is initially taken as 250μS. The inverter switching frequency is increased to 12.5kHz to cope with the short periods required.

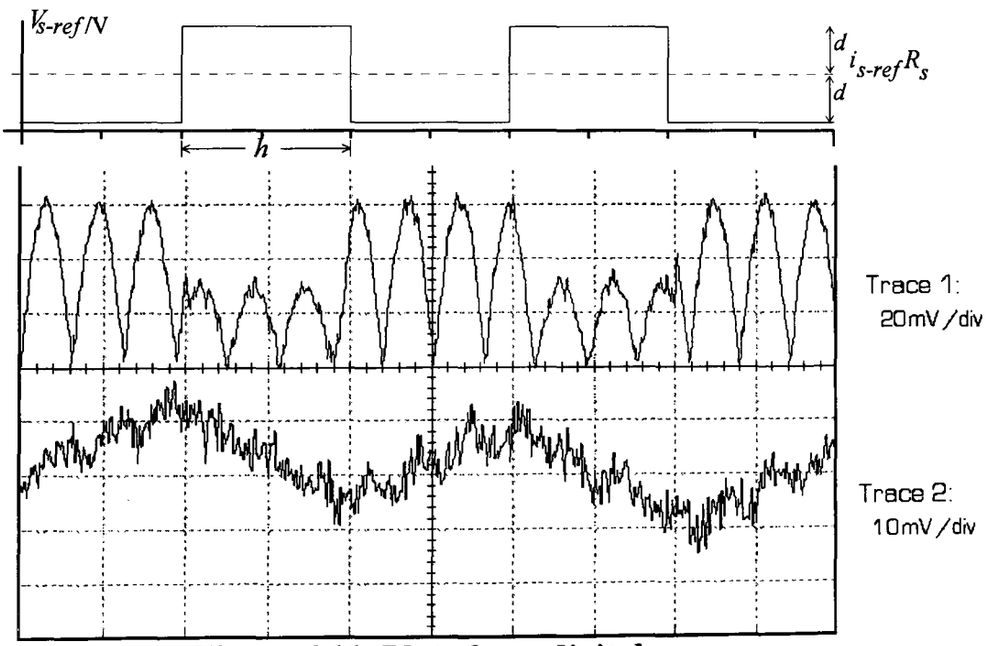

Figure 6.11. Plots from digital scope:
Trace 1: Measured voltage @ 15V per division.
Trace 2: Measured current @ 0.01A per division.
Top: Demand voltage that inverter is trying to create.

The square-wave has a relatively high frequency, typically only 3.5 cycles of the PWM waveforms, therefore the applied voltage does not appear to be smooth. The inverter voltage has been filtered by the anti-alaising filters before being fed into the digital scope. It is possible to average several traces or alternatively to use the demand voltage and compensate for the inverter with the inverter function found previously, Eq. 6.3.

$$v_{s-ref} = i_m R_s \pm d + f_{ss}(i_m). \tag{6.5}$$

For a detailed proof of the following see Rasmussen (1995).

With the magnetising current held constant the following equations hold.

$$L'_s \frac{di_s}{dt} = R_s i_s + R'_r(i_s + i_m) = v_{s-ref} - f_{ss}(i_s) \tag{6.6}$$

If d is small such that $f_{ss}(i_s)=fo$, the inverter drop is approximately constant, the solution to Eq. 6.6 in the interval $0<t<h$ with $h<<L'_s/(R_s+R'_r)$ is given as:

$$L'_s \approx \frac{hd}{\Delta i}$$

With $d=5v$, $h=250\mu S$ and the change in current is measured as Δi=21mA then:

$$L's=0.0595.$$

6.3.3 Low frequency test to find rotor time constant and resistance

For this test the stator current is stepped from plus i_m to minus i_m so that the dynamics associated with the magnetising current can be obtained. The resulting current and voltages are measured by the DSP and plotted in Fig. 6.12.

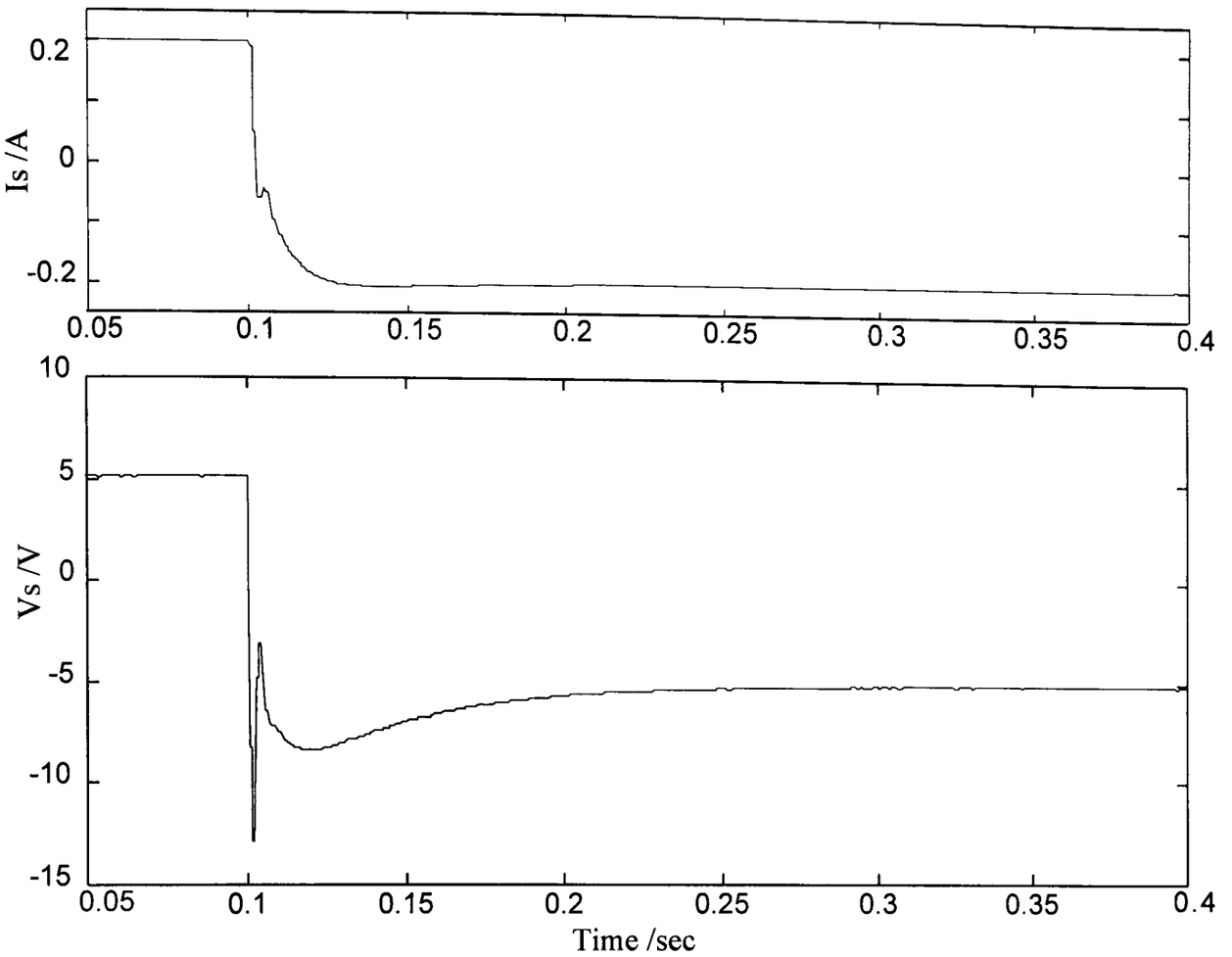

Figure 6.12. Graphs showing imposed stator current and applied voltage during a step change.

From the measured current it can be seen that the controller is unable to impress the desired current onto the stator, so this will be a source of error in the final result. The applied voltages contain three components, the very fast dynamics associated with the leakage inductances, the controller response and the slow dynamics of the mutual inductances. The latter is the required dynamic component.

The slow dynamics are given by the following equation:

$$u_s = \left(R_s + R'_r\left(1 - \frac{1}{1+T_r s}\right)\right) i_{s-ref} \tag{6.8}$$

Rasmussen uses a least-squares identification to find R'_r and Tr. However, this may also be found by inspection of the applied voltage. R'_r gives the amplitude of the transient with Tr the time constant.

The applied voltage is shown again in Fig. 6.13. The dotted line approximates the slow transient that is required. The Δv marked onto Fig. 6.13 is the amplitude, given by $R'_r I_s$ since $\frac{-1}{1+Tr s} \approx 0$ immediately after the switching instant. The time constant, Tr, is defined as the time to reach 63% of the original value.

Therefore $R'_r = \Delta v / Is = 15\Omega$ and $Tr = 0.023s$

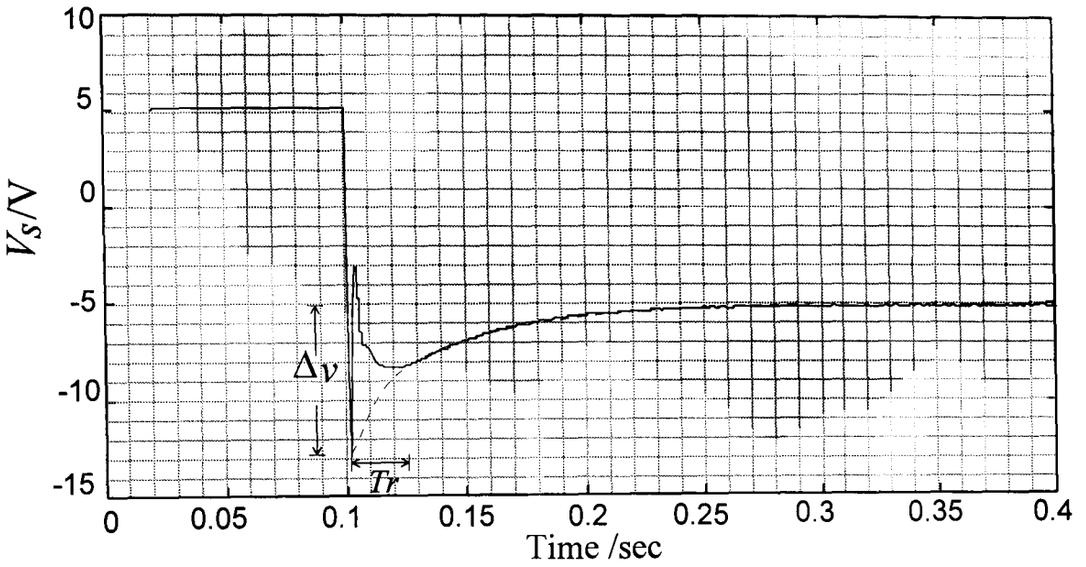

Figure 6.13. Plot of applied stator voltage against time.

The following parameters are now known: L'_s, R_s, R'_r and Tr. These are in the referred frame and must be converted into the correct form for the state space model

$$L'_m = R'_r Tr = 0.345$$

$$L_s = L'_m + L'_s = 0.4045\text{H}$$

$L_r = L_s$, assumed

$$L_m = \sqrt{1 - \frac{L'_s}{L_s}}\, L_s = 0.374\text{H}$$

$$R_r = \frac{L_s}{Tr} = 17.6\Omega$$

$R_s = 55\Omega$, as measured

Converting to a delta connection gives the following model parameters[6.3]; L_s=L_r=0.809, L_m=0.748, R_r=35.2 and R_s=55

[6.3] The manufacturer's data supplied later gave the follow values for the parameters: R_s=64, R_r=42 L_s=0.841, L_r=0.839 and L_m=0.7825, measured at 80C. Using the thermal co-efficient for resistivity for copper, 0.004C^{-1}, to compensate for temperature R_s=52, and R_r=34 at room temperature.

6.4 *State-space model of test rig induction motor*

The state space matrices are given below, Fig. 6.14 shows the loci of the poles with speed in the range 0 to 600rads^{-1}

$$A_{delta} = \begin{bmatrix} -468.5 & 0 & 275.6 & 0 \\ 0 & -468.5 & 0 & 275.6 \\ 433.1 & 0 & -298.1 & 0 \\ 0 & 433.1 & 0 & -298.1 \end{bmatrix}, \quad Nm_{delta} = \begin{bmatrix} 0 & 5.89 & 0 & 6.37 \\ -5.89 & 0 & -6.37 & 0 \\ 0 & -6.37 & 0 & -6.89 \\ 6.37 & 0 & 6.89 & 0 \end{bmatrix}$$

$$B_{delta} = \begin{bmatrix} 8.52 & 0 \\ 0 & 8.52 \\ -7.87 & 0 \\ 0 & -7.87 \end{bmatrix}$$

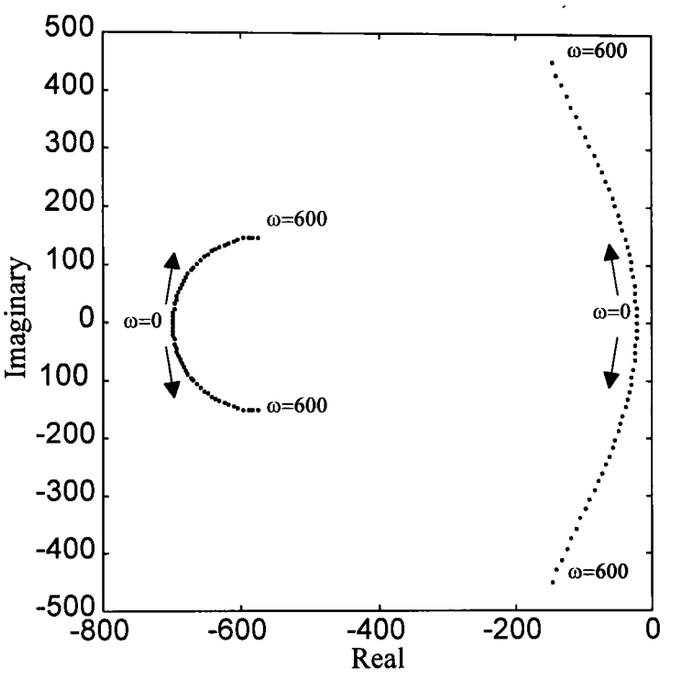

Figure 6.14. The loci of the test-rig induction motor poles with speed.

6.4.1 Validating the state space model

Since the parameters for the motor model were found with just a single axis excited, which does not correspond to a normal operating condition, it is important to validate the model against the motor under normal operating conditions. The model of the test-rig motor can be directly compared against the real motor whilst running. The model of the motor is set-up to run on the DSP using the measured voltages and the measured speed. The stator currents are then compared.

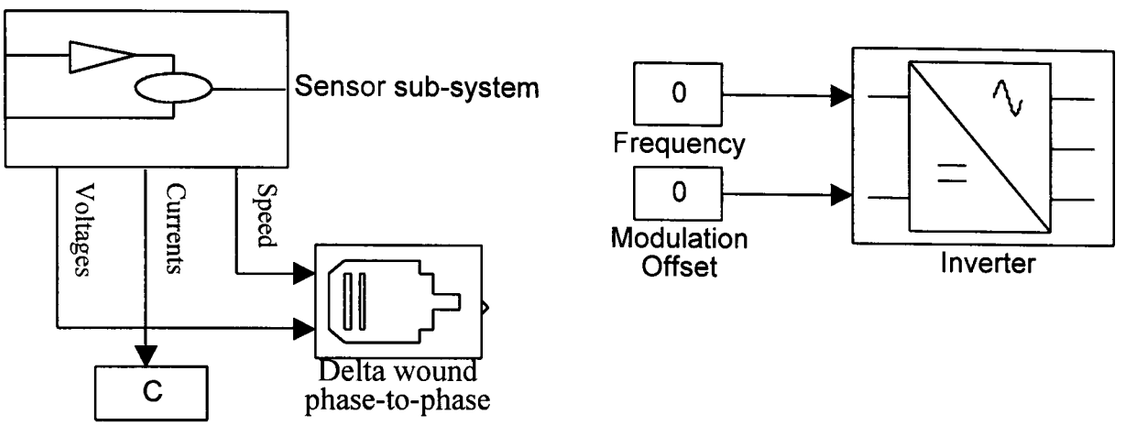

Figure 6.15. Simulink block diagram to run model in parallel with real motor.

Fig. 6.16 shows the results of a speed reversal test. The graphs show the drive voltage and the measured speed, the measured voltages which are applied to both the model and the motor, the model three phase currents and the measured currents.

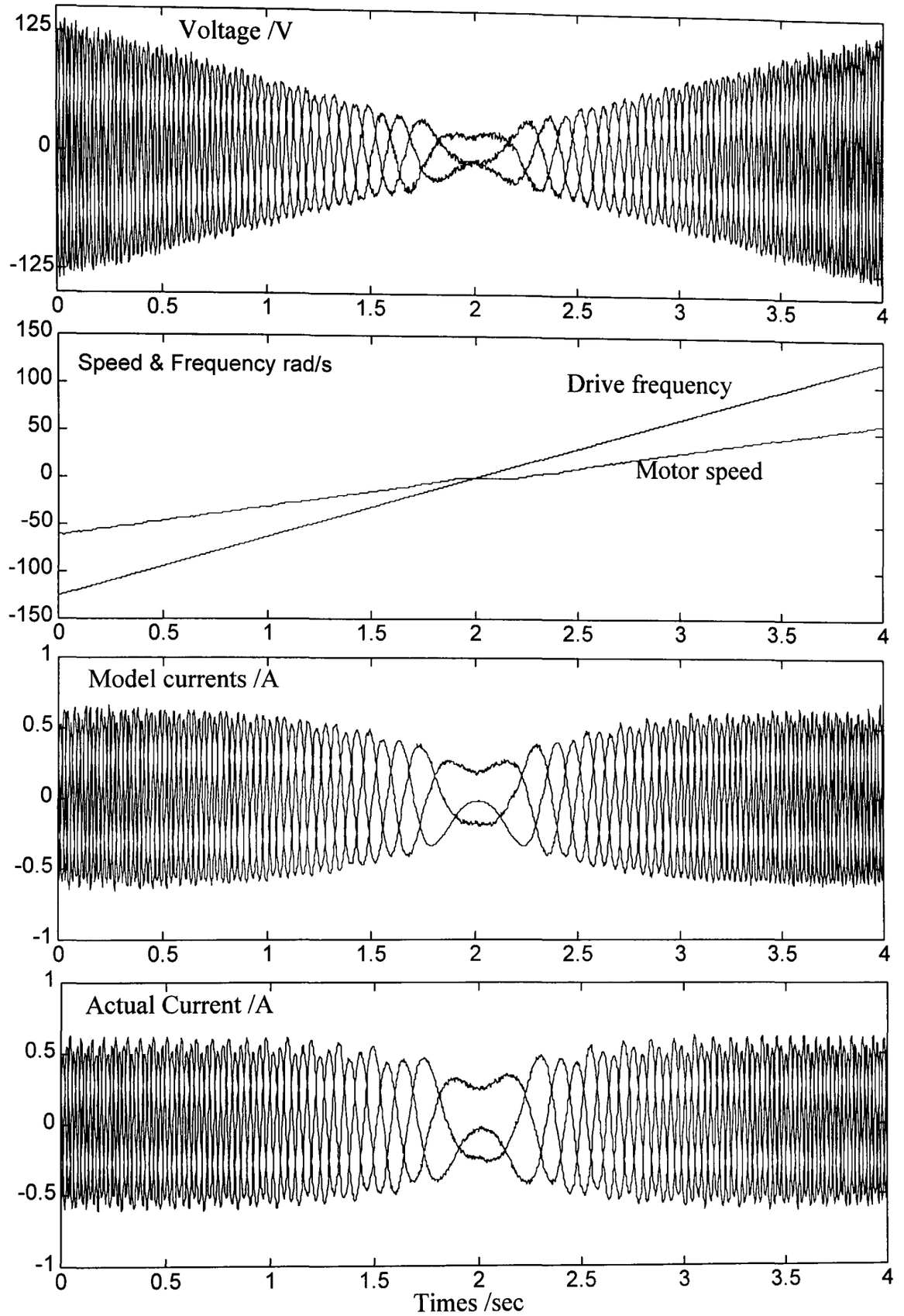

Figure 6.16. Plots from Trace during a speed reversal to validate the motor model.

The results from the model shows good agreement with the real system response, except at very low speeds, ($<5 rads^{-1}$). This is because of the offset of the volts-per-Hertz control causing the flux to increase significantly around zero.

6.5 *Assessment of DSP performance using a closed-loop observer*

The DSP has a 'raw' computing power of 40MFlops which makes it an extremely powerful processor. The code generated by the real-time workshop is not necessarily as efficient as hand written C code. The aim of this section is to confirm that the required algorithm is likely to be able to run at a suitable sampling rate.

A continuous-time observer is set up using the method of bilinear feedback developed in Section 4.7, with the assignable poles fixed at -50. This method is used because it is the simplest and most compact to implement. Fig. 6.17. shows a comparison between the measured current and the observer outputs for a range of speeds.

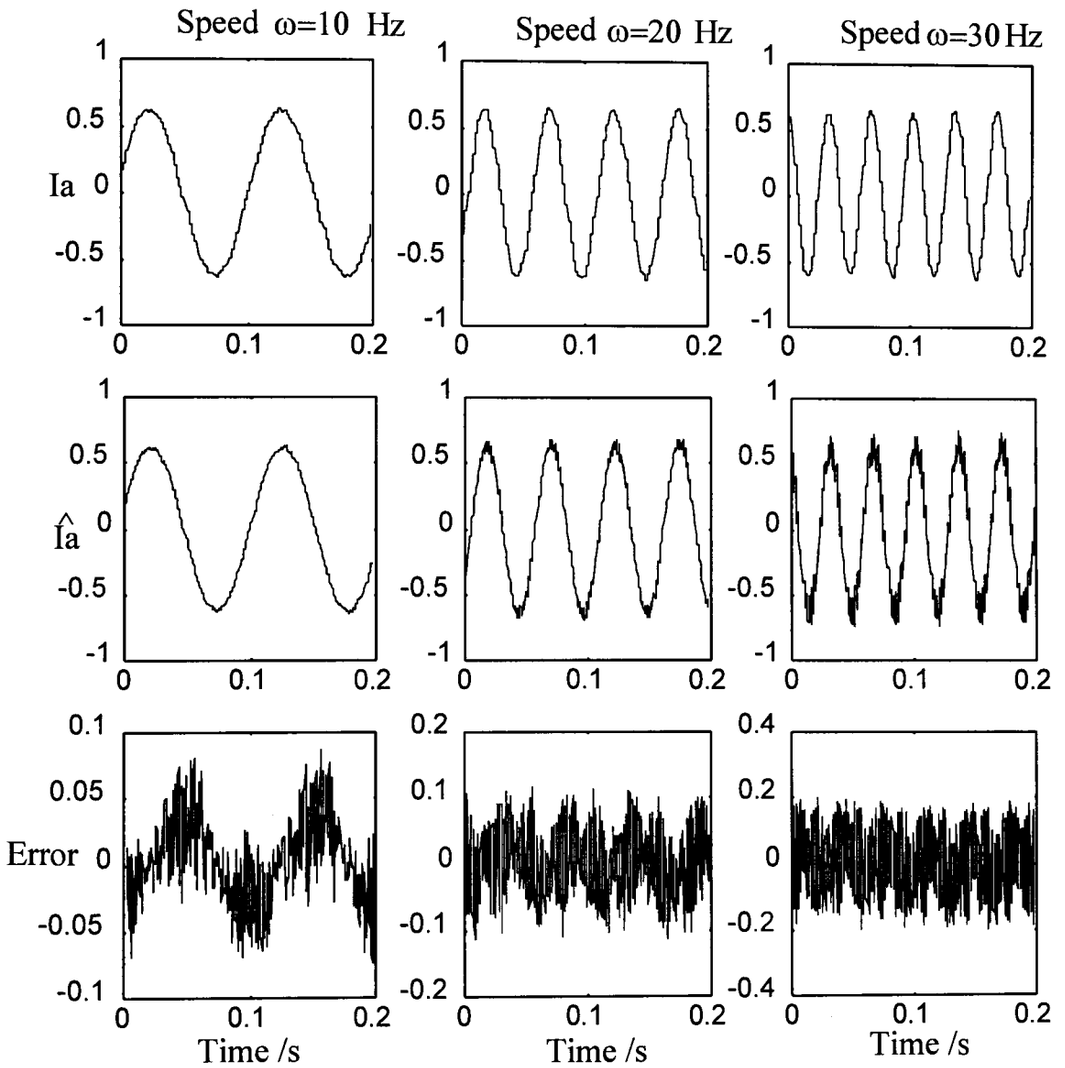

Figure 6.17. Plots of observer estimation errors for a range of speeds.

Note the high frequency component of the observer's error, in Fig. 6.17. This arises from the fact that the sensor data is only available at a quarter of the rate of the observer algorithm because of the TDM interface. With the real-time workshop it is not possible to make the integration routine's time step slower than the smallest sample time.

6.5.1 Running the DSP in multi-mode

Using a time step of 500μs gives sensor data every 2ms, the continuous-time observer with the sensor interface and inverter controller takes 400μS to run. For the complete FDI scheme three observers plus residual processing are needed. It is necessary to consider ways of speeding up the algorithm. By discretising the observer there are two possible speed improvements. Firstly a separate integration routine is no longer needed which reduces the number of operations needed to implement the observer. Secondly the DSP can be run in multi-rate mode. The D-Space software enables discrete blocks to run with different sampling rates, provided that these are integer multiples of the fastest sampling frequency. Fig. 6.18 shows the increase in DSP efficiency that will result in this case.

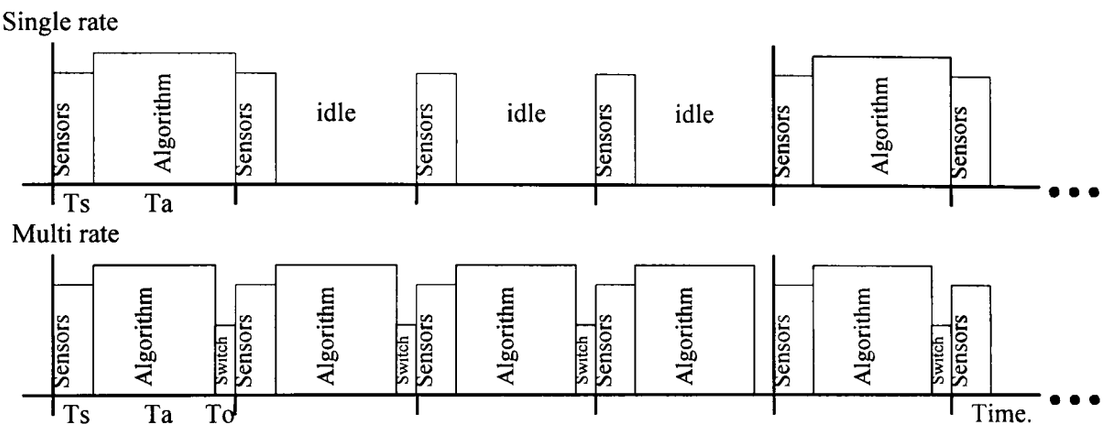

T_s = Time taken to read sensors and inverter function.

T_a = Time available to calculate algorithm.

T_o = Time taken to switch current task

Figure 6.18. Time allocation for different tasks in single and multi-rate mode.

If $T_a >> T_s$ and T_o is small then the DSP time available to the main FDI algorithm is increased by approximately a factor of four. Now it is possible to double the sampling rate and the algorithm would then still have twice the time it would in single-rate at the slower speed. However, if $T_s < T_a$ then the advantage of switching to multirate is not as great and any attempt to increase the sample rate will result in a large drop in the time available to the algorithm.

For the test-rig the overheads of the IO handling are 200μs therefore it is not possible to reduce the overall sample time much below 250μs without squeezing out the time available to the algorithm altogether.

6.6 Summary

This chapter discusses the importance of clearly demonstrating academic techniques. Initially, an interactive graphical demonstration for the simulation work is used to present the simulation results from Chapter 5. From this, limited extra funding and the use of a high performance DSP card was obtained to demonstrate the techniques in real-time on hardware.

It is not feasible for reasons of cost, safety and experience to work with anything even approaching the power of the actual traction system. Accepting this the test-rig is based around a 200W 3phase AC induction motor. For this power level the inverter design can be very simple.

For both ease of setting up and to limit the cost it is necessary to exploit fully the capacities of the available DSP card and work around its limitations. For the inverter the PWM switching signal can be generated by the slave DSP on the main card. This reduces the external electronics to just the power switches and the necessary drive electronics. The inverter is based on the use of discrete IGBTs since they closely approximate ideal switches and their gate circuit is easy to drive. The six IGBTs in the bridge can be controlled by a single chip, the IR3031, with the inputs opto-isolated between the DSP card and the driver for safety.

The current and voltage sensors are Hall effect devices. These are relatively expensive but provide isolation for safety and mimic the sensors on the real traction system. Because of the limited IO capacity of the DSP card the sensor measurements are time division multiplexed in pairs before being sampled. The speed sensor is an opto-encoder and shaft mounted disk. The slave DSP is used to count the pulses, which is differentiated to give speed.

The algorithm can be coded from the Simulink block diagrams with the minimum of programming using the autocode generator tool from the real-time toolbox for Matlab.

Once the hardware is built and the necessary software to read sensors and generate signals for the inverter is produced it is possible to use the test-rig to identify the model parameters. From the range of available techniques a simple single phase excitation

method is modified to suit the motor configuration and used to identify the motor parameters.

The identified model is set up and run in parallel with the real motor. The model is shown to give comparable currents to the real motor during a speed reversal. Two problems can be observed. Firstly, with the TDM interface the sensors measurements are made at a slower rate than the FDI algorithm. Secondly, the integration routine imposes a high computational load on the DSP. The use of a fully discrete-time implementation and multi-rate code on the DSP are suggested as a solution to these problems.

In general the hardware is shown to perform well, the model is sufficiently accurate and the DSP will have sufficient capacity to produce a real-time implementation of the FDI techniques.

Chapter 7:

Real-time DSP implementation of sensor FDI scheme.

The observer needs to be discretised. Several methods are compared for accuracy and complexity in simulation. The discrete-time model is validated against the real motor. The use of the parametrised feedback gain observer is adopted since it has been shown to be more sensitive to faults whilst being less sensitive to noise. The real effect of observer's pole locations are considered on the actual hardware.

The GOS FDI scheme is implemented in Simulink and downloaded to run in real-time on the DSP. The effect of speed and motor loading on the fault-free residuals is assessed and then the effect of sensor faults over a range of operating conditions.

All the design work so far has used a continuous-time model and observer which was then simulated in discrete-time using an integration routine such as Runge-Kutta. For a more efficient implementation on the DSP the observer design has to be discretised, as this will enable a faster sampling rate. Using an all discrete-time system on the DSP will also avoid the problems of the TDM interface causing the sensor data to be available at a rate slower than the algorithm, since the Real-time Toolbox software can run discrete-time blocks at multiple sampling rates.

7.1 Discretising the motor model

Consider the continuous-time system given by:

$$\begin{aligned} \dot{\underline{x}} &= A\underline{x} + B\underline{u} \\ \underline{y} &= C\underline{x} \end{aligned} \tag{7.1}$$

The continuous-time system, when discretised with a sampling period t_s can be represented as a difference equation given by Eq. 7.2, see Åström and Wittenmark (1884)

$$\begin{aligned} \underline{x}_{K+1} &= e^{At_s}\underline{x}_K + \int_0^{t_s} e^{As}ds B\underline{u}_K \\ \underline{y}_K &= C\underline{x}_k \end{aligned} \tag{7.2}$$

This is valid if it can be assumed that $\underline{u}$ is constant between t_K and t_{K+1}.

The matrix exponential can be expanded as a Talyor series:

$$e^{At_s} = I + At_s + \frac{A^2t_s^2}{2!} + \frac{A^3t_s^3}{3!} + \cdots \tag{7.3}$$

The integral can be expanded as a series:

$$\Psi = \int_0^{t_s} e^{As}ds = It_s + \frac{At_s^2}{2!} + \frac{A^2t_s^3}{3!} + \cdots \tag{7.4}$$

Which leads to the discrete-time system of the form:

$$\begin{aligned} \underline{x}_{K+1} &= (I + \Psi A)\underline{x}_K + \Psi B\underline{u}_K \\ \underline{y}_K &= C\underline{x}_K \end{aligned} \tag{7.5}$$

For a bilinear system, A is replaced by $A+N\omega$. The expansion is now a non-linear function of speed and requires that speed is also constant during the sampling time[7.1].

[7.1] Not unreasonable since the motor speed changes slowly relative to the sampling rate.

7.1.1 First order expansion method

Using only the first term in the expansion the discrete-time motor model becomes:

$$\begin{aligned} \underline{x}_{K+1} &= (I + (A + N\omega)t_s)\underline{x}_K + Bt_s\underline{u}_K \\ \underline{y}_K &= C\underline{x}_K \end{aligned} \tag{7.6}$$

This form is called the *first order exponential expansion.* By limiting the expansion to the first term the system remains bilinear. The first order method is also known as the *forward rectangular rule* which is represented by the transform $s \approx \frac{(z-1)}{t_s}$.

7.1.2 Higher order expansions

Taking the first two terms in the expansion of Ψ gives the second order method. The discrete-time system is no longer a bilinear system, the state dynamics are now quadratic functions of speed and the input matrix is time varying, as shown by Eq. 7.7

$$\underline{x}_{K+1}\left(I + (A + N\omega)t_s + \tfrac{1}{2}(A + N\omega)^2 t_s^2 \right)\underline{x}_K + \left(I + \tfrac{1}{2}(A + N\omega)t_s \right)B\underline{u}_K \tag{7.7}$$

State dynamics now a quadratic function of speed Input matrix function of speed.

The second order expansion is more accurate as it uses more terms in the expansion. This is demonstrated in the Section 7.1.4.

Ploix (1997) describes another method based on the partial expansion of Ψ. In the discrete system given by Eq. 7.5. the state space matrices can be decomposed into sub-matrices with a size 2×2. The system is then transformed to give two independent differential equations which can be discretised separately. The resulting 'partial exponential' expansion requires more calculations than its equivalent order 'total exponential' but is shown to give a better approximation than a higher order expansion.

7.1.3 Tustin's approximation method

The loci of the poles of the motor's dynamics shows the motor becoming increasingly oscillatory with speed, as shown in Fig. 3.6. This suggests that a more complex transform, such as Tustin's approximation $s \approx \frac{2(z-1)}{t_s(z+1)}$, which will map the pole locations more accurately may provide a better representation of the discrete-time system.

Consider the state-space system given by:-

$$\begin{aligned} \dot{\underline{x}} &= A\underline{x} + B\underline{u} \\ \underline{y} &= C\underline{x} \end{aligned} \tag{7.8}$$

The derivative $\dot{\underline{x}}$ can be rewritten as $s\underline{x}$ and the substitution $s \sim \frac{2(z-1)}{t_s(z+1)}$ made.

$$\frac{2(z-1)}{t_s(z+1)}\underline{x} = A\underline{x} + B\underline{u} \tag{7.9}$$

Rearrange and collect together terms into a difference equation:

$$\begin{aligned}(z-1)\underline{x} &= A\tfrac{t_s}{2}(z+1)\underline{x} + B\tfrac{t_s}{2}(z+1)\underline{u} \\ z\underline{x} - A\tfrac{t_s}{2}z\underline{x} &= A\tfrac{t_s}{2}\underline{x} + \underline{x} + B\tfrac{t_s}{2}(z+1)\_\end{aligned} \tag{7.10}$$

Rewritten as samples, $\underline{x}=\underline{x}_K$ and $z\underline{x}=\underline{x}_{K+1}$

$$\left(\mathrm{I} - A\tfrac{t_s}{2}\right)\underline{x}_{K+1} = \left(A\tfrac{t_s}{2} + \mathrm{I}\right)\underline{x}_K + B\tfrac{t_s}{2}\left(\underline{u}_{K+1} + \underline{u}_K\right) \tag{7.11}$$

This gives the final form:

$$\underline{x}_{K+1} = \left(\mathrm{I} - A\tfrac{t_s}{2}\right)^{-1}\left(A\tfrac{t_s}{2} + \mathrm{I}\right)\underline{x}_K + \left(\mathrm{I} - A\tfrac{t_s}{2}\right)^{-1} B\tfrac{t_s}{2}\left(\underline{u}_{K+1} + \underline{u}_K\right) \tag{7.12}$$

7.1.4 Computational load of the discrete model.

The calculation for Tustin's method requires a matrix inversion operation which is computationally intensive. Fig. 7.1 gives a table of the count of floating point operations for various mathematical operations in Matlab for two different matrix sizes. This matrix is a function of speed and needs to be re-calculated at each sample time. Alternatively this could be pre-calculated for a range of speeds and stored in a look-up table, although this is memory intensive. The use of complex vector notations, as described in Appendix B, would reduce this to the inversion of a 2×2 matrix. However, this then requires more operations to manipulate the states as complex variables.

Matrix operation on $A=\Re^{n\times n}$	Float. Ops.* n=4	n=10
A+A	16	100
A$\underline{x}$	32	200
A^2	128	2,000
inv(A)	214	2,453

* Using MATLAB *flops* function to count operations used.

Figure 7.1. Table of Flops needed for basic mathematical operations.

Using the Matlab *Flops* command the number of the floating point operations for the first order approximation and Tustin's were compared. The results were that the first order method required 100 Flops and Tustin's method 516 Flops. These are based on the uses of an Intel Pentium and may vary for other processors because of the different instruction sets. No attempt was made to optimise the calculation beyond the logical implementation, other than calculating and storing for re-use $inv(\mathrm{I}-\tfrac{1}{2}At_s)$ rather than

calculating the same inverse twice. There is a significant difference between the number of operations required, but on the DSP what is only 10μs execution time, assuming the implementation is efficient this will only make a small difference in the obtainable sampling rate.

7.1.5 Comparison of discretisation methods in simulation

The three methods, first order, second order and Tustin's approximation are set up in Simulink and compared against the continuous-time motor at three sampling speeds, 500Hz, 1kHz and 2kHz. Fig. 7.2 shows the mechanical speed and continuous-time model current during a simulated motor start up. Fig. 7.3 shows the discrete-time model currents and the error with the continuous-time model for each of the observers at the three sampling rates.

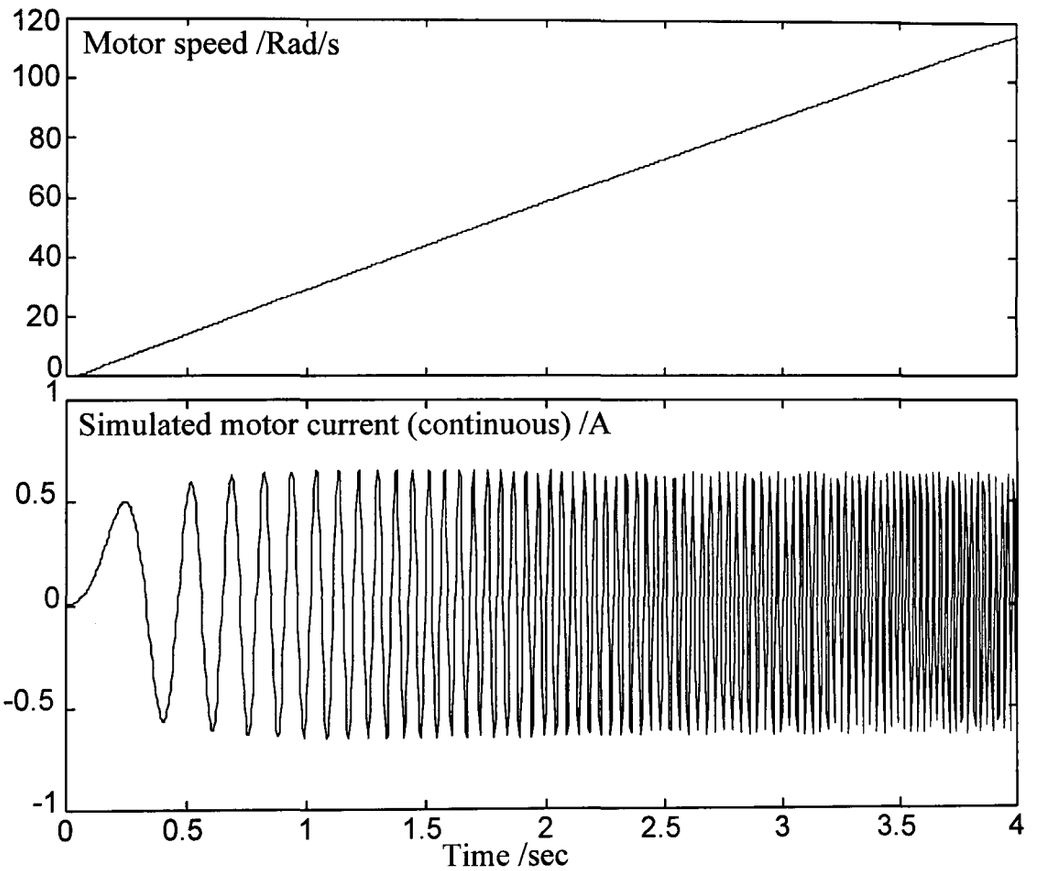

Figure 7.2. Graphs of motor speed and continuous model current taken from the Simulink simulation to compare discrete-time models.

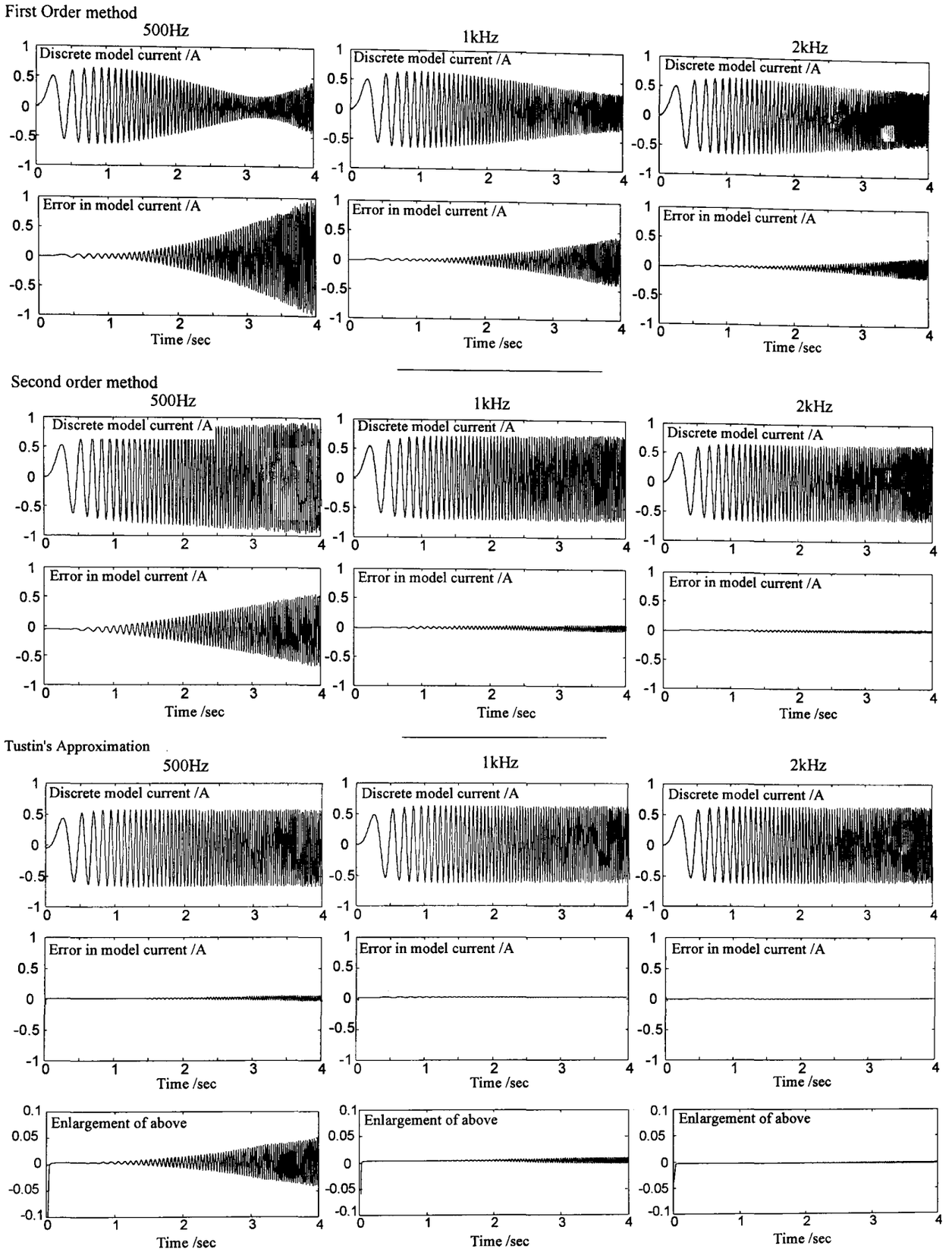

Figure 7.3 Plots of stator current and discretisation error for the three sampling methods at three different sampling rates.

7.1.6 Evaluation of first order expansion method on real hardware

If the first order method can be shown to be sufficient then there is no need to increase the complexity with more accurate methods. The effect of the sampling rate has been considered in simulation in the Section 7.1.1. It is also necessary to consider the performance of the discrete-time model against the real motor. This must be done in order to assess if noise and model uncertainty will degrade the performance of the discrete-time model significantly. The discrete-time model running in real-time on the DSP is compared against the measured motor currents during a ramp in drive frequency to the motor. Fig. 7.4 shows plots of the motor's speed and the measured currents. Fig. 7.5a-c shows the discrete-time model current and error, for three sampling rates, 500Hz, 1kHz and 2kHz.

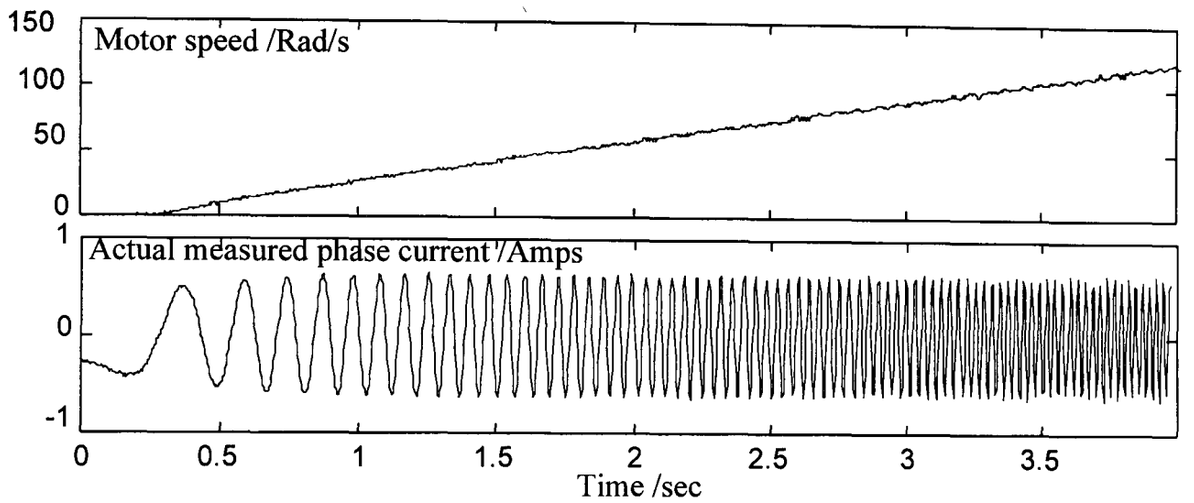

Figure 7.4. Plots of motor speed and phase current during a ramp in drive frequency.

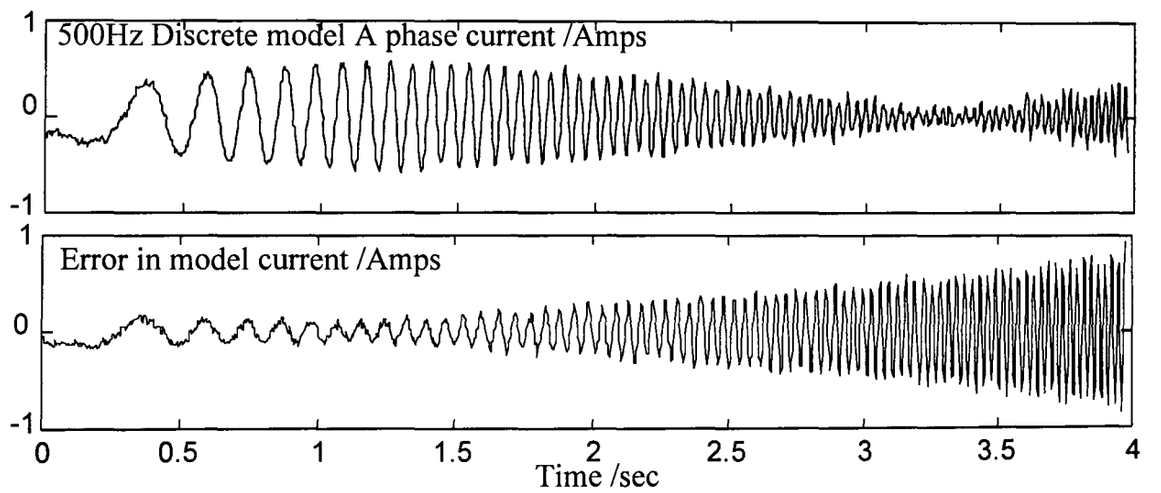

Figure 7.5a. Plots of model phase current and discrete-time model error for a sampling rate of 500Hz, during a ramp in drive frequency.

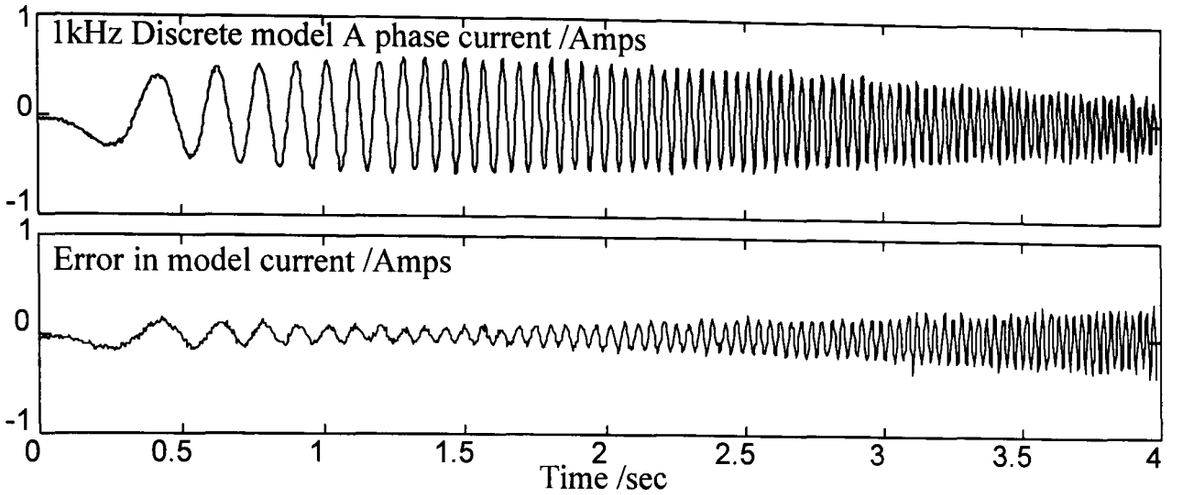

Figure 7.5b. Plots of model phase current and discrete-time model error for a sampling rate of 1000Hz. during a ramp in drive frequency.

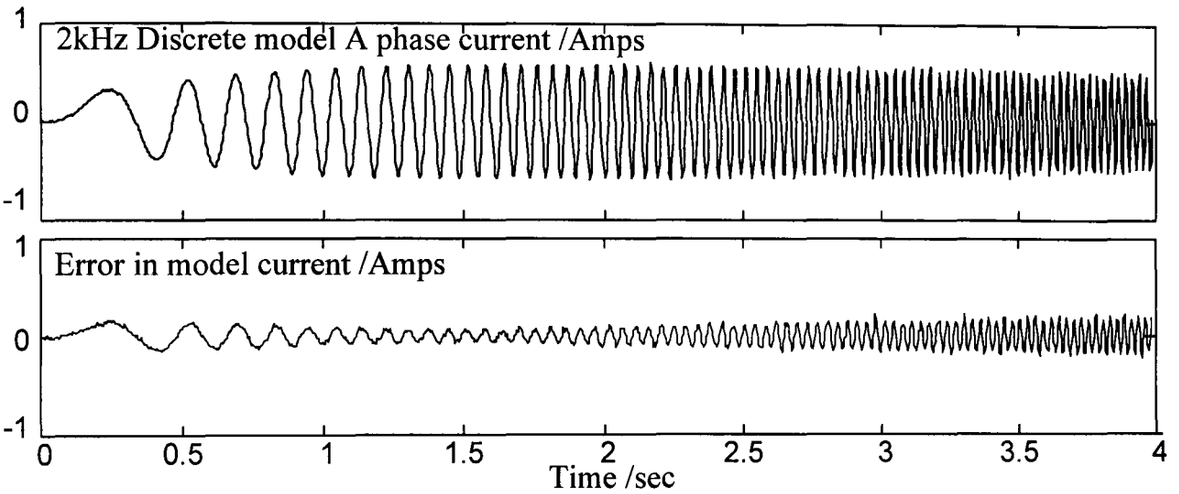

Figure 7.5c. Plots of model phase current and discrete-time model error for a sampling rate of 2000Hz, during a ramp in drive frequency.

At low speed, the effect of model non-linearity caused by the offset of the volts-per-Hertz control increasing the flux is clearly visible. At all three sampling rates a comparable mis-match is seen between the real motor and the discrete-time model. This is to be expected since a similar mis-match was seen between the motor and the continuous-time model in Section 6.4 shown in Fig. 6.16. At high speed the discrete-time model error is comparable to the simulated cases, which suggests that the filters in the instrumentation and the TDM interface are having no significant effect on the sample sensors and that noise and model uncertainty are sufficiently small. The error between the real motor currents and those from the discrete-time model using the first order method are relativity small, less than 10%, at motor speeds below 1800rpm ($180rads^{-1}$).

7.2 *Observer design*

7.2.1 Mapping of observer poles between continuous and discrete-time forms

A continuous-time system which is stable in the s-domain is not necessarily stable when transformed into a discrete-time system in the z-domain. Different continuous-to-discrete transforms map the continuous poles into the z-domain differently, see Appendix M.

7.2.2 Discretising the bilinear observer.

Using the forward rectangular rule to convert the bilinear to discrete form will result in an observer which becomes unstable as the speed increases and the discrete poles move out of the unit circle.[7.2]. The loci of the discrete poles of the bilinear observer is shown in Fig. 7.6, using the forward rectangular rule with a sampling rate of 1kHz.

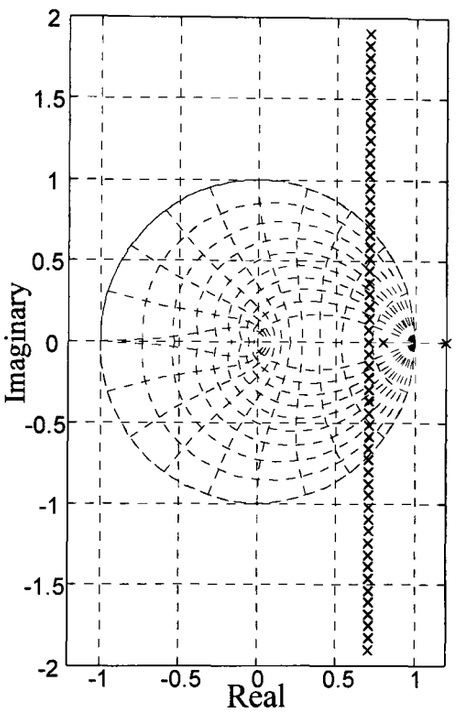

Figure 7.6. The loci of the discrete poles for the bilinear observer, using the forward rectangular rule to discretise the observer.

Using Tustin's approximation the observer poles will be contained within the unit circle. Using Tustin's approximation the continuous observer given by Eq. 4.15 is represented by the difference equation given in Eq. 7.14.

$$\underline{\hat{x}}_{K+1} = \frac{\left(A\frac{ts}{2}+1\right)}{\left(1-A\frac{ts}{2}\right)}\underline{\hat{x}}_K + \frac{B\frac{ts}{2}}{\left(1-A\frac{ts}{2}\right)}\left(\underline{u}_{K+1}+\underline{u}_K\right) + \frac{L\frac{ts}{2}}{\left(1-A\frac{ts}{2}\right)}\left(\left(\underline{y}_{K+1}-C\underline{\hat{x}}_{K+1}\right)+\left(\underline{y}_K-C\underline{\hat{x}}_K\right)\right) \tag{7.14}$$

For the bilinear model the matrix A is replaced by $A+N\omega$. The state dynamics for the discrete-time system become a fourth order polynomial fraction of speed.

[7.2] Stability in the z-domain requires that the discrete poles of the system are within the unit circle.

This is an undesirable system, since it would be very sensitive to any noise or error in the speed sensor measurement. However, once again the structure of the bilinear observer can exploited to simplify the discrete-time representation of the observer.

$$\underline{\hat{x}}_{K+1} = \frac{\left((A+N\omega-L_{(\omega)}C)\frac{t_s}{2}+1\right)}{\left(1-(A+N\omega-L_{(\omega)}C)\frac{t_s}{2}\right)}\underline{\hat{x}}_K + \frac{B\frac{t_s}{2}}{\left(1-(A+N\omega-L_{(\omega)}C)\frac{t_s}{2}\right)}\left(\underline{u}_{K+1}+\underline{u}_K\right) + \frac{L_{(\omega)}\frac{t_s}{2}}{\left(1-(A+N\omega-L_{(\omega)}C)\frac{t_s}{2}\right)}\left(\underline{y}_{K+1}+\underline{y}_K\right) \tag{7.15}$$

By transforming the observer state matrix, *A-LC* rather than the system state matrix, *A* the final form is considerably simplified. This step can be used for any observer but only as a result of the bilinear feedback does it result in a simplification of the problem. With bilinear feedback only two columns of the error dynamics are speed-dependent and these give an expression in powers of speed but only up to the speed squared.

$$\underline{\hat{x}}_{K+1} = A_D\underline{\hat{x}}_K + B_D\left(\underline{u}_{K+1}+\underline{u}_K\right) + L_D\left(\underline{y}_{K+1}+\underline{y}_K\right) \tag{7.16}$$

The loci of the poles of the observer's error dynamics with speed are shown in Fig. 7.7, using a sampling rate of 2kHz over the motor speed range 0-80Hz.

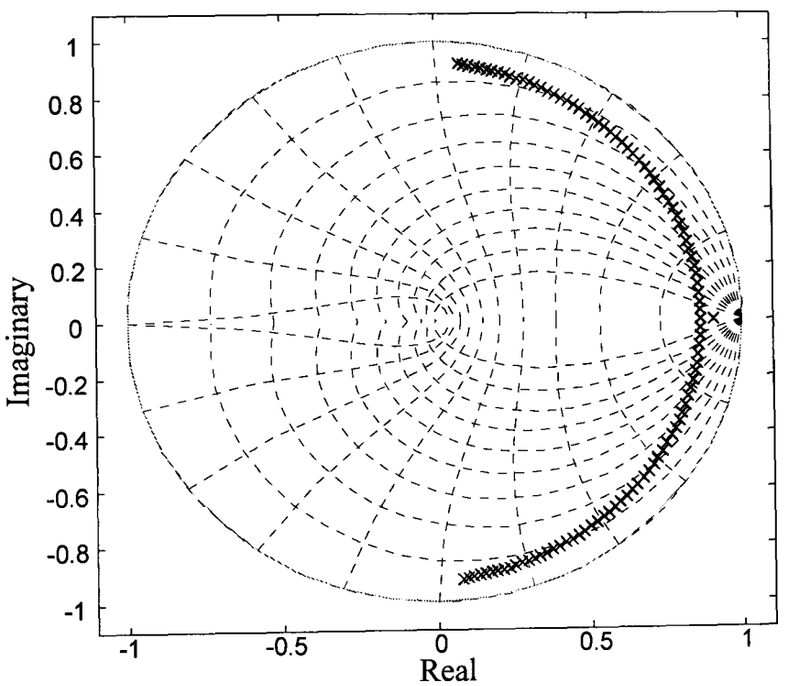

Figure 7.7. Diagram showing loci of discrete poles with increasing speed.

These pole locations are undesirable, since poles near the unit circle make the observer sensitive to numerical problems and measurement noise.

7.2.3 Feedback method

Using the forward rectangular rule to convert the bilinear to discrete form will result in an observer which becomes unstable as the speed increases. Tustin's approximation has been shown to give a discrete bilinear observer which is stable but is likely to be susceptible to noise and numerical error. The use of the speed parametrised observer from Section 4.6 is proposed, despite its greater complexity. Shown in Appendix L is the Simulink block diagram for implementing the feedback for the bilinear and the parametrised observer, which gives a comparison of the relative complexity of the two methods.

Section 7.1.2 shows that higher sampling rates are desirable for better accuracy of the model. However, in the real hardware this is limited by the available processing time. For the discretisation of the model the first order method is used. This does not give the best discrete-time representation of the motor, but the system remains bilinear and is computationally the simplest. A sampling rate of 1kHz is chosen for the observer, since at 2kHz the DSP is working close to its full load when just running the open-loop discrete-time motor model.

7.2.4 Observer pole location

With the parametrised observer it has been shown that there is freedom to place all four observer poles arbitrarily. There is a trade off between noise sensitivity against convergence rate and tolerance of model mis-match. To help set the pole locations, three very different cases are considered:-

Observer's poles:	slower than the motor poles[7.3]	0.99 and 0.5 repeated
	slightly faster	0.7 and 0.3
	significantly faster	0.1 and 0.05

The observer gain matrices for the three locations are pre-calculated and stored in look-up tables. The three observers are compared during a slow speed ramp from 0 to 30Hz drive frequency. The motor speed and measured D axis stator current is shown in Fig. 7.8. The resulting estimated currents and errors for the three observers are shown in Fig. 7.9a-c.

[7.3] The discrete-time motor model has poles at 0.47 and 0.97 repeated for zero speed, when discretised using the first order method at 1kHz.

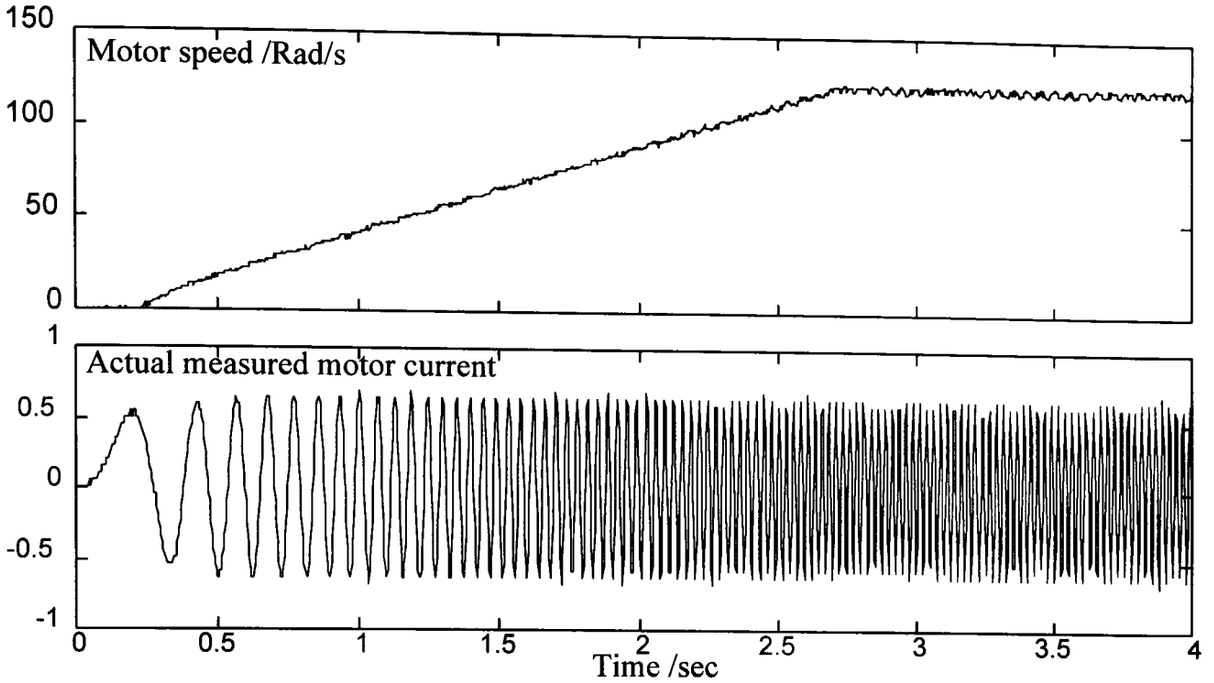

Figure 7.8. Plots showing the motor speed and measured stator current in the D axis during a ramp in speed.

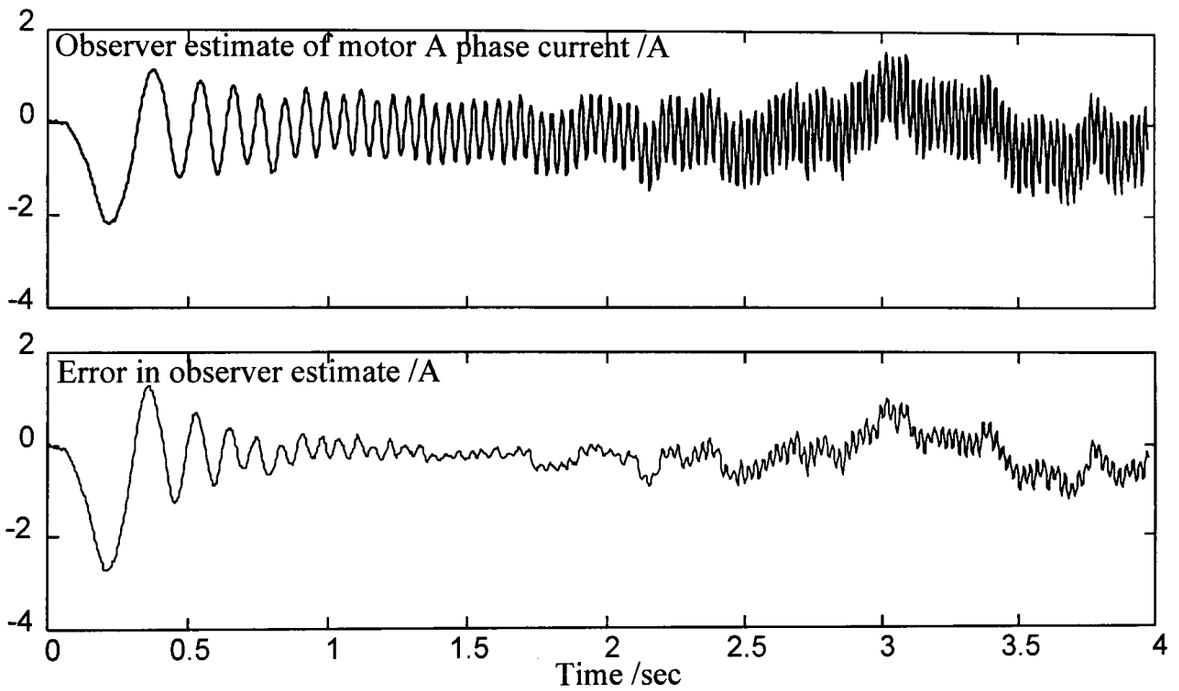

Figure 7.9a. Plots showing the observer's estimate of the D axis current and estimation error, for slow observer error dynamics.

The initial error transient is large since the convergence rate is slow, the observer then settles to a small estimation error. As the speed increases further the discretisation error increases and there is insufficient feedback gain to force the observer to track the real states in the presence of sensor noise and model uncertainty. This example was included to help stress the difference between simulation and real hardware.

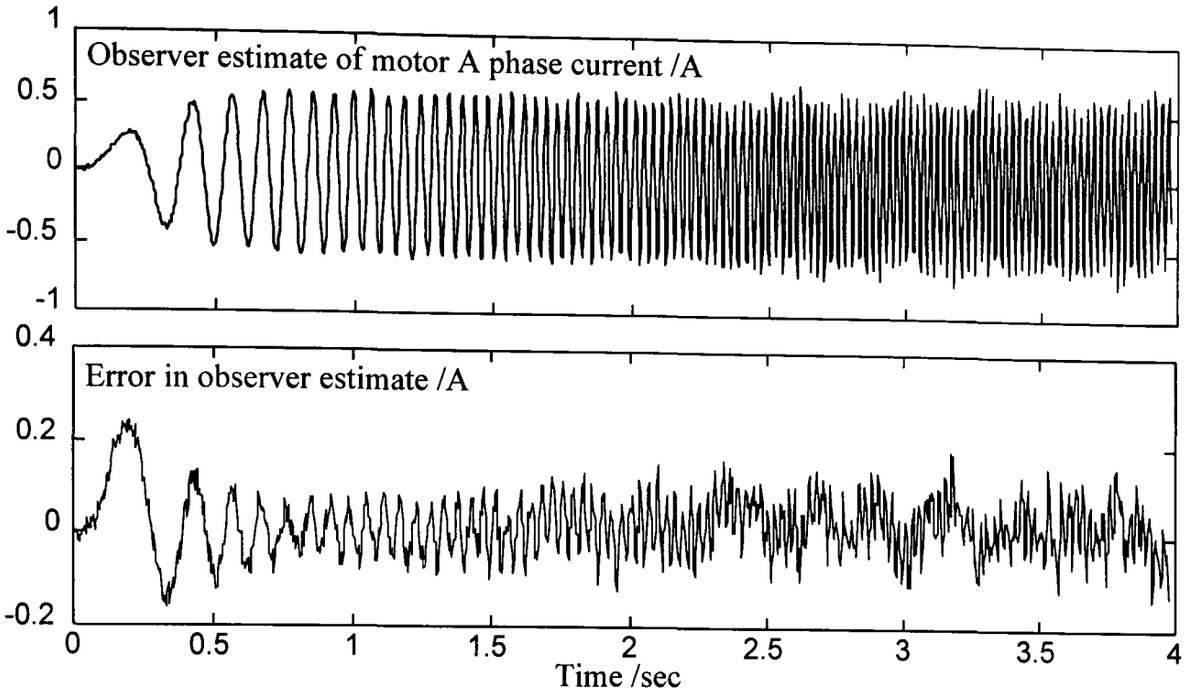

Figure 7.9b. Plots showing the observer's estimate of the d axis current and estimation error, for moderate observer error dynamics.

Fig. 7.9b show a significant error at low speeds due to the effect of the offset in the volts-per-Hertz control causing increasing flux and non-linear effects from saturation, see Sections 3.5 and 6.4.1. Beyond this the observer tracks the real model well.

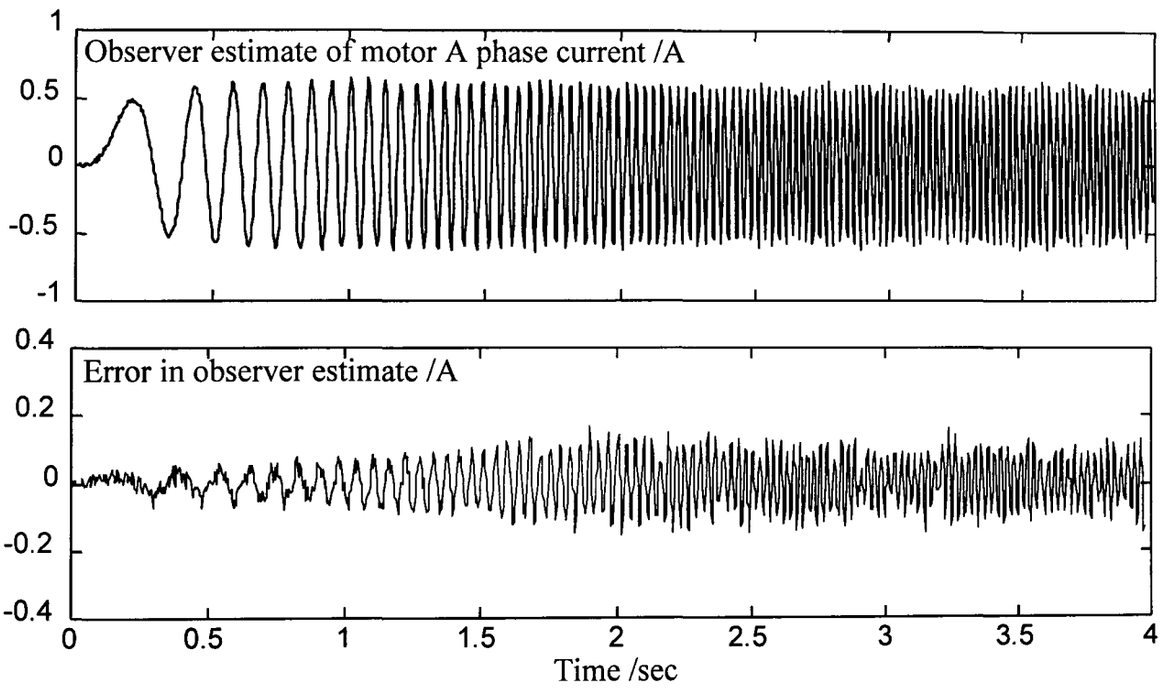

Figure 7.9c. Plots showing the observer's estimate of the D axis current and estimation error, for fast observer error dynamics.

As can be seen clearly from Fig. 7.9c the low speed performance is much improved. In this case the high feedback gain is enough to force the observer to track the motor even with the large model mis-match at start-up. The high speed performance is a little better than the previous case.

7.2.5 Implementing the observers

From the results in Section 7.2.2 and the discussion in Section 4.14 the following locations for the discrete observer poles are chosen as 0.1 and 0.3 repeated, corresponding to continuous poles of -2300 and -1200, in this case. The terms in the parametrised gain matrix are shown in Fig. 7.10, for a range of speed. The observer gain matrix is pre-calculated and stored in look-up tables. It is useful to consider how many points need to be stored, since the table will use a significant amount of memory.

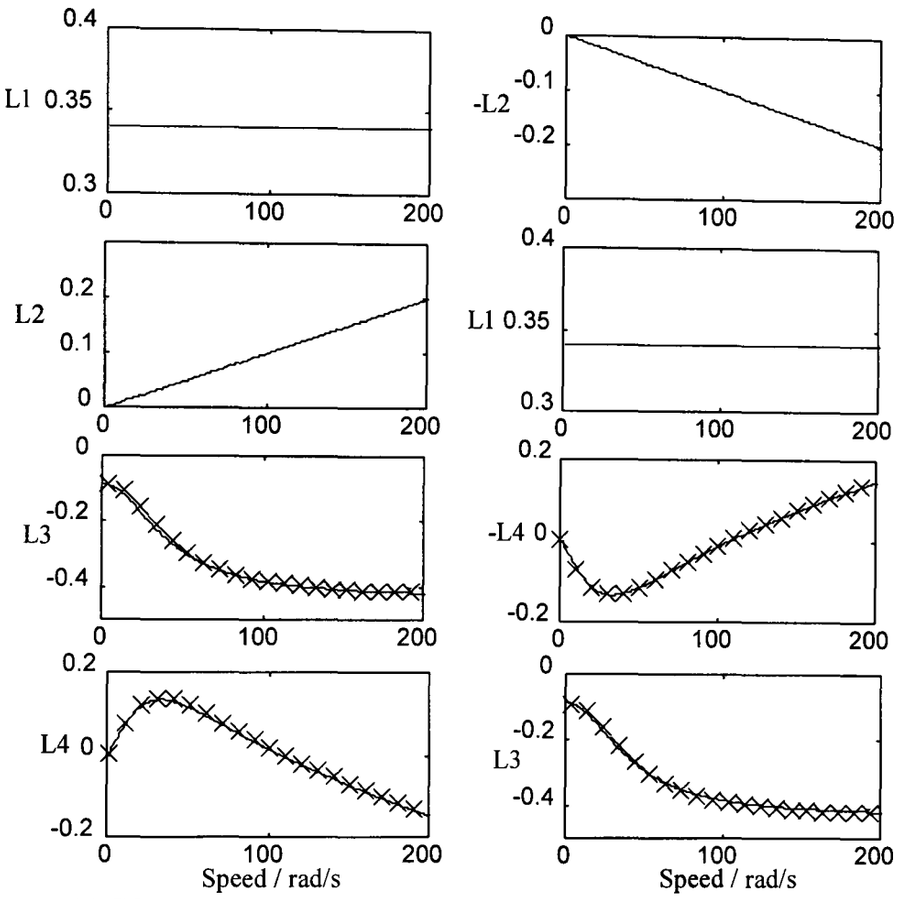

Figure. 7.10 Plots of the terms in the observer's speed dependent feedback.

The curves, in fig 7.10, are plotted using 200 points. However, this represents a large memory requirement which can be reduced by storing fewer points and interpolating between them. The look-up table is now a piece-wise approximation to the ideal gain. The crosses on the curves in Fig. 7.10 correspond to points 10rads^{-1} apart. The effect of this on the observer poles was analysed by calculating their loci as a function speed. With gains stored for points every 10rad/s the poles moved by less than 0.1% of their original values. At high speed the curves are almost linear and can be approximated by fewer points. The Simulink look-up table block can accommodate variable point spacing, so each term can be stored as ten equally spaced points below 100rad/s and ten further points up to 1000rads^{-1}.

7.3 Setting up the FDI scheme

Fig. 7.11 shows the complete scheme, showing both the hardware and the components which are implemented in software on the DSP. The Simulink blocks for the software are shown in Appendices L and N.

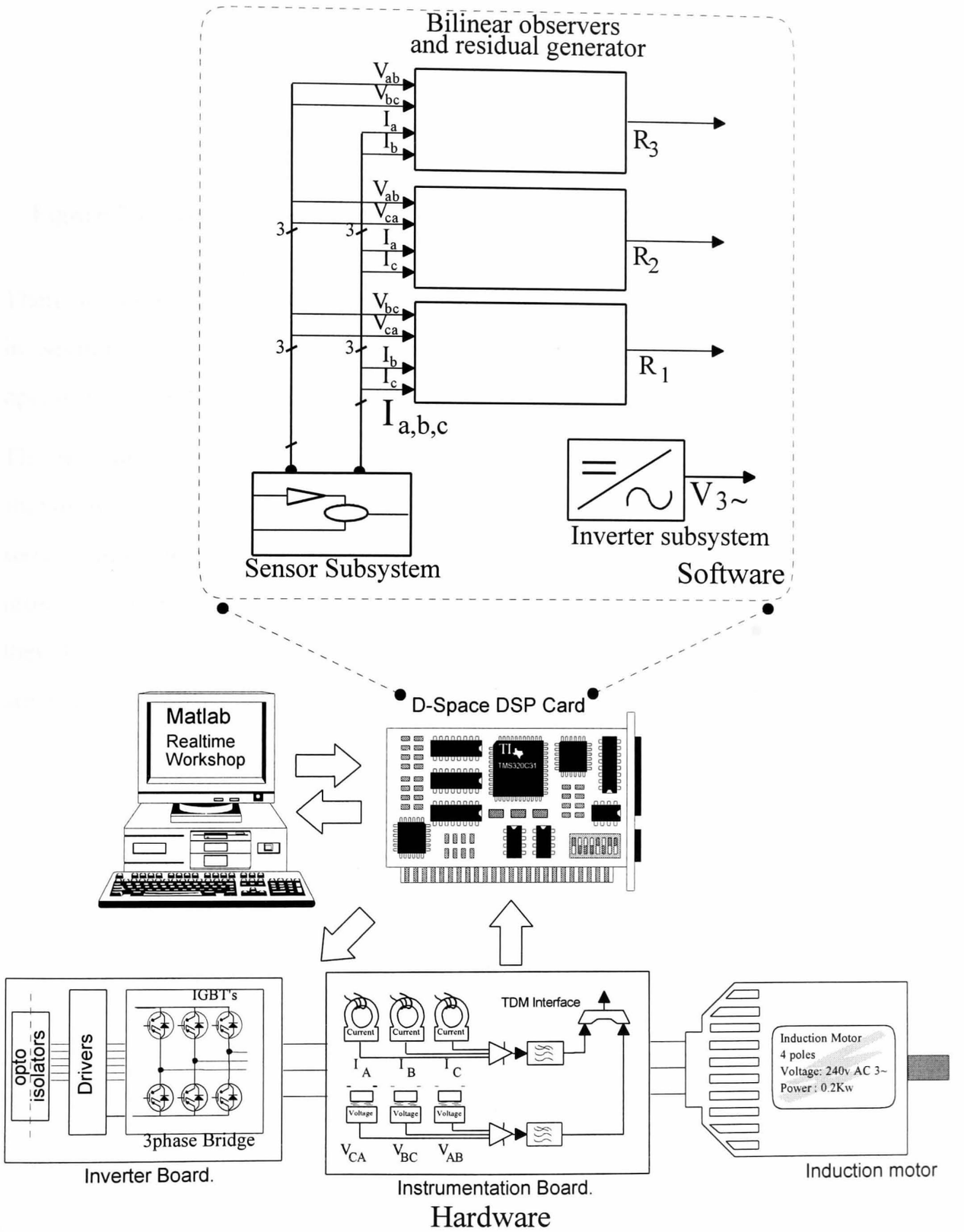

Figure 7.11. Diagram of complete FDI test-rig, showing hardware and software running on the DSP.

7.4 Sensor fault detection on the test-rig

Fig 7.12 shows that a sensor fault will only be detectable if the magnitude of the fault residual is greater than the magnitude of the fault-free residual.

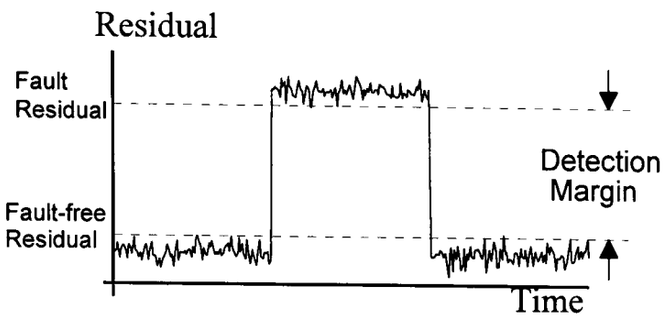

Figure 7.12. Diagram showing how the detection margin, between the fault and fault-free residuals.

There are a number of factors which will affect the detection margin, these are discussed in Section 7.7. It is anticipated that this detection margin will alter over the motor operating range, for both speed and load.

The magnitudes of the residuals when subjected to a sequence of sensors faults are shown in Figs. 7.13 to 7.18, for various fixed drive frequencies and loads. In simulation sensor faults are produced by multiplying the sensor value by zero. However, for these tests the sensors were physically disconnected by hand in sequence. The voltage sensors, then the current sensors and finally the speed sensor are disconnected in turn. The results are discussed in Sections 7.5 - 7.7 for each sensor under the various conditions.

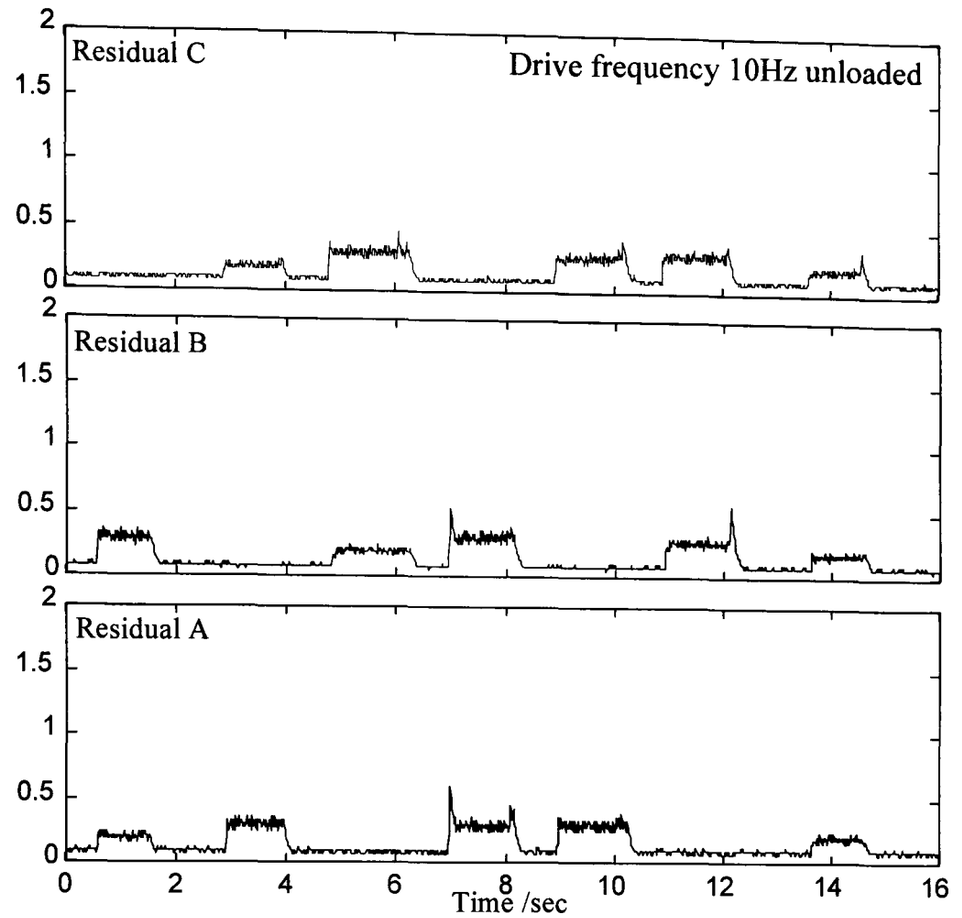

Figure 7.13. Residuals for a sequence of sensor faults at a drive frequency of 10Hz with the motor unloaded.

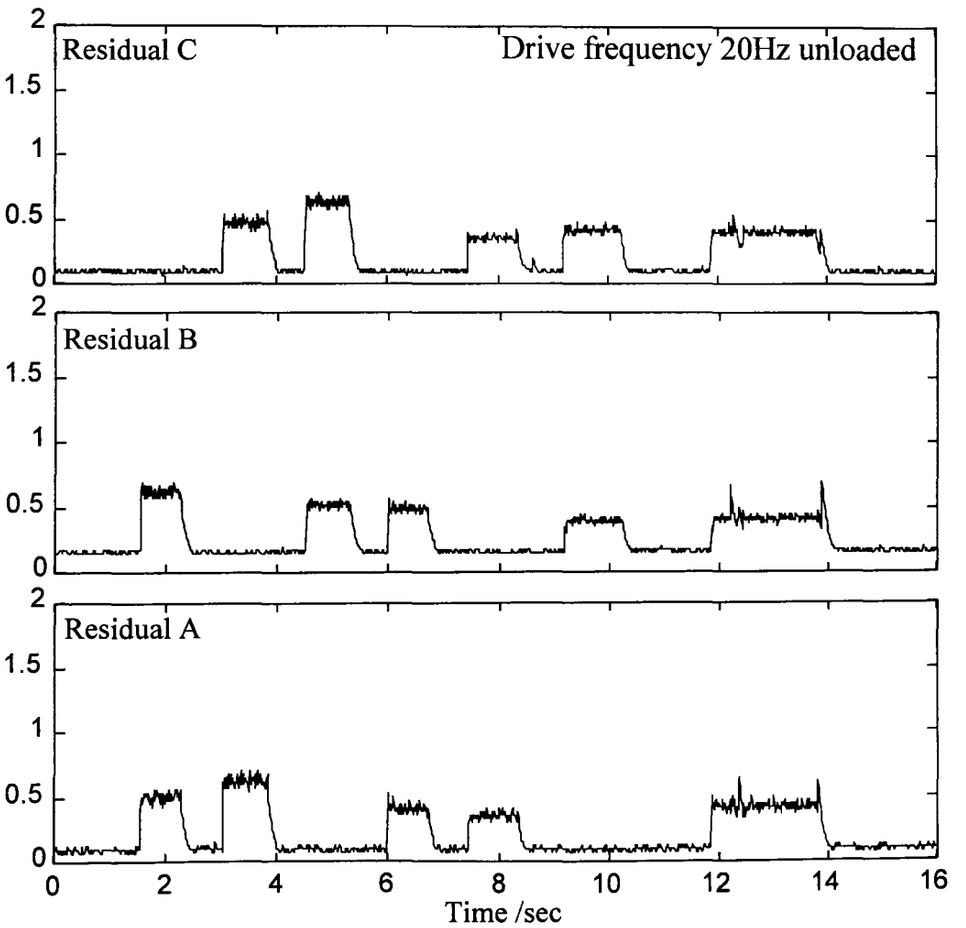

Figure 7.14. Residuals for a sequence of sensor faults at a drive frequency of 20Hz with the motor unloaded.

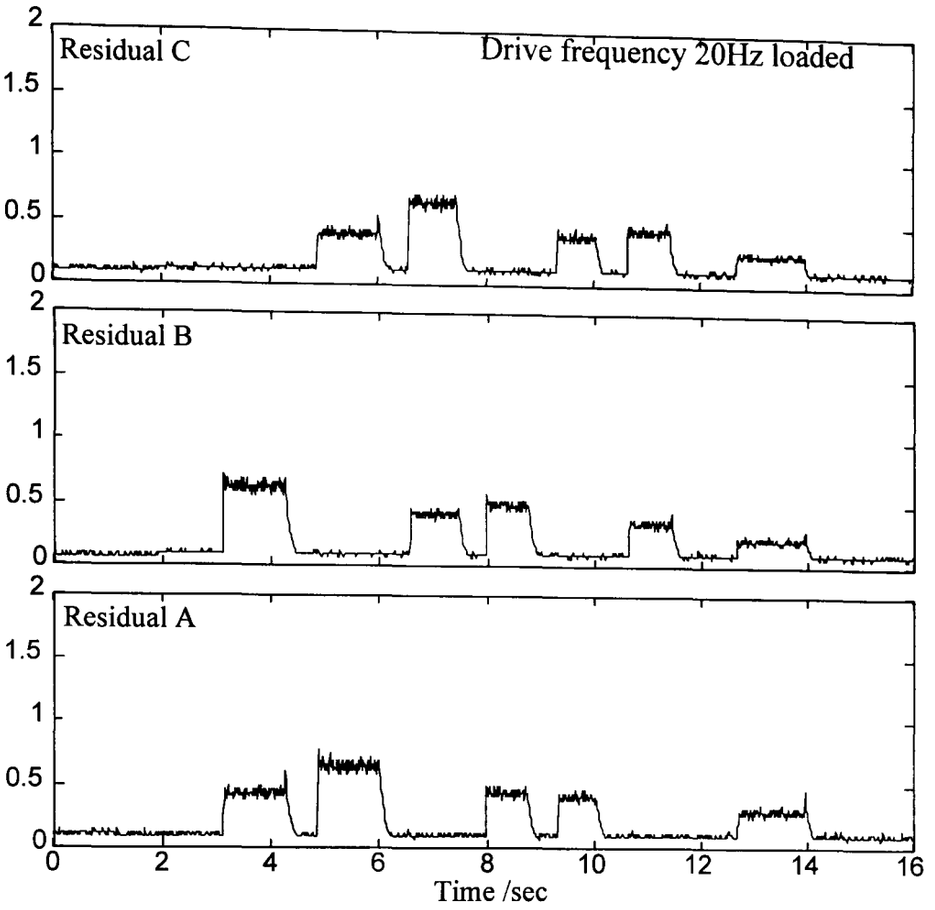

Figure 7.15 Residuals for a sequence of sensor faults at a drive frequency of 20Hz with the motor loaded.

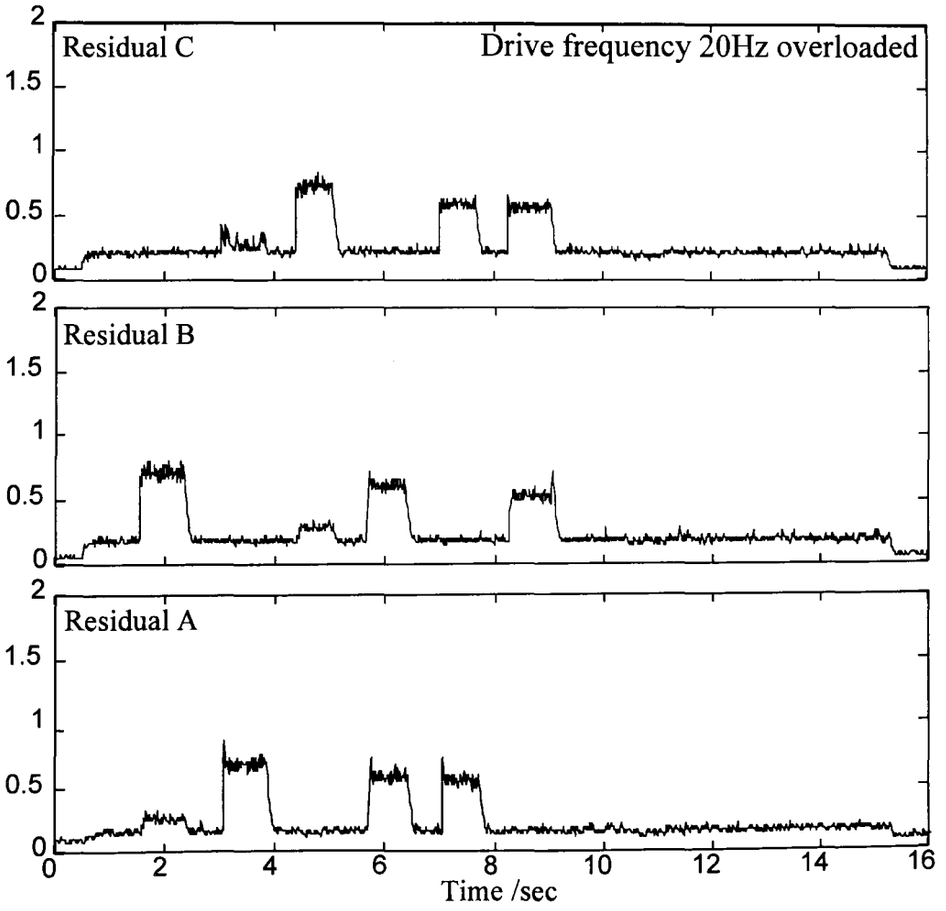

Figure 7.16 Residuals for a sequence of sensor faults at a drive frequency of 20Hz with the motor overloaded.

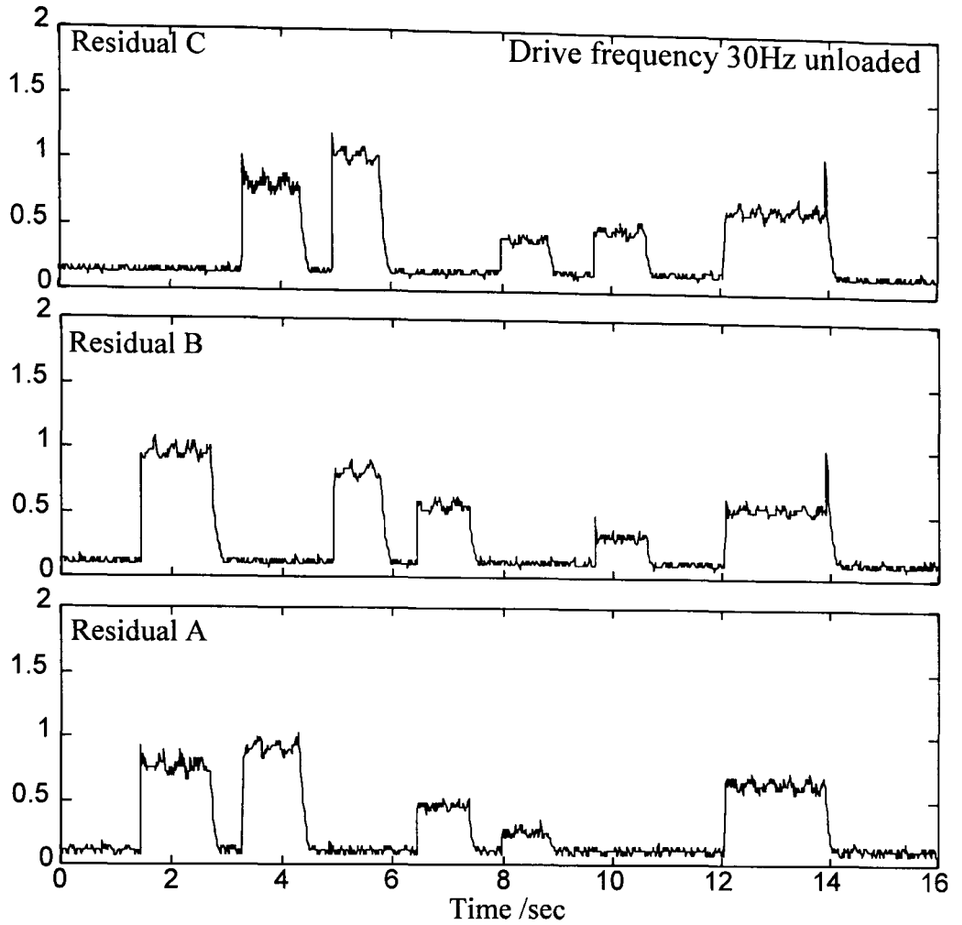

Figure 7.17. Residuals for a sequence of sensor faults at a drive frequency of 30Hz with the motor unloaded.

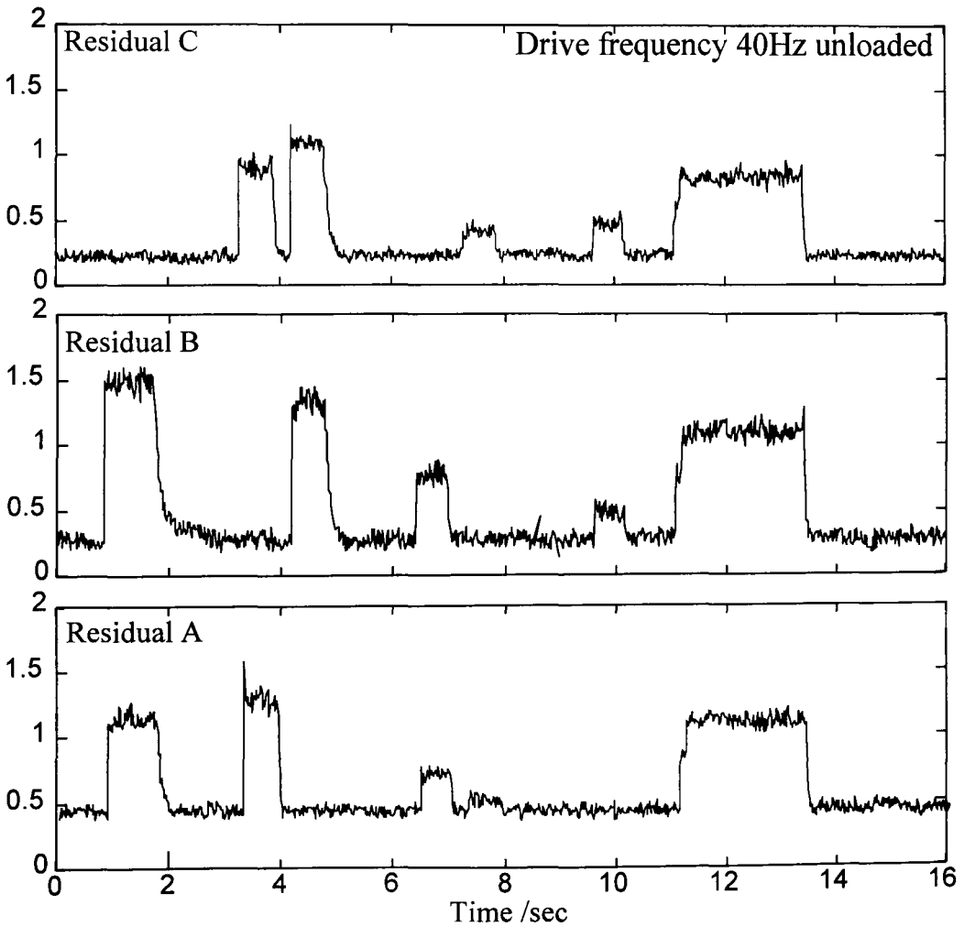

Figure 7.18. Residuals for a sequence of sensor faults at a drive frequency of 40Hz with the motor unloaded.

7.5 *Assessment of results*

7.5.1 Fault-free residuals

The fault-free residuals are a function of both motor speed and loading.

Motor speed. The effect of speed on the fault-free residuals is considered by plotting each of the three residuals during a speed reversal. Fig. 7.19 shows the fault-free residuals from the three observers and the motor speed during a reversal of drive frequency from -45Hz to +45Hz in 6 seconds.

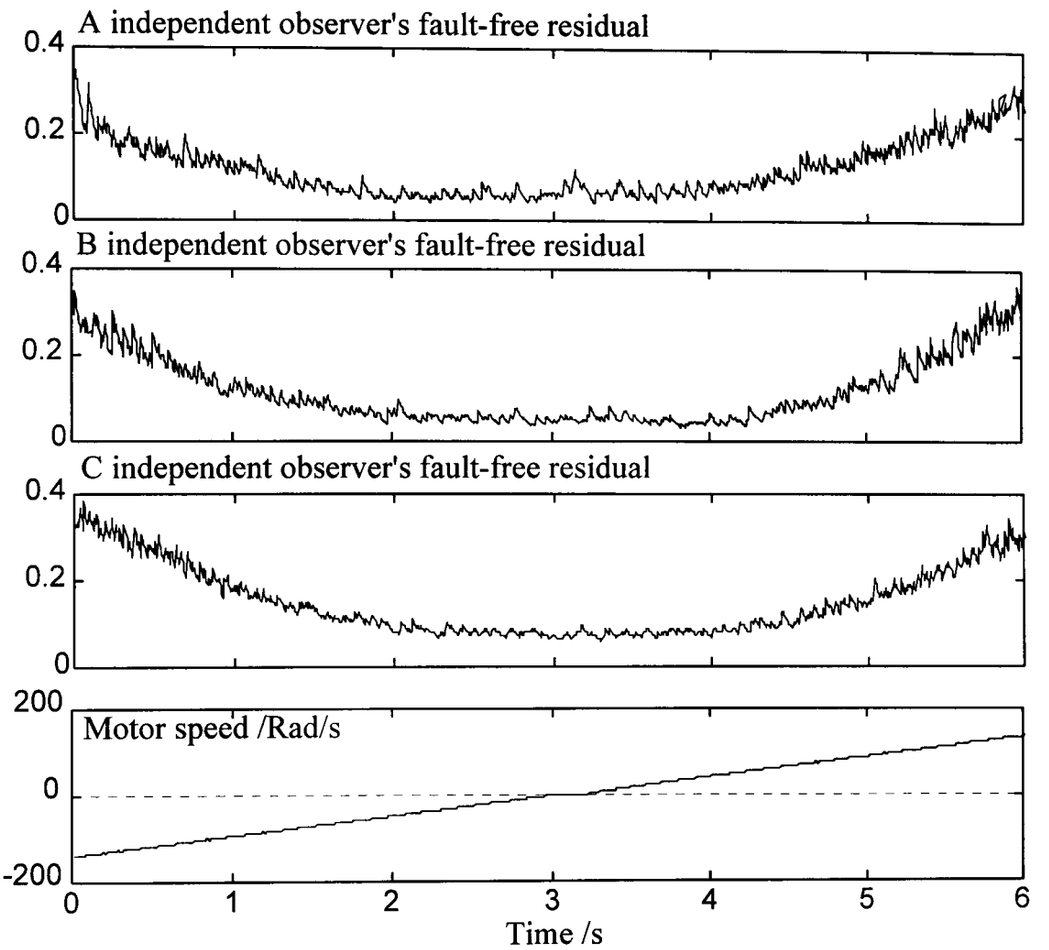

Figure 7.19. Plots of the magnitude of the three residuals during a speed reversal.

The fault-free residuals clearly increase with motor speed. A significant residual component comes from the discretisation error as discussed in Section 7.1.2.. However, the observer's sensitivity to noise and modelling errors will alter with speed, see Section 4.13. The various factors are discussed individually in Section 7.7

Motor loading. To demonstrate the effect of motor load on the fault-free residual the motor is loaded whilst running with a fixed 20Hz drive frequency. Fig. 7.20 shows the applied voltage, the measured current, the A independent residual and the motor speed. The induction motor is driving the DC motor, initially with the motor loaded with 10Ω then open circuit and 1Ω resistors.

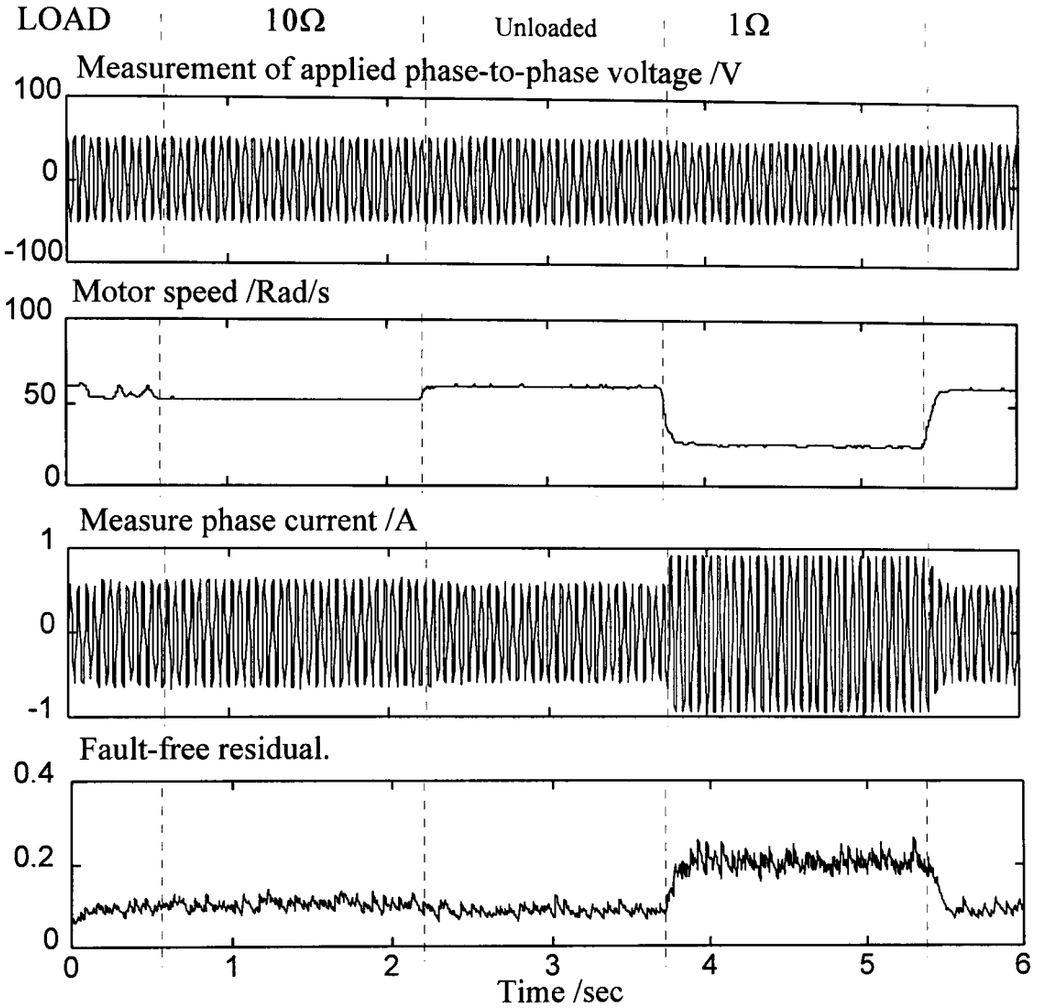

Figure 7.20. Plots showing effect of motor loading on the fault-free residuals.

The fault residual is only slightly increased by the 10Ω load. However, the 1Ω load has a significantly increases the residual. This reflects the large currents flowing in the rotor which increases the flux level and the motor-model mis-match due to saturation.

7.5.2 Fault residuals

Voltage sensors. As the drive frequency increases from 10 to 40Hz the magnitude of the fault residual increases linearly as the volts-per-Hertz control increases the applied voltages. The fault-free residual increases with speed but the fault residual is always significantly greater. Loading does not affect the detection of voltage sensors, since at high speed the large applied voltage gives a large residual. Whilst at low speed the AC motor cannot be loaded significantly by the DC motor.

Current sensors. In the unloaded case the size of the residuals remains constant as the motor's speed increases, again this is because of the volt-per-Hertz control which holds the flux (and therefore current) constant as speed increases. When the maximum voltage is reached the currents will drop as the speed increases further. Also the fault-free residuals increase, with speed, making the detection harder. Increasing the loading increases the fault-free residuals but the fault residual increases more and so the detection gets easier.

The speed sensor. With the FDI scheme running on the test-rig there is only one speed sensor and therefore all three residuals are affected by the disconnection. At low speed the residual is small. As the speed increases the magnitude of the fault residuals increase faster than the fault-free residuals and detection becomes easier. Increasing the load reduces the speed making detection harder. The detection problem is made worse still in this case by the fact that the magnitude of the fault-free residuals increases with load. Note that the speed sensor fault shown in Fig. 7.16 is undetectable even by eye with the motor heavily loaded.

7.6 Defining an area of the motors operating range where sensor faults are detectable

7.6.1 Fault-free residuals

Fig. 7.20 shows a contour plot of the magnitude of the fault-free residual for drive frequency and motor speed. This is produced from a small number of measurement points and interpolated. The reason for not using a large number of points to obtain accurate plots is that doing so would be time consuming and the precise results are only specific to this test-rig. These results may also be plotted for a load which is roughly equivalent to magnetising current, see Fig. 7.22, for a contour point of fault-free residual against speed and load.

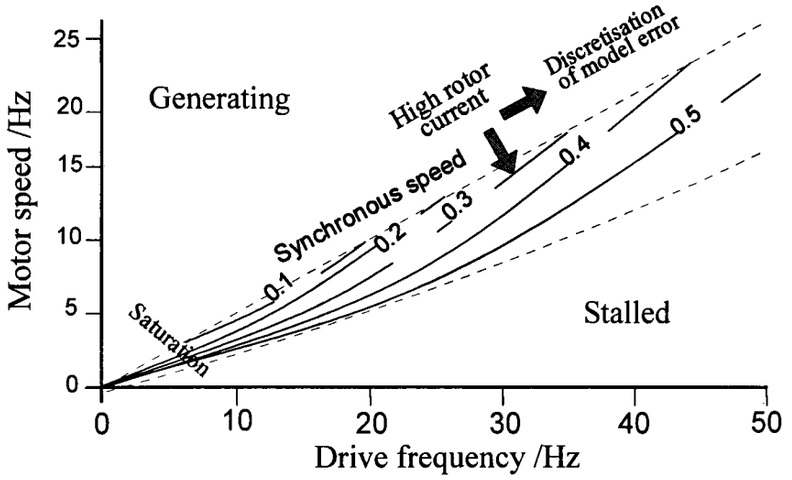

Figure 7.21 Contour plot of fault-free residuals against motor speed and drive frequency.

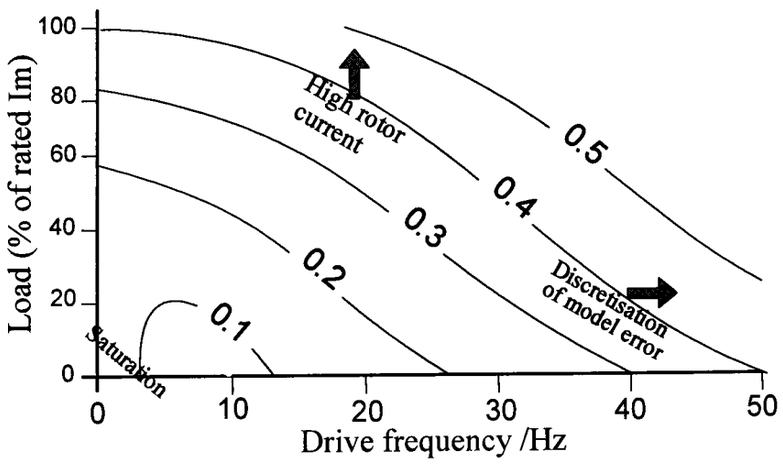

Figure 7.22 Contour plot of fault-free residuals against load and drive frequency.

In order for a fault to be detectable at a given operating condition, its residual must be greater than the fault-free residual.

7.6.2 Fault-residuals

For each sensor a contour plot of residual magnitude can be produced. By combining these with the fault-free plots a region can be defined where the fault residual is greater than the fault-free residual and therefore reliable detection is possible. The general forms of these detectable areas for each sensor are shown in Fig 7.23 for speed and load.

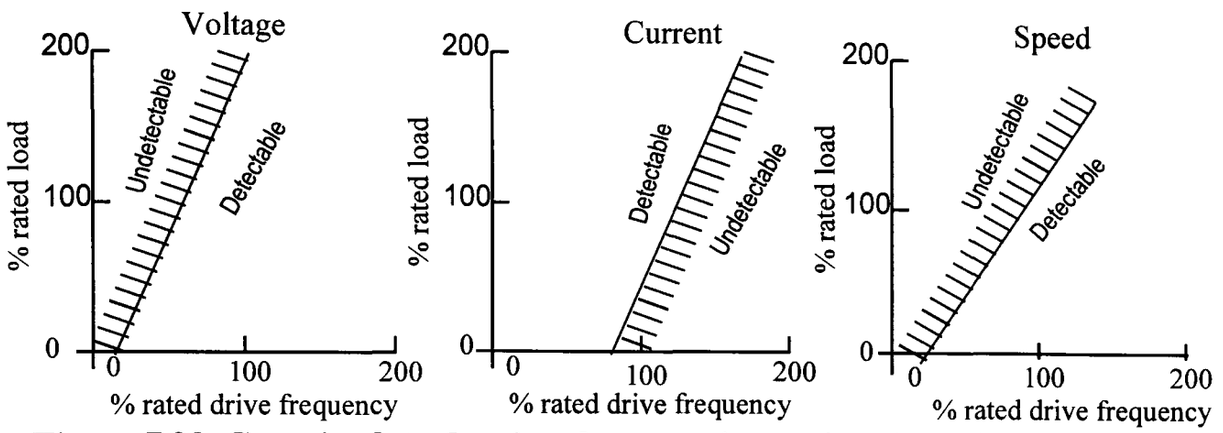

Figure 7.23. Generic plots showing the operating regions in which sensor fault detection is possible for each of the three sensor types.

The speed-load graphs of Fig. 7.23 can be completed by super-imposing a speed-load limit for the motor to prevent thermal overload. The limits for detecting the three types of sensor faults and the motor's limits are combined to give the operating range of the fault detection scheme for disconnections. As sketched in Fig. 7.24.

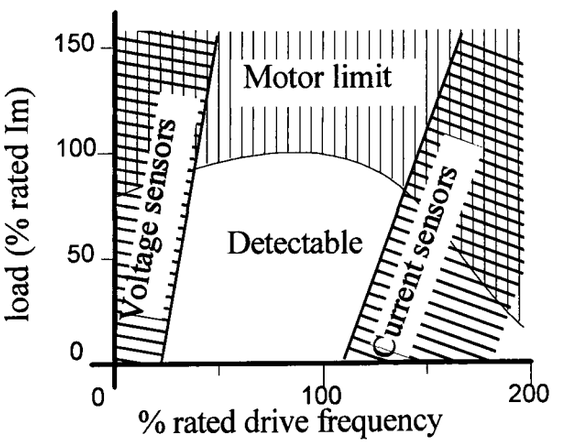

Figure 7.24. Sketch graph showing region of motor operation range where sensors faults can be detected.

The results of Section 7.5 show that the FDI scheme will work over the normal operating range of the motor even with variable speed drive and variable load, although this assumes that volts-per-Hertz control is used to avoid saturation. Only at low speeds is the detection of voltage and speed sensor faults difficult because of the small sensor readings and the offset on the volts-per-Hertz control causing non-linearities.

7.7 *Restriction on the performance of the FDI scheme in real-time*

The GOS method has been demonstrated to work on a small scale test-rig in real-time across most of the normal operating range of the motor. The notable limitation is at low speed when both the voltage and speed measurements are relatively small and saturation effects become significant. A large range of operational and implementation factors degrade the detectability of faults, either by increasing the fault-free residuals or by reducing the magnitude of the fault residual. There are too many variables which affect the real system to evaluate the observers fully on a real test-rig induction motor. The FDI performance achievable will be determined by the application. For the small motor the techniques have been shown to work. There is insufficient data available to assess the application of the sensor fault FDI scheme to the traction system fully. The rest of this section outlines the main factors which will affect the performance of the FDI scheme and explains how these can be assessed using the methods presented in this thesis.

7.7.1 Discretisation of the model

The predominant source of error on the test-rig was from the observer discretisation. Using the first order method for discretisation the fault-free residual increases significantly at high speed. In Section 7.1 the effect of different discretisation methods and sampling rates has been considered in simulation. Faster sampling will give more accurate models. By increasing the sampling rate from 1kHz to 2kHz the fault-free residual is halved, but if the DSP's software overheads are large a significant penalty occurs. A more accurate observer is found using Tustin's approximation but this makes both the state-space dynamic matrix, A, and the state input matrix, B, functions of the inverse of the bilinear state matrix. Changing from the first order method to Tustin's approximation reduces the fault-free residuals by an order of magnitude but the computational load also increases. The execution time overhead associated with this would have been small compared to the overhead from the sensor and inverter subsystems so this would have made a considerable improvement to the test-rig.

7.7.2 Model uncertainty and non-linearites

The second most significant source of error is from model mis-match. There are two issues; errors in the model parameters and neglecting motor non-linearities. The basic motor model is shown to be reasonably accurate, but volts-per-Hertz control is essential

to avoid saturation. On the EMU's traction system volts-per-Hertz control is used, with gain scheduling for other objectives, but the motor is still operated with significant saturation in order to get the required power-to-weight ratio. The effects of changes in model parameters and uncertainty in the speed measurement have been considered in Section 4.13, by evaluating a frequency domain expression for the coupling of the error and the states. This gives a method for comparing the sensitivity of different observers to disturbances. For sensitivity to modelling errors it is important to consider realistic model discrepancies such as parameter changes. The sensitivity to changes in resistance is relatively easy to analyse. For magnetising inductance it is more difficult as the calculation of the sensitivity matrix is complex and does not readily simplify. The sensitivity function being analysed here is the effect of a parameter error in the non-saturated magnetising inductance and not flux saturation, which is a still more complex problem, see Section 8.3. To limit the flux and hence avoid saturation volts-per-Hertz control of the motor is essential. Only at low frequencies where an offset is added to give sufficient starting torque is there a problem. To assess the effect of saturation a more accurate motor model is required, this is discussed in Section 8.2

On the test-rig temperature has not been a significant issue. The motor has been operating in free air with a relatively low load. The effect of temperature on the observers has been discussed in Section 4.13.3. On the EMU it is likely that some form of temperature compensation will be required. Thermal effects are discussed further in Section 8.2.

7.7.3 Sensor noise

There are two main sources of noise on the sensor measurements; white noise as is inherent in all electronics and interference from the inverter switching, this is discussed further in Section 8.1. Using the techniques outlined in Section 4.13.1 the observer's sensitivity to noise and hence that of the fault-free residuals can be calculated. Alternatively, the sensor noise can be modelled and included in simulation, as discussed in Section 8.1. There is no reason to assume that measurement noise on the trains would be significantly worse than on the test-rig. In fact it is likely to be better, since the instrumentation is better designed with electro-magnetic compatibility issues in mind and the GTO's switch less frequently and more slowly.

7.7.4 Loading

Increasing the loading increases the magnetisation current flowing in the motor. This alters the region of the magnetic characteristic in which the motor is operating, and changes the model. The motor parameter identification was carried out around a magnetising current of 0.3 Amps, which is less than the nominal rated magnetising current for the motor. Performing the identification with a larger magnetising current offset would give a better model of the loaded motor, although this would be inaccurate in the no load case. This method is used by GEC-Alsthom in the design of the EMU's control system. Therefore the magnetising inductance quoted in Fig. 3.5 is for the motor operating at 60% full rated load.

7.7.5 Pole location

There is a necessary trade off in the choice of the observer's poles locations; between high feedback gain for fast convergence and tolerance to model mis-match as opposed to low feedback gain for sensitivity to faults and noise rejection.

The effectiveness of an observer for fault detection is the difference between the magnitudes of the fault-free residual and the fault residual. For an application where noise is a greater problem than model mis-match a low gain observer can be used to achieve good detection and estimation. When faced with significant model mis-match the fault detection performance most be traded off against the quality of the fault-free estimate. On the test-rig a workable compromise can be achieved, for the GOS method but not for the DOS method.

The observer design is complicated by the speed-dependent behaviour of the induction motor model. To overcome this it is necessary to store the feedback gain matrix as a look-up table for a range of speeds. This gives scope to optimise the observer across its operating range for speed and possible load. At low speed or high load, high gain could be used to track the non-linearities in the model, whilst for high-speed and low load, a low gain could be used to maximise the fault detection performance and limit the effect of discretisation error.

7.8 Demonstrating the DOS methods on hardware

This chapter ends by considering briefly the DOS methods for current and voltage sensors. These methods have already been compared in simulation with the GOS method, as discussed in Section 5.10. They are subject to all the same application specific factors as the GOS method, discussed in Section 7.7. For these reasons, this section is only intended to demonstrate that the DOS method can be implemented in hardware and that the results agree with the predicted performance relative to the GOS method.

7.8.1 Current sensor failures

Initially, the current sensor FDI scheme, described in Section 5.5 is set up on the DSP and subjected to a sequence of faults. The motor is loaded using the 10Ω load on the output of the DC motor. The resulting residuals are plotted at two different drive frequencies, 10 Hz and 30Hz, as shown in Fig. 7.25a and b.

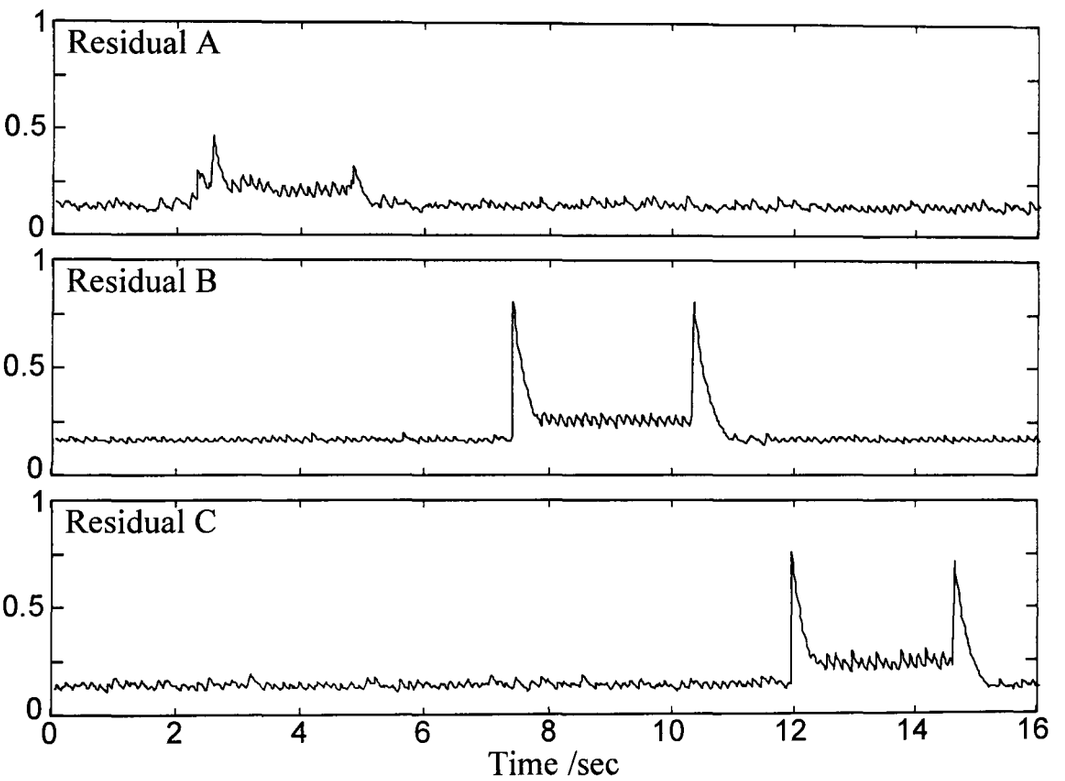

Figure 7.25a. Plots showing residual responses to a sequence of current sensor faults using the DOS method for sensor FDI at a fixed drive frequency of 10Hz

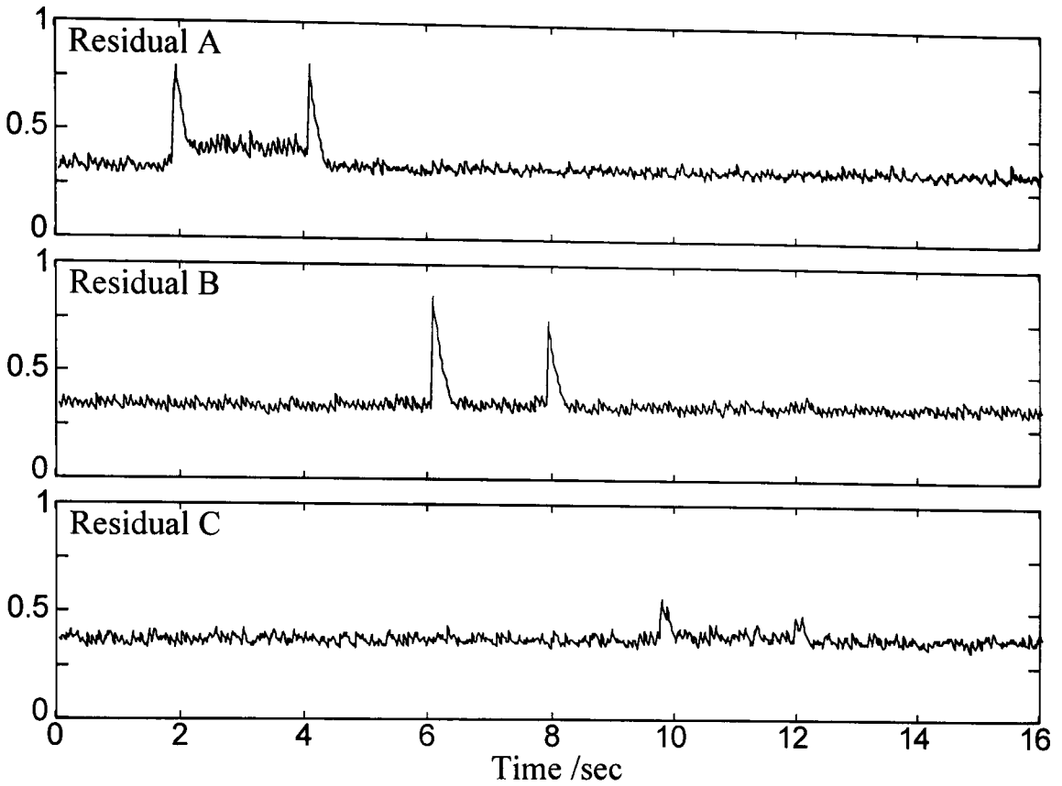

Figure 7.25b. Plots showing residual responses to a sequence of current sensor faults using the DOS method for sensor FDI at a fixed drive frequency of 30Hz

The residuals shown in Fig. 23 clearly show that for the DOS method each residual is only affected by one sensor fault. This is the main advantage of the DOS method over the GOS method. The steady state fault residuals are significantly less than those for the GOS method. The increased noise sensitivity means that the residual is swamped by noise on the fault-free residual. This is mainly due to the discretisation error rather than physical sensor noise. This result agrees with the theory in Section 5.10 which shows that the DOS method is less sensitive to faults whilst at the same time being more sensitive to noise than the GOS method with comparable pole locations.

The residuals show an interesting 'spike' when the fault first appears. This is caused by the abrupt change in the measured value causing a large difference between the measurements and the estimates, which is the residual. The observer feedback then forces the observer to track the fault rather than the real state and as it does so the residual is reduced. This is shown pictorially in Fig 7.26.

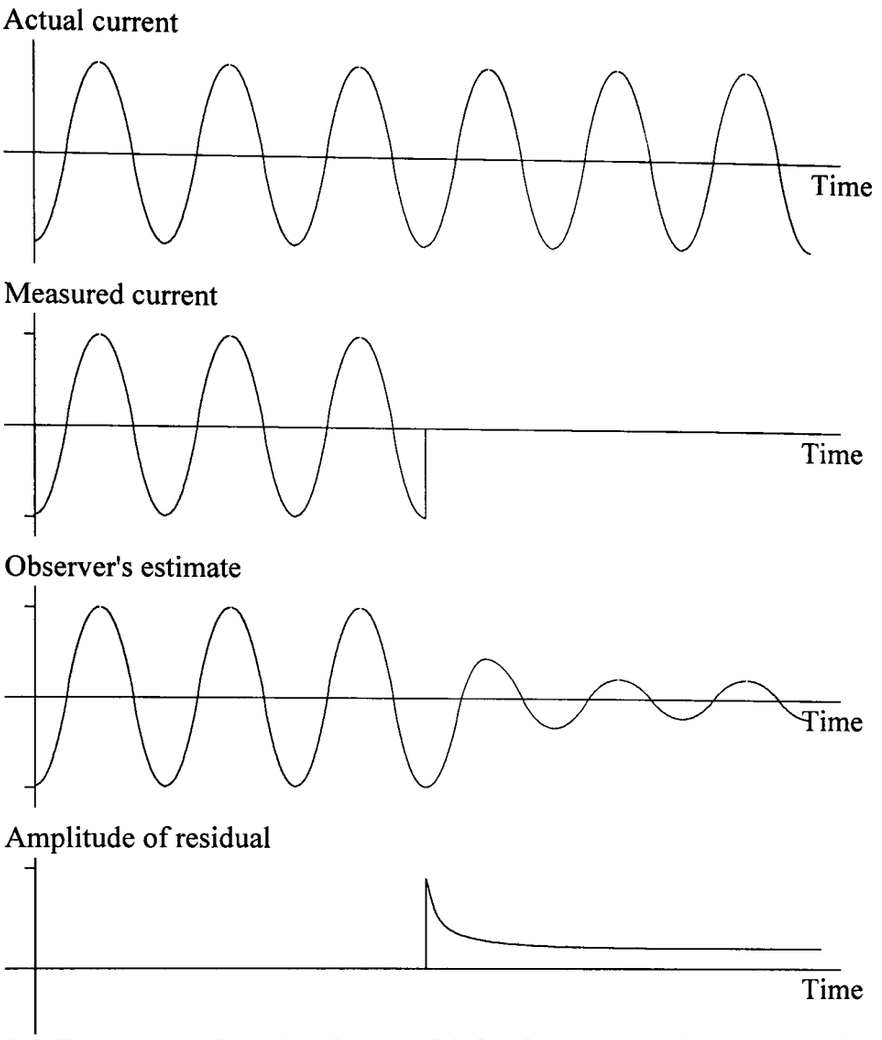

Figure 7.26. Diagram showing how a high observer gain reduce the residual.

It is not possible to use this spike to detect faults rather than the steady-state residual since it will not occur if the measurement is nearly zero at the instant the sensor fault occurs. This is the reason why not all the residuals shown in Fig. 7.25 have the spike, at the start of the fault.

7.8.2 Voltage sensor faults

The UIO method for voltage sensor FDI is shown in simulation in Section 5.6. For the induction motor, two of the design matrices are functions of speed. On the DSP, to simplify the implementation the observer is designed for a fixed operating speed corresponding to the motor speed with a drive frequency of 10Hz and 30Hz. The resulting residuals to a sequence of voltage sensor failures is shown in Fig. 7.27.

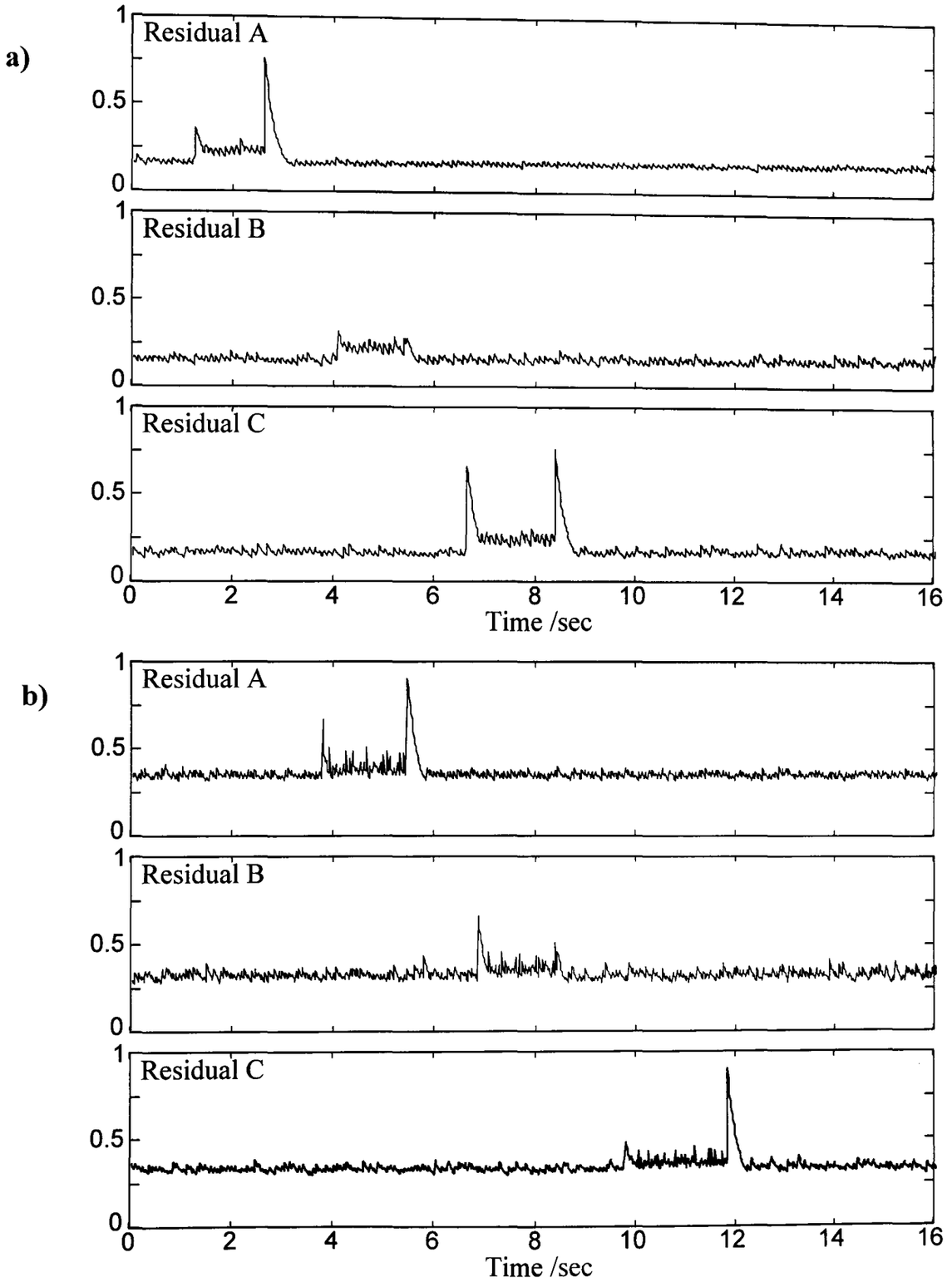

Figure 7.27. Plots of the residual signals for the UIO method for a sequence of voltage sensor faults. a) 10 and b) 30 Hz drive frequency.

The steady-state value of the residuals increases in magnitude as the applied voltages increase with speed. But as before, the increasing discretisation error prevents reliable detection of faults.

From the few results presented for the DOS method it is clear that on the test-rig the detection margin is too small. The observer is too sensitive to noise and not sufficiently sensitive to the fault.

7.9 Summary

For computational efficiency the FDI algorithm is implemented in discrete-time form. This requires that the motor model is discretised. Three different methods of increasing complexity are considered, the Forward rectangular rule, second order matrix exponential expansion and Tustin's method. These are compared for numerical complexity and accuracy. All of these methods become less accurate at high speed or lower sampling rate since the model states are changing quickly. The more sophisticated methods are shown to be significantly better but require more calculations and memory space. The parametrised observer is adopted since it has better sensitivity to faults and good noise rejection. The observer gains are pre-calculated for the discrete-time model at a range of speeds and stored in a lookup table. The choice of pole location is considered. If the feedback gain is too small the observer is unable to track the plant. At high feedback gain the observer is able to track the plant, even at low speed when saturation occurs. However, this high gain is undesirable since it would also make the observer insensitive to faults.

The complete FDI scheme is set up in Simulink and downloaded onto the DSP. The effect of motor speed and loading on the fault-free residuals is considered. It is shown that as the load on the motor increases, the observer error increases because of model mis-match when the increased magnetisation current starts to saturate. The observer error also increases with motor speed as the discretisation error increases.

The FDI scheme is subjected to a sequence of sensor disconnections at different operating conditions. The detectability of voltage, current and speed sensors faults is considered. There are many factors which affect the detectability such as, sampling rate, pole location, noise, loading, discretisation method and unmodelled non-linearities. It is therefore not possible to give a definitive set of results. For any given application additional knowledge is needed as to the nature of the noise, typical operating range and available computation power before the other variables of poles location, sampling time and discretation method can be defined. However, for each of the listed effects methods to evaluate their magnitude are presented, using the sensitivity methods described in chapters four and five. The DOS method is implemented on the test-rig, to re-inforce the theoretical comparison of fault and noise sensitivity with the GOS method.

Chapter 8:

Improving the model and simulation

This chapter describes some of the hardware issues which were neglected in the model but which are likely to affect the real application. In order to produce a more realistic simulation the inclusion of noise on the measurements, non-linear magnetisation characteristics and the behaviour of the inverter are considered.

The aim of this chapter is to look at ways of improving the simulation to produce more realistic results without the need to use hardware to evaluate the FDI schemes. This is desirable since there are a large number of variables within the scheme, such as loading, motor speed, model parameters, pole locations and method of observer feedback design. All of these influence the performance of a design. There are many differences between simulation and the real hardware. For example, noise, model uncertainty, sampling rate and precision, numerical accuracy and physical limits on sensor bandwidth. Most of these can be included in the simulation, especially using the Matlab DSP BLOCKSET toolbox which enables the inclusion of fixed point arithmetic in Simulink models. The three main effects which as yet cannot be included are noise, model mis-match and inverter non-linearity.

8.1 Noise

There are two significant sources of noise on the sensor measurements, 'background' noise from many sources[8.1] and switching transients from the IGBT's in the inverter. The switching frequency is several times higher than the sensor sampling rate, but the transients are short and unless they occur at the instant the conversion is made they have little effect. The switching time for the devices are continuously variable and so some will occur at a sampling instant. Fig. 8.1 shows the noises on a voltage measurement, with the inverter generating a small DC voltage on another phase.

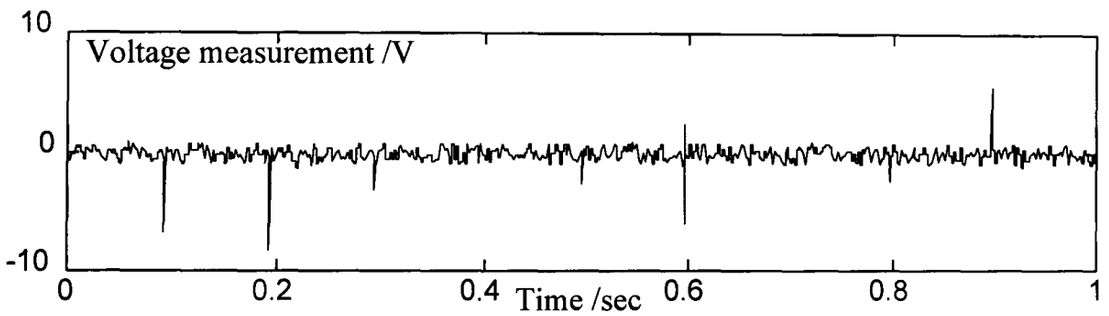

Figure 8.1 The measurement noise on the phase-to-phase voltage sensor Vab with a small DC phase-to-ground voltage being generated on phase C.

The two noise sources are visible, the background coloured noise in the electronics and the spikes from the inverter switching transients. The clock rates of the main DSP and the slave are not synchronised so the interference transients and the sampling instant drift in and out of alignment causing periodic spikes on the measurement.

[8.1] Thermal noise in the analogue electronics or ground noise from the power supplies

To improve the simulation band-limited white noise and random spikes can be added to the measurements to produce more realistic data.

8.2 Model mis-match

For normal operating conditions the motor model is reasonably accurate. The principle of the induction motor is extremely simple. However, the physical motor is rather more complex and contains non-linearities. Four main assumptions were made in producing the motor model in Section 3.2; ideal air-gap flux distribution, ideal magnetisation characteristic, zero temperature coefficient and ignoring the skin effect. The nature of these assumptions and the validity of each is considered in the following section for the test-rig motor and the real traction motor.

8.2.1 Ideal air-gap flux distribution

This is a complex subject involving the geometry of the motor. Several papers consider this in detail. Parkin & Preston 1993) and Williamson & Ralph (1983) have used finite element methods to model the magnetic field patterns within the motor. Melkebeek (1983) has used high order models for the current in each rotor bar. The models derived are not suitable for model-based FDI, since they have many states, with sparse non-linear coupling. The effect of this assumption would only be noticeable in the harmonic contents of the currents, as reported by Brudny & Rogers (1995) and at worst will only contribute to the overall noise floor for both motors.

8.2.2 Zero temperature coefficient

For a typical motor, the winding resistances will change by more than 20% over the operating range. On the test-rig this assumption seems to be valid, since the motor is not heavily loaded and no significant change occurs in the stator resistance when measured before and after sustained running. The traction motor would have to work in a temperature range of -20°C to 80°C during sustained high load operation at low speed. The resistance will vary significantly over this range. If temperature is an issue and cannot be measured, several methods for on-line estimation are available. Wade *et al* (1994) and Chan & Hauqian (1990) consider this since vector control algorithms are very sensitive to changes in rotor resistance. By assuming the temperature through the

motor is relatively constant and changing only slowly these effects can be simulated by altering R_s and R_r in the model.

Thermal models. There are three levels of detail commonly used for thermal models:-

Finite element analysis which details heat flow within the motor components. This can be used to locate 'hot-spots' in a motor design, Sarker *et al* (1991)

Thermal equivalent networks which consider the heat flow between major components in the motor. These can be used to evaluate cooling efficiency and ensure an acceptable limit to thermal stresses, Di-Gerlando & Vistoli (1993)

Solid mass models which just consider internal power losses and heat dissipation to an external environment. These give approximate operating temperatures to enable thermal compensation, Cho *et al* (1992)

8.2.3 Ignoring the skin effect

For large industrial drives the skin effect has been identified as a factor affecting model accuracy. At large slips the resistance of the rotor is observed to increase as the current flows through a reduced area. In the small test-rig motor this can be ignored, White (1996). For the traction motor the rotor current densities would need to be considered to assess the magnitude of the skin effect. This requires knowledge of the internal construction, which is not available.

8.2.4 Ideal magnetisation characteristic

At high slips or at low speed, large flux densities are produced in the motor. These cause magnetic saturation and hysteresis effects. The inductances in the motor are therefore a function of current and frequency. The motors are designed to minimise the hysteresis losses, because the internal heat dissipation would be unacceptable. This can be included in the model as an additional resistance in parallel with the mutual inductance which represent the so called *copper losses* of the motor. On the test-rig using volts-per- Hertz control the effect of the saturation is limited and the model is accurate over a reasonable operating range. For the traction motor saturation is the major non-linear effect which cannot be easily ignored or modelled.

8.3 Flux saturation

For any ideal inductor the magnetic properties would give a linear relationship between magnetising current and flux extending towards infinity in both directions, as shown in Fig. 8.2a. For real inductors, the flux will saturate. When this occurs any further increase in the current will only increase the flux slightly. When the flux is allowed to decay, the current will follow a different curve. This is called *hysteresis*. The magnetic characteristic for a real inductor is shown in Fig. 8.2b.

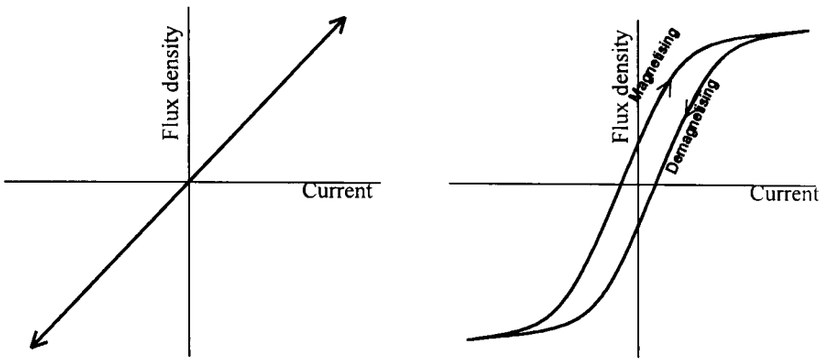

Figure 8.2a & b. Magnetisation characteristic for an ideal and non-ideal inductor.

For the test-rig induction motor it is possible to repeat the identification tests for the fast and slow dynamics to obtain a set of inductances for different magnetising currents, as shown by Rasemussen (1996).

Brown *et al* (1983) show it is not possible to simply make L_m a function of flux in the state space model since, then the core is saturated, there will be cross-coupling terms between the changing flux in one axis and an induced current in the other. Further to this Çolak *et al* (1993) point out that care is needed to distinguish between an absolute current which gets the total flux and the amount by which a change in flux will alter the current. To demonstrate this consider only the saturation effect. Fig. 8.3 shows a graph of current versus flux for the inductor.

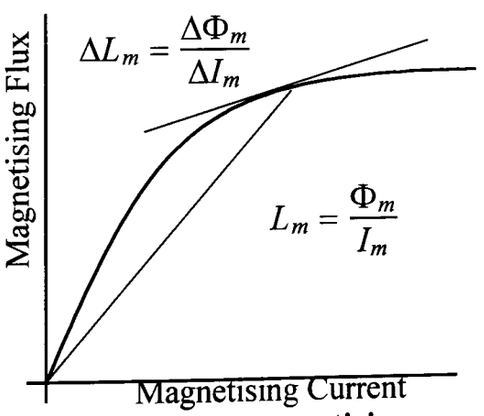

Figure 8.3. Plot of magnetising flux against magnetising current for typical motor.

The magnetic characteristic shown in Fig. 8.3 has two features, an *absolute* (static) inductance denoted by L_m and an *incremental* (dynamic) inductance denoted by ΔL_m. To model this, several methods have been proposed. A definitive review of techniques for modelling saturation is missing from the current literature.

By choosing to model the motor in an arbitrary reference frame, that is co-incident with the flux direction, Brown *et al* (1983) were able to develop a model for saturation in the motor. The use of the flux-oriented reference frame means that the magnetising current is only flowing in one direction and the cross-coupling terms are zero. The model is in the electrical equation form, $\underline{v}=[Z]\underline{i}$ and then converted into state space. The flux oriented reference frame is difficult to work with in a real application since the flux direction is unknown. For a slightly different problem, a self-exciting AC generator, Papadopoulos *et al* (1996) using the method of Brown *et al* (1983) as a starting point, convert the model into the more usable stator reference frame. This approach could be used on the induction motor.

Apart from the two papers referred to previously which derive a non-linear state-space model, most of the models for saturation are too complex to be immediately suited to control techniques. The models are best used to simulate non-linear behaviour in large motors. Amongst the modelling methods in the literature the following papers give detailed consideration to the nature and effect of saturation in motors.

Melkebeek (1983) developed an incremental model for the motor, showing how the classic state-space model alters and that additional high-order terms appear. This model is verified against a real motor. Williamson *et al* (1983) discuss previous work before developing a model to include both saturation and the skin effect. Rather than attempting to modify the state-space equation, the starting point is a new circuit model which includes both saturation and skin effect. This model is shown to produce results which better match the performance of a large industrial drive. An alternative method is given by Amin (1996) in which the field equations for each rotor bar are written down and extended to include saturation. By summing all the bars together, a model of the flux in the complete motor is produced.

8.4 Inverter non-linearities

The inverter is a complex device to model accurately. The individual switching devices can be modelled but are non-linear, Protiwa *et al* (1993). The complete inverter is difficult to model, since it incorporates rapid switching, with large $\frac{di}{dt}$ generated which will excite even the small inductances between devices. For control purposes, it is only necessary to know the steady state characteristics of the inverter. This can be modelled as the voltage difference between the demand and produced voltages, when averaged over time. The effect of load on the inverter is shown by the small drop in the applied voltage which is caused by the increased inverter voltage drop as the sourced current increases, see Fig. 7.16. Note also that the power supply is sufficiently highly rated that the DC voltage into the inverter is not noticeably reduced.

The two main factors which influence the inverter function are the guard time and the voltage drop across the switching device. The guard time is inserted by the inverter driver to prevent both devices being in conduction simultaneously. This reduces the voltages actually produced by the inverter, which become significant at high switching rates. The voltage drop is given by Rasemussen (1995) as:

$$V_{drop} = V_{supply}\left(\frac{T_{guard} - T_{off}}{T_{period}}\right) \qquad 8.1$$

The voltage drop across the switching device can be found from the device data sheet. For the IBGT's used in the test-rig the data sheet gives the model as.

$$V_{ce} = V_T + a \times I^b \qquad 8.2$$

This voltage drop is only present during the time when the bridge is high. During the off time the behaviour of the devices depend on the direction of the current flow. The model quickly becomes unmanageable, becoming a function of duty cycle, current and load reactance. For a given practical application the function can be obtained experimentally as in Section 6.3.1.

8.5 Summary

This chapter has shown how the noise on the test-rig sensor measurements has two sources; coloured noise in the electronics and transient spikes from the switching of the IGBTs. These two noise sources can be added onto measurements in the simulation.

Two significant model discrepancies exist, temperature effects and flux saturation. Temperature simply alters the winding resistances, which can be estimated or compensated for. Saturation is a much more complex effect. It can be modelled in a number of ways but these are too non-linear for classical observer design methods.

For the inverter, modelling of the switching devices is impractical, for general simulation because of the small time-steps required. The static behaviour can be modelled as a voltage drop between the inverter demand and actual voltage. This would improve the overall simulation but would have little effect on the FDI performance.

Chapter 9:

Conclusion

9.1 Identifying the aim for this thesis

This thesis has arisen as part of a larger research project run by the Mechanical Engineering Centre on rail traction and braking control as part of which an EPSRC-CASE award was funded with a brief to investigate the use of modern fault-detection and fault-tolerance techniques on the EMU's traction system. There is potentially a large scope for work on this, since with the exception of the braking system, current industry practice is limited to condition monitoring a range of measurements. In the traction system hardware redundancy is largely relied on, since the EMU concept has inherent duplication of power systems between carriages. The scope for fault-tolerance within the power electronics is limited, because of the simplicity of the devices. For the induction motors a large range of FDI techniques already exists. The remaining aspect of the traction system is the instrumentation. Although much work has been done for sensor FDI, almost no attempts have been made to apply sensor FDI to power systems. The aim of this thesis is to develop a sensor fault-tolerant torque and flux estimator for an induction motor drive.

9.2 Modelling the traction system

Despite the actual traction system and controller being a complex and non-linear system, a simple model can be derived to enable it to be simulated. This consists of four sub-models, the motor, the inverter, the controller and the mechanical model for the train. A textbook model can be used for the motor, this assumes a linear magnetising characteristic. The state-space form of this model is bilinear, with speed-dependent dynamics. The inverter can be modelled either as an ideal sinewave or PWM source. For this study a simple rotating inertia with frictional loses can be used to model the train dynamics. The controller design is important, the real controller consists of PI loops for motor torque and flux, these are gain scheduled to compensate for changing dynamics and to damp resonance in other systems. In the simulation an open-loop controller is used for the simplified model. The complete model has been validated against performance data from GEC-Alsthom and shown to give realistic torque, flux, current and acceleration.

9.3 Contribution of this thesis

It has been possible to separate the contributions of this thesis into three main areas, new theory, new applications of existing theory and the practical application.

9.3.1 New theory: Closed-loop observers for flux estimation

Existing equipment uses an open-loop estimator to calculate torque and flux. By calculating an expression for the estimation error it is shown to have a significant steady state error at low speed. It is also shown to have large transient dynamics. At low speed accurate estimation is important since the motor's torque is greatest and the potential flux is large.

Closed-loop observer techniques have been considered to produce an estimator with better dynamics and smaller steady state error. It is proved that the standard methods to decouple bilinear terms cannot be applied for the induction motor problem. The motor dynamic's are strongly speed dependent and desirable error dynamics cannot be obtained across the entire operating range with a fixed gain.

The motor model has significant speed-dependent dynamics and this has had to be included in the design of the observer feedback. To limit the amount of storage required an attempted was made to find the observer feedback as an implicit function of speed. This is shown to become complex and likely to be sensitive to numerical errors. It is necessary to pre-calculate the feedback matrix and store in a lookup table for a range of speeds. Using the structure inherent in the model a simple design using bilinear feedback has been found, where by two poles can be freely assigned, with the other two forming a complex conjugate pair, with negative real parts. Using a simple Lyapanov proof this is shown to be stable but the poles become very oscillatory with speed. The motor control is especially suited to sliding mode control, since the actuators are inherently discontinuous. There has been a small but sustained interest in sliding mode observer designs in the literature. A basic sliding mode observer design based on Utkin's method has been extended to include feedback parametrised for speed for the motor. The use of soft switching is also considered to avoid chattering. This thesis has shown, in simulation, that the sliding observers are unsuitable for oscillatory plants especially with high feedback gains. The main drawback of sliding observers lies in their implementation, where the observer algorithm is event driven rather than calculated at

regular fixed times. The use of error feedback significantly reduces the steady state error in the estimates. It also enables the dynamics of the error to be assigned. By increasing the gain this convergence rate can be made arbitrarily fast.

All of the observers developed in the thesis have been shown to work in simulation. To assess the merits of these under more realistic condition a toolbox of methods has been put together. Using data from a real motor the bilinear and parametrised observers have been shown to give accurate estimates of motor torque, with both good steady state and transient behaviour. Only a very limited set of data was available which constrained the amount of on-line testing. The data is sufficient to demonstrate the features of the observers, the noise sensitivity of the bilinear observer and advantages of being able to assign all the poles of the error dynamics. Calculating the frequency domain coupling between the disturbance sources and the estimated state vector enables comparison to be made, for sensitivity to noise, parameter changes and errors on the speed sensor. The results of the frequency domain analysis are verified in time domain simulation. The poor noise performance of the bilinear observer is clearly visible as a high coupling between the noise and the states at high speed. The observer gain also affects the noise sensitivity and robustness to model mismatch. The sensitivity analysis shows that these two have conflicting criteria for the selection of the feedback gain. High gain will force the observer to converge in the presence of small model discrepancies, as shown practically on the test-rig motor. Low gain is required for good noise rejection. For the induction motor drive the eigenvalues of the error dynamics need not be placed more than a couple of time faster than the poles of the motor dynamics. For an individual system the feedback gain can be optimised with knowledge of the real application.

9.3.2 New applications: Sensor fault tolerant estimation

Despite large amounts of independent research for fault detection and power electronics, there is little overlap between these fields. The most significant work has been done on the detection of mechanical faults with parameter identification or frequency analysis. This thesis has shown that there is considerable scope either for sensor fault detection or for reducing the number of sensors on the drive. From simple parity equations to observer based methods a range of schemes exist for handling sensor faults.

Using Kirchoff's laws a single sensor fault correction scheme has been developed. When a fault is detected the measurement can be switched to an estimate from the other two sensors. A small delay in detecting a fault, passes an error to the estimator. This has been shown to excite significant transients in the estimator, which an intermittent fault would continually excite.

The estimator for flux and torque can be improved using a closed-loop observer. This has the drawback of requiring a speed measurement, through this is readily available on the train. The observer feedback can also be used to achieve other objectives such as fault isolation. By designing a bank of observers which are independent of a subset of sensors, a sensor fault can be isolated. Two basic methods for observer based fault detection are reported in the literature for linear plants, the generalised and dedicated observer schemes, (GOS and DOS). In this thesis these methods for linear systems have been extended to the bilinear motor model.

For the DOS method it is necessary to consider the current and voltage sensors separately. The motor model is fully observable with only one current sensor. This enabled an observer feedback design which was independent of two sensors. The same feedback can be used in the other two phases by rotating the reference axes. Giving all three observers the same dynamics. To isolate a voltage sensor fault an observer which uses only one input to produce a states estimate is needed. For linear plants this technique is well developed and called the unknown input observer, (UIO). This technique has been extended to the bilinear motor model, for which it is possible to decouple two voltages sensors. The GOS method as presented in the literature is not suitable for combining the two different type of sensors. However, a bank of observers each using a different pair of current and voltage sensors can be produced by exploiting Kirchoff's law to estimate one sensor measurements from the other two. This leaves the basic observer design unchanged, it is supplied with two pairs of measured currents and voltages and the two estimates. In this way any of the observer designs can be used. In simulation this technique is shown to be able to cope with any one sensor fault, but with a restriction on the minimum separation of faults of different sensors. The dedicated observer is able to detect and correct for up to two sensor faults in one type of sensors.

9.3.3 Practical application. Building a hardware test-rig

Since it is impractical to attempt to evaluate the fault detection scheme on a motor of similar power to the traction system a small test-rig was built. The use of modern IBGT and drivers has been used to produce a compact inverter with minimal components. The flexibility of the DSP Card meant that most of the inverter could be implemented in software. Time division multiplexing was necessary to overcome the limited analogue IO capacity of the DSP card, this also reduced the cost. The DSP software was auto-coded from the Simulink diagrams using the Matlab Real-Time Workshop. This enabled rapid development of the real-time code, though not necessarily efficient. The thesis demonstrates the enormous potential of the D-Space card and the Real-time workshop for rapid proto-typing of control systems, whilst acknowledging the substantial cost of this type of development suite.

The motor parameters can be identified with a simple single phase method. For simulation the continuous-time motor model and observers have been implemented discretely using an integration routine such as Rutta-Kutta. Such methods are accurate but are computationally intensive. To implement the observer on the DSP in real-time a simple discrete-time form is needed. Simulation shows that the first order method with a sampling rate of 1KHz is sufficient for the application.

9.4 Discussion of the results from the test-rig

By plotting the magnitude of the fault-free residual and the fault residual against the two operating variables; speed and load; a contour plot is produced. When the fault free residual is greater than the fault residual the fault is detectable. For voltage sensors the detection is affected by the volts-per-Hertz control, which applies small voltages at low speed. Detection of voltage sensor faults is better at high speed and low loads, whilst current sensor fault detection is better at low speed with high loads. Combining the data for the fault-free and fault-present residuals defines an operating region for reliable detection of faults for each sensor. These are only shown qualitatively since they are very implementation specific. With the test-rig the FDI techniques have be demonstrated in real hardware but this is only for a limited set of conditions.

For the test-rig the most significant factor to degrade the detectability was discretisation error. However, the simulation results show that by using Tustin's approximation to

produce the discrete from of the observer the error an be significantly reduced. This does have a computational penalty but this is small on a fast DSP. The effect of noise, model mis-match and observer design can be assessed using sensitivity analysis. By storing the observer gains as a look-up table, further speed advantage is obtained and freedom to assign all four poles of the observer's error dynamics for all speeds. For both the test-rig and the traction motor, model mis-match is the most significant effect. For estimation the observer design is predominantly influenced by model mis-match. Temperature which can be compensated for and saturation which requires further investigation. The sensitivity analysis for magnetising inductance is mis-leading. The sensitivity function is the effect of a parameter error in the non-saturated magnetising inductance and not the effect of saturation. On the test-rig FDI scheme is dependent on the volts-per-Hertz control limiting the flux saturation. The traction motors are operated with some degree of saturation to optimise the power-to-weight ratio. More detailed modelling of the motor is needed to incorporate saturation into the simulation, to enable testing before committing to hardware. At present the data required to do this and not available.

9.5 Future work

The aim of this thesis was not to detail the construction of a induction motor test bed, but considerable work has gone into setting one up. It is hoped that the hardware and experience gained from it will be put to good use. The test-rig has sufficient flexibility to explore other problems in both FDI and control of induction motors, presently it is being used for evaluating fuzzy observers, Lopez *et al* (1998)

The scope for further work on the practical side still remains large. The next major step would be to assess the factors affecting the implementation on real traction equipment of a model based FDI scheme for sensor faults. This would require detailed knowledge of the actual traction system and operation environment. A preliminary assessment of the application can be made using the analysis tools developed in Chapters 4 and 5 with the more detailed simulation outlined in Chapter 8.

On the theoretical side, the effect of the motor non-linear magnetisation characteristic needs to be better modelled so that it can be incorporated into the fault detection method.

9.6 Concluding remarks.

This thesis has explored a significant gap in the literature, relating to the application of observer based fault detection to the instrumentation of electric drives. No single definitive result is given, the thesis develops a range of techniques and the necessary tools to evaluate them. However, the GOS method has been clearly demonstrated to work on a small scale test-rig in real-time across most of the normal operating range of the motor. Also shown is the large 'gulf' it is necessary to negotiate in taking the theory beyond simulation to run in real-time on the an induction motor.

Appendices

Appendix A: Reference frames and transformations

A.1 Three phase voltages and currents

The inverter generates voltages relative to the ground supply. These are called *phase-to-ground* voltages and labelled V_a,V_b,V_c for the three phases. The currents flowing in each phase are I_a,I_b,I_c referred to as phase-to-ground currents. See Fig. A1.

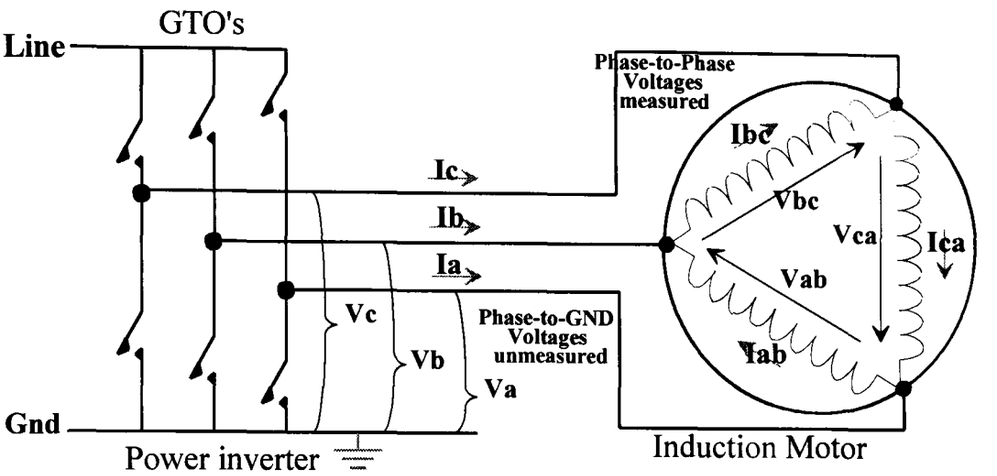

A.2 Two phase notation

The three circuits are resolved into 2 orthogonal axes called direct and quadrature referred to as DQ axis notation. In this two-axis notation two different alignments can be used, depending on whether the phase-to-phase quantities or the phase-to-ground quantities are aligned with the D Q axes. Fig. A2a and b show the two cases.

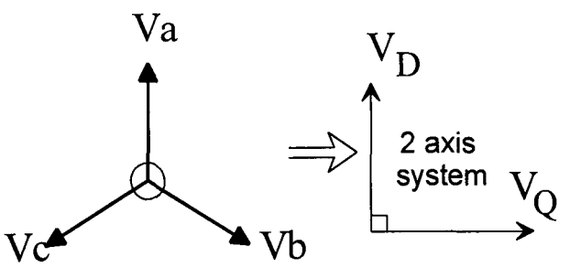

Figure A.2a. Diagram showing orientation of phase-to-ground voltages in 3 phase and 2 axis forms.

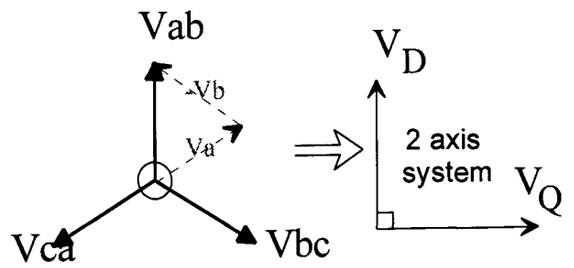

Figure A.2b. Diagram showing orientation of phase-to-phase voltages in 3 phase and 2 axis forms. Dotted lines show the rotation of the axes relative to the phase-to-ground voltages.

A.3 Transforms between 3 phase and 2 axis notation

The following basic transforms are needed between the three phase and two axis notation. This can be written down from basic trigonometry, the three phase voltage and current directions are resolved into their direct and quadrature components. A scaling factor of √⅔ is included to give a power invariant transform. Ioannidis (1994) describes this as being "*equivalent to rewinding the motor with √⅔ times as many turns per winding before reconnecting as a two phase machines. This means that both the rated phase currents and voltages are increased by √1½. The power per phase is increased by 1½, but because the number of phases has been reduced by ⅔ the total power is unchanged and therefore the transform is called power invariant transformation.*"

$$\begin{bmatrix} Vo \\ Vd \\ Vq \end{bmatrix}_{2axis} = \sqrt{\frac{2}{3}} \underbrace{\begin{bmatrix} 1/\sqrt{2} & 1/\sqrt{2} & 1/\sqrt{2} \\ 1 & -\frac{1}{2} & -\frac{1}{2} \\ 0 & \sqrt{3}/2 & \sqrt{3}/2 \end{bmatrix}}_{At} \times \begin{bmatrix} Va \\ Vb \\ Vc \end{bmatrix}_{3phase} \quad \text{(A1)}$$

The 3 phase-to-ground voltages are measured with respect to ground, and form a closed loop. This is used as a dummy equation to make the transform invertible so that the reverse transform can be obtain, *Vo* is always zero. The reverse transform is simply the inverse of the 3phase to 2axis transform *At*.

$$\begin{bmatrix} Va \\ Vb \\ Vc \end{bmatrix}_{3phase} = \begin{bmatrix} 0.33 & 0.8165 & 0 \\ 0.33 & -0.4082 & 0.7071 \\ 0.33 & -0.4082 & -0.7071 \end{bmatrix} \times \begin{bmatrix} Vo \\ Vd \\ Vq \end{bmatrix}_{2axis} \quad \text{(A2)}$$

These transforms can be used on either currents of voltages in either phase-to-phase or phase-to-ground orientations, as long as care is taken to ensure consistency in any given system.

Ioannidis D.A., (1994) Networker Motor Controller Report, Internal report. GEC Alsthom Traction.

A.4 Converting phase-to-phase and phase-to-ground orientations.

The following two transforms can be written down by inspection of Fig. A.2.

$$I_{phase-to-ground} = \begin{bmatrix} 1 & -1 & 0 \\ 0 & 1 & -1 \\ -1 & 0 & 1 \end{bmatrix} I_{phase-to-phase} \quad \text{from } Ia = Iab - Iac \text{ etc}$$

$$V_{phase-to-phase} = \begin{bmatrix} 1 & -1 & 0 \\ 0 & 1 & -1 \\ -1 & 0 & 1 \end{bmatrix} V_{phase-to-ground} \quad \text{from } Vab = Va - Vb \text{ etc}$$

Both if these transform matrices are not invertible. For this thesis these inverse transforms are not required.

A.5 Transforms required in the thesis

The following transforms are required in the thesis.

A.5.1 Three phase voltage phase-to-phase to 2 axis voltage phase-to-ground.

The inverse of this can be written down as $T1$.

$$T1\text{: } V_{3\sim phase-to-phase} = \begin{bmatrix} 1 & -1 & 0 \\ 0 & 1 & -1 \\ -1 & 0 & 1 \end{bmatrix} At \times V_{DQphase-to-ground} \text{ which is not invertible.}$$

The required transform, $T2$, can be calculated from three phase theory, with an additional dummy equation to maintain the balance in the 3 phase system, Ioannidis (1994). This is used to make the transform orthogonal such that $X \times X^T = I$ The dummy equation is used to find X such that $X^{-1}=X^T$.

Alternative the psuedo-inverse can be used.

$$T2\text{: } V_{DQphase-to-ground} = pinv\left([T1] \right) \times V_{3\sim phase-to-phase}$$

$$T2 = \begin{bmatrix} 0.4048 & 0 & -0.4082 \\ -0.2357 & 0.4724 & -0.2375 \end{bmatrix}$$

But from Kirchoff's laws $-V_{ab} - V_{ca} = V_{bc}$ therefore

$$T2 = \begin{bmatrix} 0.4048 & 0 & -0.4082 \\ 0 & 0.7071 & 0 \end{bmatrix}$$

A.5.2 Three phase currents phase-to-ground to 2 axis currents phase-to-phase.

Once again this can be found from the psuedo-inverse of the reverse transform for give.

$$T3 = \begin{bmatrix} 0.4082 & -0.4082 & 0 \\ 0.2357 & 0.2357 & -0.4083 \end{bmatrix}$$

Appendix B. Simulink block diagram of inverter

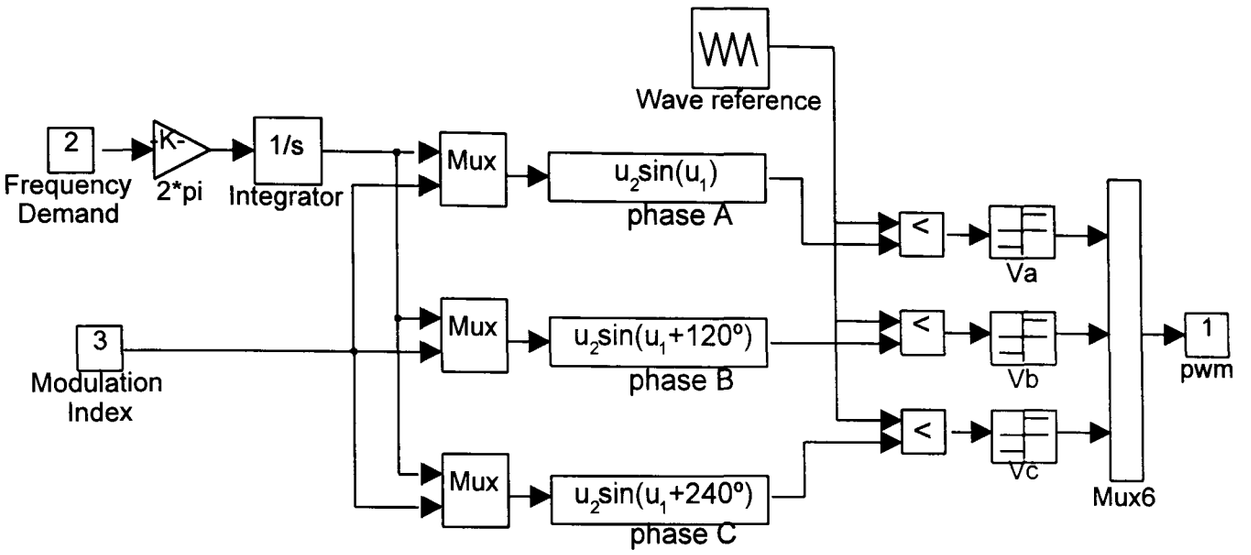

Figure B.1 Simulink block diagram for the asynchronous PWM inverter.

Appendix C. Compact electrical notation

The applied voltages and motor currents then resolved into two orthogonal axes can be expressed as complex quantities. For example the stator current $Is = I_{sD}+jI_{sQ}$

The electrical equation for the motor given as Eq 3.1;

$$\begin{bmatrix} V_{sD} \\ V_{sQ} \\ 0 \\ 0 \end{bmatrix} = \begin{bmatrix} R_s+s(L_s) & 0 & sL_m & 0 \\ 0 & R_s+s(L_s) & 0 & sL_m \\ sL_m & \omega_r L_m & R_r+s(L_r) & \omega_r(L_r) \\ -\omega_r L_m & sL_m & -\omega_r(L_r) & R_r+s(L_r) \end{bmatrix} \begin{bmatrix} I_{sD} \\ I_{sQ} \\ I_{rD} \\ I_{rQ} \end{bmatrix}$$

can be rewritten using the complex quantities

$$\begin{bmatrix} V_{sD} \\ V_{sQ} \\ - \\ - \end{bmatrix} = \begin{bmatrix} a & b & c & d \\ -b & a & -d & c \end{bmatrix} \begin{bmatrix} I_{sD} \\ I_{sQ} \\ I_{rD} \\ I_{rQ} \end{bmatrix} \Longrightarrow \tilde{V}_s = (a-jb)\tilde{I}_s + (c-jd)\tilde{I}_r$$

to give the compact form Eq. C1.

$$\begin{bmatrix} \tilde{V}_s \\ 0 \end{bmatrix} = \begin{bmatrix} R_s+s(L_s) & sL_m \\ (s-j\omega_r)L_m & R_r+(s-j\omega_r)L_r \end{bmatrix} \begin{bmatrix} \tilde{I}_s \\ \tilde{I}_r \end{bmatrix} \qquad \text{(C1)}$$

The matrix of impedances in Eq. C1 can be separated into constant terms and those in the Laplace operator s. The equation can then be re-arranged into a state-space form.

$$\begin{bmatrix} \dot{\tilde{I}}_s \\ \dot{\tilde{I}}_r \end{bmatrix} = \begin{bmatrix} L_r R_s - j\omega_r L_m^2 & L_s R_r - j\omega_r L_m L_r \\ -L_m R_s - j\omega_r L_m L_s & L_s R_r - j\omega_r L_r L_s \end{bmatrix} \begin{bmatrix} \tilde{I}_s \\ \tilde{I}_r \end{bmatrix} + \begin{bmatrix} L_r \\ -L_m \end{bmatrix} \tilde{V}_s \qquad \text{(C2)}$$

Appendix D. Train speed and motor speed

D.1 Maximum motor speed

The maximum motor speed has not actually been quoted by the manufacture but can be easily calculated. From the basic train parameters the maximum motor speed can be calculated as follows.

- The maximum train speed is 120km/h which is 33.3m/s.
- The wheel diameter of 0.8m gives a circumference of 2.5m.
- At 33.3m/s the wheels will rotate 13.25 times a second.
- With a gear-ratio of 1:6.93 the motor will rotate 91.46 times per second.
- This gives the maximum motor speed of 574.42 rad/s

The motor has 2 pole-pairs and hence two complete rotations of the applied field is need for each rotation of the motor. Allowing for a ten percent slip, the maximum electrical drive frequency will be 200Hz.

Appendix E. Existence criteria for a bilinear observer for an induction motor

It is readily shown that the motor model given as Eq. E1. satisfies the general observability condition, that is the observability matrix is full rank. This result means that an observer can be designed for a specific rotor speed but does not guarantee that a single fixed gain observer is suitable for all speeds.

$$\begin{aligned}\dot{\underline{x}} &= (A + N\omega_r)\underline{x} + B\underline{u} \\ \underline{y} &= C\underline{x}\end{aligned} \tag{E1}$$

Hac (1992), proposed a disturbance decoupling observer design in which the observer poles are made independent of the bilinear inputs. This was work was an extension of the designs first proposed by Hara *et al* (1976). Further extensions have recently been proposed by Shields *et al* (1995) to deal specifically with the fault detection problem. The method would appear at first sight to be ideal for this application, however, a number of conditions must be satisfied. For the system model in Eq. E1 a bilinear observer given Hac (*1992*) takes the form

$$\begin{aligned}\dot{\underline{v}} &= H\underline{v} + L\underline{y} + J\underline{u} + \hat{B}\omega\underline{y} \\ \hat{\underline{x}} &= \underline{v} + P\underline{y}\end{aligned} \tag{E2}$$

If the observation error is defined as

$$\underline{e} = \hat{\underline{x}} - \underline{x} \tag{E3}$$

then its dynamics are governed by

$$\dot{\underline{e}} = H\underline{e} \tag{E4}$$

E4 where H is an arbitrary matrix if the following conditions are satisfied

$$\hat{B}C + (PC - I)N = 0 \tag{E5}$$

$$H(PC - I) - (PC - I)A - LC = 0 \tag{E6}$$

$$J = -(PC - I)B \tag{E7}$$

By noting the form of C in Eq. E1 and partitioning N into 2x2 sub-matrices as

$$N = \begin{bmatrix} N_{11} & N_{12} \\ N_{21} & N_{22} \end{bmatrix} \tag{E8}$$

then it is a relatively straightforward procedure to show that the unique solution to Eq. E5 is:

$$\hat{B} = \begin{bmatrix} 0 \\ N_{21} - N_{22}N_{12}^{-1}N_{11} \end{bmatrix} \tag{E9}$$

$$P = \begin{bmatrix} I \\ N_{22}N_{12}^{-1} \end{bmatrix} \tag{E10}$$

With similar 2x2 partitions for H and A and using Eqs. E9 and E10, Eq. E5 can be rewritten as:

$$\begin{bmatrix} H_{12}N_{22}N_{12}^{-1} & -H_{12} \\ H_{22}N_{22}N_{12}^{-1} & -H_{22} \end{bmatrix} - \begin{bmatrix} 0 & 0 \\ N_{22}N_{12}^{-1}A_{11} - A_{21} & N_{22}N_{12}^{-1}A_{12} - A_{22} \end{bmatrix} - \begin{bmatrix} L_1 & 0 \\ L_2 & 0 \end{bmatrix} = \begin{bmatrix} 0 & 0 \\ 0 & 0 \end{bmatrix} \tag{E11}$$

From which it follows that:

$$H_{12} = 0$$

$$L_1 = 0$$

$$H_{22} = A_{22} - N_{22}N_{12}^{-1}A_{12}$$

$$L_2 = (A_{22} - N_{22}N_{12}^{-1}A_{12})N_{22}N_{12}^{-1} - N_{22}N_{12}^{-1}A_{11} - A_{21}$$

H_{11} and H_{21} can be selected arbitrarily and since H_{12}=0 the error dynamics in Eq. E.4 are defined by the eigenvalues of H_{11} and H_{22}. However, for the structure of the model defined in E1 it can be shown that

$$H_{22} = \begin{bmatrix} 0 & 0 \\ 0 & 0 \end{bmatrix}$$

regardless of the various parameter values. As a result, the method of Hara *et al* (1976) and more importantly the method of Shields & Du (1995) cannot be applied to obtain a stable observer.

Appendix F. Problems with the implementation of the variable gain observer

During simulation the observer's estimation error becomes unstable and also there is an undesirable transient when there is an initial condition error. Fig. F.1 shows the error in the torque estimate obtained from the estimated states.

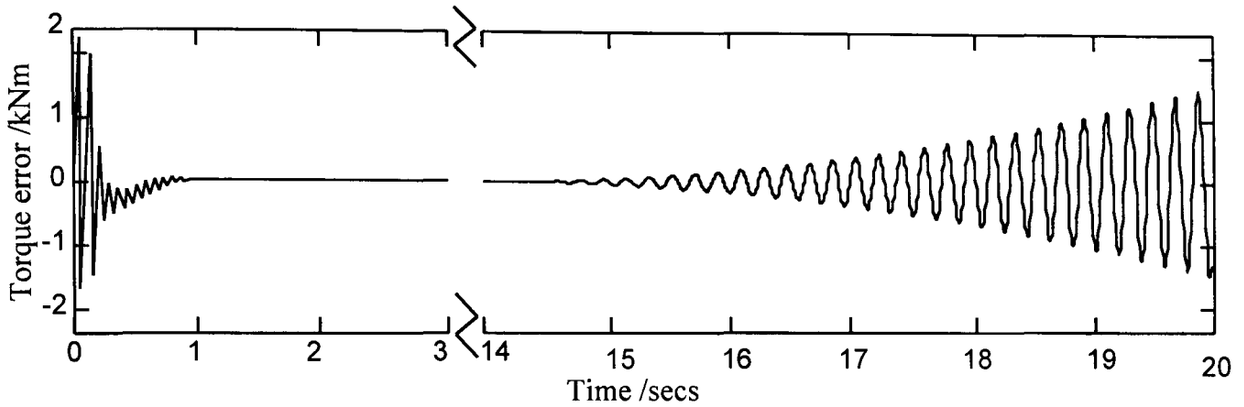

Figure F.1. A graph of the error in the torque estimate with no error in initial conditions.

The elements in the gain matrix have a large range of magnitudes within the coefficients and high powers of speed. This is likely to cause errors in the calculation of $L_{(\omega)}$. By removing the sub-system for generating the feedback matrix from the observer it is possible to plot the actual observer gain with speed. This is done by applying a ramp in speed to its input and plotting the output of the variable gain block. In this way it is possible to check the accuracy of the gain matrix calculations.

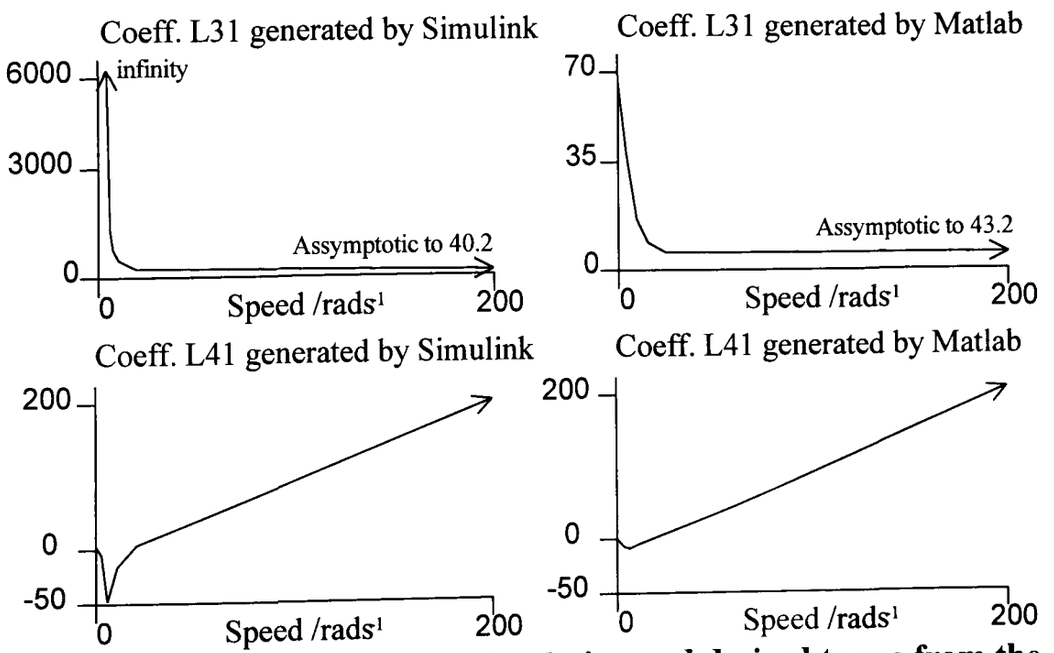

Figure F.2. Gain terms calculated by simulation and desired terms from the symbolic expression.

The coefficient terms L11, L12, L21 & L22 are clearly acceptable since they are constant or linear. Two of the polynomial fraction terms are shown in Fig. F.2. The plots of L31 & L41 against speed, as generated from the Simulink implementation of the equations are shown with their desired shape produced from the Symbolic Matlab expression, evaluated to at least 16 digit accuracy. The errors in these terms are also reflected in L32 & L42.

The poles of any observer are sensitive to the coefficients of the feedback matrix. The four polynomial terms display considerable errors and it is likely that these will be reflected in the eigenvalue locations of the state error dynamics. The root locus of the error dynamics, $\dot{e} = (A + N\omega - L_{(\omega)}C)e$, varies with speed is shown in Fig. F.3. The eigenvalues of the error dynamics are plotted for intervals of 0.1 rads^{-1} of the speed ω.

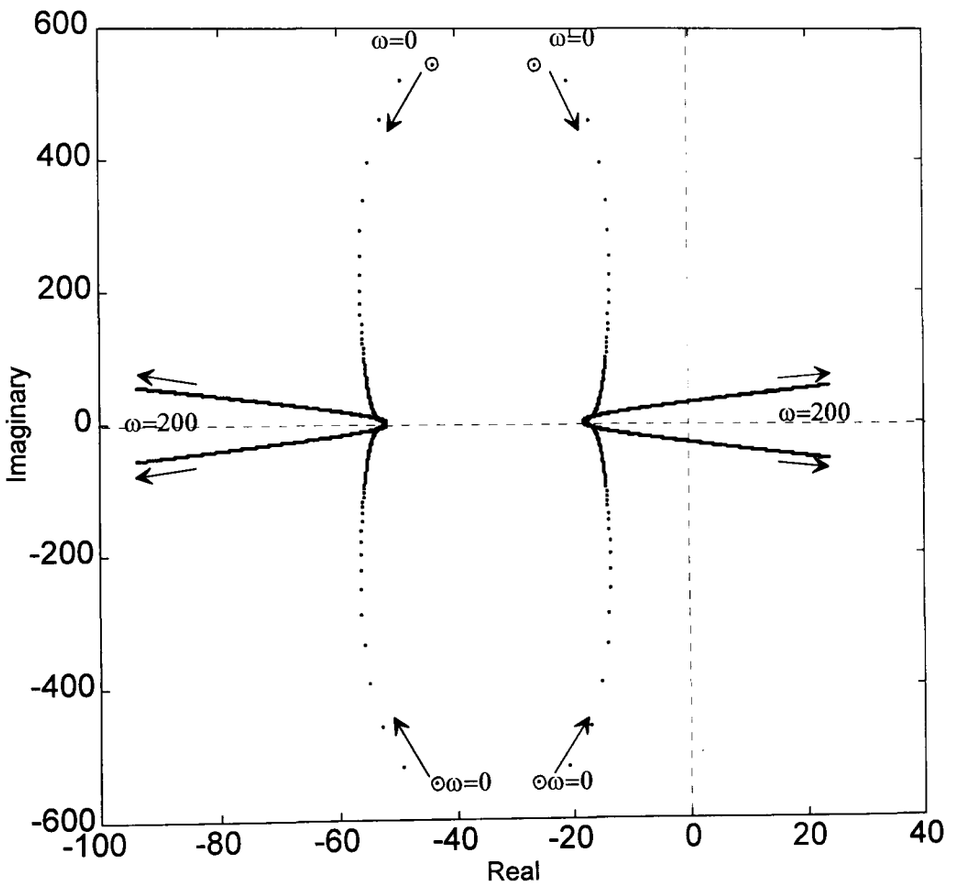

Figure F.3. The locus of the eigenvalues of the Simulink observer with speed.

The poles of the error dynamics move with speed. At low speeds they form two oscillatory pairs which explains the initial behaviour. By 2rads^{-1} the poles are close to the desired location and they remain there until about 100rads^{-1}. They then track out in a star burst fashion, by 120 rads^{-1} two of the poles have crossed into the right-hand half plane. This explains why the observer goes unstable as the motor accelerates.

Appendix G. Relationship between rotor time constant and motor power

Section 4.7 has shown that the bilinear observer is less oscillatory for induction motors were $R_r >> L_r$. To explore how this inequality relates to the physical motor the rotor time constant, *Tr,* is plotted against the rated power of the motor as shown in Fig. G.1. The parameters for these motors were taken from papers included in the references section of this thesis.

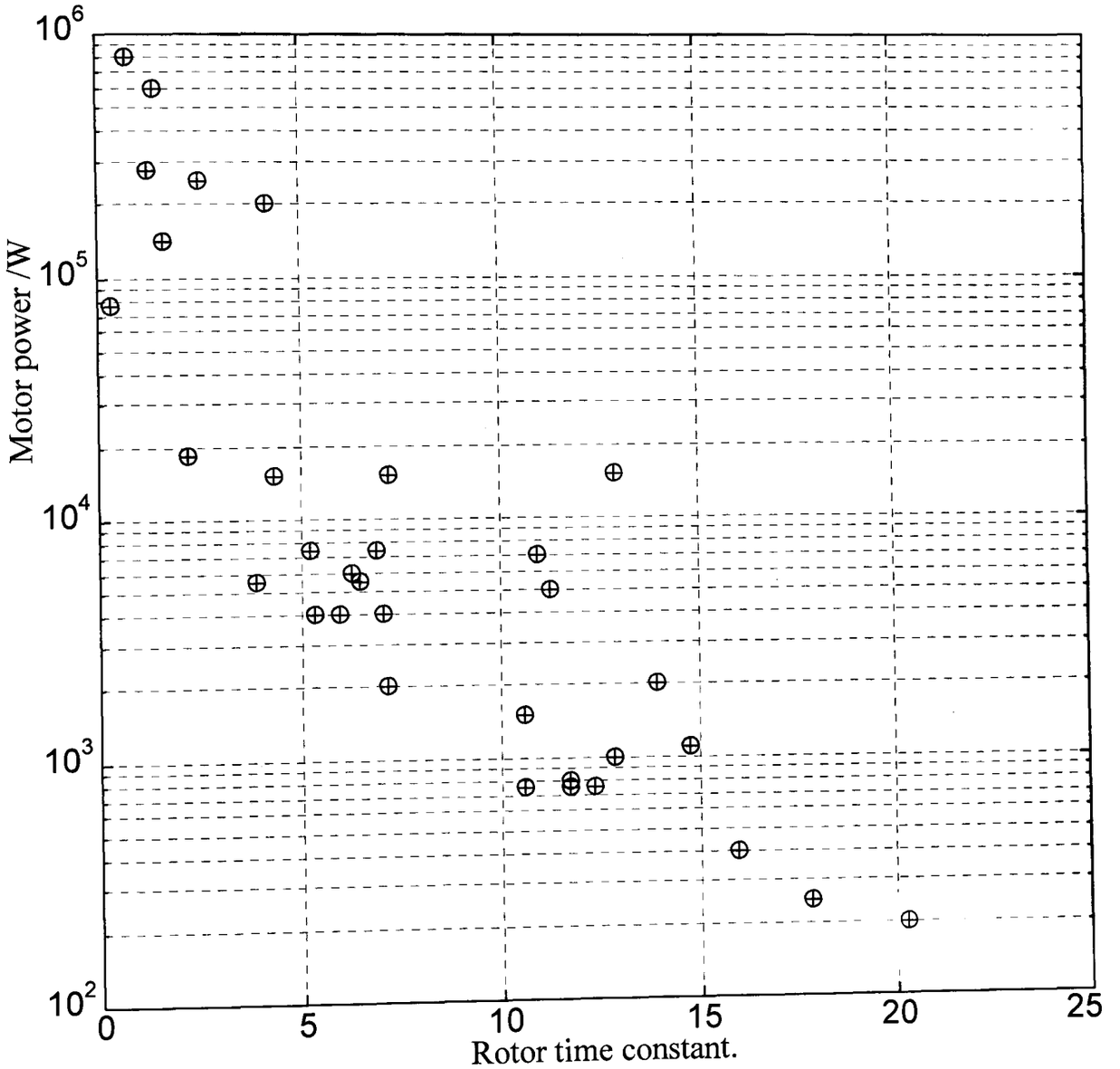

Figure G.1. Graph of motor power against rotor time constant for a range of induction motors.

Appendix H. Occurrence of limit-cycle at high speed in a sliding mode observer

The sliding mode observer described in Section 4.8 goes into a limit-cycle at high speed. To show that this is an effect of the eigenvalue locations rather than the bilinear model. Consider the state dynamics matrix A matrix for a fixed speed, $\omega=0$, then use the '*place*' function to assign increasingly more oscillatory poles to the observer's estimation error.

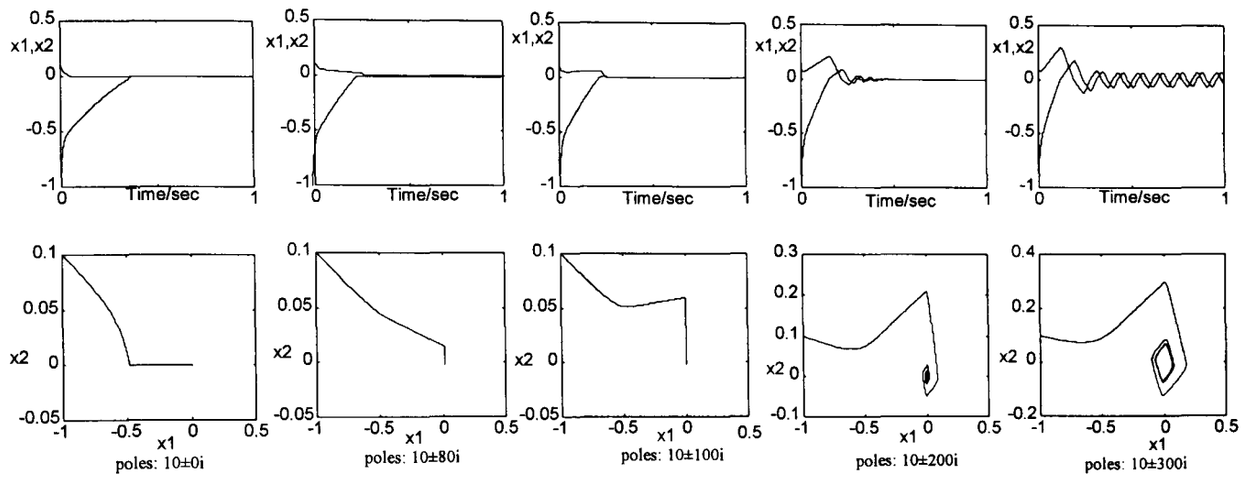

Figure H.1. State trajectory plots for sliding mode observer with increasingly oscillatory pole locations.

Fig. H.1 shows the effect of the sliding mode observers eigenvalues having complex conjugate pairs with increasing larger imaginary parts. This shows why the state estimates of the sliding mode observer, goes into a limit cycle as the speed increases. This behaviour is also gain dependent, the higher the switching gain the lower the imaginary value at which a limit cycle occurs.

Appendix I. Envelope detection of the residual signals

The residual signal will be sinusoidal. In order to convert this into a Boolean fault signal an envelope detector is used. This is then either threshold detected to obtain the fault signal or several are compared to select the minimum, which is then assumed to be fault-free. The block diagram for the envelope detector is shown in Fig. I1.

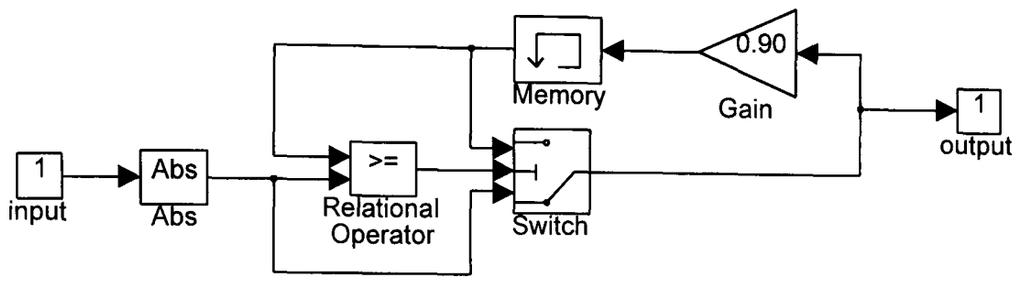

Figure I.1. Simulink Block diagram of envelope detector.

Fig. I2 shows a fault signal, the corresponding residual, the output of the envelope detector and the resulting detected fault after a threshold is applied.

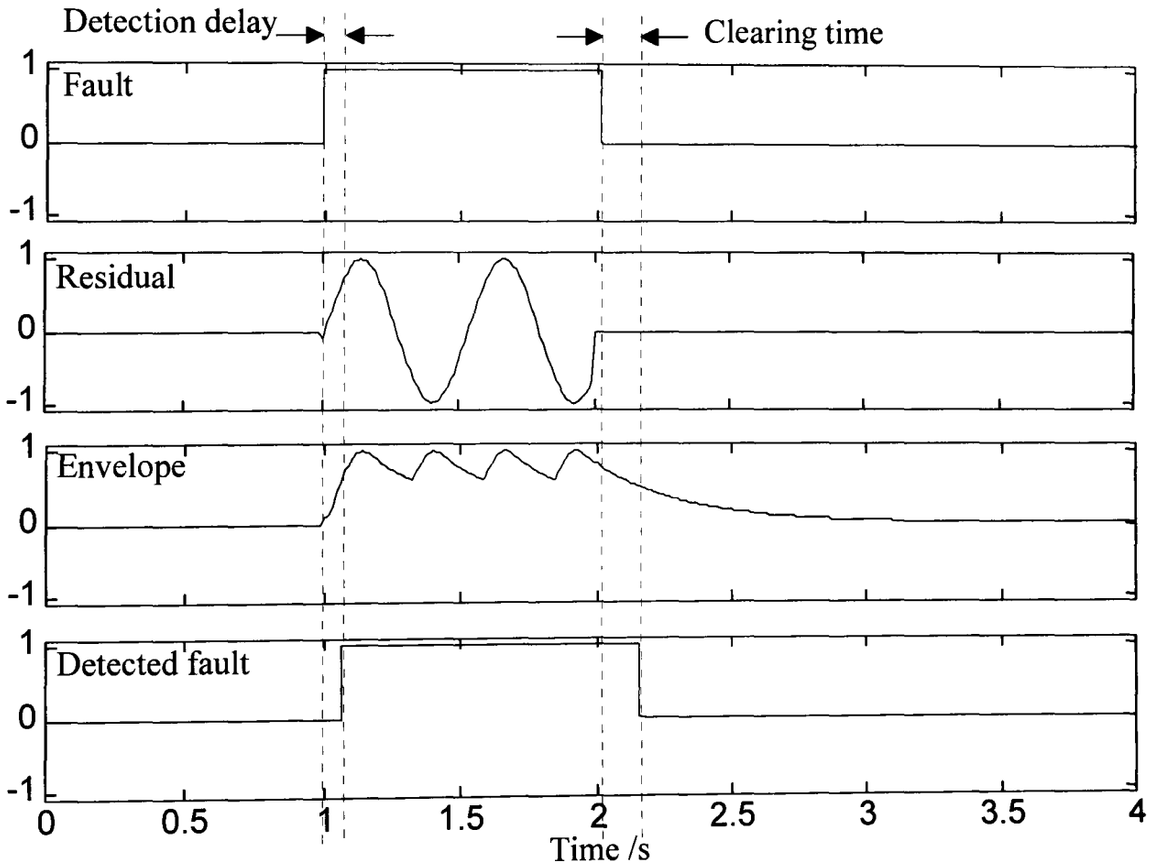

Figure I.2. Sketch showing how a fault is detected from the residual.

There is a delay in detecting the fault, this is because the residual signal takes sometime to reach the threshold. There is also a delay in detecting that the fault has cleared, this is due to the time taken for the envelope detector to decay.

Appendix J. Schematic Diagram of test-rig inverter

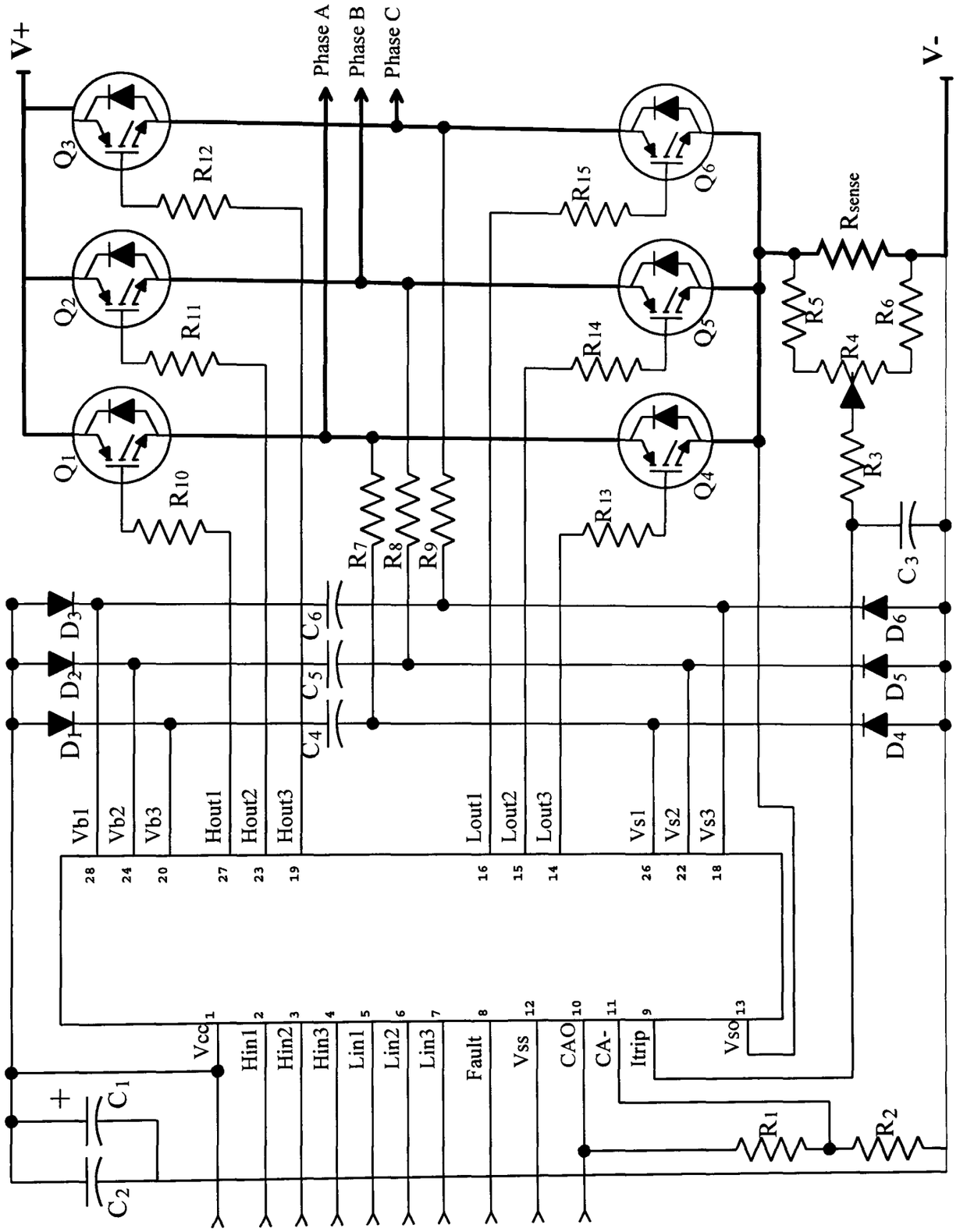

Figure J.1. Schematic diagram of the inverter power electronics and driver.

Appendix K. Photograph of Test-rig

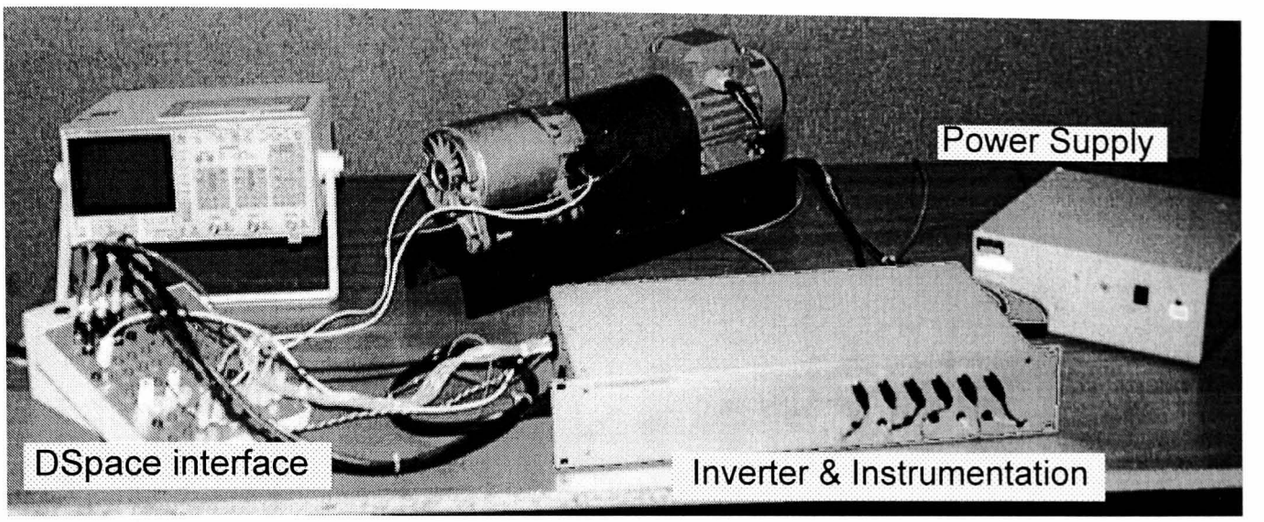

Figure K.1. Photograph of test-rig hardware.

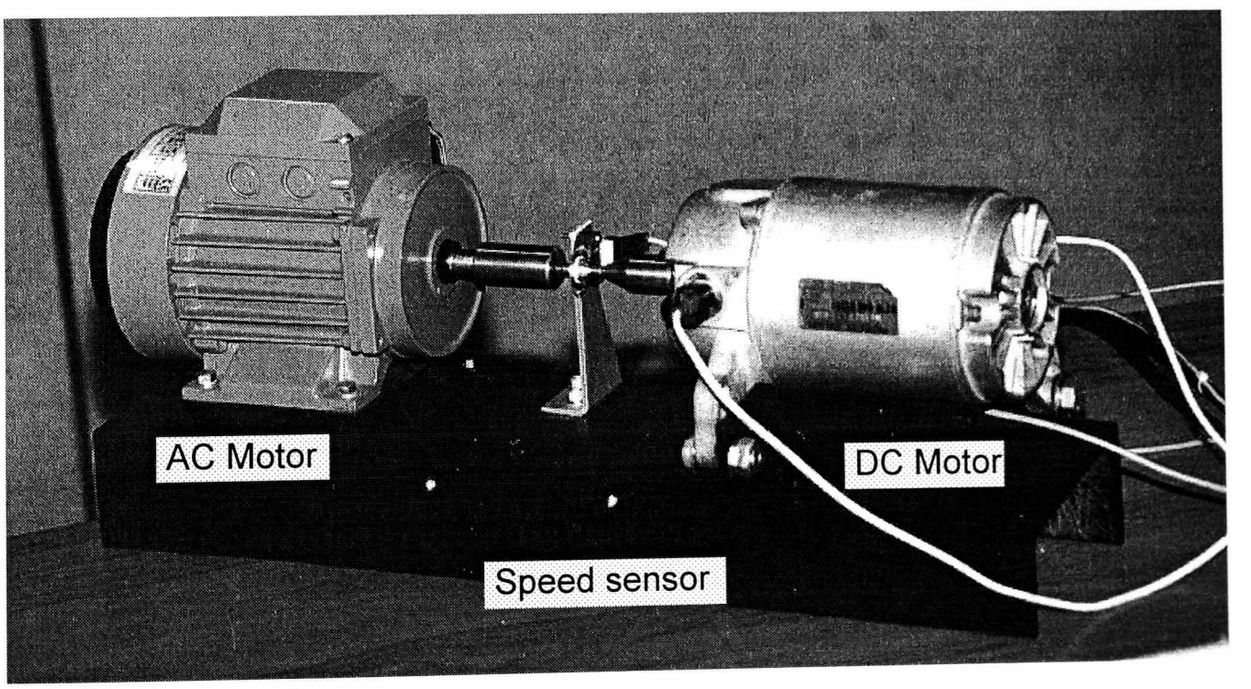

Figure K.2. Close-up of AC Motor and DC load machine, with safety gaurd removed.

Appendix L. Simulink block diagrams of test-rig software

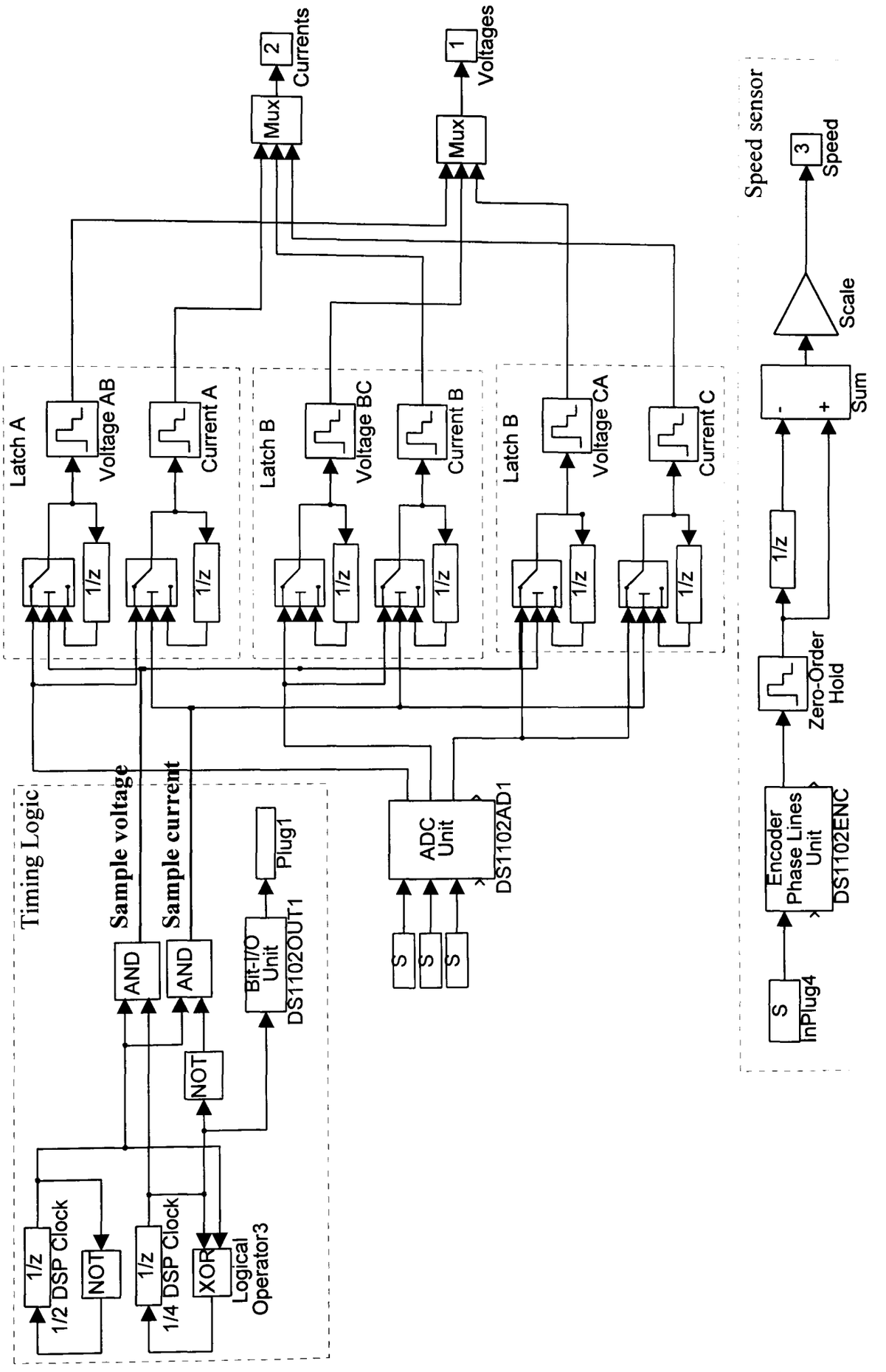

Figure L.1. Simulink block diagram of TDM instrumentation interface, for current and voltage sensors and opto-wheel decoder.

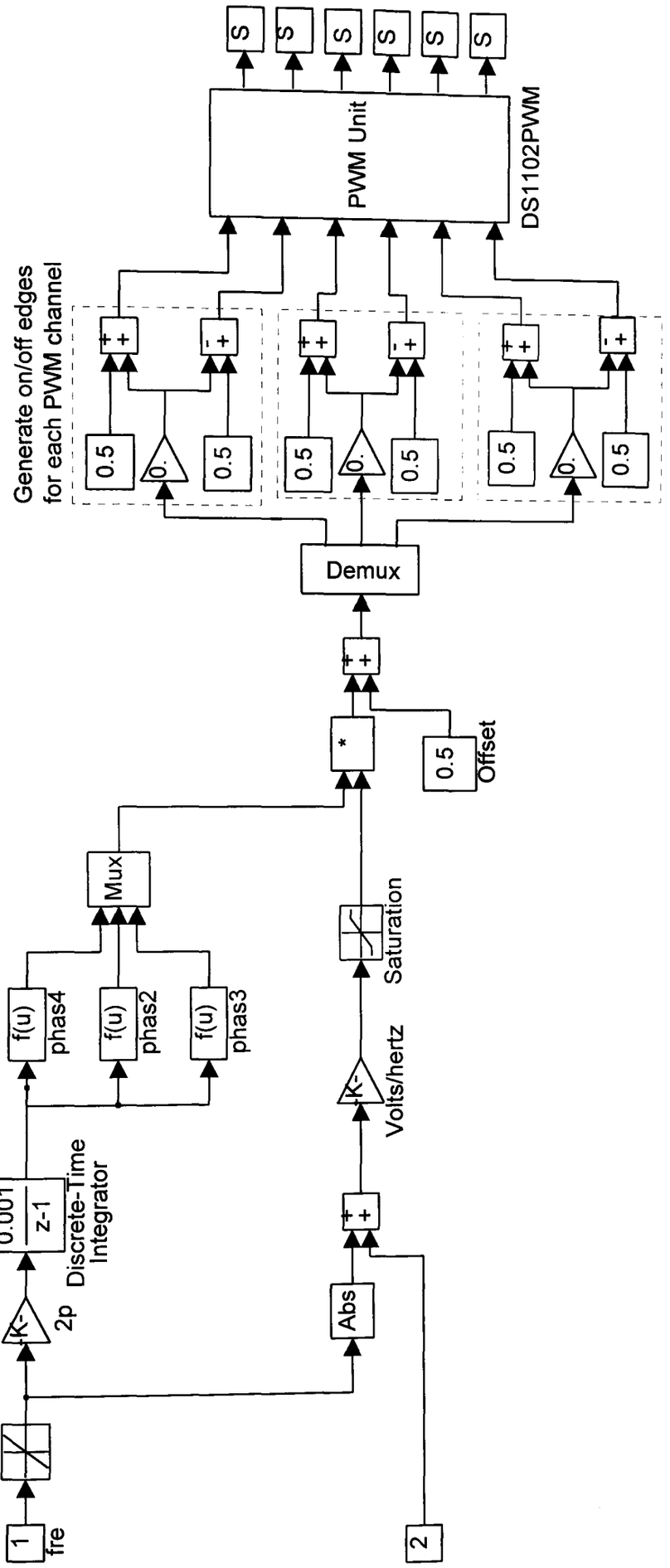

Figure L.2. Simulink block diagram of waveform generators and PWM output.

Appendix M. Mapping between continuous and discrete models

A continuous-time system which is stable in the s-domain is not necessarily stable when transformed into a discrete-time system in the z-domain. The stability in the z-domain requires that the discrete poles of the system are contained within the unit circle. Different continuous-to-discrete transforms map the continuous poles into the z-domain differently.

The forward rectangular rule maps the stable left-land of the s-domain into a column in the z-domain which is not all stable, as shown in Fig. M.1 below.

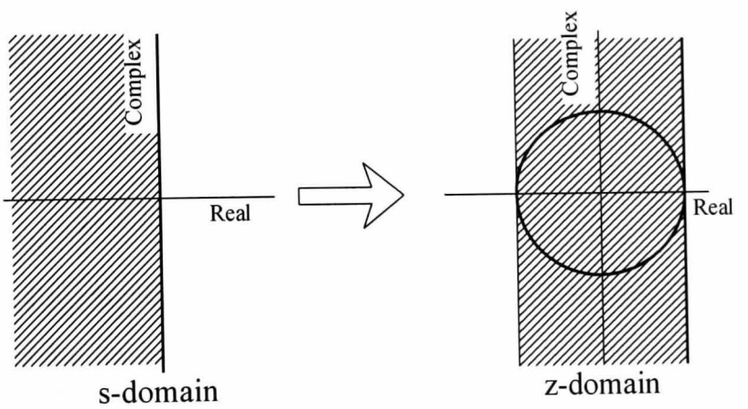

Figure M.1. Graphical representation of mapping between s and z domain using forward rectangular rule.

Tustin's approximation is a more complex transform but it maps the entire left-right plane in the s-domain into the unit circle in the z-domain.

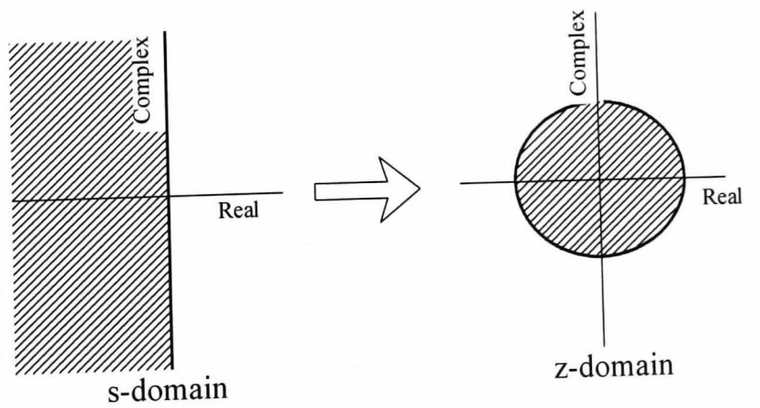

Figure M.2. Graphical representation of mapping between s and z domain using Tustin's approximation.

Appendix N. The Simulink diagrams for the real-time FDI

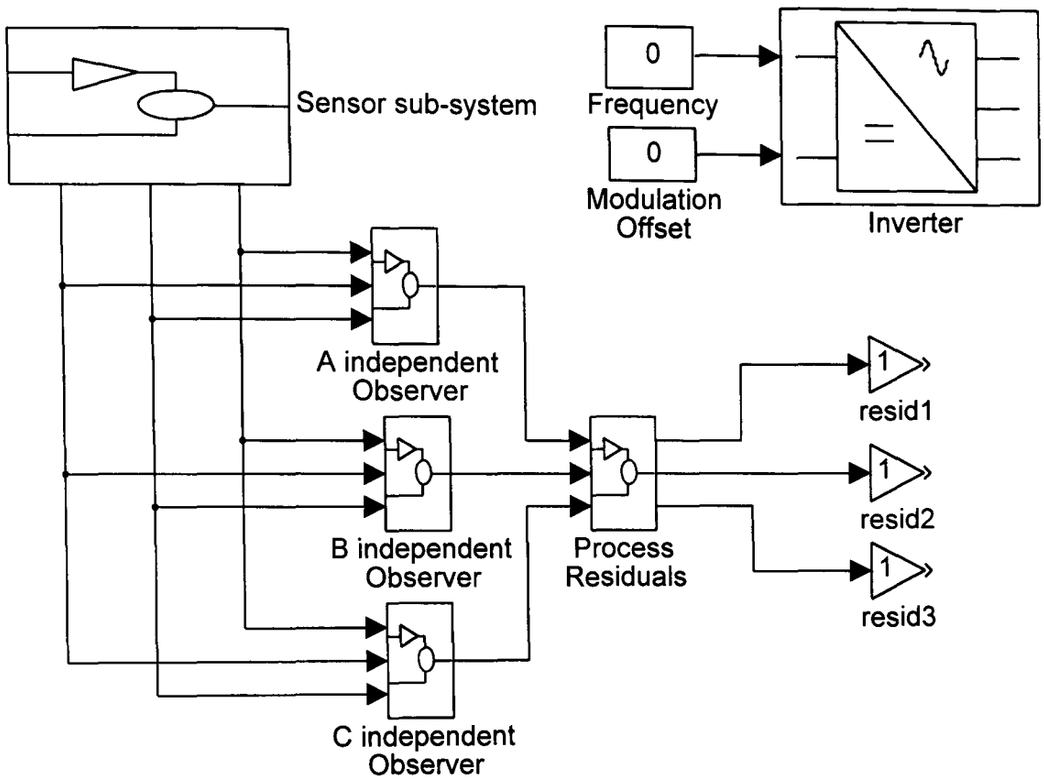

Figure N.1. Top level block diagram of the FDI scheme.

The contents of the inverter and sensor sub-systems is shown in Appendix L.

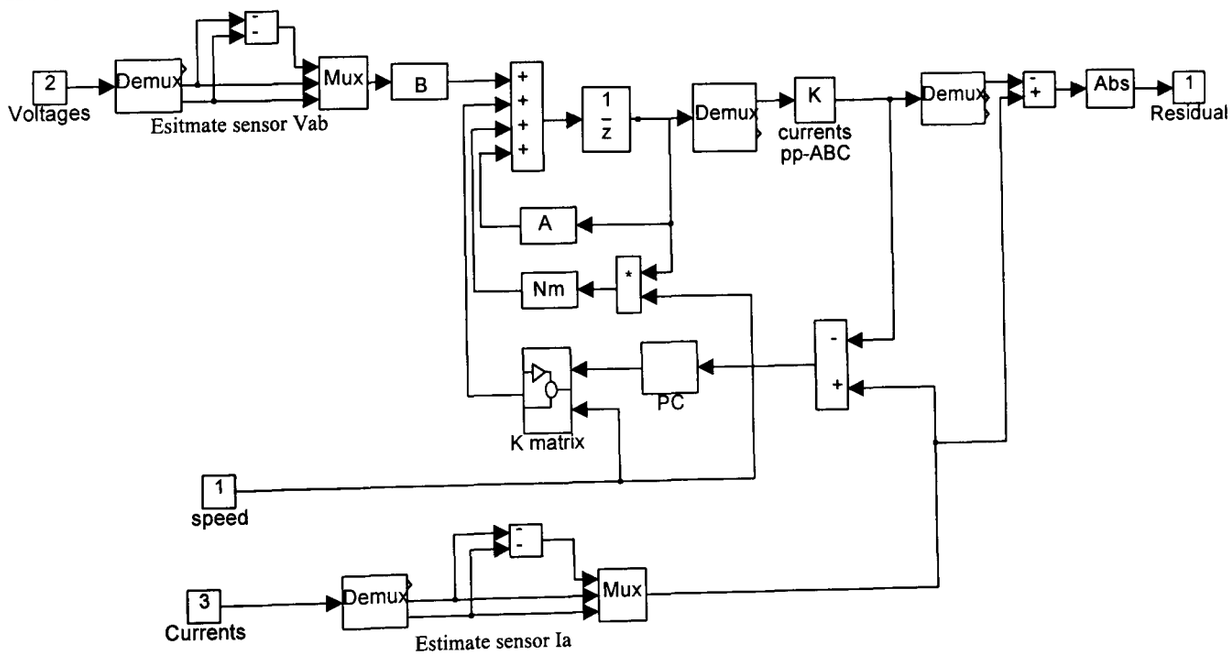

Figure N.2. Simulink block diagram of observer.

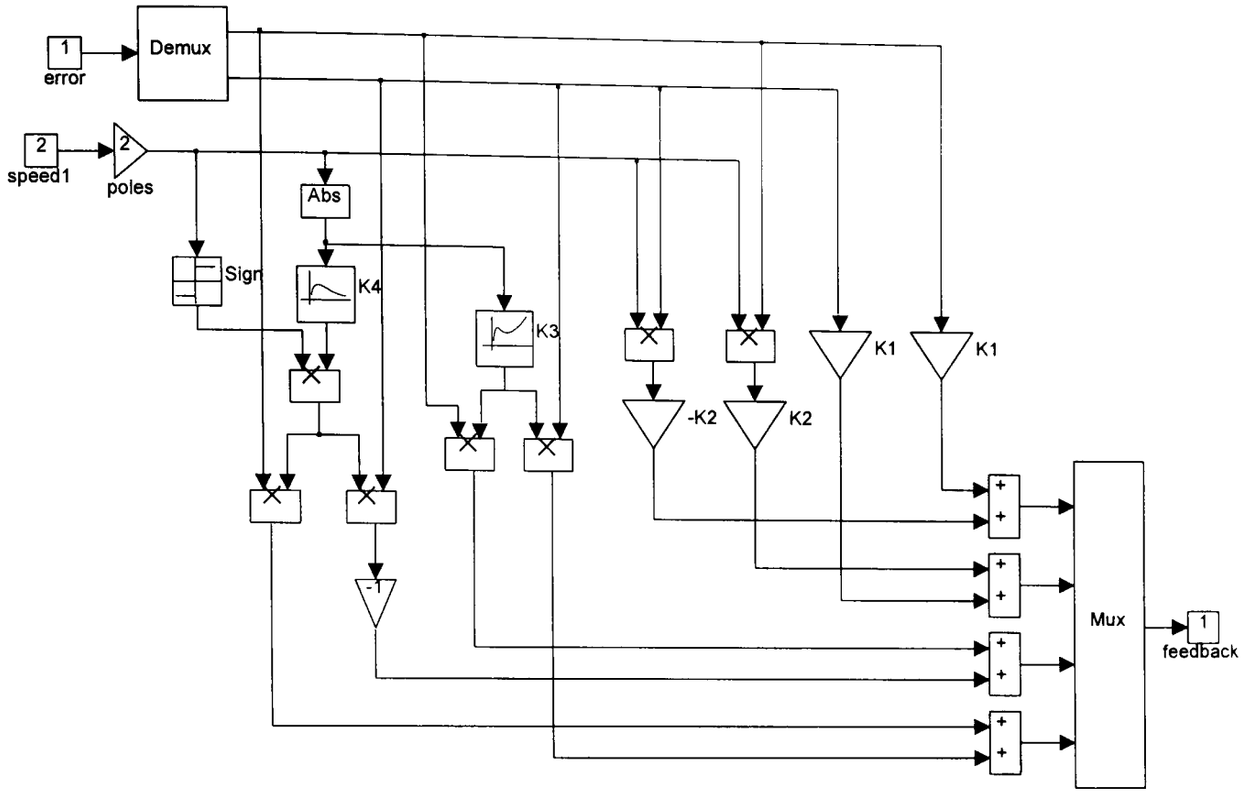

Figure N.3. Simulink block diagram of observer feedback matrix *K* using parametrised feedback

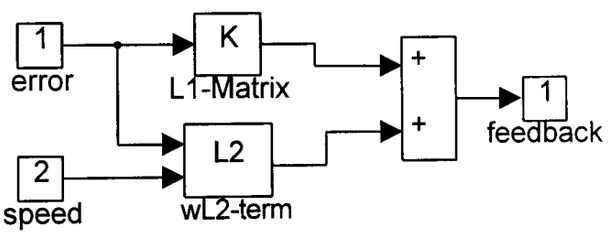

Figure N.4. Simulink block diagram of observer feedback matrix *K* using bilinear feedback.

References

Amin B., (1996), Slot-bassed analysis of induction motors including the effects of space harmonics and magnetic saturation. PEMC Vol. 2 pp356-360

Åström K.J. & Wittenmark B., (1984), Computer Controlled Systems; Theory and Design. Prentice Hall.

Atkinson D., Finch J. and Acarnley P., (1990), A reduced order parameter estimator for vector controlled induction motors. Proceedings of the Universities Power Electronic Conference, UPEC 90, Aberdeen. pp517-520.

Atkinson D., Acarnley P. & Finch J., (1991) Observers for induction motor state and parameter estimation. IEEE Trans. on Industrial Applications. Vol. 27. No 6. pp1119-1127

Bailey D.F., (1995), Once in ten thousand years. International Conference on Electric Railways in a united Europe. IEE Conf. Pub. 405. pp158-160.

Beilharz J. & Filbert D., (1997), Using the functionality of PWM inverters for fault diagnosis of induction motors. Proceeding of the IFAC Symposium SAFEPROCESS '97, HULL, UK, Vol. 1 pp246-251.

Bellini A., Figalli G., & Ulivi G., (1979), Realization of a bilinear observer of the induction machine. Proceedings of 2nd International Conference on electrical variable speed drives, pp175-177

Ben-Brahim L. and Kawamura. A., (1992), Digital Control of induction motor current with Deadbeat response using Predictive State Observer. IEEE Trans. on Power Electronics. Vol. 7, No. 3 pp551-558

Bird I.G & Zelaya-dela-Parra H., (1996), Practical evaluation of two stator flux estimation techniques for high performance torque control. Proceedings of Power Electronics and Variable Speed Drives 23-25 September 1996. IEE Conf. pub. 429 pp465-470

Birk J. & Zeitz M., (1998), Extended Luenberger observers for non-linear multivariable systems. International Journal of Control. Vol. 47 No.6. pp1823-1836.

Blanke M., Izadi-Zamanabadi R. , Bøgh S.A. & Lunau C.P.,(1997), Fault-Tolerant Control Systems: A Holistic View. Control Engineering Practice Vol. 5 pp693-702.

Bose, B.K., (1986) 'Power electronics and AC drives', Published by Prentice Hall

Bottura C.P., Silvino J.L. & de-Resende P., (1993), A flux observer for induction machines based on a time variant discrete model. IEEE Trans. on Industrial. Applications. Vol. 29, No 2. pp349-354

Boyd S., Ghaoui L., Feron E. & Balakrishnan V., (1994), Linear Matrix Inequalities in system and control theory, SIAM Philadelphia. -

Brdys M. & Du T., (1991), Algorithms for joint state and parameter estimation in induction motor drives systems'. Proceedings of CONTROL 91, IEE Conf. Pub. 332, Vol. 2 pp915-920

Brown J.E., Kovacs K.P. & Vas P., (1983), A Method of including the effect of main flux path saturation in the generalised equations of AC machines. IEEE Trans. on Power Apparatus and Systems. Vol. 102 No. 1 pp96-103

Bruce R. & Hatton. T., (1989), Tangra Train management system. Concept Design and experience. State Rail authority of New South Wales, Australia. International Conference on Main Line Railway Electrification. IEE Conf. Pub. 312. pp197-202.

Brudny J.F. & Roger D., (1996), Induction machine speed sensor based on stator current measurement. Proceeding of Power Electronics and Variable Speed drives, IEE Conf. Pub. 429. pp322-327.

Burrage K.W. (1995), Railway safety standards, Railtrack safety & standards directorate. International conference on electric railways in a united Europe. IEE Conf. Pub. 405. pp153-157.

Burth M. & Filbert D., (1997), Fault diagnosis of universal motors during run-down by non-linear signal processing. Proceedings of the IFAC Symposium SAFEPROCESS '97, HULL, UK, Vol. 1 pp426-431.

Chan C. & Huaqian W., (1990), An effective method for rotor resistance identification for high performance induction motor vector control. IEEE Trans. Industrial Electronics Vol. 37, No 6. pp477-482.

Chen J., Patton R.J. & Zhang H., (1996), Design of unknown input observer and fault detection filter. International Journal of Control. Vol. 63 No. 1 pp85-105

Chen. J and Zhang H., (1991), Robust detection of faulty actuators via unknown input observers. International Journal of Control. Vol. 22 No. 10 pp1829-189.

Cho K., Lang J. & Umans S., (1992) Detection of Broken rotor bars in induction motors using state and parameter estimation., IEEE Trans. on Industry Applications, Vol. 30 No.3 pp702-709.

Clark R., (1978), Instrument fault detection. IEEE Trans. on Aerospace and Electronic systems. Vol. 14, No. 3 pp456-465.

Çolak I., S.Garvey & M.T.Wright. Estimation of the induction machine parameters for simulation of a mixed frequency test. Proceedings of the Sixth International Conference on Electrical Machines and Drives. IEE Conf. Pub. 376. pp208-211.

Di-Gerlando A. & Vistoli I., (1993), Improved thermal modelling of induction motors for design purposes. Proceedings on the Sixth International Conference on Electrical Machines and Drives. IEE Conf. Pub. 376, pp381-386.

Dorling C. M. & Zinober A.S.I., (1983), A Comparative study of the sensitivty of observers. Proceedings of the IASTED Symposium on applied control and identification. Copenhagen Vol. 6 pp32-37.

Du T. & Brdys. M.A., (1993), Shaft speed, load torque and rotor flux estimation of induction motor drives using an Extended Luenberger observer. Proceedings of the sixth international conference on Electrical machines and drives. IEE Conf. Pub. 376 pp179-184

Du T, Vas P. & Stronach F., (1995), Design and application of extended observers for joint state and parameter estimation in high performance AC drives. IEE Proceedings on Power Electronic Applications. Vol. 142, No.2 pp71-78

Edwards C. & Spurgeon S.K., (1994), On the development of discontinuous observers, International Journal of Control. Vol. 59, No. 5, pp1211-1229

Edwards. C., Spurgeon S.K.,Patton R.J. & Klotzek P., (1997), Sliding Mode observers for fault detection. Proceedings of the IFAC Symposium SAFEPROCESS '97, HULL, UK, Vol. 1 pp522-527.

Elkasabgy N., Eastman A., & Dawson. G., (1992) Detection of broken bars in the cage rotor on an induction machine. IEEE Trans. on Industry Applications. Vol. 28. No. 1 pp155-170.

Frank P.M., (1991), Enhancement of robustness in observer based fault detection. Proceedings of the IFAC Symposium SAFEPROCESS '91, Baden-Baden, Germany, Vol. 1 pp275-287.

Fry K.N., (1995), Diesel locomotive reliability improvement by system monitoring, British Rail Research. Proceeding of the IMechE, Part F, Vol. 209 pp1-10.

Ferrah A., Bradley K.J., Asher G.M. & Woolfson M.S., (1993), An investigation into speed measurement of induction motor drives using rotor slot harmonics and spectral estimation techniques. Proceedings of the Sixth International Conf. on Electrical Machines and Drives. p185-189

Franklin G.B., Powell J.D. & Emami-Naeini A.,(1995) Feedback control of dynamic systems. Addison-Wesley Publishing

Goode P.V & Chow M., (1995), Using a Neural/Fuzzy system to extract Heuristic Knowledge of Incipient Faults in Inductin Motors: Part I Methology and Part II Application. IEEE Trans. on Industrial Electronics Vol. 42 No. 2. pp131-138 and pp139-146.

Hac. A., (1992), Design of disturbance decoupled observer for bilinear systems. Trans. of ASME. Journal of dynamic system, measurement and control. Vol 114, pp556-562

Hara, S. & Furuta, K., (1976), Minimal order state observer for bilinear systems, International Journal of Control, Vol. 24, pp705-718,

Hari-narayanan N. & Viswanadham N., (1986), A methodolgy for knowledge acquistion and reasoning in failure Analysis of systems.' IEEE Trans. System Man and Cybernetics. Vol. 17, pp274-288

Harrison R. & A. Dare, (1995), The 'Universal' Networker Electric Multiple Unit. ABB Rail Vehicles Ltd, International Conference on Electric Railways in a united Europe. IEE Conf. Pub. 405. pp1-14.

Hou M. & Pugh A.C., (1997), Observing state in bilinear systems: An UIO approach, Proceedings of the IFAC Symposium SAFEPROCESS '97, HULL, UK, Vol. 2, pp789-794.

Isermann R., (1982),. Process Fault Detection based on modelling and estimation methods: A Survey, Automatica Vol. 20 No. 4 pp387-404.

Isermann R. & Ballé P., (1996), Trends in the application of model based fault detection and diagnosis of technical processes. Proceeding of the IFAC 13th World Congress. San-Francisco pp1-12

Isermann R. & Freyermuth B., (1991), Process fault diagnosis based on process knowlegde- Parts I: Principles for fault diagnosis with parameter estimation. Journal of Dynamic Systems Measurement and Control, Trans. of ASME Vol. 133 No. 4 620-626. Part II: Case study experiments. pp627-633

Jahns. T. , (1980), Improved reliability in solid-state AC drives by means of multiple independent Phase-Drive units. IEEE Trans. on Industry Applications. Vol. 16, No. 3, pp321-331

Jansen P.L. & Lorenz R.D., (1994), A physically insightful approach to the design and accuracy assessment of flux observers for field oriented induction machine drives. IEEE Trans. on Industry Applications. Vol. 30 No.1 pp101-109

Jezernik, K. Volcanjk V., Hern A. and Premzl B., (1993), Robust Observer based VSS Tracking control of an IM servodrive. Proceedings of 3rd Conference on Power Electronics and Application. IEE Conf. Pub. 377 Vol.4 pp428-433

Kalker J., (1991), Wheel Rolling contact theory. Wear Vol. 144 pp243-261

Kastha D. & Bose. B., (1994), Investigation of Fault Modes of Voltage-Fed Inverter Systems for induction motor drives. IEEE Trans. on Industry Applications Vol. 30, No 4., pp1028-1037

Kataoka T., Toda S. & Sato Y., (1993), On-line estimation of induction motor parameters by extended Kalman filter. Proceedings of 3rd Conference on Power Electronics and Application. IEE Conf. Pub. 377. Vol. 4. p325-329

Kliman G.B., J. Stein J. & Endicott R.D., (1988), Noninvasive detection of broken bars in operating induction motors, IEEE Trans. on Energy Conversion, Vol.3. No.4 pp873-879

Koegl R., Stein J., & Endicott R., (1988), Non-invasive detection of broken rotor bars in operating induction motors. G.Kliman, IEEE Trans. on Energy Conversion. Vol. 3. No. 4 pp873-879

Köppen-Seliger B. & Frank P.M., (1996), Neural Networks in model-based fault diagnosis. Proceeding of IFAC 13th Triennial world Congress. San Francisco, USA. Vol. X pp67-72

Korbicz J., (1997), Neural networks and their application in fault detection and diagnosis. Proceedings of the IFAC Symposium SAFEPROCESS '97. HULL. UK, Vol. 1 pp377-382.

Ljung, L., (1979), Asymptotic behaviour of the extended Kalman filter as a parameter estimator for linear systems. IEEE Trans. on Automatic Control. Vol. 24 pp. 36-50

Loron L. and Laiberté G., (1993), Application of the extended kalman filter to parameter estimation of the induction motor. Proceedings of 3rd Conference on Power Electronics and Application. IEE Conf. Pub. 377. Vol. 1. pp85-90

Lopez C.J, Benkhedda H. & Patton R.J., (1997), Fuzzy Observers for FDI: Application to bilinear systems. Proceedings of the IFAC Symposium SAFEPROCESS '97, HULL, UK, Vol. 2. pp1148-1152.

Lopez C.J, Patton R.J. & S. Daley., (1998), Fault-Tolerant traction system control using fuzzy inference modelling. IFAC Workshop, Online fault detection and supervision in the Chemical Process Industries. Lyon, France June. Session 2B pp1-5.

McDonald M. & Richards A., (1995),Vehicle health monitoring on the docklands light railway. IEE Colloquium on Advanced condition monitoring systems for railways. Digest No. 1995/161. October.

Melkebeek. J., (1983), Magnetising-field saturation and dynamic behaviour of induction machines, Part 1: Improved calculation method for induction-machine dynamics. IEE Proc. Pt. B Vol. 130. No. 1. pp1-9.

Morrelly C., (1995), Neural morphing and intrinsic health monitoring systems for pre-emptive maintenance, IEE Colloquium on Advanced condition monitoring systems for railways. Digest No. 1995/161. October 1995.

Morris A.J. and Martin E.B., (1997), Process Performance monitoring and fault detection through multivariate Statistical Process Control. Proceedings of the IFAC Symposium SAFEPROCESS '97, HULL, UK, Vol. 1 pp.1 -14

Mylroi I., (1995), Reliability growth of the Networker fleet. Network train engineering services, International conference on electric railways in a united Europe. IEE Conf. Pub. 405. pp183-185.

Nagase K., (1989), A Study of adhension between the rails and running wheels on main lines: results of investigations by slipping adhension test bogie. Proceedings of the IMechE. Part. F. Vol. 203. pp33-43

Natarajan. R., (1989), Failure identification of induction motors by sensing unbalanced stator currents, IEEE Trans. on energy conversion. Vol. 4. No. 4 pp585-589

Newton D.A., (1995), Advanced Traction and Braking Systems. GEC Review Vol.10 No.2 pp72-80

Orlowska-Kowalska T., (1989), Application of the extended luenberger observer for flux and rotor time-constant estimation in induction motor drives. IEE Proc. Vol. 136 Pt. D pp324-330

Papadopoulos M.P., Papathanassiou S.A. and Tentzerakis S.T., (1996), Modelling of induction machine main flux saturation in the arbitrary reference frame - A case study on wind turbine self-excitation. Proceedings of the Int. Conf. on Electrical Machines. Vol. 2 pp51-57.

Parkin T.S. and Preston T.W., (1993) Induction motor analysis using finite elements. , GEC Alsthom ERC. Proceeding on the 6th International Conference on Electrical machines and drives. IEE Conf. Pub. 376, pp20-24.

Patton R.J., (1997), Robustness in model-based fault diagnosis: The 1997 situation. Annual Reviews of Control. Vol. 21 pp101-121.

Patton R.J. and Chen J., (1993), A Survey of robustness problems in quantitative model-based fault diagnosis. Applied Mathematics and computer science. Vol. 3 No. 3. pp399-416

Patton R.J., Chen J. & Nielsen S.B., (1995), Model-based methods for fault diagnosis: some guide-lines. Transactions of the Institute of measurement and control. Vol. 17 No. 2 pp1-11

Patton R.J., Frank P.M. & Clark R.N. (Eds), (1998), Advances in Fault Diagnosis for dynamic systems. Springer-Verlag. London.

Patton R.J., (1997), Fault Tolerant control: The 1997 situation. Proceedings of the IFAC Symposium SAFEPROCESS '97, HULL, UK, Vol. 2 pp1033-1055.

Pena R.S. & Asher G.M., (1993), Parameteer sensitivity studies for induction motor parameter identification using extended kalman filters. Proceedings of 3rd Conference on Power Electronics and Application IEE Conf. pub. 377 Vol.4 pp306-311.

Ploix S., Villiere C. & Ragot J., (1997), Discrete time models of induction machines with additive uncertainties. Proceedings of the IFAC Symposium SAFEPROCESS '97, HULL, UK, Vol. 1 pp264-269.

Pouliezos A.D. & Stavrakakis G.S., (1994), Real-Time Fault Monitoring of Industrial Processes. Kluwer Academic Publishers.

Preston K., (1995), Vehicle systems monitoring technology at BR Research. BR Research. IEE Colloquium on Advanced Condition Monitoring Systems for Railways. Digest No. 1995/161.

Protiwa F.F., Apeldoorn O. & Groos N., (1993), New IGBT Model for Pspice. Proceeding of 3rd Conference on Power Electronics and Application Vol.2 pp226-231 IEE Conf. pub. 377

Quevedo J., Guasch A. & Milne R., (1997), Controller based diagnosis for gas turbines. Proceeding of SafeProcess97. Vol. 1 pp60-65.

Rae-Cho K., Jeffrey H. & Umans S.D., (1992), Detection of broken rotor bars in induction motors using state and parameter estimation. IEEE Trans. on Industry Applications, Vol. 28, No.3 pp702-707

Rasmussen H., (1995), Self-tuning Torque Control of Induction Motors for High Performance Applications. Ph.D Thesis. Department of Control Engineering, Aalborg University.

Rasmussen H., Knudsen M. & Tønnes M., (1996), Parameter Estimation of inverter and motor model at standstill using measured currents only. Proceedings of the IEEE International Symposium on Industrial Electronics, Poland.. Vol. 1 pp331-336.

Rasphorst A., Netten B., & Vingerhoed R., (1995), Automated fault tree generation for operational fault diagnosis. International conference on electric railways in a United Europe. IEE Conf. Pub. 405. p173-177.

Roberts R., (1989), Propulsion and friction braking diagnosis and self test capabilities. AEG Westinghouse Transportation Systems Inc. International Conference on Main Line Railway Electrification IEE Conf. Pub. 312. pp63-66.

Sabanovic A. & Izosimov D., (1981), Application of sliding modes to induction motor control. Vol. 17 No. 1, pp41-48

Salvator P.L. & Trotta A. (1988) Flat-top window for PWM waveform processing via DFT. IEE Proceedings Pt. B Vol. 35 No. 6 pp349-361 .

Sarker D., Murkherfer P. & Sen S., (1991), Use of 3D finite element analysis for compatution of the temperature distribution in the stator of a induction motor. IEE Proceedings Pt. B Vol. 138 No. 2 pp75-86.

Sathiakumar S., Rajashekara K.S. & Baburaj K.V., (1996), A novel speed estimator for high performance speed control of an induction motor. PEMC Vol. 2 pp210-214.

Say M. G., (1963), The performance and design of alternating current machines. 3rd Edition. Chapter 14, Induction motor testing. Published by Pitmans Press.

Schierling H., (1988), Self-Commissing - A Novel feature of modern inverter-fed induction motor drives. Proceedings 3rd International conference on Power Electronics and Variable speed drives. IEE Conf. Pub. 291. pp287-290.

Schneider H. & Frank P.M., (1996), Observer-Based Supervision and Fault Detection in Robots Using Non-linear and Fuzzy Logic Residual Evaluation. IEEE Trans on Control Systems Technology Vol. 4 No. 3 pp274-282

Scot-Smith K., Ran L. & Penman. J., (1997) Real-time detection of intermittent Mis-fire in a voltage fed PWM invertor induction motor drive. IEEE Trans. Industrial Electronics Vol. 44, No. 4, pp468-476

Shields D & Yu D., (1995), 'A review of observer approaches for fault diagnosis based on bilinear systems. IEE colloquium, York 1995, IEE Digest 1995/079

Shirsavar S.A. & McCulloch M.D., (1996). Speed sensorless vector control of induction motors with parameter estimation. Proceedings of Power Electronics and Variable Speed Drives. Sept 1996. IEE Conf. Pub. 429. pp267-272.

Shyu K. & Shieh H., (1995), Variable structure current control for induction motor drives by space voltage vector PWM. IEEE Trans. on Industrial Electronics Vol. 42, No. 6. p572-577.

Siu C., Shen Q. & Milne R., (1997), TM-Doctor: A fuzzy rule and Case-Based Expert Systems for turbomachinery diagnosis. Proceedings of the IFAC Symposium SAFEPROCESS '97, HULL, UK, Vol. 1 pp556-563.

Slotine J. J. E. , Hedrick J.K. and Misawa E. A., (1987), On sliding observers for non-linear systems. Journal of Dynamics Systems, Measurement and Control. Vol. 109, pp245-252

Takagi T. and Sugeno N., (1985), Fuzzy identification of systems and its applications to modelling and cotrol. IEEE Trans. on Systems Man and Cybernetics. Vol 15.No. 1 pp116-132

Tavner P., Gaydon B. and D.Ward., (1982), Monitoring generators and large motors. IEE Proceedings. Pt. B Vol.133 No. 3 pp169-180.

Wade S., Dunnigan M. and B. Williams., (1994), Parameter identification for vector controlled induction motors. Proceedings of Control 94, IEE Conf. Pub. 389 pp1187-1192

Walcott. B.L., Corless M.J. and Zak S.H., (1987), Comparative study of non-linear state-observation technique. International Journal of Control. Vol 45, No.6. pp2109-2132.

Wang H., Kropholler H. and Daley S., (1993), Robust observer based FDI and its application to monitoring a distillation column'. Trans. of the Institution of Measurement and Control. Vol. 15 No. 5 pp221-227

White T., (1996), Compensation for the skin effect in vector controlled induction motor drives systems. 7th International Conf on electrical machines and drives. IEE Conf. Pub. 412 pp301-307 1995

Williamson S. and Ralph J., (1983), Finite Element analysis of an induction motor fed from a constant-voltage source. IEE Proceedings Pt. B Vol. 130. No. 1. pp18-24.

Willis J.R., Brock, G. J. and Edmons, J. S., (1989), Deriviation of induction model models from standstill frequency response tests. IEEE Trans. on Energy Conversion Vol. 4 pp608-615.

Utkin, V.I., (1992), Sliding Modes in Control Optimisation published Berlin: Springer-Verlag.

Yoo H. & Ha I., (1996), A polar coordinate-oriented method of identifying rotor flux and speed of induction motors without rotational transducers. IEEE Trans. on control systems technology. Vol. 4. No.3 pp230-243

Young P., (1981), Parameter estimation for continuous time models, A survey. Automatica Vol. 17 No. 1 pp23-39.

Yu, D. & Shields D.N., (1995), Fault diagnosis in bilinear systems - A Survey. Proceedings of the 3rd European Control Conference, pp360-365.

Zhang J., Morris A.J. & Martin E.B., (1996), Robust process fault detection and diagnosis using neuro-fuzzy networks.. Proceeding of IFAC 13th Triennial world Congress. San Francisco 1996. Vol. X pp169-174.

Zamora J.L. & Garcia-Cerrada A., (1996) Rotor speed estimation for induction motor drives. Proceedings of the International Conference on Electrical Machines, Vigo, Spain.Vol 2. pp180-185 ,

Zhao Y & T. Lipo., (1996), Modelling and control of a multi-phase induction machine with structure umbalance. IEEE Trans. Energy Conversion. Vol. 11, No.3 pp570-584

International Rectifer Datasheets.

Limjuco G. & Wilhelm D., (1996), DT 93-6B Miniaturisation of the power electronics for motor drives. International Rectifier Control Intergrated Circuits Designer's Manual. C89-95

AN-985B. Six Output 600V Drivers Simplify Three-Phase Motor Drives for Low / High-side Switching. Control Intergrated Circuits Designer's Manual. C33-40

Clemente S., (1996), Application Characterisation of IGBTs. Control Intergrated Circuits Designer's Manual. C33-40

AN990 C41-C58